ILMENAU UNIVERSITY OF
TECHNOLOGY

Faculty of Electrical Engineering and Information Technology
Institute for Microelectronics and Nanoelectronics
Department of Microelectronic and Nanoelectronic Systems

BERKELEY LAB
ERNEST ORLANDO LAWRENCE
BERKELEY NATIONAL LABORATORY

A U.S. Department of Energy National Laboratory operated by the University of California
The Molecular Foundry
Imaging and Manipulation of Nanostructures Facility

Fabrication and characterization of self-sensing and self-actuating piezoresistive microscale silicon cantilevers for an integrated scanning probe microscopy and scanning electron microscopy system

PhD thesis

author:
Dipl.-Ing. Ute Wenzel

supervisor:
Univ.-Prof. Dr.-Ing. habil. Ivo W. Rangelow
Dr D. Frank Ogletree

21st June 2011

urn:nbn:de:gbv:ilm1-2012000108

Fabrication and characterization of self-sensing and self-actuating piezoresistive microscale silicon cantilevers for an integrated scanning probe microscopy and scanning electron microscopy system

Disseration
zur Erlangung des akademischen Grades
Doktoringenieur (Dr.-Ing.)

vorgelegt der Fakultät für Elektrotechnik und Informationstechnik
der Technischen Universität Ilmenau

von Dipl.-Ing., Wenzel, Ute
geboren am 19.10.1982 in Hildburghausen (Thüringen, Deutschland)

vorgelegt am: 21.06.2011

Gutachter:

1. Univ.-Prof. Dr.-Ing. habil. Ivo W. Rangelow
   (Fachgebiet für Mikro- und Nanoelektronische Systeme, Fakultät für Elektrotechnik und Informationstechnik, Technische Universität Ilmenau, Ilmenau, Thüringen, Deutschland)
2. Dr D. Frank Ogletree
   (Imaging and Manipulation Facility, The Molecular Foundry, Ernest Orlando Lawrence Berkeley National Laboratory, Berkeley, California, USA)
3. prof. PWr dr hab. inz. Teodor P. Gotszalk
   (Wydziałowy Zakład Metrologii Mikro- i Nanostruktur, Wydział Elektroniki Mikrosystemów i Fotoniki, Politechnika Wrocławska, Wrocław, Województwo dolnośląskie, Polska)

Verteidigung am: 02.02.2012

Verf.-Nr.: EI

urn:nbn:de:gbv:ilm1-2012000108

By three methods we may learn wisdom:
First, by reflection, which is noblest;
Second, by imitation, which is easiest;
And third by experience, which is the bitterest.

Confucius

Contents

1 Introduction **1**
- 1.1 Motivation . . . 1
- 1.2 State of the art . . . 3

2 Theory **5**
- 2.1 Introduction . . . 5
- 2.2 Self-actuation of cantilever . . . 6
  - 2.2.1 Bimorph effect . . . 6
  - 2.2.2 Drive power . . . 7
  - 2.2.3 Heat transfer . . . 8
  - 2.2.4 Temperature profile . . . 10
  - 2.2.5 Thermal time constant . . . 14
  - 2.2.6 Pure beam bending . . . 16
  - 2.2.7 Beam oscillation . . . 23
  - 2.2.8 Actuation efficiency . . . 33
- 2.3 Self-sensing of the cantilever . . . 33
  - 2.3.1 Piezoresistive effect . . . 33
  - 2.3.2 Wheatstone bridge . . . 38
  - 2.3.3 Deflection sensitivity . . . 40
- 2.4 Influence on cantilever performance . . . 41
  - 2.4.1 Change of beam temperature . . . 41
  - 2.4.2 Noise . . . 42
    - 2.4.2.1 Thermomechanical noise . . . 42
    - 2.4.2.2 Electrical noise . . . 44
    - 2.4.2.3 Noise reduction . . . 45
  - 2.4.3 Air damping . . . 47
  - 2.4.4 Capacitive crosstalk . . . 51

3 Fabrication process **55**

4 Characterization and imaging **81**
- 4.1 Introduction . . . 81
- 4.2 Measurement . . . 81
  - 4.2.1 Set-up . . . 81
  - 4.2.2 Measurement configuration . . . 85
  - 4.2.3 Measurement errors . . . 88
- 4.3 Performance of the self-actuating and self-sensing piezoresistive microscale silicon cantilever . . . 89
  - 4.3.1 Pre-bending . . . 89
  - 4.3.2 Fundamental frequency . . . 90
  - 4.3.3 Quality factor . . . 92
  - 4.3.4 Deflection at pure beam bending . . . 94
  - 4.3.5 Amplitude of beam oscillation at fundamental frequency . . . 94
  - 4.3.6 Actuation efficiency . . . 96
  - 4.3.7 Deflection sensitivity . . . 96
  - 4.3.8 Thermal time constant . . . 97
  - 4.3.9 Pressure dependency of cantilever performance . . . 99
  - 4.3.10 Noise . . . 100
  - 4.3.11 Capacitive crosstalk . . . 101
  - 4.3.12 Summary . . . 102
- 4.4 AFM imaging . . . 103
  - 4.4.1 Tip forming . . . 103
    - 4.4.1.1 Tip sharpening by FIB . . . 103
    - 4.4.1.2 Tip growing by electron beam deposition . . . 103
  - 4.4.2 FM-AFM imaging in vacuum . . . 104

5 Conclusion **111**

6 Acknowledgements **113**

7 Publications **115**

8 Abstract **117**
8.1 English abstract 117
8.2 German abstract 118

9 Theses **119**

10 Affidavit **121**

11 Curriculum vitae **123**

Appendices **125**
Nomenclature 132
Acronyms 134
Bibliography 142
List of Figures 144
List of Tables 146

1 Introduction

1.1 Motivation

Today, science and industries widely use information gained from investigation on the nanoscale to develop new techniques, materials, and devices, or to improve existing ones. One of the foremost tools for characterization and manipulation of surfaces on micro- and nanoscale, far beyond the optical diffraction limit, is atomic force microscopy (AFM). The first atomic force microscope (also abbreviated to AFM) was demonstrated by Binnig et al. [1] in 1986. It consists of a batch-fabricated cantilever [2, 3] with a sharp tip at its free end that is used to scan a surface. When the tip is brought into the proximity of a surface, forces between tip and surface lead to beam deflection in accordance with Hooke's law. These forces may be those of mechanical contact, van der Waals, capillary, chemical, electrostatic, and magnetic forces among others. They enable not only topography to be measured with atomic resolution [4, 5] but also mechanical, electrical, or magnetic properties [6, 7]. Traditionally, beam deflection has been measured using a laser beam reflected from the back of the cantilever onto an array of photodiodes. This method is referred to as optical beam deflection detection.

An AFM has several advantages over an electron microscope. First of all, it provides a three-dimensional surface profile. Unlike electron microscopes and scanning tunnelling microscope (STM), AFM does not require the specimen surface to be conductive. The addition of such metal or carbon coatings will change or damage surfaces before characterization. AFM operates without need of a vacuum environment. The freedom gives to work in air or even in liquid has made AFM essential for the study of living organisms in life sciences [8, 9].

However, use of AFM does have its limitations. The image size of a single scan is quite small and the scanning speed low compared to electron microscopes and STM. For improvement, arrays of parallel cantilevers have been introduced and shown to be capable of parallel imaging [10], data storage [11, 12], nanoscale lithography [13, 14], and patterning [15]. Fast scanning AFM designs have also been developed [8, 16, 17]. Crucial disadvantages of conventional AFM are the size of the instrument and the skill and knowledge demanded of the operator. Optical beam deflection detection comprises several optical components that require precise alignment and must be accessed from different sides. They take up a lot of instrument space. This is problematic in a sealed vacuum chamber or at low temperatures where maintenance of precise optical component alignment is difficult. Without these disadvantages applications of AFM would be beneficial in routine examination during fabrication processes and parallel cantilever processing for manufacturing in industries, biomedical investigation in hospitals or imaging inside an electron microscope, a scanning electron microscope (SEM) for instance. The latter combination would offer several opportunities. The specimen surface could be scanned two ways, in AFM and SEM mode, providing more diverse information. SEM gives an overview within a short time and AFM scans the area of interest in detail. Since the whole examination is done in one place with no need to change instruments, the spot is not lost and a later, time-consuming search for it is avoided. Depending on the type of preparation of the tip, several AFM methods including measurement of mechanical, electrical, and magnetic properties are possible. If the tip is conductive, even STM is feasible. Then, the sample surface is not only characterized but also manipulated, i.e. lithographed. Conditions such as temperature, pressure, and gas may be controlled enabling further investigation. Since all these AFM methods and STM require a cantilever, which is also considered a probe, they are grouped under the term scanning probe microscopy (SPM).

To enable these beneficial applications and open up new ones, the complexity of AFM must be reduced. To reduce the instrument size and increase the ease of use, new methods of beam deflection detection and beam actuation have been introduced. Interferometric [18], piezoelectric [19], capacitive [20, 21], magnetomotive [22], thermal [23], or piezoresistive [16, 24–29] techniques have been made to serve for integrated beam displacement sensing, also integrated beam actuation mechanisms have been created, such as electrostatic [20], electromagnetic [30], piezoelectric [16, 25, 31, 32], or thermal bimorph actuation [27, 33–36]. With actuation and sensing integrated into the cantilever, i.e. with a self-actuating and self-sensing cantilever, the size of the AFM is much reduced and the handling is simplified, because neither a laser system nor precise alignment is necessary.

Integration of the sensing and actuation into the cantilever offers improvements and innovations. If the cantilever is self-actuating and self-sensing, it can be used for mass and chemical sensing [37, 38]. Each cantilever of an array is separately actuated and its deflection detected. By contrast, it is almost impossible to install optical beam deflection detection in the case of a cantilever array. In the innovative design, the AFM can be made so small as to be portable. Use of AFM in liquid is facilitated, since the deflection signal will not be distorted by optical diffraction and will not depend on the transparency of the liquid as would be true of a laser beam. Indeed, there is no laser beam to damage the surface. The imaging of living cells at video rates to investigate their behaviour and reaction to manipulation is one of the visions of the future, in which a high speed AFM with a self-actuating and self-sensing cantilever will be able to compete with real-time electron microscopy.

The aim of the present PhD thesis research work was to fabricate and characterize a self-actuating and self-sensing piezoresistive microscale silicon cantilever with an electrically shielded conductive tip (Figure 1.1) to be used for AFM, set-up inside a SEM. The integration of actuation and detection into the cantilever makes the AFM so small, that it may easily be built up into a SEM. The electrically shielded conductive tip makes STM possible. An example of this completely new combination of SPM and SEM is demonstrated. Although a commercially available system combining SEM, AFM, and focused ion beam (FIB) was presented recently [39], the detection there still depends on optical beam deflection detection.

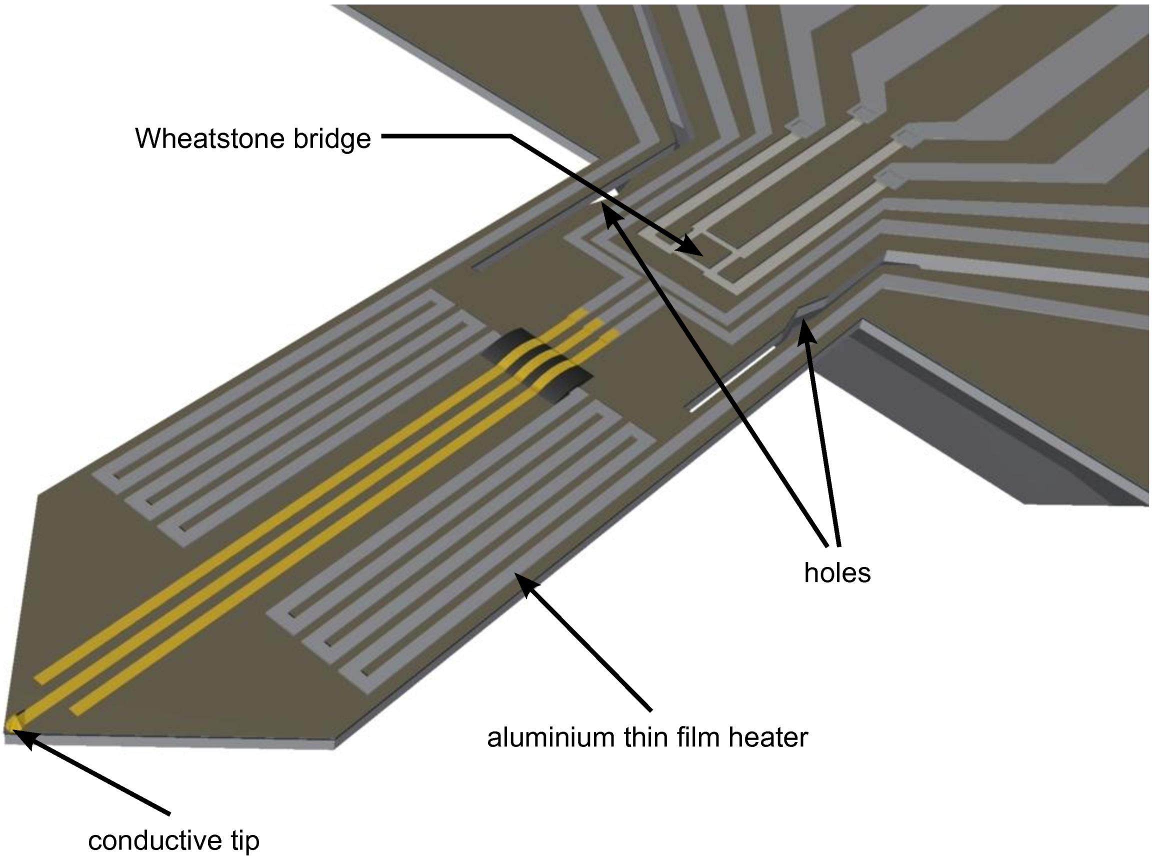

Figure 1.1: Self-actuating and self-sensing piezoresistive microscale silicon cantilever

In the present system, the self-actuation is thermally based and exploits the bimorph effect using an aluminium thin film heater at the free end of the cantilever, the self-sensing relies on the piezoresistive effect: a Wheatstone bridge is integrated into the beam support. Holes next to the Wheatstone bridge increase the stress in the cantilever and improve the self-sensing. The new feature of the conductive tip is the fact that tip and cantilever are a single item. The integration of actuation and sensing integration into the cantilever is already a huge advantage. However, the intention is that the beam deflection detection by piezoresistive means should be as sensitive as that by optical means. To this end, properties of the self-actuating and self-sensing piezoresistive microscale silicon cantilever with an electrically shielded conductive tip are determined in the present work and the self-actuation and self-sensing performance is extensively characterized. These characteristics define the suitability for any application.
The PhD thesis research work was carried out at

- Ilmenau University of Technology (Ilmenau, Thüringen, Germany): Faculty of Electrical Engineering and Information Technology, Department of Microelectronic and Nanoelectronic Systems, supervisor: Univ.-Prof. Dr.-Ing. habil. Ivo W. Rangelow
- Ernest Orlando Lawrence Berkeley National Laboratory (Berkeley, California, USA): The Molecular Foundry, Imaging and Manipulation of Nanostructures Facility, supervisor: Dr D. Frank Ogletree

and constitutes one element of the project PRONANO which is concerned with technology for the production of massively parallel intelligent cantilever probe platforms for nanoscale analysis and synthesis and which is funded by the European Commission within the 6^{th} framework programme (IP 515739-2 PRONANO).

1.2 State of the art

Currently, beam defelection detection is a major issue in cantilever operation. Among the alternatives to the optical technique, piezoresistive displacement sensing is the most common approach, mainly because of the high sensitivity of subnanometer detectable deflection [24] and its ease of fabrication and implementation. This type of sensing was invented by Tortonese *et al.*[24, 40] at the beginning of the 1990s and is based on the change in piezoresistivity due to mechanical stress caused by bending of the self-actuating and self-sensing piezoresistive microscale cantilever. Tortonese *et al.* started with a uniformly doped cantilever serving as one piezoresistor connected to an external Wheatstone bridge and found that the piezoresistive layer must be made shallow close to the surface where the stress is maximum. For an ultra-shallow piezoresistive layer either a passivating oxide was grown before ion implantation [41], the implant energy was lowered [42] or the piezoresistor was epitaxially grown [43–45]. Ried *et al.*[42] placed the piezoresistor at the cantilever base because this is the region where the bending stress is at its maximum, so that the piezoresistive sensor is at its most sensitive at this position [46]. In addition, Manalis *et al.* [16] integrated a ZnO piezoelectric actuator at the fixed end of the cantilever and were thus the first to produce a self-actuating and self-sensing cantilever in 1996. Lutwyche *et al.*[11] put three additional piezoresistors on the chip so as to form an integrated Wheatstone bridge. A highly symmetrical full Wheatstone bridge was placed on the chip by Thaysen *et al.*[47], with two piezoresistors on the cantilever, one for detection and one as reference, and two on the substrate. The symmetry significantly decreases non-linearities of the deflection signal. Duc *et al.*[48] presented a cantilever with two resistors located on the beam for stress sensing and two others on the chip used in a Wheatstone bridge configuration. Isolation holes were introduced by Lu *et al.*[49] to separate actuator and piezoresistive detector both mechanically and thermally.

Rangelow's group already started with a fully integrated piezoresistive Wheatstone bridge for deflection sensing located at the base of the cantilever [26, 50]. The cantilever was oriented along the <110> in-plane crystallographic axis of silicon, where the piezoresistive effect is maximum. With the integration of a tip, the capability of AFM and lateral force microscopy was demonstrated right away [51–54]. To increase the sensitivity, a hole was placed at the centre of the bridge, because this concentrates the mechanical stress in the area of the piezoresistors [55]. An aluminium thin film heater at the free end of the cantilever was used for beam deflection that is thermally based and exploits the bimorph effect [35]. The advantage is that there is no external beam actuation such as a piezoelectric quartz crystal mounted onto the cantilever. Depending on application, advantegeous new features have been introduced. A conductive tip that is electrically isolated from the beam has been implemented to perform electrostatic force and scanning capacitance microscopy [56]. The integration of the heater has enabled calorimetry [57, 58]. Functionalized cantilevers were demonstrated to be capable of chemical sensing [37, 38]. Biological samples were imaged in fluid [9]. Shear force microscopy has been demonstrated [59]. Eventually, self-actuating and self-sensing cantilevers have also been implemented in an array so as to be independently controllable [60].

2 Theory

2.1 Introduction

The self-actuating and self-sensing piezoresistive microscale silicon cantilever is a composite beam made of multiple material layers (Figure 2.1). The biggest layer is the silicon (Si) layer at the bottom. Its surface on top is covered by isolating layers of silicon dioxide (SiO_2) and silicon nitride (Si_xN_y). The aluminium (Al) thin film heater is placed at the free end of the beam. Chromium (Cr) and gold (Au) layer are for the conductive tip and conducting traces. The beam is fixed to the cantilever chip.

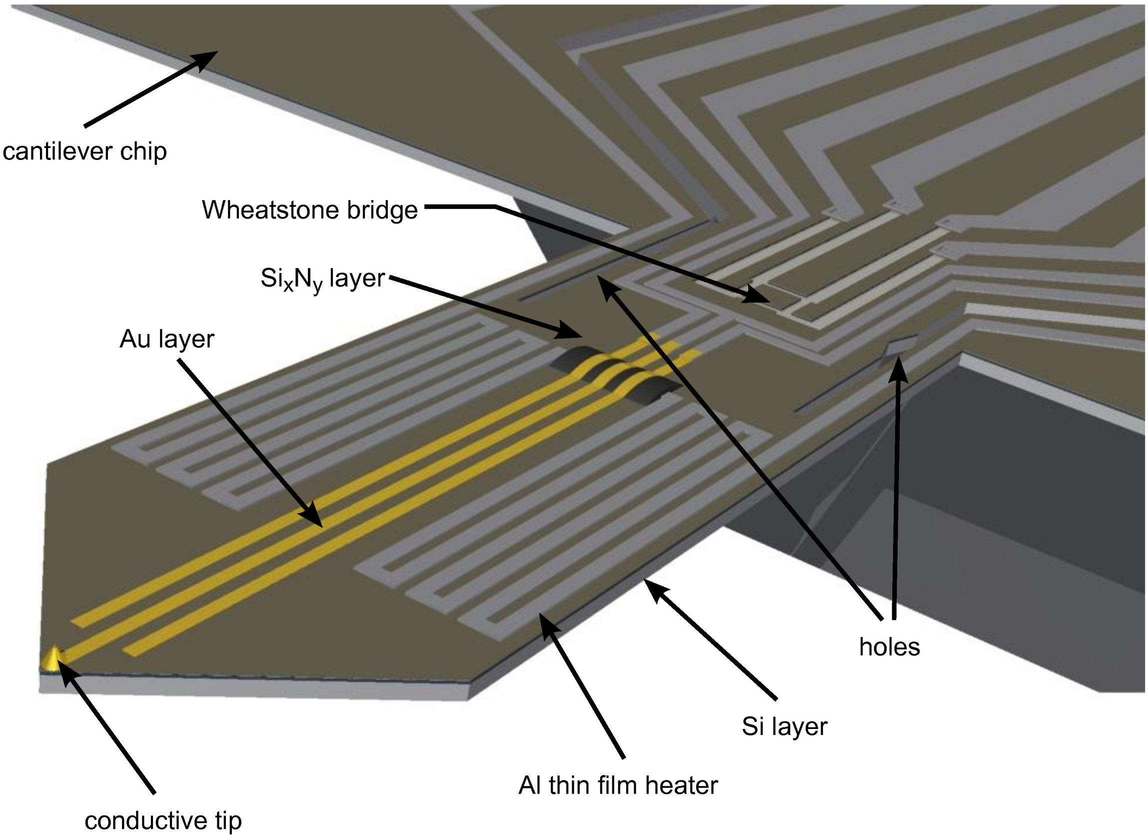

Figure 2.1: Self-actuating and self-sensing piezoresistive microscale silicon cantilever

The self-actuation of the device under consideration is based on the bimorph effect (section 2.2.1). The beam bends because of temperature change induced by the aluminium thin film heater at the free end of the cantilever (section 2.2.2). Through heat transfer (section 2.2.3) a certain temperature profile is established within the beam (section 2.2.4) within a certain time (section 2.2.5). The drive power applied to the heater is either a direct current (DC) signal or an alternating current (AC) signal resulting in either pure beam bending (section 2.2.6) or beam oscillation (section 2.2.7). The actuation mechanism means that the cantilever is thermally driven. The self-actuation is characterized by the actuation efficiency (section 2.2.8).
The self-sensing is based on the piezoresistive effect (section 2.3.1). Four ultra-shallow ion-implanted p-type silicon piezoresistors are connected in a Wheatstone bridge configuration placed at a point on the beam support where there is the maximum stress (section 2.3.2). The cantilever's sensitivity to deflection is what defines the self-sensing performance (section 2.3.3).
The performance of the device is influenced by extrinsic and intrinsic temperature change (section 2.4.1), noise (section 2.4.2), air damping (section 2.4.3), and capacitive crosstalk (section 2.4.4).
At the end of several sections examples are given in which the self-sensing and self-actuating piezoresistive microscale silicon cantilever is approximated by a single- or multi-layered beam with a rectangular cross-section neglecting holes.

2.2 Self-actuation of cantilever

2.2.1 Bimorph effect

By bimorph effect is meant the thermally-induced deformation of a composite beam of a rectangular cross-section which is made up of two layers of materials having different coefficients of thermal expansion (CTE) α. The two layers expand as the beam temperature rises (Figure 2.2(a)). The dimensions width b_i, thickness d_i, and length L_i of each layer i increase with change in beam temperature ΔT according to

$$\epsilon_i = \frac{\Delta b_i}{b_i} = \frac{\Delta d_i}{d_i} = \frac{\Delta L_i}{L_i} = \alpha_i \Delta T \tag{2.1}$$

causing strain ϵ_i within layer i. Because of the difference in the coefficient of thermal expansion (CTE) the changes in width, thickness, and length of each layer are unequal. Because the materials are tightly joined at the interface, the beam must curve toward the layer made of the material with the smaller strain, i.e. a lower CTE (Figure 2.2(b)). This constitutes beam bending. The geometry is changed. If the beam temperature changes periodically, the layers expand and shrink as they heat up and cool down. so that the beam bends and returns to its original state time after time, i.e. it moves up and down. This is how beam oscillation is generated.

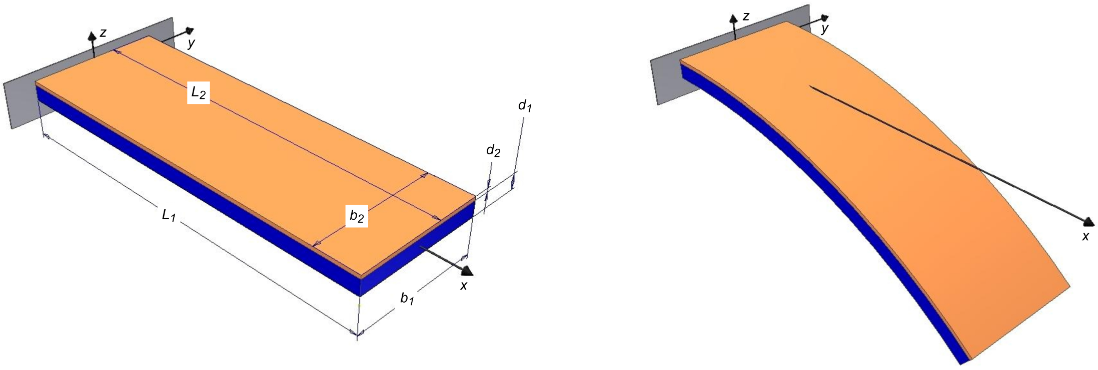

(a) (b)

Figure 2.2: Two-layered beam: (a) unbent and (b) bent

Because of the change in dimensions the density ρ_i of each material layer changes

$$\frac{\Delta \rho_i}{\rho_i} = -3\alpha_i \Delta T \tag{2.2}$$

Increased beam temperature does not only result in larger dimensions but also in the reduction of the modulus of elasticity E_i, i.e. the Young's modulus. The relationship between E_i and temperature change ΔT can be written as

$$\frac{\Delta E_i}{E_i} = \beta_i \Delta T \tag{2.3}$$

with the temperature coefficient of the modulus of elasticity β_i. Equation 2.3 assumes that the modulus of elasticity decreases directly with temperature in the simplest case. However, an exponential temperature dependence of the modulus of elasticity is suggested by several studies and is also valid for silicon [61–63]. It is described by Wachtman's equation [61]

$$E_i(T) = E_{0\mathrm{K},i} - B_i T \exp\left(-\frac{A_i}{T}\right) \tag{2.4}$$

where the constants $B_i > 0$ and $A_i > 0$ are temperature independent, and $E_{0\mathrm{K},i}$ is the modulus of elasticity at 0 K. The constants are defined

$$B_i = \frac{\gamma_{\text{Grüneisen},i}\delta_{\text{Anderson-Grüneisen},i}R_{ideal}}{V_{0\mathrm{K},i}} \tag{2.5}$$

$$A_i \approx \frac{\theta_{\text{Debye},i}}{2} \tag{2.6}$$

where $\gamma_{\text{Grüneisenn},i}$ is the Grüneisen parameter, $\delta_{\text{Anderson-Grüneisen},i}$ the Anderson-Grüneisen parameter, $V_{0\mathrm{K},i}$ the volume at 0 K, and $\theta_{\text{Debye},i}$ the Debye temperature.
The present description of the bimorph effect makes certain assumptions:

- that the materials are isotropic: CTE and modulus of elasticity do not depend on the crystallographic direction, i.e. they are the same for width, thickness, and length.
- that the beam temperature is the same at all points of the beam.
- that the same temperature change is experienced at all points of the beam.

In the case of the self-actuating and self-sensing piezoresistive microscale silicon cantilever the bimorph effect is employed in a multi-layered beam where the thermomechanical interaction between aluminium with the highest CTE and silicon dioxide with the lowest CTE causes the beam bending. For this only the change in length due to temperature rise is necessary. Changes of width, thickness, and the modulus of elasticity are incidental.

2.2.2 Drive power

The aluminium thin film heater introduces the temperature change necessary for the beam actuation based on the bimorph effect. It is a linear resistor R_{heater} described by Ohm's law

$$R_{heater} = \frac{U}{I} \tag{2.7}$$

where U is the voltage and I the current. If drive power

$$P_{drive} = UI \tag{2.8}$$

is supplied to the heater, it carries a current. By Joule heating the resistor warms up, i.e. it is an intrinsically dissipative element [64]. Through conduction heat transfer all layers heat up, i.e. the beam temperature is increased.
If DC drive power

$$P_{drive,DC} = UI = I^2_{drive,DC} R_{heater} \tag{2.9}$$

with the drive DC signal $I_{drive,DC}$ is supplied to the heater, pure beam bending is generated. Applied AC drive power

$$P_{drive,AC} = UI = \frac{U^2_{drive,AC}}{R_{heater}} \tag{2.10}$$

results in beam oscillation, because the beam temperature changes periodically. The AC drive voltage $U_{drive,AC}$ is a sinusoidal drive voltage signal

$$U_{drive,AC} = U_{DC} + \hat{U}_{AC} \sin(\omega_d t) \tag{2.11}$$

where U_{DC} is the offset, $\hat{U}_{AC}$ the amplitude, t the time, and ω_d the angular drive frequency, which is related to the drive frequency f_d as follows

$$\omega_d = 2\pi f_d \tag{2.12}$$

The drive frequency defines the speed of temperature change and thus, of beam oscillation. The AC drive power is calculated from equations 2.10 and 2.11

$$\begin{align} P_{drive,AC} &= \frac{U^2_{drive,AC}}{R_{heater}} \tag{2.13} \\ &= \frac{(U_{DC} + \hat{U}_{AC} \sin(\omega_d t))^2}{R_{heater}} \tag{2.14} \\ &= \frac{U^2_{DC} + 2U_{DC}\hat{U}_{AC} \sin(\omega_d t) + \hat{U}^2_{AC} \sin^2(\omega_d t)}{R_{heater}} \tag{2.15} \\ &= \frac{U^2_{DC} + 2U_{DC}\hat{U}_{AC} \sin(\omega_d t) + \frac{\hat{U}^2_{AC}}{2} - \frac{\hat{U}^2_{AC}}{2} \cos(2\omega_d t)}{R_{heater}} \tag{2.16} \end{align}$$

with

$$\sin^2(\omega_d t) = \frac{1}{2} - \frac{1}{2} \cos(2\omega_d t) \tag{2.17}$$

Because of sine and cosine term, it is possible to drive the beam at ω_d or $\frac{1}{2}\omega_d$ to make it oscillate at ω_d. If ω_d is applied, the cosine term is neglected. Then, the sine term, i.e. the dynamic AC drive power,

$$P_{drive,AC,dynamic} = \frac{2U_{DC}\hat{U}_{AC}}{R_{heater}} \tag{2.18}$$

describes beam oscillation, whereas the static AC drive power

$$P_{drive,AC,static} = \frac{U_{DC}^2 + \frac{\hat{U}_{AC}^2}{2}}{R_{heater}} \tag{2.19}$$

stands for pure beam bending. This means that, while the beam oscillates, it is bent at the same time, because the beam temperature is increased. So, two effects happen at the same time, although beam bending is a parasitic, undesirable effect. Whether the drive power supplied to the heater is DC or AC, it is not completely used for beam actuation as there is intrinsic and extrinsic energy dissipation (see section 2.4.2.1).

2.2.3 Heat transfer

The heat provided by the aluminium thin film heater has to be transferred to all layers along width, thickness, and length if the beam temperature is to rise and enable beam actuation. Three different types of heat transfer processes are distinguished: conduction, convection, and radiation. Within the beam, conduction heat transfer is due to the atomic motion in the form of lattice vibration. Convection heat transfer occurs between a fluid, i.e. air, and a bounding beam surface and is attributed to both random molecular motion and bulk fluid motion. On heat transfer by radiation, energy is emitted by the beam surface [65]. For a layer i, these three heat transfer processes are quantified in terms of the appropriate rate equations with the heat flux or heat transfer rate $q^{''}$ [65]:

conduction: Fourier's law
$$q^{''}_{cond,i} = -k_{th,i}\frac{\partial T}{\partial x} = -k_{th,i}\frac{T_s - T_{sur}}{L} \tag{2.20}$$

convection: Newton's law of cooling
$$q^{''}_{conv,i} = h_{conv}(T_s - T_\infty) \tag{2.21}$$

radiation:
$$q^{''}_{rad,i} = \zeta k_{SB}(T_s^4 - T_{sur}^4) \tag{2.22}$$

where $k_{th,i}$ is the thermal conductivity, T the absolute temperature, T_s the absolute surface temperature, T_{sur} the absolute ambient temperature, $h_{conv,air}$ the convection heat transfer coefficient, T_∞ the absolute fluid temperature, ζ the emissivity, and k_{SB} the Stefan-Boltzmann's constant. These statements are made on certain assumptions:

- that the materials are isotropic: Thermal conductivity does not depend on the crystallographic direction, i.e. it is the same for width, thickness, and length.
- that the conduction heat transfer process along thickness can be neglected, because it is very small compared to length for any layer. Additionally, the aluminium thin film heater is almost as wide as the self-actuating and self-sensing piezoresistive microscale silicon cantilever. Therefore, it is assumed that heat is homogeneously introduced along the width and conduction along width does not occur.
- that conduction is only necessary to consider along length.
- that heat is homogeneously supplied to the cross-sectional surface of any layer at the free end of the beam.
- that heat is homogeneously transferred from the free end of beam to its base, i.e. the thermal conductivity is constant and all layers are of the same length.
- that the beam temperature is in the beginning the same at all points of the beam.
- that the cantilever chip at the fix end of the beam is a large heat sink and remains at constant temperature.

From rate equations it is clear that beam actuation works through heat transfer by conduction. Convection and radiation stand for heat loss. Equations 2.20, 2.21, and 2.22 may be used to estimate the amount of energy being transferred by these processes. For comparison the heat transfer rates are normalized by either cross-sectional area ($b_i d_i$) for conduction or surface area ($2b_i L_i$) including top and bottom for convection and radiation:

$$q^{''}_{cond,Anorm,i} = -k_{th,i}\frac{T_s - T_{sur}}{L_i}(b_i d_i) \tag{2.23}$$

$$q^{''}_{conv,Anorm,i} = h_{conv}(T_s - T_\infty)(2b_i L_i) \tag{2.24}$$

$$q^{''}_{rad,Anorm,i} = \zeta k_{SB}(T_s^4 - T_{sur}^4)(2b_i L_i) \tag{2.25}$$

In the case of the self-actuating and self-sensing piezoresistive microscale silicon cantilever, heat transfer by convection and radiation can be neglected, while conduction predominates. Furthermore, heat is mainly transferred by the silicon layer from the free end of the beam to the fixed end (see example).

Calculated example of heat transfer processes

A composite beam made of multiple material layers with rectangular cross-sections is given in Table 2.1. Steady-state conditions in air are assumed. The normalized heat transfer rates of conduction, convection, and radiation are estimated for each material layer according to equations 2.23, 2.24, and 2.25. In this case, the layers are assumed to be separated and not joined, so that convection and radiation is possible. Parameters are listed in Table 2.2 and values of thermal conductivity $k_{th,i}$ in Table 2.3. Surface temperature equals beam temperature. The beam temperature change is consistent with finite element method (FEM) calculations done for a similar self-actuating and self-sensing piezoresistive microscale silicon cantilever within Rangelow's group [66].

The conduction heat transfer rates of all layers are compared according to

$$q^{''}_{cond,Anorm,all,i} = \frac{q^{''}_{cond,Anorm,i}}{\sum_{i=1}^{6} q^{''}_{cond,Anorm,i}}$$

Material layer i	Width b_i µm	Thickness d_i µm	Length L_i µm
Si	150	6	460
SiO_2	150	1.1	460
Si_xN_y	150	0.3	460
Al	150	0.3	460
Cr	10	0.03	460
Au	10	0.13	460

Table 2.1: Dimensions of layers of composite beam

Parameter	Unit	Value
Convection heat transfer coefficient $h_{conv,air}$	$\frac{W}{m^2 \cdot K}$	15 [65]
Emissivity ζ [65]		1
Stefan-Boltzmann's constant k_{SB}	$\frac{W}{m^2 \cdot K^4}$	$5.6704 \cdot 10^{-8}$
Absolute ambient/ fluid temperature $T_{sur} = T_{\infty}$	K	295 (~ 22°C)
Absolute surface temperature T_s	K	320 (~ 57°C)

Table 2.2: Parameters for heat transfer processes

Material layer i	Thermal conductivity $k_{th,i}$ $\frac{W}{m \cdot K}$
Si	156 [67]
SiO_2	1.38 [68]
Si_xN_y	30 [68]
Al	205 [69]
Cr	93.9 [70]
Au	314 [69]

Table 2.3: Thermal conductivity of materials

Material layer i	$q''_{cond,Anorm,i}$ %	$q''_{conv,Anorm,i}$ %	$q''_{rad,Anorm,i}$ %	$q''_{cond,Anorm,total,i}$ %
Si	99.0	0.7	0.3	92.59
SiO_2	14.2	59.6	26.2	0.15
Si_xN_y	49.6	35.0	15.4	0.89
Al	87.0	9.0	4.0	6.08
Cr	23.6	53.1	23.3	0.02
Au	81.7	12.7	5.6	0.27

Table 2.4: Normalized heat transfer rates of layers

By far, the conduction heat transfer process predominates for almost every layer, and would do so even if the air convection heat transfer coefficient were greater (up to 25). Things are different for the SiO_2 and Cr layers (Table 2.4), because both of the materials have very low thermal conductivity $k_{th,i}$ (Table 2.3). Since both layers are between other ones, neither convection nor radiation is possible. Consequently, heat transfer by convection and radiation can be neglected for the self-actuating and self-sensing piezoresistive microscale silicon cantilever, as already stated for a similar self-actuating and self-sensing piezoresistive microscale silicon cantilever within Rangelow's group [71].

The comparative Table 2.4 shows that the conduction heat transfer rate of silicon is the largest, i.e. heat is mainly transferred by the silicon layer from the free end of the beam to its fixed end.

2.2.4 Temperature profile

By conduction heat is transferred towards the base through all layers from the point at the free end of the beam where the aluminium thin film heater is placed. A distinctive temperature profile within the beam is established. This is determined by the heat equation for transient conduction [65]:

$$\begin{array}{lll} \text{conduction heat transfer} & +\text{energy source} & =\text{energy storage} \\ \left[\frac{\partial}{\partial x}\left(k_{th}\frac{\partial T}{\partial x}\right)+\frac{\partial}{\partial y}\left(k_{th}\frac{\partial T}{\partial y}\right)+\frac{\partial}{\partial z}\left(k_{th}\frac{\partial T}{\partial z}\right)\right] & +\dot{q} & =\rho c_p\frac{\partial T}{\partial t} \end{array} \tag{2.26}$$

where k_{th} is the thermal conductivity, T the absolute temperature, $\dot{q}$ the energy generation rate per unit volume, ρ the density, c_p the specific heat capacity at constant pressure, and t the time. The heat generated is both conducted to all points of the beam (conduction heat transfer) and stored (energy storage) resulting in beam temperature change. Conduction is described by the thermal conductivity and storage by the specific heat capacity. Under specific boundary conditions the calculation of the temperature profile can be reduced to a one-dimensional case [65, 72]. These assumptions are clearly the same as for heat transfer (see section 2.2.3) plus the one additional condition listed here:

- that heat transfer by convection or radiation is neglected.

The heat equation for such a one-dimensional conduction problem is then

$$k_{th}\frac{\partial^2 T}{\partial x^2}+\dot{q}=\rho c_p\frac{\partial T}{\partial t} \tag{2.27}$$

Since analytical solutions to transient conduction problems are restricted to simple geometries and boundary conditions, numerical techniques are used. The advantage of numerical methods is that they can be readily extended to two-dimensional and three-dimensional problems. In any numerical analysis the cantilever is subdivided into a number of small segments with a nodal point n_p at their centre [65]. Heat equation 2.27 is approximated by a explicit finite-difference form, i.e. the conduction problem is discretized in space x and time t [65, 72]

$$k_{th}\frac{T^t_{n_p+1}+T^t_{n_p-1}-2T^t_{n_p}}{(\Delta x)^2}+\dot{q}=\rho c_p\frac{T^{t+1}_{n_p}-T^t_{n_p}}{\Delta t} \tag{2.28}$$

Solving for the nodal temperature at the new time t+1, it follows that

$$T^{t+1}_{n_p}=\frac{k_{th}}{\rho c_p}\frac{\Delta t}{(\Delta x)^2}(T^t_{n_p+1}+T^t_{n_p-1}-2T^t_{n_p})+\frac{\Delta t}{\rho c_p}\dot{q}+T^t_{n_p} \tag{2.29}$$

This method is explicit because unknown nodal temperatures for the new time t+1 are determined from known nodal temperatures at the previous time t. Initial conditions define the temperature at each node: $t = 0$. The accuracy of the method is improved by decreasing the values of Δx and Δt. However, Δt is subject to the stability criterion that the value must be maintained below a certain limit [65]. For a one-dimensional interior node this is [65]

$$Fo = \frac{k_{th}}{\rho c_p} \frac{\Delta t}{(\Delta x)^2} \leq \frac{1}{2} \tag{2.30}$$

where Fo is a finite-difference form of the the Fourier number. The value of Δt is then given by

$$\Delta t \leq \frac{1}{2} \frac{\rho c_p}{k_{th}} (\Delta x)^2 \tag{2.31}$$

The energy generation rate per unit volume is set to

$$\dot{q} = \frac{P_{drive}}{V_{beam}} \tag{2.32}$$

where the beam volume is

$$V_{beam} = \sum_{i=1}^{n} V_i \tag{2.33}$$

where V_i is the volume of layer i. This equation inserted into equation 2.29 shows the linear relationship between drive power and temperature

$$T_{n_p}^{t+1} = \frac{k_{th}}{\rho c_p} \frac{\Delta t}{(\Delta x)^2} (T_{n_p+1}^t + T_{n_p-1}^t - 2T_{n_p}^t) + \frac{\Delta t}{\rho c_p} \frac{P_{drive}}{V_{beam}} + T_{n_p}^t \tag{2.34}$$

The analogy between conduction heat transfer and conduction of electricity is used as the basis for defining thermal resistance R_{th} and heat capacity C_{th} of a multilayered beam. Similarly to an electrical circuit, the material layers are in parallel [72, 73]. According to this, the thermal resistance is

$$R_{th,beam} = \frac{1}{\sum_{i=1}^{n} \frac{1}{R_{th,i}}} \tag{2.35}$$

with the thermal resistance of layer i

$$R_{th,i} = \frac{L_i}{k_{th,i} b_i d_i} \tag{2.36}$$

where b_i is the width, d_i the thickness, and L_i the length. The heat capacity is

$$C_{th,beam} = \sum_{i=1}^{n} C_{th,i} \tag{2.37}$$

with the heat capacity of layer i

$$C_{th,i} = c_{p_i} m_i = c_{p_i} \rho_i b_i d_i L_i \tag{2.38}$$

where m_i is the mass. Taking the definitions of thermal resistance (equation 2.35) and heat capacity (equation 2.37) into account, the thermal conductivity of a multilayered beam is defined by weighing

$$k_{th,beam} = \frac{\sum_{i=1}^{n} \frac{L_i}{b_i d_i}}{\sum_{i=1}^{n} \frac{L_i}{k_{th,i} b_i d_i}} \tag{2.39}$$

as well as the density-specific heat capacity term

$$(\rho c_p)_{beam} = \frac{\sum_{i=1}^{n} c_{p_i} \rho_i b_i d_i L_i}{\sum_{i=1}^{n} b_i d_i L_i} \tag{2.40}$$

Regarding equation 2.29 the nodal temperature at the new time t+1 is

$$T_{n_p}^{t+1} = \frac{k_{th,beam}}{(\rho c_p)_{beam}} \frac{\Delta t}{(\Delta x)^2} (T_{n_p+1}^t + T_{n_p-1}^t - 2T_{n_p}^t) + \frac{\Delta t}{(\rho c_p)_{beam}} \frac{P_{drive}}{V_{beam}} + T_{n_p}^t \tag{2.41}$$

FEM simulations of the temperature profile of a similar self-actuating and self-sensing piezoresistive microscale silicon cantilever based on these calculations have already been done within Rangelow's group [66, 74].

Calculated example of temperature profile within beam

The temperature profile of a composite beam made of multiple material layers with rectangular cross-sections is estimated according to equation 2.41. The beam dimensions are given in Table 2.1 (see example in section 2.2.3). Values for thermal conductivity, density, and specific heat capacity are listed in Tables 2.3 (see example in section 2.2.3) and 2.5. Beam thermal conductivity is calculated from equation 2.39, the density-specific heat capacity term from equation 2.40, and the beam volume from equation 2.33. The DC drive power is given by equation 2.9, the static AC drive power by equation 2.19, and the dynamic AC drive power by equation 2.18 (section 2.2.2). Offset and amplitude are the same: $U_{DC} = \hat{U}_{AC}$. The parameters are listed in Table 2.6.

Material layer i	Density ρ_i $\frac{\text{g}}{\text{cm}^3}$	Specific heat capacity $c_{p,i}$ $\frac{\text{J}}{\text{kg}\cdot\text{K}}$
Si	2.329 [75]	713 [67]
SiO_2	2.2 [68]	740 [68]
Si_xN_y	3.29 [68]	711 [76]
Al	2.7 [69]	900 [69]
Cr	7.19 [70]	450 [70]
Au	19.3 [69]	126 [69]

Table 2.5: Density and specific heat capacity of materials

Parameter	Unit	Value
Beam thermal conductivity $k_{th,beam}$	$\frac{\text{W}}{\text{m}\cdot\text{K}}$	96
$(\rho c_p)_{beam}$	$\frac{\text{J}}{\text{m}^3\cdot\text{K}}$	$1.7\cdot10^6$
Beam volume V_{beam}	m^3	$5\cdot10^{-13}$
Δx	µm	10
Δt	s	$6\cdot10^{-7}$
DC drive power $P_{drive,DC}$	mW	15
Static AC drive power $P_{drive,AC,static}$	mW	15
Dynamic AC drive power $P_{drive,AC,dynamic}$	mW	20
Drive frequency f_d	kHz	1, 10, 50

Table 2.6: Parameters for temperature profile estimation

The temperature profiles show the change of beam temperature along the beam length L_{beam} over time t (Figures 2.3(a) and 2.3(b)). They are the same if the DC drive power equals the static AC drive power: $P_{drive,DC} = P_{drive,AC,static}$, i.e. these two powers determine the temperature profiles and therefore, the pure beam bending. FEM simulations carried out within Rangelow's group [66] have produced a similar temperature profile for a similar self-actuating and self-sensing piezoresistive microscale silicon cantilever driven at 15 mW. The time scale shows that it takes some time to establish the temperature profile because of thermal inertia (see next section 2.2.5).

The temperature of the temperature profile increases in direct ratio to DC drive power or static AC drive power, whether only the offset U_{DC}, only the amplitude $\hat{U}_{AC}$ or both are changed by equal increments (Figures 2.4(a) and 2.4(b)), because of the linear relationship between drive power and temperature (equation 2.41) and the definitions of DC and static AC drive power (equations 2.9 and 2.19 in section 2.2.2).

The sinusoidal temperature change that is caused by the dynamic AC drive power $P_{drive,AC,dynamic}$ and, in turn, causes beam oscillation depends on the drive frequency f_d (Figure 2.5(a)). f_d obviously influences the speed of temperature change, as already stated in section 2.2.2. The higher is f_d, the faster and smaller is the change in sinusoidal temperature which results in beam oscillation. This is also referred to as thermal inertia. The temperature profile is the same either way.

There is a linear increase in the sinusoidal temperature change necessary for beam oscillation with increasing dynamic AC drive power $P_{drive,AC,dynamic}$, whether only the offset U_{DC}, only the amplitude $\hat{U}_{AC}$ or both are changed by equal increments (Figure 2.5(b)). This is due to the linear relationship between drive power and temperature (equation 2.41) and the definition of the dynamic AC drive power (equation 2.18 in section 2.2.2).

If the sinusoidal temperature change is applied to voltage, it increases in linear fashion when only the offset U_{DC} or only the amplitude $\hat{U}_{AC}$ changes but parabolically when both are changed by equal increments (Figure 2.6). This is based on the definition of the dynamic AC drive power (equation 2.18 in section 2.2.2) and on the linear relationship between drive power and temperature (equation 2.41).

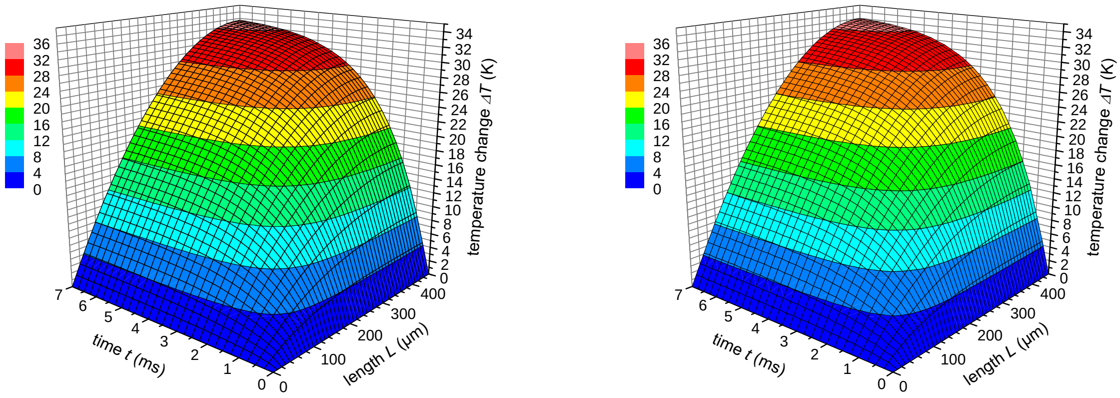

(a)

(b)

Figure 2.3: Temperature profile within beam depending on time:
(a) DC drive power and (b) AC drive power at f_d = 50 kHz

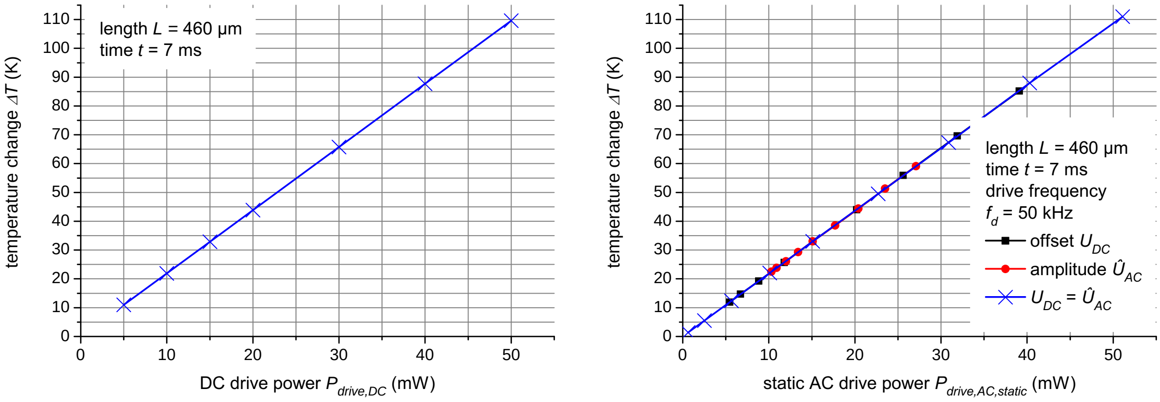

(a)

(b)

Figure 2.4: Temperature change of temperature profile:
(a) DC drive power and (b) static AC drive power at f_d = 50 kHz

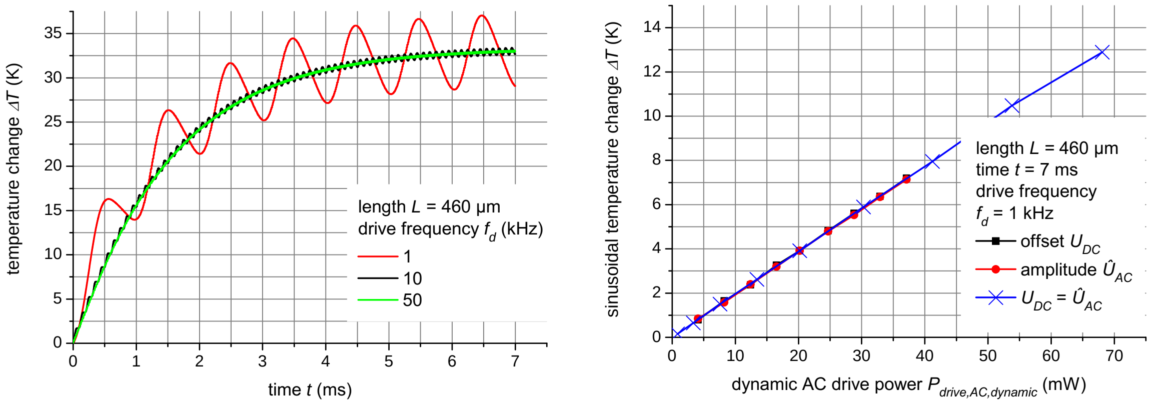

(a) (b)

Figure 2.5: Sinusoidal temperature change:
(a) versus time depending on drive frequency;
(b) versus dynamic AC drive power at $f_d = 1$ kHz

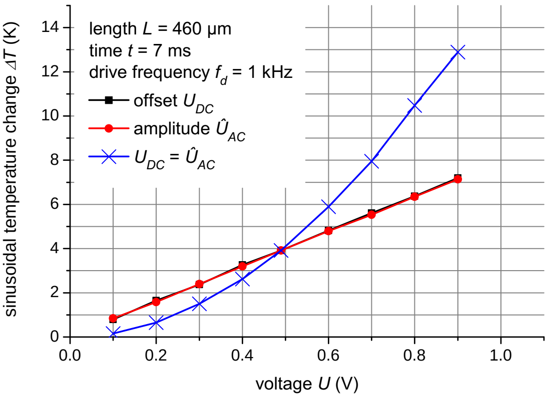

Figure 2.6: Sinusoidal temperature change versus voltage

2.2.5 Thermal time constant

The time needed for the establishment of the temperature profile within the cantilever here described is called the thermal time constant of the beam [77, 78]

$$\tau_{th,beam} = R_{th,beam} C_{th,beam} \tag{2.42}$$

where $R_{th,beam}$ is the thermal resistance and $C_{th,beam}$ the heat capacity. It takes this time to reach thermal equilibrium. The time dependency of temperature is already clear from the calculation of the temperature profile (equation 2.41 in section 2.2.4), behaviour which is due to the thermal inertia described by thermal conductivity $k_{th,beam}$ and specific heat capacity $c_{p,beam}$ of the beam (equations 2.35 to 2.40 in section 2.2.4)

$$\tau_{th,beam} \sim \frac{c_{p,beam}}{k_{th,beam}} \tag{2.43}$$

The lower $c_{p,beam}$ and the higher $k_{th,beam}$ are, i.e. the less heat is stored and the faster it is transferred, the faster the cantilever comes into steady state. At AC drive power, the higher is the drive frequency f_d is, the faster and smaller is the change in sinusoidal temperature of the beam (see Figure 2.5(a) in section 2.2.4). The drive power changes faster than the aluminium thin film heater warms up by Joule heating and faster than heat is transferred, i.e. only a portion of the heat that could have theoretically been provided is used for beam oscillation. Consequently, the amplitude of beam oscillation decreases. The drive frequency at which this effect starts is the cut-off frequency of the beam

$$f_{cut-off,beam} = \frac{1}{2\pi\tau_{th,beam}} = \frac{1}{2\pi R_{th,beam} C_{th,beam}} \tag{2.44}$$

It is the boundary in the frequency response of the cantilever, at which the amplitude of beam oscillation falls to $\sqrt{\frac{1}{2}}$ of its original value, i.e. it begins to decline, tending towards zero. From this the cantilever can be understood as a thermal low-pass filter.

At high drive power not only does the beam warm up but also the cantilever chip at the base. Since its volume and, therefore, its heat capacity is much bigger, the establishment of thermal equilibrium takes more time. The thermal time constant of the cantilever chip is

$$\tau_{th,chip} = R_{th,chip} C_{th,chip} \tag{2.45}$$

where $R_{th,chip}$ is the thermal resistance and $C_{th,chip}$ the heat capacity calculated the same way as for the beam according to equations 2.35 and 2.37 (section 2.2.4).

The thermal time constant of the beam may be derived from the exponential decay or growth of the voltage output signal of the DC Wheatstone bridge $U_{out,bridge,DC}$ (see section 2.3.2) which occurs at pure beam bending if DC drive power is supplied to the aluminium thin film heater

$$U_{out,bridge,DC,decay} = U_{out,bridge,DC} \exp\left(\frac{-t}{\tau_{th,beam}}\right) \tag{2.46}$$

$$U_{out,bridge,DC,growth} = U_{out,bridge,DC} \left[1 - \exp\left(\frac{-t}{\tau_{th,beam}}\right)\right] \tag{2.47}$$

Figure 2.7 shows the graphs of corresponding drive and output signals.

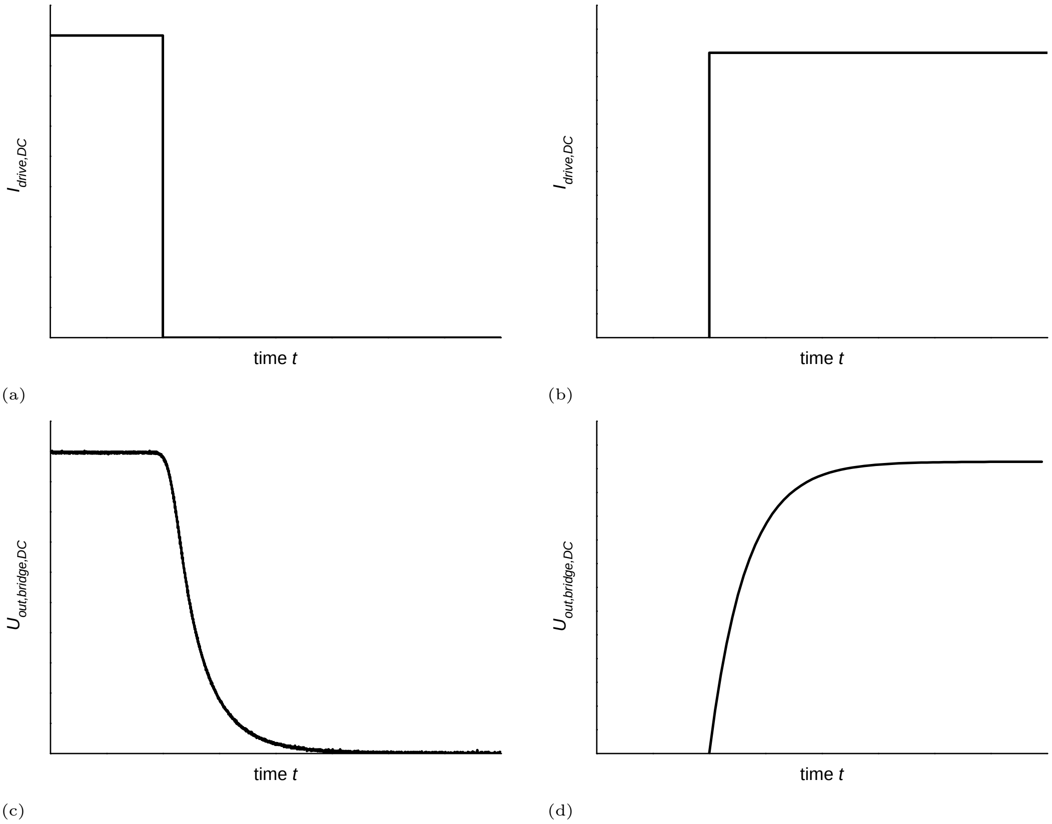

Figure 2.7: (a) and (c) decaying drive DC and DC Wheatstone bridge output voltage;
(b) and (d) increasing drive DC and DC Wheatstone bridge output voltage

---

Calculated example of thermal time constant of beam and cantilever chip

The thermal time constant of a composite beam made of multiple material layers with rectangular cross-sections is estimated according to equation 2.42. The beam dimensions are given in Table 2.1 (see example in section 2.2.3). Values for thermal conductivity, density, and specific heat capacity are listed in Tables 2.3 (see example in section 2.2.3) and 2.5 (see example in section 2.2.4). The cut-off frequency of the beam results from equation 2.44. The thermal time constant of the cantilever chip made of multiple material layers is calculated from equation 2.45. The dimensions of the cantilever chip are given in Table 2.7. The conducting traces of aluminium are neglected, since their volume is very much smaller than that of the silicon, SiO_2, and Si_xN_y layers.

Results are given in Table 2.8. The thermal time constant of the beam is also seen in the temperature profiles presented by the example in section 2.2.3.

Material layer i	Width b_i µm	Thickness d_i µm	Length L_i µm
Si	1300	275	4000
SiO_2	1300	1.1	4000
Si_xN_y	1300	0.3	4000

Table 2.7: Dimensions of layers of cantilever chip

Parameter	Unit	Value
$\tau_{th,beam}$	ms	2.8
$f_{cut-off,beam}$	Hz	58
$\tau_{th,chip}$	ms	171

Table 2.8: Thermal time constant and cut-off frequency of beam, and thermal time constant of cantilever chip

2.2.6 Pure beam bending

It is possible to estimate the beam bending due to temperature rise under certain initial conditions according to the one-dimensional Euler-Bernoulli beam theory, a simplification of the theory of elasticity [79–82]. These initial conditions are:

- that the beam consists of multiple material layers with the same length and rectangular cross-sections (Figure 2.8(a)).
- that the beam is initially straight with the longitudinal axis lying along the x-axis, i.e. it is unbent and there is no internal stress.
- that the x-axis is the neutral axis, where there is no strain.
- that the y-axis is an axis of symmetry passing through all cross-sections.
- that shear is not considered. Hence, the beam is in a state of pure bending. From this it is concluded that all cross-sections remain plane and are perpendicular to the deformed longitudinal axis. Therefore, the theory will cover only small deflections.
- that the strain at the interfaces of the layers is continuous.
- that the beam temperature is the same at all points of the beam.
- that the same temperature rise is experienced at all points of the beam.
- that the length is much larger than width or thickness, i.e. temperature-dependent changes in width and thickness are neglected. Therefore, the strain is uniaxial along the x-axis.
- that the modulus of elasticity does not depend on temperature.
- that all materials are isotropic: CTE and modulus of elasticity do not depend on the crystallographic direction.
- that all materials behave as linear elastic materials in accordance with Hooke's law provided that stress and strain are sufficiently small during beam bending.

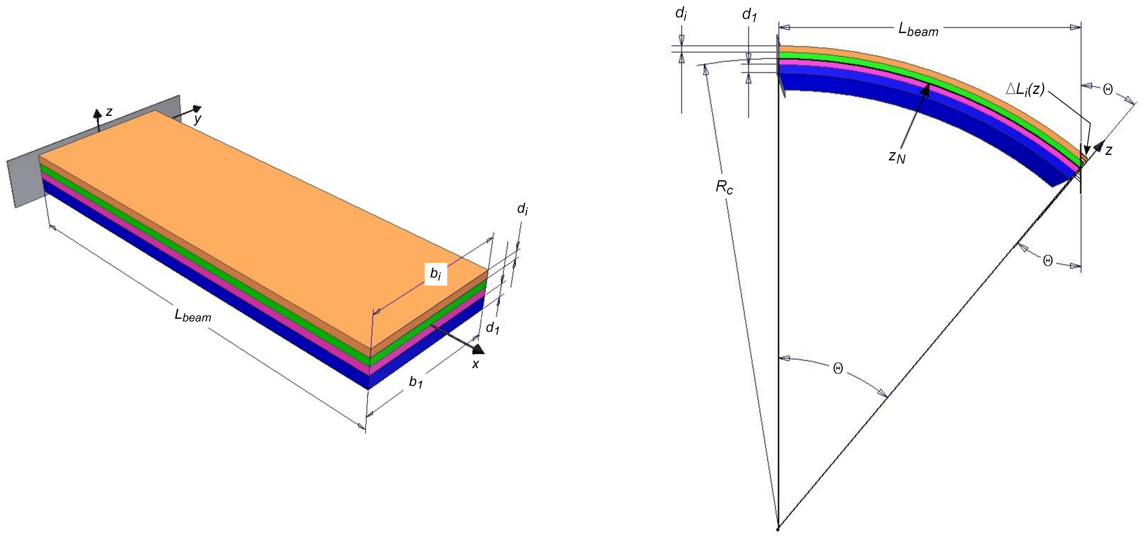

(a) (b)

Figure 2.8: Multi-layered beam: (a) unbent and (b) bent

Beam bending is based on the bimorph effect. It is caused by the difference in strain $\epsilon_{x,i}$ on each material layer i along the x-axis at temperature rise ΔT due to different CTEs α_i

$$\epsilon_{x,i} = \frac{\Delta L_i}{L_{beam}} = \alpha_i \Delta T \tag{2.48}$$

where ΔL_i is the change in length of layer i and L_{beam} the beam length. The uniaxial strain is a measure of the intensity of layer deformation. The cantilever will curve toward the layers with lower CTEs (Figure 2.8(b)). The strain introduces uniaxial, normal or bending stress within each layer. In the particular case of linear elastic materials, stress and strain are in direct ratio related that is given by Hooke's law

$$\pm\sigma_{x,i} = E_i \epsilon_{x,i} \tag{2.49}$$

where the proportionality constant E_i is called the modulus of elasticity or the Young's modulus. Layers with higher CTEs are in compressive stress, the ones with lower CTEs in tensile stress. Tension is defined as positive stress and marked by a plus sign, whereas compression is defined as negative stress and marked by a minus sign. The normal stress is a measure of the intensity of internal normal forces $F_{x,i}$ acting on any cross-section A_i within a layer. It varies over the cross-sectional area of the layer in z-direction [81]

$$\pm\sigma_{x,i}(z) = \frac{\partial \pm F_{x,i}(z)}{\partial A_i} \tag{2.50}$$

Within the convex part of the bent layer, normal force and stress are tensile. Within in the concave part, they are compressive. The resultant normal force acting on any cross-section of a layer is [81]

$$\pm F_{x,i} = \int \partial \pm F_{x,i}(z) = \int \int_A \pm\sigma_{x,i}(z) \partial A_i \tag{2.51}$$

It is either a tensile force (plus sign) at lower CTE or a compressive force (negative sign) at higher CTE. Since for pure bending, the beam is in equilibrium, the sum of the resultant normal forces on any cross-section of any layer must vanish [72, 81]

$$\sum_{i=1}^{n} \pm F_{x,i} = 0 \tag{2.52}$$

$$= \sum_{i=1}^{n} \int \int_A \pm\sigma_{x,i}(z) \partial A_i \tag{2.53}$$

$$= \sum_{i=1}^{n} E_i \frac{\Delta L_i}{L_{beam}} b_i d_i \tag{2.54}$$

with the cross-section

$$A_i = b_i d_i \tag{2.55}$$

where b_i is the width and d_i is the thickness of a layer. The strain difference between the bottom layer of the beam and any other layer i is [82]

$$\epsilon_{x,i} - \epsilon_{x,1} = \frac{\Delta L_i}{L_{beam}} - \frac{\Delta L_1}{L_{beam}} = \alpha_i \Delta T - \alpha_1 \Delta T = (\alpha_i - \alpha_1)\,\Delta T \tag{2.56}$$

Equation 2.56 is re-arranged

$$\frac{\Delta L_i}{L_{beam}} = \frac{\Delta L_1}{L_{beam}} + (\alpha_i - \alpha_1)\,\Delta T \tag{2.57}$$

and put into equation 2.54

$$\sum_{i=1}^{n} \pm F_{x,i} = \sum_{i=1}^{n} E_i \left(\frac{\Delta L_1}{L_{beam}} + (\alpha_i - \alpha_1)\,\Delta T \right) b_i d_i = 0 \tag{2.58}$$

The solution to equation 2.58

$$\frac{\Delta L_1}{L_{beam}} = \left(\alpha_1 - \frac{\sum_{i=1}^{n} \alpha_i b_i d_i E_i}{\sum_{i=1}^{n} b_i d_i E_i} \right) \Delta T \tag{2.59}$$

is inserted into the same equation 2.58 resulting in the sum of the resultant normal forces that act on the cross-sections of all layers [72]

$$\sum_{i=1}^{n} \pm F_{x,i} = \sum_{i=1}^{n} b_i d_i E_i \left(\alpha_i - \frac{\sum_{i=1}^{n} \alpha_i b_i d_i E_i}{\sum_{i=1}^{n} b_i d_i E_i} \right) \Delta T \tag{2.60}$$

The resultant normal forces cause a bending moment about the y-axis due to beam bending [72]

$$\begin{align} M_y &= \sum_{i=1}^{n} \pm F_{x,i} \left(\sum_{k=1}^{i} d_k - \frac{d_i}{2} - z_N \right) \tag{2.61} \\ &= \sum_{i=1}^{n} \pm F_{x,i} \left(\sum_{k=1}^{i} d_k - \frac{d_i}{2} \right) - z_N \sum_{i=1}^{n} \pm F_{x,i} \tag{2.62} \end{align}$$

where z_N is the neutral axis and there is no change in length. Since (see equation 2.52)

$$\sum_{i=1}^{n} \pm F_{x,i} = 0 \tag{2.63}$$

the bending moment is, with equation 2.60,

$$\begin{align} M_y &= \sum_{i=1}^{n} \pm F_{x,i} \left(\sum_{k=1}^{i} d_k - \frac{d_i}{2} \right) \tag{2.64} \\ &= \sum_{i=1}^{n} b_i d_i E_i \left(\alpha_i - \frac{\sum_{i=1}^{n} \alpha_i b_i d_i E_i}{\sum_{i=1}^{n} b_i d_i E_i} \right) \Delta T \left(\sum_{k=1}^{i} d_k - \frac{d_i}{2} \right) \tag{2.65} \end{align}$$

This equals the sum of the bending moments of all layers introduced by the variation of normal force over the cross-sectional area of any layer in the z-direction

$$M_y = \sum_{i=1}^{n} \pm M_{y,i} \tag{2.66}$$

The normal forces $F_{x,i}(y)$ acting on the cross-section A_i of layer i result in a bending moment $M_{y,i}$ about the y-axis taking into account equations 2.48, 2.49, and 2.51 [72]

$$\pm M_{y,i} = \int_{\sum_{k=1}^{i-1} d_k}^{\sum_{k=1}^{i} d_k} \partial \pm F_{x,i}(z)\,(z - z_N) = \int_{\sum_{k=1}^{i-1} d_k}^{\sum_{k=1}^{i} d_k} \pm\sigma_{x,i}(z)\partial A_i\,(z - z_N) \tag{2.67}$$

$$= \int_{\sum_{k=1}^{i-1} d_k}^{\sum_{k=1}^{i} d_k} E_i \epsilon_{x,i}(z) b_i \partial z\,(z - z_N) \tag{2.68}$$

$$= \int_{\sum_{k=1}^{i-1} d_k}^{\sum_{k=1}^{i} d_k} E_i \frac{\Delta L_i(z)}{L_{beam}} b_i\,(z - z_N)\,\partial z \tag{2.69}$$

where z_N is the neutral axis of the beam. The beam curvature of the bent beam can be derived geometrically. Along the neutral axis, the beam length does not change after deformation. Therefore, the arc angle θ is given by the radius of beam curvature R_c and the arc length L_{beam} (Figure 2.8(b)). This relation can also be found for the change in length of layers located at some distance from the neutral axis:

$$\theta = \frac{L_{beam}}{R_c} = \frac{\Delta L_i(z)}{z - z_N} \tag{2.70}$$

Putting equation 2.70 into equation 2.69

$$\pm M_{y,i} = \frac{b_i E_i}{R_c} \int_{\sum_{k=1}^{i-1} d_k}^{\sum_{k=1}^{i} d_k} (z - z_N)^2 \partial z \tag{2.71}$$

the bending moment of a layer is

$$\pm M_{y,i} = \frac{b_i E_i}{3R_c} \left\{ \left[\sum_{k=1}^{i} d_k - z_N \right]^3 - \left[\sum_{k=1}^{i} d_k - (d_i + z_N) \right]^3 \right\} \tag{2.72}$$

Equations 2.65 and 2.72 can be equated by the virtue of equation 2.66

$$\begin{aligned} &\sum_{i=1}^{n} b_i d_i E_i \left(\alpha_i - \frac{\sum_{i=1}^{n} \alpha_i b_i d_i E_i}{\sum_{i=1}^{n} b_i d_i E_i} \right) \Delta T \left(\sum_{k=1}^{i} d_k - \frac{d_i}{2} \right) = \\ &\sum_{i=1}^{n} \frac{b_i E_i}{3R_c} \left\{ \left[\sum_{k=1}^{i} d_k - z_N \right]^3 - \left[\sum_{k=1}^{i} d_k - (d_i + z_N) \right]^3 \right\} \end{aligned} \tag{2.73}$$

resulting in the beam curvature κ [72]

$$\kappa = \frac{1}{R_c} = \frac{\sum_{i=1}^{n} b_i d_i E_i \left(\alpha_i - \frac{\sum_{i=1}^{n} \alpha_i b_i d_i E_i}{\sum_{i=1}^{n} b_i d_i E_i} \right) \left(\sum_{k=1}^{i} d_k - \frac{d_i}{2} \right)}{\sum_{i=1}^{n} \frac{b_i E_i}{3} \left(\left[\sum_{k=1}^{i} d_k - z_N \right]^3 - \left[\sum_{k=1}^{i} d_k - (d_i + z_N) \right]^3 \right)} \Delta T \tag{2.74}$$

A different approach with the same solution is found in [74]. For a beam made of two layers, the beam curvature is

$$\kappa = \frac{1}{R_c} = \frac{6(d_1 + d_2)(\alpha_2 - \alpha_1)}{\frac{b_1}{b_2}\frac{d_1^3}{d_2}\frac{E_1}{E_2} + \frac{b_2}{b_1}\frac{d_2^3}{d_1}\frac{E_2}{E_1} + 4d_1^2 + 6d_1 d_2 + 4d_2^2} \Delta T \tag{2.75}$$

which is also reported in literature [83–85]. The neutral axis z_N of the beam is calculated from the beam in equilibrium, where the sum of resultant normal forces vanishes (equation 2.52) taking account of equations 2.48, 2.49, 2.51, and 2.70 [72]

$$\begin{aligned}
\sum_{i=1}^{n} \pm F_{x,i} = 0 \qquad\qquad & (2.76)\\
= \sum_{i=1}^{n} \int_{\sum_{k=1}^{i-1} d_k}^{\sum_{k=1}^{i} d_k} \partial \pm F_{x,i}(z) = \sum_{i=1}^{n} \int_{\sum_{k=1}^{i-1} d_k}^{\sum_{k=1}^{i} d_k} \pm\sigma_{x,i}(z)\partial A_i \qquad & (2.77)\\
= \sum_{i=1}^{n} \int_{\sum_{k=1}^{i-1} d_k}^{\sum_{k=1}^{i} d_k} E_i \epsilon_i b_i \partial z \qquad & (2.78)\\
= \sum_{i=1}^{n} \int_{\sum_{k=1}^{i-1} d_k}^{\sum_{k=1}^{i} d_k} E_i \frac{\Delta L_i(z)}{L_{beam}} b_i \partial z \qquad & (2.79)\\
= \sum_{i=1}^{n} \frac{b_i E_i}{R_c} \int_{\sum_{k=1}^{i-1} d_k}^{\sum_{k=1}^{i} d_k} (z - z_N)\partial z \qquad & (2.80)\\
= \sum_{i=1}^{n} \frac{b_i E_i}{2R_c} \left\{ \left[\sum_{k=1}^{i} d_k - z_N \right]^2 - \left[\sum_{k=1}^{i} d_k - (d_i + z_N) \right]^2 \right\} \qquad & (2.81)
\end{aligned}$$

The solution is then

$$z_N = \frac{\sum_{i=1}^{n} b_i d_i E_i \left(\sum_{k=1}^{i} d_k - \frac{d_i}{2} \right)}{\sum_{i=1}^{n} b_i d_i E_i} \qquad (2.82)$$

The displacement at the free end of the beam on pure bending is estimated from geometry, applying the Pythagoras' theorem and assuming $L_{beam} << R_c$ (Figure 2.9) [82, 86]

$$(R_c - z_{DC})^2 + L_{beam}^2 = R_c^2 \qquad (2.83)$$

$$2R_c = \frac{L_{beam}^2}{z_{DC}} + z_{DC} \qquad (2.84)$$

As $z_{DC} << L_{beam}$, the deflection of the bent beam is

$$z_{DC} = \frac{L_{beam}^2}{2R_c} \qquad (2.85)$$

$$= \frac{L_{beam}^2}{2} \frac{\sum_{i=1}^{n} b_i d_i E_i \left(\alpha_i - \frac{\sum_{i=1}^{n} \alpha_i b_i d_i E_i}{\sum_{i=1}^{n} b_i d_i E_i} \right) \left(\sum_{k=1}^{i} d_k - \frac{d_i}{2} \right)}{\sum_{i=1}^{n} \frac{b_i E_i}{3} \left(\left[\sum_{k=1}^{i} d_k - z_N \right]^3 - \left[\sum_{k=1}^{i} d_k - (d_i + z_N) \right]^3 \right)} \Delta T \qquad (2.86)$$

Variation in dimensions and CTEs influences the bending more strongly than does variation of any kind in moduli of elasticity. There is a linear increase in the deflection with rising beam temperature: a purely thermal effect. Because of the linear relationship between drive power and temperature (equation 2.41 in section 2.2.4), the deflection is directly proportional to the DC drive power

$$z_{DC} \sim \Delta T \sim P_{drive,DC} \qquad (2.87)$$

The ratio of layer thickness affects the extent of deflection, which is at its greatest at a certain thickness ratio. For a two-layered beam, this dependency is a bell-shaped distribution [86].

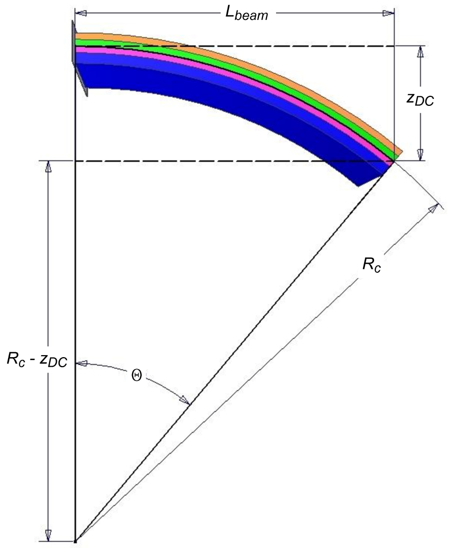

Figure 2.9: Estimation of deflection of bent multi-layered beam

Because the aluminium thin film heater placed at the free end of the beam introduces temperature change, a certain temperature profile is established by conduction heat transfer within the self-actuating and self-sensing piezoresistive microscale silicon cantilever, so that its temperature is not uniform. That is why, the beam bending must not be estimated the same way as done above. The cantilever may be subdivided into a number of segments s for which not only the temperature profile but also the number of layers, which may vary from design to design must be taken into account [72, 79]. The segments' curvature is calculated from equation 2.74. For a small amount of beam bending the differential equation of the bending moment of a layer i is derived from the one-dimensional Euler-Bernoulli beam theory and can be equated with equation 2.71

$$\pm M_{y,i} = E_i I_{area,i} \frac{\partial^2 z}{\partial x^2} = \frac{b_i E_i}{R_c} \int_{\sum_{k=1}^{i-1} d_k}^{\sum_{k=1}^{i} d_k} (z - z_N)^2 \partial z \tag{2.88}$$

$$= \frac{E_i}{R_c} \int_{\sum_{k=1}^{i-1} d_k}^{\sum_{k=1}^{i} d_k} (z - z_N)^2 \partial A \tag{2.89}$$

$$= \frac{E_i I_{area,i}}{R_c} \tag{2.90}$$

where $I_{area,i}$ is the area moment of inertia of layer i. Then, the differential equation of the beam curvature is

$$\kappa(x) = \frac{1}{R_c(x)} = \frac{\partial^2 z}{\partial x^2} \tag{2.91}$$

The integral of the beam curvature gives the arc angle of the beam curvature

$$\theta(x) = \int_0^x \frac{1}{R_c(x)} \partial x \tag{2.92}$$

and the integral of the arc angle results in the deflection

$$z_{DC}(x) = \int_0^x \theta(x) \partial x \tag{2.93}$$

taking into account two boundary conditions at the fixed end of the beam

$$z_{DC}(0) = 0 \tag{2.94}$$

$$z'_{DC}(0) = 0 \tag{2.95}$$

For any beam segment, its arc angle is with the first segment $s = 1$ at the fixed end of the beam

$$\theta_s = \frac{\Delta x}{R_{c,s}} + \theta_{s-1}, \quad \theta_{s=1} = 0 \tag{2.96}$$

where Δx is the beam segment length and $R_{c,s}$ the radius of the beam segment curvature. The temperature change of a beam segment necessary for the estimation of the $R_{c,s}$ is

$$\Delta T_s = T_s - T_{s-1} \tag{2.97}$$

The deflection of a beam segment s is calculated from

$$z_{DC,s} = \theta_s \Delta x + z_{DC,s-1} = \left(\frac{\Delta x}{R_{c,s}} + \theta_{s-1} \right) \Delta x + z_{DC,s-1}, \quad z_{DC,s=1} = 0 \tag{2.98}$$

Calculated example of deflection on pure beam bending

The deflection of a composite beam made of multiple material layers with rectangular cross-sections is estimated according to equation 2.98. The beam dimensions are given in Table 2.1 (see example in section 2.2.3). The radius of the beam segment curvature of any segment is calculated from equation 2.74 defining the radius coefficient

$$R_{c,s} = \frac{R_C}{\Delta T_s} \tag{2.99}$$

Values of linear thermal expansion coefficient and modulus of elasticity are listed in Table 2.9. The temperature change is taken from the temperature profile at DC drive power at $t = 7$ ms. Consequently, the beam segment length is chosen to be the same as for the calculation of the temperature profile (see example in section 2.2.4). Parameters are given in Table 2.10.

The curvature of the beam on pure beam bending at DC drive power $P_{drive,DC} = 15$ mW is shown in Figure 2.10(a). There is a linear increase in the deflection z_{DC} with rising $P_{drive,DC}$ (Figure 2.10(b)) because of the linear relationship between z_{DC} and temperature change ΔT (equation 2.86) and between drive power and temperature (equation 2.41 in section 2.2.4). This is the case even though the same temperature rise is not experienced at all points of the beam as assumed by the one-dimensional Euler-Bernoulli beam theory for the estimation of deflection in pure beam bending, since the length of each beam segment changes with temperature in linear relation as does the beam length (equation 2.48).

Material layer i	Linear thermal expansion coefficient α $\frac{10^{-6}}{\mathrm{K}}$	Modulus of elasticity E GPa
Si	2.616 [67]	168.9 [87]
SiO_2	0.55 [68]	73
Si_xN_y	3.3 [68]	317 [76]
Al	24 [69]	70
Cr	4.9 [88]	279
Au	14 [69]	78 [88]

Table 2.9: Linear thermal temperature coefficient and modulus of elasticity of materials

Parameter	Unit	Value
Radius coefficient C_R	m·K	3.7
Beam segment length Δx	µm	10

Table 2.10: Parameters for deflection estimation

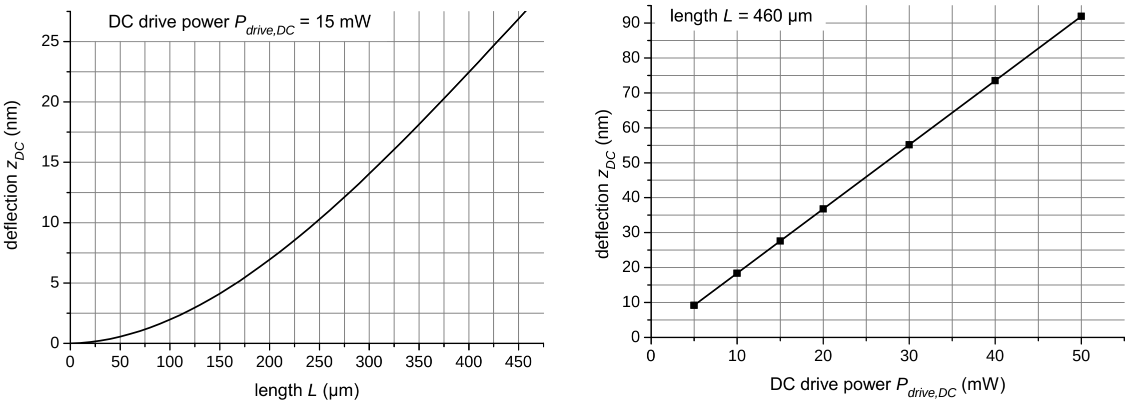

(a) (b)

Figure 2.10: (a) Beam curvature on pure beam bending and (b) deflection depending on DC drive power

2.2.7 Beam oscillation

Beam oscillation is sinusoidal beam bending at a certain frequency. The beam moves up and down (Figure 2.11). In the course of this, the beam is considered as a mechanical oscillator characterized by the fundamental or natural frequency. At this frequency resonance occurs, i.e. the amplitude of beam oscillation is a maximum. At certain multiples of the fundamental frequency, at the so-called resonant frequencies, the phenomenon happens again. The fundamental or natural frequency is the frequency of the 1^{st} resonance.

Beam oscillation may be described by the one-dimensional Euler-Bernoulli beam theory in a similar way to the pure beam bending under certain initial conditions [80]. They are:

- that the beam consists of one material layer with a rectangular cross-section.
- that the beam is initially straight with the longitudinal axis lying along the x-axis, i.e. it is unbent and there is no internal stress.
- that the x-axis is the neutral axis, where there is no strain.
- that the y-axis is an axis of symmetry passing through the cross-section.
- that shear is not considered. Hence, the beam is in a state of pure bending. From this is concluded, that all cross-sections remain plane and are perpendicular to the deformed longitudinal axis. Therefore, the theory will cover only small beam oscillation.
- that the beam temperature is the same at all points of the beam.
- that the material is isotropic: The modulus of elasticity does not depend on the crystallographic direction.
- that the material behaves as linear elastic material in accordance with Hooke's law provided that stress and strain are sufficiently small during beam oscillation.
- that there is no damping. The beam is regarded a non-damped harmonic oscillator.

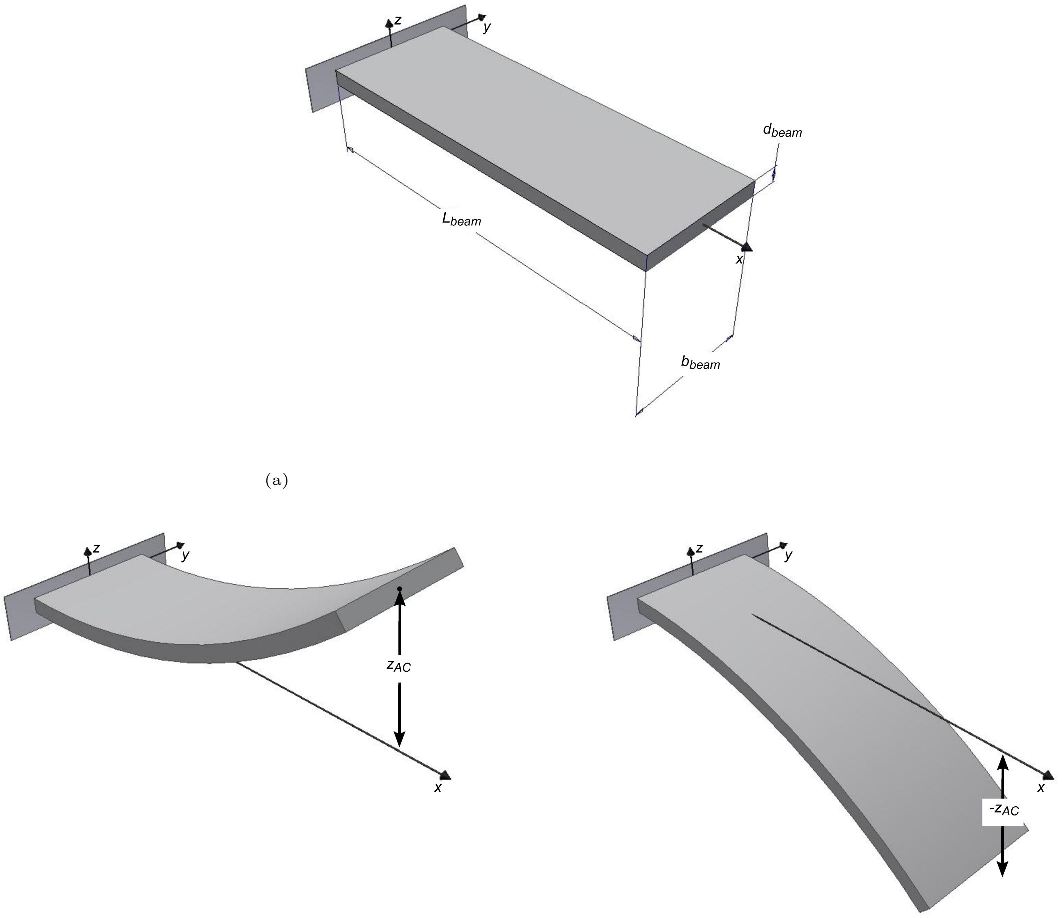

(a)

(b)

(c)

Figure 2.11: Oscillation of the beam: (a) non-oscillating beam; oscillating beam: (b) beam up and (c) beam down

The one-dimensional Euler-Bernoulli beam equation of a non-damped harmonic oscillator is given by [80, 89]

$$\frac{\partial^2 M_y(x)}{\partial x^2} \quad - F_{inertia}(t) \quad = 0 \tag{2.100}$$

$$\frac{\partial^2}{\partial x^2}\left(-E_{beam} I_{area,beam} \frac{\partial^2 z}{\partial x^2}\right) \quad - \rho_{beam} A_{beam} \frac{\partial^2 z}{\partial t^2} \quad = 0 \tag{2.101}$$

where $M_y(x)$ is the bending moment about the y-axis, $F_{inertia}$ the inertia, E_{beam} the modulus of elasticity or the Young's modulus of the beam, $I_{area,beam}$ the area moment of inertia, ρ_{beam} the density, A_{beam} the cross-sectional area, and t the time. Beam bending introduces a bending moment $M_y(x)$ about the y-axis. During beam oscillation the beam mass is accelerated. The inertia $F_{inertia}$ opposes the beam bending in accordance with Newton's second law of motion [80, 90]. The solution to the homogeneous fourth order differential equation of motion is the harmonic oscillation [80, 89]

$$z(x,t) = z_{AC}(x)\cos(\omega_m t - \varphi) \tag{2.102}$$

where z_{AC} is the maximum amplitude of the beam during oscillation, ω_m the angular frequency of the m^{th} resonance, and φ the phase. By defining variable β_m as in [80, 89]

$$\beta_m^4 = \omega_m^2 \frac{\rho_{beam} A_{beam}}{E_{beam} I_{area,beam}} \tag{2.103}$$

equation 2.101 can be reduced to

$$\frac{\partial^4}{\partial x^4} z_{AC}(x) - \beta_m^4 z_{AC}(x) = 0 \tag{2.104}$$

The general solution to this equation of motion may be expressed as the sum of trigonometric and hyperbolic functions with constants of integration C_1, C_2, C_3, and C_4 [80]

$$\begin{aligned} z_{AC}(x) = C_1 \left[\sinh(\beta_m x) + \sin(\beta_m x)\right] + C_2 \left[\sinh(\beta_m x) - sin(\beta_m x)\right] \\ + C_3 \left[\cosh(\beta_m x) + \cos(\beta_m x)\right] + C_4 \left[\cosh(\beta_m x) - \cos(\beta_m x)\right] \end{aligned} \tag{2.105}$$

To solve equation 2.104, appropriate initial and boundary conditions must be specified. At the fixed end of the beam they are [80]

$$\left.\begin{aligned} z_{AC}(0) = 0 \\ z'_{AC}(0) = 0 \end{aligned}\right\} \quad C_1 = 0 \quad \text{and} \quad C_3 = 0 \tag{2.106}$$

and at the free end

$$z''_{AC}(L_{beam}) = 0 \tag{2.107}$$

$$z'''_{AC}(L_{beam}) = 0 \tag{2.108}$$

where the second and the third derivative of $z_{AC}(x)$ is

$$\frac{\partial^2 z_{AC}}{\partial x^2} = C_2 \left[\sinh(\beta_m x) + \sin(\beta_m x)\right] + C_4 \left[\cosh(\beta_m x) + \cos(\beta_m x)\right] \tag{2.109}$$

$$\frac{\partial^3 z_{AC}}{\partial x^3} = C_2 \left[\cosh(\beta_m x) + \cos(\beta_m x)\right] + C_4 \left[\sinh(\beta_m x) - sin(\beta_m x)\right] \tag{2.110}$$

Considering the boundary conditions 2.107 and 2.108, the system of equations 2.109 and 2.110 results in

$$\begin{aligned} \left[\sinh(\beta_m L_{beam}) - \sin(\beta_m L_{beam})\right] \left[\sinh(\beta_m L_{beam}) + \sin(\beta_m L_{beam})\right] \\ + \left[\cosh(\beta_m L_{beam}) + \cos(\beta_m L_{beam})\right]^2 = 0 \end{aligned} \tag{2.111}$$

which reduces to the simple implicit equation

$$\cos(\beta_m L_{beam}) \cosh(\beta_m L_{beam}) + 1 = 0 \tag{2.112}$$

The wave number $\beta_m L_{beam}$ is found by iteration [80]

$$\beta_m^{(i+1)} L_{beam} = (2n-1)\frac{\pi}{2} - (-1)^n \sin^{-1}\left(\frac{1}{\cosh(\beta_m^i L_{beam})}\right) \tag{2.113}$$

For the first resonance $m = 1$, the wave number is [80]

$$\beta_1 L_{beam} = 1.8751 \tag{2.114}$$

and for the second resonance $m = 2$

$$\beta_2 L_{beam} = 4.6941 \tag{2.115}$$

Putting the wave number $\beta_m L_{beam}$ into equation 2.103 gives the angular frequency of the m^{th} resonance [80]

$$\omega_m = \frac{(\beta_m L_{beam})^2}{L^2} \sqrt{\frac{E_{beam} I_{area,beam}}{\rho_{beam} A_{beam}}} \tag{2.116}$$

The area moment of inertia of a beam with a rectangular cross-section is

$$I_{area,beam} = \int \int_A z^2 \partial A_{beam} \tag{2.117}$$

$$= b_{beam} \int_{-\frac{d}{2}}^{\frac{d}{2}} z^2 \partial z \tag{2.118}$$

$$= \frac{b_{beam} d_{beam}^3}{12} \tag{2.119}$$

where be_{beam} is the width and d_{beam} the thickness of the beam. Angular frequency ω_m and frequency f_m of the m^{th} resonance of a one-layered non-damped harmonic beam oscillator are

$$\omega_m = 2\pi f_m \tag{2.120}$$

$$= \frac{(\beta_m L_{beam})^2}{L_{beam}^2}\sqrt{\frac{E_{beam} I_{area,beam}}{\rho_{beam} A_{beam}}} \tag{2.121}$$

$$= \frac{(\beta_m L_{beam})^2}{2}\frac{d_{beam}}{L_{beam}^2}\sqrt{\frac{E_{beam}}{3\rho_{beam}}} \tag{2.122}$$

According to this definition, the resonant frequencies of a beam depend on beam dimensions and modulus of elasticity. The relation between the frequencies of the first and second resonance is given by [80]

$$\frac{f_2}{f_1} = \frac{(\beta_2 L_{beam})^2}{(\beta_1 L_{beam})^2} = 6.2669 \tag{2.123}$$

In reality the beam oscillation is not only restricted by the inertia but also by the spring force and the damping. The beam is a damped driven harmonic oscillator (DHO). It is driven by an alternating drive force $F_{drive,AC}$, i.e. a continuous sinusoidal drive force over time t with the amplitude F_{AC} at the angular drive frequency ω_d standing for the AC drive voltage (equation 2.11 in section 2.2.2). Thereby the beam mass is accelerated. The inertia $F_{inertia}$ opposes the beam bending in accordance with Newton's second law of motion (Figure 2.12). The spring force F_{spring} acts against the direction of increasing beam bending and pushes the beam back towards the equilibrium position resulting from the beam stiffness which is described by the spring constant k_{beam}. Within a viscous medium the amplitude of beam oscillation is damped and decays exponentially with time. Due to friction characterized by the damping coefficient r_{beam} energy is lost, i.e. dissipated. Like F_{spring} the damping force $F_{damping}$ acts in the direction opposite to that of beam bending. The dynamic balance of forces assumes the beam mass m_{beam} to be concentrated at one point [89, 91, 92]

$$F_{inertia} = F_{drive,AC} - F_{damping} - F_{spring} \tag{2.124}$$

$$m_{beam}\frac{\partial z^2}{\partial^2 t} = F_{AC}\cos(\omega_d t) - r_{beam}\frac{\partial z}{\partial t} - k_{beam} z(t) \tag{2.125}$$

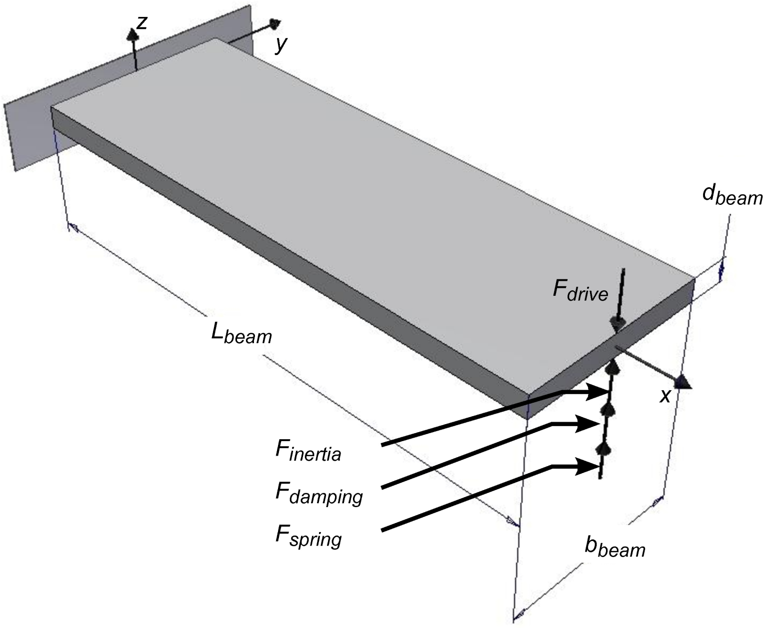

Figure 2.12: Forces acting on oscillating beam

Equation 2.125 is re-arranged resulting in an inhomogeneous second order linear differential equation of motion that is satisfied by the damped DHO

$$m_{beam}\frac{\partial z^2}{\partial^2 t}+r_{beam}\frac{\partial z}{\partial t}+k_{beam}z(t)=F_{AC}\cos(\omega_d t) \tag{2.126}$$

The complete solution to equation 2.126 consists of two terms [89, 91, 92]

$$z(t)=z_{transient}(t)+z_{steady-state}(t) \tag{2.127}$$

The “transient” term $z_{transient}(t)$ is the solution to the homogeneous differential equation of a damped harmonic oscillator [89, 91, 92]

$$m_{beam}\frac{\partial z^2}{\partial^2 t}+r_{beam}\frac{\partial z}{\partial t}+k_{beam}z(t)=0 \tag{2.128}$$

and decays exponentially with time. The “steady-state” term $z_{steady\ state}(t)$ is the solution to the inhomogeneous differential equation 2.126 showing the ultimate behaviour of the oscillator after the transient term has vanished [89, 91, 92]. In order to solve equation 2.126, solution

$$z_{steady-state}(t)=z_{AC}\cos(\omega_d t+\varphi) \tag{2.129}$$

is used, where z_{AC} is the amplitude of beam oscillation and φ the phase [89, 92]. Equation 2.126 becomes

$$-m_{beam}z_{AC}\omega_d^2\cos(\omega_d t+\varphi)-r_{beam}z_{AC}\omega_d\sin(\omega_d t+\varphi)+k_{beam}z_{AC}\cos(\omega_d t+\varphi)=F_{AC}\cos(\omega_d t) \tag{2.130}$$

The drive force is defined as

$$F_{drive,AC}=F_{AC}\cos(\omega_d t)=F_{AC}\sin(\omega_d t+\varphi)\sin\varphi+F_{AC}\cos(\omega_d t+\varphi)\cos\varphi \tag{2.131}$$

Equation 2.130 is reduced to

$$z_{AC}(k_{beam}-m_{beam}\omega_d^2)=F_{AC}\cos\varphi \tag{2.132}$$

$$-z_{AC}r_{beam}\omega_d=F_{AC}\sin\varphi \tag{2.133}$$

The system of equations 2.132 and 2.133 is

$$z_{AC}^2\left((k_{beam}-m_{beam}\omega_d^2)^2+r_{beam}^2\omega_d^2\right)=F_{AC}^2(\cos^2\varphi+\sin^2\varphi) \tag{2.134}$$

Solving for z_{AC} gives both amplitude of beam oscillation and phase [89, 91]

$$z_{AC}=\frac{F_{AC}}{\sqrt{(k_{beam}-m_{beam}\omega_d^2)^2+r_{beam}^2\omega_d^2}} \tag{2.135}$$

and

$$tan\varphi=-\frac{r_{beam}\omega_d}{k_{beam}-m_{beam}\omega_d^2} \tag{2.136}$$

At low drive frequencies the amplitude is stiffness-controlled [91]

$$z_{AC,low\ \omega_d}\approx\frac{F_{AC}}{k_{beam}} \tag{2.137}$$

and at high drive frequencies it is mass-controlled [91]

$$z_{AC,high\ \omega_d}\approx\frac{F_{AC}}{m_{beam}\omega_d^2} \tag{2.138}$$

tending to zero as ω_d becomes very large, because of the mechanical or mass inertia. The maximum is reached when the denominator is a minimum. This takes place when the function under the square root is differentiated and set to zero [91, 92]

$$\frac{\partial}{\partial\omega_d}\left((k_{beam}-m_{beam}\omega_d^2)^2+r_{beam}^2\omega_d^2\right)=0 \tag{2.139}$$

so that

$$\omega_d^2 = \frac{k_{beam}}{m_{beam}} - \frac{r_{beam}^2}{2m_{beam}^2} \tag{2.140}$$

where the angular frequency of the 1st resonance, i.e. the angular fundamental or natural frequency, is

$$\omega_1^2 = 4\pi f_1^2 = \frac{k_{beam}}{m_{beam}} \tag{2.141}$$

Thus, the maximum amplitude of beam oscillation occurs at a frequency slightly less than ω_1 [91, 92]

$$\begin{aligned} z_{AC,max} &= \frac{F_{AC}}{\sqrt{\left(m_{beam}\omega_1^2 - m_{beam}\left(\omega_1^2 - \frac{r_{beam}^2}{2m_{beam}^2}\right)\right)^2 + r_{beam}^2\left(\omega_1^2 - \frac{r_{beam}^2}{2m_{beam}^2}\right)}} && (2.142) \\ &= \frac{F_{AC}}{r_{beam}\sqrt{\omega_1^2 - \frac{r_{beam}^2}{4m_{beam}^2}}} && (2.143) \end{aligned}$$

That results from damping. The angular frequency of the 1th resonance of the one-layered damped DHO is given by

$$\omega_{1,damped}^2 = \omega_1^2 - \frac{r_{beam}^2}{4m_{beam}^2} \tag{2.144}$$

The maximum amplitude is then

$$z_{AC,max} = \frac{F_{AC}}{r_{beam}\omega_{1,damped}} \tag{2.145}$$

The lighter the damping, i.e. the smaller the damping coefficient r_{beam} is, the more marked is the increase in amplitude and it can be approximated by [92]

$$z_{AC,max} \approx \frac{F_{AC}}{r_{beam}\omega_1} \tag{2.146}$$

The general solution of the damped DHO referring to equation 2.127 is [89, 91, 92]

$$z(t) = A_{transient} e^{\left(-\frac{r_{beam}}{2m_{beam}}t\right)} \cos(\omega_{1,damped}t + \varphi_{transient}) + z_{AC}\cos(\omega_d t + \varphi) \tag{2.147}$$

where $A_{transient}$ is the amplitude of the transient term. The transient term decays exponentially with time and becomes irrelevant at some point. It describes a damped non-driven harmonic oscillator. The steady-state term stands for the long-term or steady-state behaviour of the beam, i.e. a continuous sinusoidal motion [89, 91, 92].

In order to maintain steady-state beam oscillation, the alternating drive force must replace any energy lost or dissipated in each cycle through friction. The ratio between the energy stored by the beam W and the energy lost per cycle or complete oscillation ΔW is constant and provides the quality factor Q of a damped DHO [91, 92]

$$Q = \frac{2\pi W}{\Delta W} = \frac{m_{beam}}{r_{beam}}\omega_{1,damped} \tag{2.148}$$

If r_{beam} is small, Q is very large and to a very close approximation [91, 92]

$$Q \approx \frac{m_{beam}}{r_{beam}}\omega_1 \tag{2.149}$$

The same quality factor Q is met in two other roles. Firstly, it is a measure of the resonance bandwidth at half of the maximum amplitude (Figure 2.13) [85, 91, 92]

$$Q = \frac{\omega_1}{\Delta\omega} = \frac{f_1}{\Delta f} \tag{2.150}$$

where f_1 is the non-angular fundamental or natural frequency. For large Q, the resonance peak is narrow and sharp.

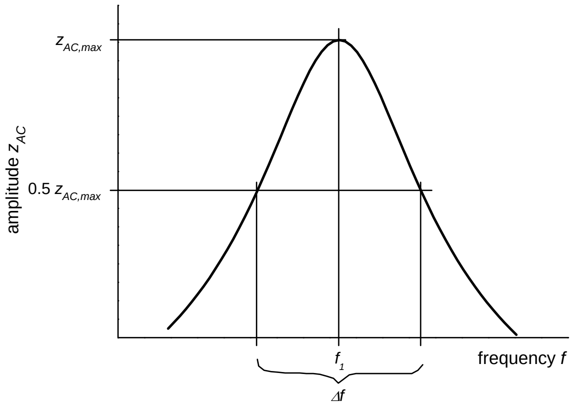

Figure 2.13: Resonance peak

Secondly, Q is the factor by which the deflection at pure beam bending is amplified at resonance. At very low drive frequencies $\omega_d \rightarrow 0$, the displacement at the free end of the beam equals the deflection at pure beam bending referring to equation 2.135 [89, 91, 92]

$$z_{AC,low\ \omega_d} \approx z_{DC} = \frac{F_{AC}}{k_{beam}} \tag{2.151}$$

so that [91]

$$\left(\frac{z_{AC,max}}{z_{DC}}\right)^2 = \left(\frac{F_{AC}}{r_{beam}\omega_{1,damped}}\frac{k_{beam}}{F_{AC}}\right)^2 = \frac{m_{beam}^2\omega_1^4}{r_{beam}^2\omega_1^2 - \frac{r_{beam}^4}{4m_{beam}^2}} \tag{2.152}$$

$$= \frac{Q^2}{1-\frac{1}{4Q^2}} \tag{2.153}$$

For large Q [89, 91, 92]

$$\frac{z_{AC,max}}{z_{DC}} \approx Q \tag{2.154}$$

The angular fundamental or natural frequency of the 1^{st} resonance is also defined by [93]

$$\omega_1^2 = \frac{k_{beam}}{M_{eff}m_{beam}} \tag{2.155}$$

where M_{eff} is the effective mass factor addressing the fact that the beam mass is distributed along its width, thickness, and length instead of being concentrated at one point. For a beam with a rectangular cross-section the effective mass factor is [93]

$$M_{eff} = 0.24 \tag{2.156}$$

The effective mass factor can be applied to all formulas incorporating the beam mass within this section.
Equating equation 2.121 with equation 2.155 leads to the definition of the spring constant of the beam

$$k_{beam} = \frac{(\beta_m L_{beam})^4}{L_{beam}^4} M_{eff} m_{beam} \frac{E_{beam} I_{area,beam}}{\rho_{beam} A_{beam}} \tag{2.157}$$

$$= \frac{(\beta_1 L)^4 M_{eff}}{12} \frac{b_{beam} d_{beam}^3}{L_{beam}^3} E_{beam} \tag{2.158}$$

where

$$m_{beam} = \rho_{beam} V_{beam} = \rho_{beam} b_{beam} d_{beam} L_{beam} \tag{2.159}$$

with the beam volume V_{beam}. So, the spring constant of the beam depends on beam dimensions and modulus of elasticity. From equation 2.141 it is clear that a stiffer beam with a bigger spring constant has a higher fundamental or natural frequency f_1. Putting equations 2.151, 2.154, and 2.158 together shows that both deflection at pure beam bending and amplitude of beam oscillation depend on the spring constant of the beam, i.e. on beam dimensions and modulus of elasticity

$$z_{AC,max} \approx z_{DC} Q = \frac{F_{AC}}{k_{beam}} Q = \frac{12}{(\beta_1 L)^4 M_{eff}} \frac{L_{beam}^3}{b_{beam} d_{beam}^3} \frac{F_{AC}}{E_{beam}} Q \tag{2.160}$$

For a multi-layered beam, the ratio of layer thickness affects the extent of $z_{AC,max}$ the same way as z_{DC} with the biggest value at a certain thickness ratio due to direct proportionality between z_{AC} and z_{DC} (see section 2.2.6). This dependency is a bell-shaped distribution for a two-layered beam [86].

In the case of the self-actuating and self-sensing piezoresistive microscale silicon cantilever, the maximum amplitude of beam oscillation $z_{AC,max}$ is generated by the sinusoidal change of beam temperature caused by the dynamic AC drive power $P_{drive,AC,dynamic}$ (see section 2.2.4). Since $z_{AC,max}$ may be regarded as an alternating deflection on pure beam bending z_{DC}, which is directly proportional to temperature change (equation 2.86 in section 2.2.6), and because of the linear relationship between drive power and temperature (equation 2.41 in section 2.2.4), the maximum amplitude is directly proportional to beam temperature change and dynamic AC drive power

$$z_{AC,max} \sim \Delta T \sim P_{drive,AC,dynamic} \tag{2.161}$$

The alternating drive force $F_{drive,AC}$ with the amplitude F_{AC} makes the beam oscillate, i.e. bend up and down. As with pure beam bending (see section 2.2.6), the convex part of the beam is elongated and in tensile normal stress (positive sign), whereas the concave part is shortened and in compressive normal stress (negative sign). The neutral axis does not suffer any strain and stress, i.e. it retains its initial length. The magnitude of normal stress $\sigma(x,z)$ at any point on any cross-section of the beam is directly proportional to the distance z from the neutral axis, reaching maximum at the surface [85]

$$\frac{\pm\sigma(x,z)}{z} = \frac{\pm\sigma_{max}(x)}{\frac{d_{beam}}{2}} \tag{2.162}$$

$$\pm\sigma(x,z) = 2\frac{z}{d_{beam}} \left(\pm\sigma_{max}(x)\right) \tag{2.163}$$

On any cross-section of the beam A_{beam} it can be said that tensile and compressive normal stresses and, therefore, normal forces are in equilibrium (see equations 2.50 and 2.51 in section 2.2.6) [85]

$$\int\int_{A_{beam}} +\sigma(x,z)\partial A_{beam} = \int\int_{A_{beam}} -\sigma(x,z)\partial A_{beam} \tag{2.164}$$

$$\int \partial + F(x,z) = \int \partial - F(x,z) \tag{2.165}$$

Since the alternating drive force is concentrated at the free end of the beam, it introduces a non-uniform stress distribution within the beam along length (Figure 2.14).

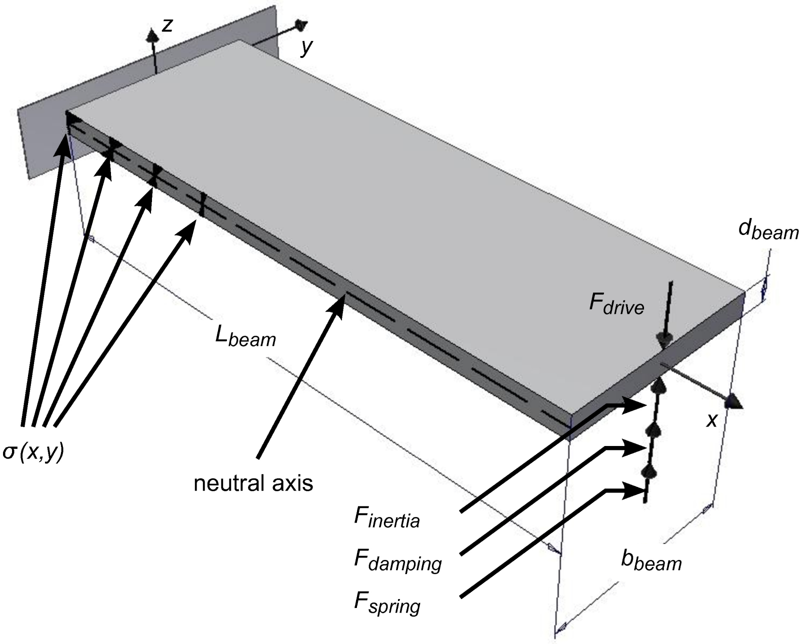

Figure 2.14: Non-uniform stress distribution within beam along length

At the fixed end there is the maximum normal stress at the beam surface due to beam bending [85]

$$\sigma(x = 0, z = \frac{d_{beam}}{2}) = \sigma_{max} \tag{2.166}$$

and at the free end there is the minimum

$$\sigma(x = L_{beam}, z) = 0 \tag{2.167}$$

Normal forces cause a bending moment about the y-axis at any cross-section [85]

$$M_y(x) = \int\int_{A_{beam}} \partial F(x, z)z \tag{2.168}$$

$$= \int_{b_{beam}} \int_{z=-\frac{d_{beam}}{2}}^{z=\frac{d_{beam}}{2}} (\sigma(x, z)\partial A_{beam})\, z \tag{2.169}$$

where

$$\partial A_{beam} = b_{beam}\partial z \tag{2.170}$$

It follows that

$$M_y(x) = \int_{b_{beam}} \int_{z=-\frac{d_{beam}}{2}}^{z=\frac{d_{beam}}{2}} \left(2\frac{b_{beam}}{d_{beam}}\sigma_{max}(x)\right) z^2\partial z \tag{2.171}$$

$$= \left|\frac{2}{3}\frac{b_{beam}}{d_{beam}}\sigma_{max}(x)z^3\right|_{-\frac{d_{beam}}{2}}^{\frac{d_{beam}}{2}} \tag{2.172}$$

The bending moment about the y-axis at any cross-section yields

$$M_y(x) = \frac{b_{beam}d_{beam}^2}{6}\sigma_{max}(x) \tag{2.173}$$

Consequently, the bending moment of the beam about the y-axis is given by

$$M_{beam} = F_{AC} L_{beam} = M_y(x=0) = \frac{b_{beam} d_{beam}^2}{6} \sigma_{max} \tag{2.174}$$

Equation 2.160 becomes

$$z_{AC,max} \approx z_{DC} Q = \frac{F_{AC}}{k_{beam}} Q = \frac{2}{(\beta_1 L)^4 M_{eff}} \frac{L_{beam}^2}{d_{beam}} \frac{\sigma_{max}}{E_{beam}} Q \tag{2.175}$$

showing the linear relationship between deflection on pure beam bending or amplitude of beam oscillation and maximum normal stress at the beam surface at the fixed end of the beam.
So far, all calculations are made for a beam made of one material layer with a rectangular cross-section. Applying the equivalent width method, it is possible to estimate the fundamental or natural frequency and spring constant of a beam consisting of multiple material layers with rectangular cross-sections and same length and width. A reference material layer with an equivalent cross-section is chosen. The width of any layer is increased in the same proportion that the modulus of elasticity of this layer makes with the modulus of the reference material layer [94]. Referring to equation 2.121, the fundamental or natural frequency f_1 of a multi-layered beam may be approximated by [74]

$$f_{1,multi} = \frac{1}{2\pi} \frac{(\beta_1 L_{beam})^2}{L_{beam}^2} \sqrt{\frac{E_{reference} I_{area,sum}}{\sum_{i=1}^{n} \rho_i A_i}} \tag{2.176}$$

where $E_{reference}$ is the modulus of elasticity of the reference material layer, $I_{area,sum}$ the sum of the area moments of inertia of all layers, ρ_i the density and A_i the cross-section of layer i. The sum of the area moments of inertia of all layers is defined as [74]

$$I_{area,sum} = \sum_{i=1}^{n} \left(\frac{b_i d_i^3}{12} + A_i \left[\left(\sum_{k=0}^{i-1} d_k + \frac{d_i}{2} \right) - z_c \right]^2 \right), \quad d_0 = 0 \tag{2.177}$$

where b_i is the width, d_i the thickness, and A_i the cross-section of layer i

$$A_i = b_i d_i \tag{2.178}$$

and z_c the centroid [74]

$$z_c = \frac{\sum_{i=1}^{n} \left(\left[\sum_{k=0}^{i-1} d_k + \frac{d_i}{2} \right] A_i \right)}{\sum_{i=1}^{n} A_i}, \quad d_0 = 0 \tag{2.179}$$

Regarding equation 2.157, the spring constant of a multi-layered beam may be estimated thus

$$k_{multi} = \frac{(\beta_1 L)^4}{L^4} M_{eff} m_{beam} \frac{E_{reference} I_{area,sum}}{\sum_{i=1}^{n} \rho_i A_i} \tag{2.180}$$

where

$$m_{beam} = \rho_{beam} V_{beam} = \sum_{i=1}^{n} \rho_i A_i L_{beam} = \sum_{i=1}^{n} \rho_i b_i d_i L_{beam} \tag{2.181}$$

Calculated example of fundamental frequency and spring constant
The fundamental frequency $f_{1,multi}$ and the spring constant k_{multi} of a composite beam made of multiple material layers with rectangular cross-sections given in Table 2.11 is estimated according to equations 2.176 and 2.180. The equivalent width method is applied to the dimensions defined in Table 2.1 (see example in section 2.2.3). Since the chromium layer and the gold layer are much smaller, only a fifteenth of the calculated values is considered. Values of density and modulus of elasticity are listed in Tables 2.5 (see example in section 2.2.4) and 2.9 (see example in section 2.2.6). The wave number of the first resonance is given by equation 2.114 and the effective mass factor by equation 2.156. Results are presented in Table 2.12.

Material layer i	Width b_i µm	Thickness d_i µm	Length L_i µm
Si	150	6	460
SiO_2	65	1.1	460
Si_xN_y	282	0.3	460
Al	62	0.3	460
Cr	17 ($\frac{1}{15}$)	0.03	460
Au	5 ($\frac{1}{15}$)	0.13	460

Table 2.11: Dimensions of layers of composite beam according to equivalent width method

Parameter	Unit	Value
$f_{1,multi}$	kHz	48.1
k_{multi}	$\frac{\mathrm{N}}{\mathrm{m}}$	26

Table 2.12: Fundamental frequency and spring constant

2.2.8 Actuation efficiency

The actuation efficiency is the maximum amplitude of beam oscillation $z_{AC,max}$, i.e. the amplitude at the fundamental or natural frequency f_1 that is caused by the dynamic AC drive power $P_{drive,AC,dynamic}$ of 1 mW (equation 2.18 in section 2.2.2)

$$actuation\ efficiency = \frac{z_{AC,max} \text{ in nm}}{P_{drive,AC,dynamic} \text{ in mW}} \tag{2.182}$$

The advantage of high actuation efficiency is, that only small $P_{drive,AC,dynamic}$ is necessary to cause $z_{AC,max}$. Additionally, the beam temperature is lower (equation 2.29 in section 2.2.3). Increased temperature of the piezoresistors at the base of the beam may reduce piezoresistive coefficients (see section 2.3.1), the AC Wheatstone bridge output voltage signal (equation 2.221 in section 2.3.2) and therefore, the deflection sensitivity (equation 2.225 in section 2.3.3). Thermomechanical noise may increase (equation 2.235 in section 2.4.2). At low beam temperature sensitive samples are not damaged by the tip as it is not hot.

Through $z_{AC,max}$ the actuation efficiency depends on beam dimensions and modulus of elasticity E_{beam} (equation 2.160 in section 2.2.7). It varies inversely with the spring constant k_{beam} and, therefore, with beam width b_{beam}, the cube of beam thickness d_{beam}, and E_{beam}, and it is directly proportional to the cube of beam length L_{beam}

$$actuation\ efficiency \sim z_{AC,max} \sim \frac{1}{k_{beam}} \sim \frac{L_{beam}^3}{b_{beam} d_{beam}^3} \frac{1}{E_{beam}} \tag{2.183}$$

From this relationship it may be concluded that a long and thin, hence soft beam with a small spring constant has high actuation efficiency.

2.3 Self-sensing of the cantilever

2.3.1 Piezoresistive effect

The functioning of a piezoresistor relies on the piezoresistive effect. The piezoresistor changes its resistivity due to mechanical stress caused by strain. Strain occurs if the piezoresistor is bent, i.e. if the self-actuating and self-sensing piezoresistive microscale silicon cantilever is bent. Such a piezoresistor is made by selectively doping the semiconductor silicon with dopant atoms. The result will be either a p-type or a n-type piezoresistor. When either of them experiences strain, the atomic spacing changes. This affects the electronic band structure of the semiconductor and hence its conductivity. A detailed quantum-physical explanation is given in [66].

The stress within the piezoresistor results from strain in accordance with Hooke's law. That is the same as for pure beam bending (see section 2.2.6). The general description of the linear relationship between stress and strain in a three-dimensional material is a fourth rank tensor. Because of various symmetry arguments it may be re-written as a square 6 x 6 symmetric matrix with six independent stress, normal stress σ_i and shear stress τ_i, and strain ϵ_j components, and stiffness coefficients C_{ij} as proportionality constants [64]

$$\sigma_i = \sum_j C_{ij}\epsilon_j \tag{2.184}$$

$$\begin{pmatrix} \sigma_x \\ \sigma_y \\ \sigma_z \\ \tau_{yz} \\ \tau_{zx} \\ \tau_{xy} \end{pmatrix} = \begin{bmatrix} C_{11} & C_{12} & C_{12} & 0 & 0 & 0 \\ C_{12} & C_{11} & C_{12} & 0 & 0 & 0 \\ C_{12} & C_{12} & C_{11} & 0 & 0 & 0 \\ 0 & 0 & 0 & C_{44} & 0 & 0 \\ 0 & 0 & 0 & 0 & C_{44} & 0 \\ 0 & 0 & 0 & 0 & 0 & C_{44} \end{bmatrix} \begin{pmatrix} \epsilon_x \\ \epsilon_y \\ \epsilon_z \\ \epsilon_{yz} \\ \epsilon_{zx} \\ \epsilon_{xy} \end{pmatrix} \tag{2.185}$$

where ϵ_j is the strain of direction j defined as the change in length ΔL_j in relation to the length L_j

$$\epsilon_j = \frac{\Delta L_j}{L_j} \tag{2.186}$$

The matrix equation may be inverted with compliance coefficients S_{ij} as proportionality constants [64]

$$\epsilon_i = \sum_j S_{ij}\sigma_j \tag{2.187}$$

In cubic materials there are only three independent stiffness or compliance coefficients. From the latter, the compliance coefficients, the modulus of elasticity $E_{<lmn>}$, i.e. the Young's modulus, is calculated [95]

$$\frac{1}{E_{<lmn>}} = S_{11} - 2\left(S_{11} - S_{12} - \frac{1}{2}S_{44}\right)\left(l^2m^2 + l^2n^2 + m^2n^2\right) \tag{2.188}$$

where *l, m, n* are direction cosines between an arbitrary crystallographic direction and the cubic crystal axes. The more common form of Hooke's law is then

$$\sigma_{<l,m,n>} = E_{<l,m,n>}\epsilon_{<l,m,n>} \tag{2.189}$$

For a (100) cubic crystal, the modulus of elasticity for the <110> in-plane crystallographic direction is [95]

$$\frac{1}{E_{<110>}} = S_{11} - \frac{1}{2}\left(S_{11} - S_{12} - \frac{1}{2}S_{44}\right) \tag{2.190}$$

For single-crystal silicon the compliance coefficients and the modulus of elasticity for the <110> crystallographic direction are given in Table 2.13.

S_{11} $\frac{1}{\text{Pa}}$	S_{12} $\frac{1}{\text{Pa}}$	S_{44} $\frac{1}{\text{Pa}}$	$E_{<110>,Si}$ GPa
$0.768\cdot10^{-11}$	$-0.214\cdot10^{-11}$	$1.26\cdot10^{-11}$	168.9

Table 2.13: Compliance coefficients and Young's modulus of single-crystal silicon [87]

As already shown in section 2.2.1, the modulus of elasticity depends on temperature. Therefore, the stiffness coefficients are not only dependent on the crystallographic direction but also on the temperature. Referring to the linear dependence of the modulus of elasticity on temperature (equation 2.3 in section 2.2.1), a linear temperature dependency may be attributed to the stiffness coefficients with temperature coefficients of elasticity $K_{C_{ij}}$ as proportionality constants

$$\frac{\Delta C_{ij}}{C_{ij}} = K_{C_{ij}}\Delta T \tag{2.191}$$

Thus, the temperature coefficient of the modulus of elasticity $\beta_{<lmn>}$ for an arbitrary crystallographic direction in cubic crystals may be determined from

$$\beta_{<lmn>} = K_{C_{11}} - 2\left(K_{C_{11}} - K_{C_{12}} - K_{C_{44}}\right)\left(l^2m^2 + l^2n^2 + m^2n^2\right) \tag{2.192}$$

For a (100) cubic crystal the temperature coefficient of the modulus of elasticity for the <110> in-plane crystallographic direction is

$$\beta_{<110>} = \frac{1}{2}\left(K_{C_{11}} + K_{C_{12}} + K_{C_{44}}\right) \tag{2.193}$$

Since the temperature coefficients of elasticity $K_{C_{ij}}$ are negative for single-crystal silicon, not only is the temperature coefficient of the modulus of elasticity for the <110> crystallographic direction $\beta_{<110>}$ negative but also, for the same reason, the modulus of elasticity decreases with rising temperature (Table 2.14).

$K_{C_{11}}$ $\frac{1}{\mathrm{K}}$	$K_{C_{12}}$ $\frac{1}{\mathrm{K}}$	$K_{C_{44}}$ $\frac{1}{\mathrm{K}}$	$\beta_{<110>,Si}$ $\frac{1}{\mathrm{K}}$
$-75.3 \cdot 10^{-6}$	$-24.5 \cdot 10^{-6}$	$-55.5 \cdot 10^{-6}$	$-77.65 \cdot 10^{-6}$

Table 2.14: Temperature coefficients of elasticity and temperature coefficient of Young's modulus of single-crystal silicon [96]

The linear relationship between modulus of elasticity for an arbitrary crystallographic direction in cubic crystals $E_{<lmn>}$ and temperature change ΔT may be written as follows

$$\frac{\Delta E_{<lmn>}}{E_{<lmn>}} = \beta_{<lmn>}\Delta T \tag{2.194}$$

The change in piezoresistivity results from stress induced by strain. Consequently, for this change, too, a similar matrix as for the strain-stress relationship (equation 2.184) may be found with six independent fractional piezoresistivity change $\frac{\Delta\rho_{piezo,i}}{\rho_{piezo}}$ and stress, normal stress σ_j and shear stress τ_j, components, and piezoresistive coefficients π_{ij} as proportionality constants [97]

$$\frac{\Delta\rho_{piezo,i}}{\rho_{piezo}} = \sum_j \pi_{ij}\sigma_j \tag{2.195}$$

$$\begin{pmatrix} \frac{\Delta\rho_{piezo,x}}{\rho_{piezo}} \\ \frac{\Delta\rho_{piezo,y}}{\rho_{piezo}} \\ \frac{\Delta\rho_{piezo,z}}{\rho_{piezo}} \\ \frac{\Delta\rho_{piezo,yz}}{\rho_{piezo}} \\ \frac{\Delta\rho_{piezo,zx}}{\rho_{piezo}} \\ \frac{\Delta\rho_{piezo,xy}}{\rho_{piezo}} \end{pmatrix} = \begin{bmatrix} \pi_{11} & \pi_{12} & \pi_{12} & 0 & 0 & 0 \\ \pi_{12} & \pi_{11} & \pi_{12} & 0 & 0 & 0 \\ \pi_{12} & \pi_{12} & \pi_{11} & 0 & 0 & 0 \\ 0 & 0 & 0 & \pi_{44} & 0 & 0 \\ 0 & 0 & 0 & 0 & \pi_{44} & 0 \\ 0 & 0 & 0 & 0 & 0 & \pi_{44} \end{bmatrix} \begin{pmatrix} \sigma_x \\ \sigma_y \\ \sigma_z \\ \tau_{yz} \\ \tau_{zx} \\ \tau_{xy} \end{pmatrix} \tag{2.196}$$

where $\Delta\rho_{piezo,i}$ is the piezoresistivity change and ρ_{piezo} the isotropic resistivity of the unstressed piezoresistor. In cubic materials there are only three independent piezoresistive coefficients analogous to the stiffness coefficients. Piezoresistive coefficients strongly depend on the type of dopant. Furthermore, they are influenced by doping concentration and temperature. Beyond doping concentrations of $\frac{10^{18}}{\mathrm{cm}^{-3}}$, piezoresistive coefficients drop markedly [98, 99]. They decrease with increasing temperature in a non-linear dependency. At higher doping, the temperature influence becomes smaller [98, 100]. Piezoresistive coefficients for an arbitrary crystallographic direction in cubic crystals are formulated with reference to the orientation of a piezoresistor in relation to the direction of stress. If the electric current through the piezoresistor is in the direction of stress (top in Figure 2.15(a)), i.e. this is a longitudinal piezoresistor experiencing longitudinal stress, the longitudinal piezoresistive coefficient is [97, 101]

$$\pi_L = \pi_{11} - 2(\pi_{11} - \pi_{12} - \pi_{44})\left(l_1^2 m_1^2 + l_1^2 n_1^2 + m_1^2 n_1^2\right) \tag{2.197}$$

If the electric current through the piezoresistor is perpendicular to the direction of stress (bottom in Figure 2.15(a)), i.e. this is a transverse piezoresistor experiencing transverse stress, the transverse piezoresistive coefficient is [97, 101]

$$\pi_T = \pi_{12} + (\pi_{11} - \pi_{12} - \pi_{44})\left(l_1^2 l_2^2 + m_1^2 m_2^2 + n_1^2 n_2^2\right) \tag{2.198}$$

where l_1, m_1, n_1 are the direction cosines between the longitudinal piezoresistor direction and the cubic crystal axes, and l_2, m_2, n_2 are the direction cosines between the transverse piezoresistor direction and the cubic crystal axes [64, 97].

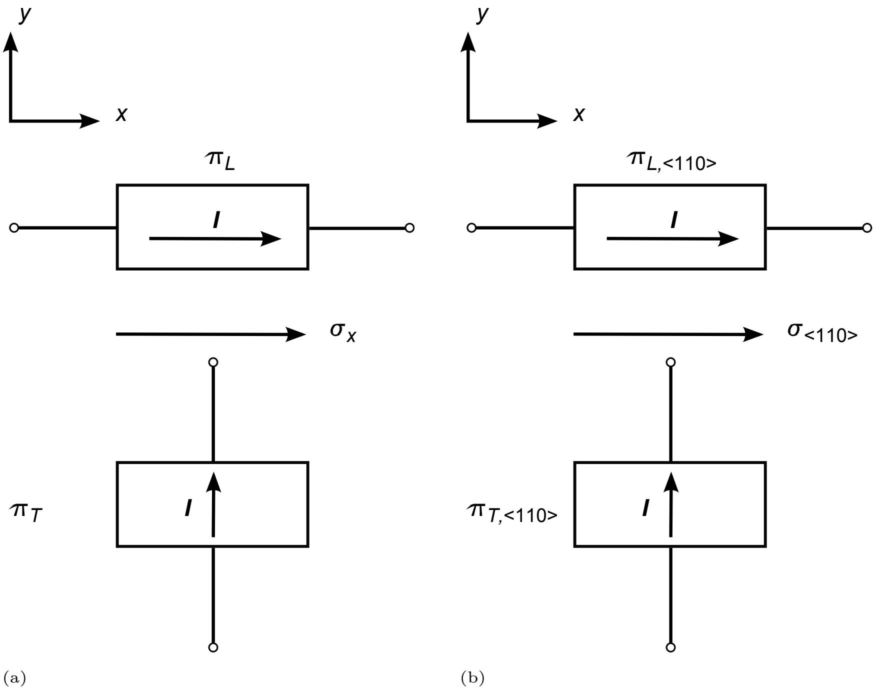

Figure 2.15: Piezoresistive coefficient: longitudinal (top) and transverse (bottom)

For a (100) cubic crystal the longitudinal piezoresistive coefficient for the <110> in-plane crystallographic direction is [101]

$$\pi_{L,<110>} = \frac{1}{2}(\pi_{11} + \pi_{12} + \pi_{44}) \tag{2.199}$$

and the transverse piezoresistive coefficient [101]

$$\pi_{T,<110>} = \frac{1}{2}(\pi_{11} + \pi_{12} - \pi_{44}) \tag{2.200}$$

Taking into account equation 2.195, the corresponding fractional piezoresistivity changes caused by stress $\sigma_{<110>}$ oriented along the <110> in-plane crystallographic direction are

$$\frac{\Delta\rho_{piezo,L}}{\rho_{piezo}} = \pi_{L,<110>}\sigma_{<110>} \tag{2.201}$$

$$\frac{\Delta\rho_{piezo,T}}{\rho_{piezo}} = \pi_{T,<110>}\sigma_{<110>} \tag{2.202}$$

The piezoresistivity is directly proportional to the resistance of the piezoresistor given by

$$R_{piezo} = \rho_{piezo}\frac{L_{piezo}}{A_{piezo}} \tag{2.203}$$

It is assumed that the piezoresistor is a rectangular cuboid, where L_{piezo} is the length of the piezoresistor and A_{piezo} its cross-sectional area

$$A_{piezo} = b_{piezo}d_{piezo} \tag{2.204}$$

where b_{piezo} is the width of the piezoresistor and d_{piezo} the thickness. The isotropic resistivity of the unstressed piezoresistor is [99]

$$\rho_{piezo} = \frac{1}{\mu_p q c_{doping}} \tag{2.205}$$

where μ_p is the hole mobility, q the electron charge, and c_{doping} the doping density or concentration, so that

$$R_{piezo} = \frac{1}{\mu_p q c_{doping}}\frac{L_{piezo}}{b_{piezo}d_{piezo}} \tag{2.206}$$

Due to proportionality, the fractional resistance change for the longitudinal piezoresistor is

$$\frac{\Delta R_{piezo,L}}{R_{piezo}} = \pi_{L,<110>} \sigma_{<110>} \tag{2.207}$$

and for the transverse piezoresistor

$$\frac{\Delta R_{piezo,T}}{R_{piezo}} = \pi_{T,<110>} \sigma_{<110>} \tag{2.208}$$

where $\Delta R_{piezo,L}$ and $\Delta R_{piezo,T}$ are the resistance change of the longitudinal and the transverse piezoresistor, respectively. For the <110> in-plane crystallographic direction of single-crystal silicon, the piezoresistive coefficients are greater for a p-type piezoresistor (Table 2.15). Under stress they result in a bigger change of the piezoresistivity and resistance (equations 2.201 and 2.202, 2.207 and 2.208). Therefore, a p-type silicon piezoresistor is better suited for deflection sensing.

Doping type	Resistivity $\Omega \cdot \mathrm{cm}$	Piezoresistive coefficients $\frac{10^{-11}}{\mathrm{Pa}}$				
		π_{11}	π_{12}	π_{44}	$\pi_{L,<110>,Si}$	$\pi_{T,<110>,Si}$
n	11.7	-102.2	53.4	-13.6	-31.2	-17.6
p	7.8	6.6	-1.1	138.1	71.8	-66.3

Table 2.15: Resistivity and piezoresistive coefficients of n-type and p-type single-crystal silicon [101]

2.3.2 Wheatstone bridge

Since the self-actuating and self-sensing piezoresistive microscale silicon cantilever is oriented along the <110> crystallographic direction of single-crystal silicon in the (100) plane, it is appropiate to use p-type silicon piezoresistors for deflection sensing because of their larger piezoresistive coefficients compared to n-type ones (see Table 2.15 section 2.3.1). Four piezoresistors are connected in a Wheatstone bridge configuration (Figure 2.16). This provides several advantages. The temperature dependency of the Wheatstone bridge is cancelled out because all four piezoresistors have the same temperature. The sensitivity is four times higher that that of a single piezoresistor, but there is also twice the noise [102]. The symmetry of the Wheatstone bridge significantly decreases any non-linearity in the output signal [47].

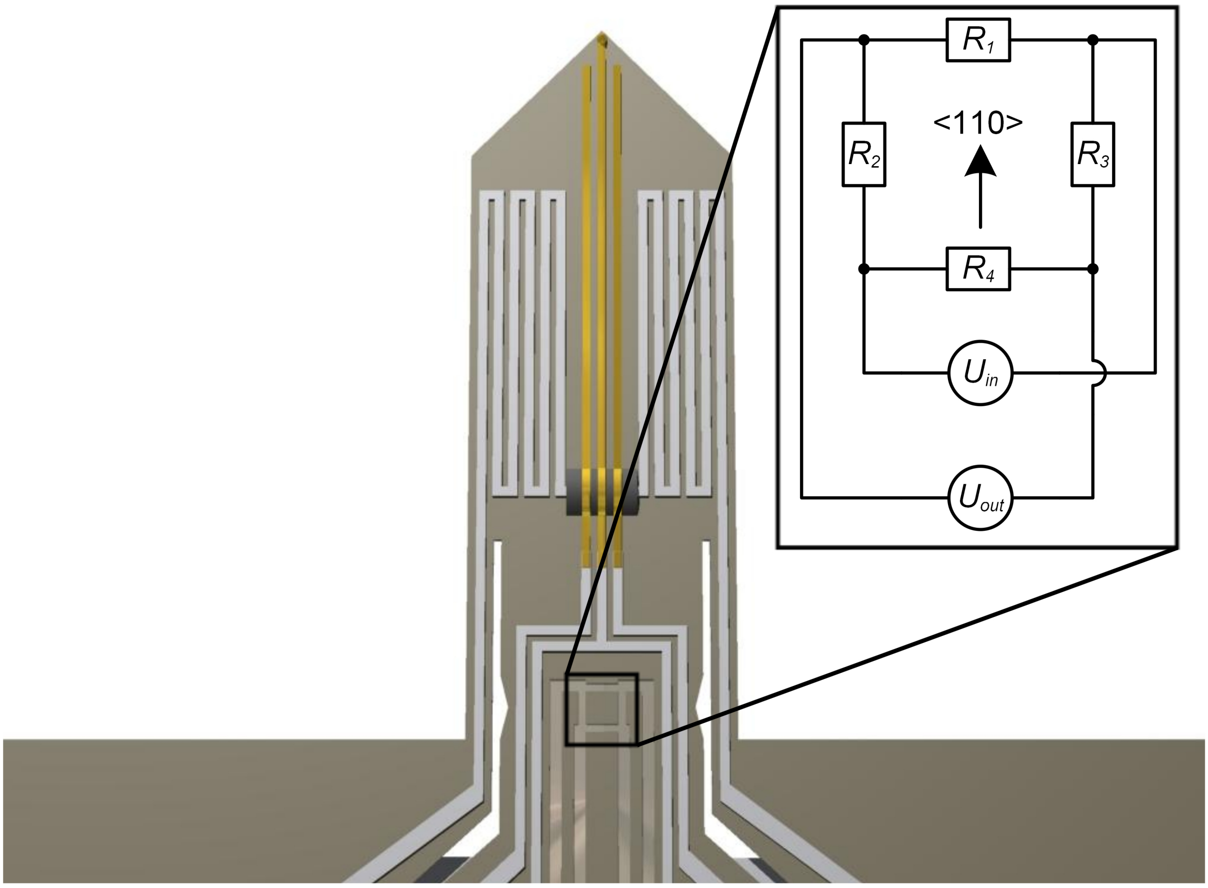

Figure 2.16: Wheatstone bridge of four p-type silicon piezoresistors at base of beam in <110> crystallographic direction

Furthermore, the Wheatstone bridge is placed at the beam base and the piezoresistors are ultra-shallow, i.e. they are confined to the beam surface, where they experience the maximum normal stress $\sigma_{<110>,max}$ along the <110> crystallographic direction during beam bending (equation 2.166 in section 2.2.7) so that there is maximum resistance change (equations 2.207 and 2.208 in section 2.3.1). $\sigma_{<110>,max}$ is further increased by introducing holes next to the Wheatstone bridge (Figure 2.16). These holes reduce the cross-section of the beam and increase the stress, since the internal normal forces are still the same (equation 2.50 in section 2.2.6). If the piezoresistor were thicker taking up more of the depth of the cantilever, it would experience less stress in total, because the normal stress varies over the cross-sectional area of the beam, tending towards zero at the neutral axis (Figure 2.14 in section 2.2.7). This would result in a smaller change of resistance. In an extreme case, a piezoresistor as thick as the cantilever would have no change in resistance, since tensile and compressive stress would cancel each other out (equation 2.164 in section 2.2.7). Both the correct positioning and the small thickness of the piezoresistors increase resistance change and sensitivity.

During beam bending, two of the Wheatstone bridge piezoresistors, R_2 and R_3, experience longitudinal stress and the other two, R_1 and R_4, transverse stress (Figure 2.16). They are longitudinal and transverse piezoresistors, respectively, changing their resistance (equations 2.207 and 2.208 in section 2.3.1). The output voltage signal of the Wheatstone bridge $U_{out,bridge}$ is generally given by

$$\frac{U_{out,bridge}}{U_{in,bridge}} = \frac{R_2 R_3 - R_1 R_4}{(R_1 + R_2)(R_3 + R_4)} \tag{2.209}$$

where $U_{in,bridge}$ is Wheatstone bridge input voltage for driving the bridge, and R_1, R_2, R_3, and R_4 are ohmic resistors.

Fractional voltage change and fractional resistance change are related in that

$$\frac{\Delta U}{U} = \frac{\Delta R}{R} \tag{2.210}$$

where

$$\frac{\Delta U}{U} = \frac{U_{out,bridge}}{U_{in,bridge}} \tag{2.211}$$

$$\frac{\Delta R}{R} = \frac{\Delta R_{bridge}}{R_{bridge}} \tag{2.212}$$

and R_{bridge} is the Wheatstone bridge resistance. The output of the Wheatstone bridge with a DC bridge input voltage signal $U_{in,bridge,DC}$ may then be re-written as

$$\frac{U_{out,bridge}}{U_{in,bridge,DC}} = \frac{\Delta R_{bridge}}{R_{bridge}} \tag{2.213}$$

The DC Wheatstone bridge power for driving the bridge is then

$$P_{bridge,DC} = UI = \frac{U^2_{in,bridge,DC}}{R_{bridge}} \tag{2.214}$$

The bridge resistance is

$$R_{bridge} = \frac{(R_1 + R_2)(R_3 + R_4)}{R_1 + R_2 + R_3 + R_4} \tag{2.215}$$

Since the four Wheatstone bridge piezoresistors are ideally all the same

$$R_1 = R_2 = R_3 = R_4 = R_{piezo} \tag{2.216}$$

the Wheatstone bridge resistance is

$$R_{bridge} = R_{piezo} \tag{2.217}$$

The resistance change of the piezoresistors varies as they experience longitudinal or transverse stress

$$\Delta R_2 = \Delta R_3 = \Delta R_{piezo,L} \quad \text{and} \quad \Delta R_1 = \Delta R_4 = \Delta R_{piezo,T} \tag{2.218}$$

Accordingly, the resistance change of the Wheatstone bridge is

$$\Delta R_{bridge} = \frac{\Delta R_{piezo,L} + \Delta R_{piezo,T}}{2} \tag{2.219}$$

Taking equations 2.207 and 2.208 (section 2.3.1) into account, this results in

$$\Delta R_{bridge} = \frac{1}{2}\left(\pi_{L,<110>,pSi} - \pi_{T,<110>,pSi}\right) R_{piezo}\sigma_{<110>,max} \tag{2.220}$$

where $\pi_{L,<110>,pSi}$ is the longitudinal and $\pi_{T,<110>,pSi}$ the transverse piezoresistive coefficient of p-type silicon for the <110> in-plane crystallographic direction. Since $\pi_{T,<110>,pSi}$ has a negative value, this has to be neutralized for calculation purposes. Otherwise, the resistance changes would cancel each other out. The output voltage signal of the Wheatstone bridge $U_{out,bridge}$ directly proportionally depending on the maximum normal stress $\sigma_{<110>,max}$ is then

$$\frac{U_{out,bridge}}{U_{in,bridge,DC}} = \frac{1}{2}(\pi_{L,<110>,pSi} - \pi_{T,<110>,pSi})\sigma_{<110>,max} \tag{2.221}$$

The maximum normal stress is caused by beam displacement, which is either deflection z_{DC} for pure beam bending or maximum amplitude $z_{AC,max}$ for beam oscillation (equation 2.175 in section 2.2.7). In turn, the Wheatstone bridge output voltage signal is either a DC or an AC signal

$$U_{out,bridge,DC} \sim \sigma_{<110>,max} \sim z_{DC} \tag{2.222}$$

$$U_{out,bridge,AC} \sim \sigma_{<110>,max} \sim z_{AC,max} \tag{2.223}$$

The output voltage signal of the Wheatstone bridge depends on its quality, position, and orientation. The fabrication process for the four piezoresistors means that their resistance may not be the same. Variation is caused by varying length and width due to lithography (equation 2.206 in section 2.3.1). The dopant profile, i.e. the thickness of the piezoresistor, is formed by ion implantation which depends on implantation energy followed by annealing: The ions are electrically activated through diffusion which depends on annealing time and temperature. The dopant profile is well-approximated by a Gaussian distribution [99]. It is also influenced by possible defects in silicon. The piezoresistivity is determined by dopant and doping concentration (equation 2.205 section 2.3.1). The difference in resistance results in a Wheatstone bridge output voltage signal $U_{out,bridge}$ (equation 2.209), even though the self-actuating and self-sensing piezoresistive microscale silicon cantilever is neither purely bent nor oscillating. Additionally, as the piezoresistors do not all experience stress to the exactly same extent, their resistance changes will differ. The transverse piezoresistors experience different levels of stress at different points because of the non-uniform stress distribution along the beam length (Figure 2.14 in section 2.2.7), though there is constant stress along the length of the piezoresistors. In contrast, not every part of the longitudinal piezoresistors experiences the same stress. The transverse piezoresistor positioned closest to the beam support might entirely experience maximum stress if it is exactly placed. Moreover, to be affected by the maximum stress the piezoresistors have to be aligned with the <110> in-plane crystallographic direction, since the beam is oriented this way. The placement is very susceptible to small photolithographic alignment errors. The output of the Wheatstone bridge may even be reduced and with it the sensitivity.

In the Wheatstone bridge there is a parabolic relationship between the DC power $P_{bridge,DC}$ and the output voltage signal $U_{out,bridge}$ and this may be derived from equations 2.214 and 2.221 with the bridge power parabolically amplifying the output signal

$$U_{out,bridge} = \frac{1}{2}(\pi_{L,<110>,pSi} + \pi_{T,<110>,pSi})\sigma_{<110>,max}\sqrt{P_{bridge,DC}R_{bridge}} \tag{2.224}$$

2.3.3 Deflection sensitivity

The deflection sensitivity is effectively the AC Wheatstone bridge output voltage signal $U_{out,bridge,AC}$ that is generated by the maximum amplitude of beam oscillation $z_{AC,max}$ of 1 nm, i.e. by the amplitude at the fundamental or natural frequency f_1

$$\textit{deflection sensitivity} = \frac{U_{out,bridge,AC} \text{ in µVrms}}{z_{AC,max} \text{ in nm}} \tag{2.225}$$

The advantage of high deflection sensitivity is that small $z_{AC,max}$ causes big $U_{out,bridge,AC}$. The higher the deflection sensitivity is, the smaller may be $z_{AC,max}$ that is detected by the Wheatstone bridge. For instance, on AFM imaging tiny sample features are only imaged if $z_{AC,max}$ is very small and may be still detected.

The deflection sensitivity is limited by quality, position, and orientation of the Wheatstone bridge and increased by the holes next to the bridge affecting the AC Wheatstone bridge output voltage signal (see section 2.3.2). Another influencing factor is noise interfering with $U_{out,bridge,AC}$ (see section 2.4.2). Air damping decreases $z_{AC,max}$ (see section 2.4.3) and, as a consequence of the proportionality, $U_{out,bridge,AC}$(equation 2.223 in section 2.3.2). A smaller signal is harder to detect because on this scale noise plays a bigger role.

Due to the proportionality of $U_{out,bridge,AC}$ to maximum normal stress $\sigma_{<110>,max}$ and amplitude $z_{AC,max}$ (equation 2.223 in section 2.3.2), the deflection sensitivity depends on beam dimensions and modulus of elasticity E_{beam} (equation 2.175 in section 2.2.7). It increases in linear fashion with beam thickness d_{beam} and E_{beam}, and varies inversely with the square of beam length L_{beam}

$$\textit{deflection sensitivity} \sim \frac{\sigma_{<110>,max}}{z_{AC,max}} \sim \frac{d_{beam}}{L_{beam}^2}E_{beam} \tag{2.226}$$

The effect is that a short, thick and, therefore, stiff beam with a big spring constant k_{beam} (equation 2.158 in section 2.2.7) shows high deflection sensitivity. In addition, such a beam has a high fundamental or natural frequency f_1 (equation 2.141 in section 2.2.7). So, as stated in literature a beam with high f_1 is more sensitive [99].

Besides deflection sensitivity, force sensitivity is also determined from AC Wheatstone bridge output voltage signal $U_{out,bridge,AC}$ that is generated by the amplitude F_{AC} of the alternating drive force $F_{drive,AC}$ (equation 2.221 in section 2.3.2 and equation 2.174 (section 2.2.7):

$$\textit{force sensitivity} = \frac{U_{out,bridge,AC} \text{ in V}}{F_{AC} \text{ in N}} \tag{2.227}$$

$$= 3\beta_{eff}(\pi_{L,<110>,pSi} - \pi_{T,<110>,pSi})\frac{L_{beam}}{b_{beam}d_{beam}^2}U_{in,bridge,DC} \tag{2.228}$$

where β_{eff} is the efficiency factor, $\pi_{L,<110>,pSi}$ the longitudinal and $\pi_{T,<110>,pSi}$ the transverse piezoresistive coefficient of p-type silicon for the <110> in-plane crystallographic direction, b_{beam} the beam width, and $U_{in,bridge,DC}$ the DC bridge input voltage signal. The efficiency factor β_{eff} is a function to the finite thickness of the piezoresistor and proportionally reduces $U_{out,bridge,AC}$ [99, 103].

Calculated example of force sensitivity

The force sensitivity of a beam made of a silicon layer with a rectangular cross-section is estimated from equation 2.228. Beam dimensions and parameters are listed in Table 2.16. The force sensitivity in this example is close to the value of 330 $\frac{\mathrm{V}}{\mathrm{N}}$ for a cantilever with a fully integrated piezoresistive Wheatstone bridge presented in literature [102].

Parameter		Value
Beam width b_{beam}	µm	150
Beam thickness d_{beam}	µm	6
Beam length L_{beam}	µm	460
Longitudinal piezoresistive coefficient $\pi_{L,<110>,pSi}$	$\frac{10^{-11}}{\mathrm{Pa}}$	71.8 [101]
Transverse piezoresistive coefficient $\pi_{T,<110>,pSi}$	$\frac{10^{-11}}{\mathrm{Pa}}$	-66.3 [101]
DC Wheatstone bridge input voltage $U_{in,bridge,DC}$	V	1
Efficiency factor β_{eff} at piezoresistor thickness $d_{piezo} = 100$ nm		0.98 [99]
Force sensitivity	$\frac{\mathrm{V}}{\mathrm{N}}$	346

Table 2.16: Parameters for estimation of force sensitivity and value of force sensitivity

2.4 Influence on cantilever performance

2.4.1 Change of beam temperature

Since beam dimensions and properties such as the modulus of elasticity depend on temperature (see section 2.2.1), any extrinsically or intrinsically introduced change of beam temperature may affect any cantilever property, for example the fundamental or natural frequency f_1 and the spring constant k_{beam}. First and foremost, it is the aluminium thin film heater which triggers intrinsic beam temperature change. However, any change of beam properties with temperature is a side effect of the thermal beam actuation and is undesirable. On beam oscillation the static AC drive power $P_{drive,AC,static}$ determines the temperature profile within the beam and permanently changes the beam temperature that causes pure beam bending, whereas the dynamic AC drive power $P_{drive,AC,dynamic}$ periodically changes the beam temperature that results in beam oscillation (see example in section 2.2.4). Thus, $P_{drive,AC,static}$ influences fundamental frequency and spring constant of the beam. The temperature dependency is derived from the first derivative of either f_1 or k_{beam}. Although changes of width, thickness, and modulus of elasticity are side effects and can be ignored in terms of beam actuation, they have to be considered here. The temperature dependency of the fundamental or natural frequency $f_{1,multi}$ of a multi-layered beam (equation 2.176 in section 2.2.7) is

$$\begin{aligned}\Delta f_{1,multi}(T) &= \frac{\partial f_{1,multi}}{\partial b_i}\Delta b_i + \frac{\partial f_{1,multi}}{\partial d_i}\Delta d_i + \frac{\partial f_{1,multi}}{\partial L_{beam}}\Delta L_{beam} + \frac{\partial f_{1,multi}}{\partial \rho_i}\Delta \rho_i \\ &\quad + \frac{\partial f_{1,multi}}{\partial E_{beam}}\Delta E_{beam} \\ \Delta f_{1,multi}(T) &\sim -\Delta T\end{aligned} \tag{2.229}$$

where b_i is the width, d_i the thickness, and ρ_i the density of material layer i, L_{beam} the beam length and E_{beam} the modulus of elasticity. Because of the linear relationship between drive power and beam temperature (equation 2.41 in section 2.2.4), the frequency is directly proportional to $P_{drive,AC,static}$

$$\Delta f_{1,multi}(T) \sim -\Delta T \sim -P_{drive,AC,static} \tag{2.230}$$

The temperature dependency of the spring constant k_{multi} of a multi-layered beam (equation 2.180 in section 2.2.7) is

$$\begin{aligned}\Delta k_{multi}(T) &= \frac{\partial k_{multi}}{\partial b_i}\Delta b_i + \frac{\partial k_{multi}}{\partial d_i}\Delta d_i + \frac{\partial k_{multi}}{\partial L_{beam}}\Delta L_{beam} + \frac{\partial k_{multi}}{\partial \rho_i}\Delta \rho_i \\ &\quad + \frac{\partial k_{multi}}{\partial E_{beam}}\Delta E_{beam}\end{aligned} \tag{2.231}$$

$$\Delta k_{multi}(T) \sim -\Delta T \sim -P_{drive,AC,static} \tag{2.232}$$

Both the fundamental frequency and the spring constant decrease linearly with increasing beam temperature and static AC drive power under the influence of the linear temperature dependency of beam dimensions, density, and modulus of elasticity (equations 2.1, 2.2, and 2.3 in section 2.2.1). This is still the case even if the same temperature rise is not experienced at all points of the beam and there is a distinctive temperature profile within the beam (see example in section 2.2.4) because of these linear temperature dependencies. The same applies to the deflection at pure beam bending (see example in section 2.2.6).

In addition, the quality factor Q is affected by the beam temperature through its linear dependency on the fundamental frequency (equations 2.149 and 2.150 in section 2.2.7)

$$\Delta Q(T) \sim \Delta f_{1,multi}(T) \sim -\Delta T \sim -P_{drive,AC,static} \tag{2.233}$$

Furthermore, the piezoresistors of the Wheatstone bridge warm up by Joule heating: since drive power $P_{bridge,DC}$ is supplied to the bridge, they carry a current. The introduced beam temperature change also linearly reduces fundamental frequency, spring constant, and quality factor

$$\Delta f_{1,multi}(T),\ \Delta k_{multi}(T),\ Q(T) \sim -\Delta T \sim -P_{bridge,DC} \tag{2.234}$$

Consequently, there are two heat sources on the beam: the aluminium thin film heater and the Wheatstone bridge, although the latter introduces much less heat. However, the position of the Wheatstone bridge at the beam base is crucial as this is where the beam experiences maximum normal stress. It could be argued that any temperature change in this area might have a bigger influence on fundamental frequency and spring constant. At the free end of the beam where the aluminium thin film heater is positioned, normal stress tends towards zero.

It is possible that the Wheatstone bridge output voltage signal $U_{out,bridge}$ is reduced as the beam temperature and, hence, the temperature of the piezoresistors increase, because the piezoresistive coefficients decrease with temperature [98] (equation 2.221 in section 2.3.2).

Calculated example of temperature dependency of fundamental frequency and spring constant

The temperature dependency of the fundamental frequency $\Delta f_{1,multi}$ and the spring constant Δk_{multi} of a composite beam made of multiple material layers with rectangular cross-sections given in Table 2.11 (see example in section 2.2.7) is estimated according to equations 2.229 and 2.231. Values of density and modulus of elasticity are listed in Tables 2.5 (see example in section 2.2.4) and 2.9 (see example in section 2.2.6). The wave number of the first resonance is given by equation 2.114 and the effective mass factor by equation 2.156 (section 2.2.7). The temperature coefficient of the Young's modulus of silicon is taken from Table 2.14 (section 2.3.1).

The estimation of values is in good agreement with actual measurements taken with the self-sensing and self-actuating piezoresistive microscale silicon cantilevers fabricated within the research work for this PhD thesis, where the temperature change was extrinsically introduced [104, 105] (Table 2.17).

Parameter	Unit	Value
$\Delta f_{1,multi}(T)$	$\frac{10^{-5}}{\text{K}}$	-3.6$\cdot f_{1,multi} \cdot \Delta T$
$\Delta f_{1,multi}(T)$	$\frac{10^{-5}}{\text{K}}$	-3$\cdot f_{1,multi} \cdot \Delta T$ [104]
$\Delta k_{multi}(T)$	$\frac{10^{-5}}{\text{K}}$	-7.3$\cdot k_{multi} \cdot \Delta T$
$\frac{\Delta f_{1,multi}(T)}{\Delta T}$	$\frac{\text{Hz}}{\text{K}}$	-1.7
$\frac{\Delta f_{1,multi}(T)}{\Delta T}$	$\frac{\text{Hz}}{\text{K}}$	-3 [105]

Table 2.17: Change of fundamental frequency and spring constant due to beam temperature change

2.4.2 Noise

Any type of noise is deleterious the deflection sensing of the self-actuating and self-sensing piezoresistive microscale silicon cantilever. Especially for precise measurement of small Wheatstone bridge output voltage signals, noise plays a significant role, since small signals might get lost in noise.

2.4.2.1 Thermomechanical noise

Thermomechanical noise results from random thermal beam oscillation. It is caused by Brownian motion of beam atoms [103] or by the Brownian motion of gas or liquid molecules surrounding a resting beam [106]. The energy stored by the beam is converted into thermal energy due to energy dissipation [106, 107]. The thermomechanical noise force $F_{n,thermomechanical}$

is given by the equipartition theorem [66, 108]

$$F_{n,thermomechanical} = \sqrt{\frac{2k_B T_{beam} k_{beam}}{Q\omega_1} \Delta\omega_{meas}} \tag{2.235}$$

where k_B the Boltzmann's constant, T_{beam} the absolute beam temperature, k_{beam} is the spring constant of the beam, Q the quality factor of the beam, ω_1 its angular fundamental or natural frequency, and $\Delta\omega_{meas}$ the angular measurement frequency bandwidth

$$\Delta\omega_{meas} = \omega_{max} - \omega_{min} \tag{2.236}$$

The random thermal beam oscillation is the greatest at the fundamental frequency. Therefore, the resonance peak due to thermomechanical noise should be easily detectable in the frequency response of the cantilever in vacuum [99]. The mean square amplitude of thermomechanical noise at a temperature of 22°C is defined [108]

$$\sqrt{z^{\hat{2}}_{th}} = \sqrt{\frac{k_B T_{beam}}{k_{beam}}} \tag{2.237}$$

Energy dissipation is quantified by the quality factor Q, as already described by equation 2.148 (section 2.2.7). It will be recalled that the quality factor Q of a damped DHO is the ratio between the energy stored by the beam W and the energy lost per cycle or complete oscillation ΔW [91, 92, 107, 109]

$$Q = \frac{2\pi W}{\Delta W} \tag{2.238}$$

Since the mechanisms responsible for energy loss are diverse [107]

$$\Delta W = \sum_{i=1}^{n} \Delta W_i \tag{2.239}$$

where ΔW_i is the energy lost because of dissipation mechanism i, the inverse of Q may be written as follows [107]

$$\frac{1}{Q} = \sum_{i=1}^{n} \frac{1}{Q_i} \tag{2.240}$$

where Q_i presents the quality factor of dissipation mechanism i. The mechanisms or sources of energy dissipation are either intrinsic to the cantilever or extrinsic:

- Intrinsic energy dissipation results from internal friction which is caused by various physical mechanisms that are influenced by beam geometry, material properties, fabrication process, and beam temperature. Examples are volume effects including lattice defects and phonon-phonon scattering, surface effects due to contaminants on the surface, and surface defects from fabrication process. For very thin beams the dominant loss mechanism is surface related [107, 110]. thermoelastic dissipation (TED) results from an irreversible heat flow across the thickness of an oscillating beam. Regions under compression warm up, while regions under tension cool down creating a temperature gradient across beam thickness [107, 111–113]. In the case of single-crystal silicon cantilevers, TED is negligible if they are thinner than 10 µm [107].
- Extrinsic energy dissipation is caused by fluid damping and clamping. Fluid damping noise is introduced by the Brownian motion of fluid molecules, either gas or liquid, surrounding an oscillating beam (see section 2.4.3). The damping noise force is [114]

  $$F_{n,damping} = \sqrt{k_B T_{beam} k_{beam}} \tag{2.241}$$

  Clamping loss describes energy dissipation via coupling to the supportive structure, i.e. to the cantilever chip. The main reason is elastic vibration of the chip. Using a two-dimensional theory that models the supportive structure as an infinitely large elastic body, the quality factor at the frequency of the first resonance is estimated [107, 115]

  $$Q_{clamping} = 2.17 \frac{L^3_{beam}}{d^3_{beam}} \tag{2.242}$$

  where L_{beam} is the beam length and d_{beam} the beam thickness. If $Q_{clamping}$ is significantly larger than any of the other measured Q values, one can conclude that clamping loss does not limit the quality factor for the beam [107].

2.4.2.2 Electrical noise

Electrical noise is introduced by the p-type silicon piezoresistors of the Wheatstone bridge:

- Johnson noise results from the random thermal motion of carriers in an electrical resistor. Since this thermal noise is constant over frequency, it is called white noise. It depends on the resistance of the piezoresistor R_{piezo} and its absolute temperature T_{piezo} [66]

  $$\overline{U^2_{Johnson}} = 4k_B T_{piezo} R_{piezo} \tag{2.243}$$

  Through R_{piezo} (equation 2.206 in section 2.3.1), Johnson noise is influenced by piezoresistor dimensions and doping

  $$\overline{U^2_{Johnson}} = 4k_B \frac{1}{\mu_p q c_{doping}} \frac{L_{piezo}}{b_{piezo} d_{piezo}} T_{piezo} \tag{2.244}$$

  where μ_p the hole mobility, q the electron charge, c_{doping} the doping density or concentration, L_{piezo} is the length of the piezoresistor, b_{piezo} the width, and d_{piezo} the thickness. The fabrication process, lithography and ion implantation in particular, define dimensions and doping of the piezoresistor.

- Hooge noise is the dominant $1/f$-noise source for silicon piezoresistors [99]. It is caused by the fluctuation in resistor conductance which may be attributed to lattice defects in the piezoresistor volume [116]. This conductivity noise does not depend on the resistance of the piezoresistor R_{piezo} but on the bias voltage U_{piezo} and varies inversely with the number of carriers in the piezoresistor N_{piezo} [66, 99]

  $$\overline{U^2_{Hooge}} = \frac{\alpha_{Hooge} U^2_{piezo}}{N_{piezo}} \ln \frac{f_{max}}{f_{min}} \tag{2.245}$$

  with the measurement frequency bandwidth

  $$\Delta f_{meas} = f_{max} - f_{min} \tag{2.246}$$

  The Hooge noise parameter α_{Hooge} depends on the lattice quality and is experimentally measured [102, 103, 116]. For an ion-implanted piezoresistor, α_{Hooge} is reduced by annealing and surface treatment [99]. The number of carriers N_{piezo} is related to the doping concentration c_{doping} and the piezoresistor volume V_{piezo}. Since the piezoresistor is assumed to be a rectangular cuboid, it is [99]

  $$N_{piezo} = c_{doping} V_{piezo} \tag{2.247}$$

  with

  $$V_{piezo} = b_{piezo} d_{piezo} L_{piezo} \tag{2.248}$$

  Hooge noise is then

  $$\overline{U^2_{Hooge}} = \frac{\alpha_{Hooge} U^2_{piezo}}{c_{doping} b_{piezo} d_{piezo} L_{piezo}} \ln \frac{f_{max}}{f_{min}} \tag{2.249}$$

  Thus, the Hooge noise varies inversely with doping concentration and piezoresistor volume. At low frequencies, it is dominant and will thus affect low-frequency measurements [64, 99].

If equation 2.174 (section 2.2.7) of the bending moment of the beam is put into equation 2.221 (section 2.3.2) of the Wheatstone bridge output voltage signal and Johnson or Hooge noise is integrated over the measurement frequency bandwidth as given in [66], the Johnson noise force is

$$F_{Johnson} = \frac{b_{beam} d^2_{beam}}{3L_{beam}(\pi_{L,<110>,pSi} - \pi_{T,<110>,pSi}) U_{in,bridge,DC}} \sqrt{\frac{8k_B T_{piezo} R_{piezo}}{Q\omega_1} \Delta\omega_{meas}} \tag{2.250}$$

and the Hooge noise force is

$$\begin{aligned} F_{Hooge} = & \frac{b_{beam} d^2_{beam}}{3L_{beam}(\pi_{L,<110>,pSi} - \pi_{T,<110>,pSi}) U_{in,bridge,DC}} \\ & \sqrt{\frac{2\alpha_{Hooge}}{c_{doping} b_{piezo} d_{piezo} L_{piezo}} \frac{U^2_{piezo}}{Q\omega_1} \ln \frac{f_{max}}{f_{min}} \Delta\omega_{meas}} \end{aligned} \tag{2.251}$$

where b_{beam} is the width of the beam, d_{beam} the thickness, L_{beam} the length, $\pi_{L,<110>,pSi}$ the longitudinal and $\pi_{T,<110>,pSi}$ the transverse piezoresistive coefficient of p-type silicon for the <110> in-plane crystallographic direction, $U_{in,bridge,DC}$ the

DC Wheatstone bridge input voltage signal, Q the quality factor of the beam, and ω_1 its angular fundamental or natural frequency. The minimum detectable force resolution in vacuum is [99]

$$F_{min} = \sqrt{F^2_{n,thermomechanical} + F^2_{Johnson} + F^2_{Hooge}} \tag{2.252}$$

Taking into account the deflection on pure beam bending (equation 2.151 in section 2.2.7) and the spring constant of the beam (equation 2.158 in section 2.2.7), the minimum detectable displacement resolution in vacuum is [99]

$$z_{min} = \frac{1}{(\beta_1 L)^4 M_{eff}} \frac{12 L^3_{beam}}{b_{beam} d^3_{beam} E_{beam}} F_{min} \tag{2.253}$$

where $\beta_1 L$ is the wave number of the first resonance, M_{eff} the effective mass factor, and E_{beam} the modulus of elasticity or Young's modulus of the beam. Since the four piezoresistors of the Wheatstone bridge are ideally the same (equation 2.217 in section 2.3.2), the bridge resistance equals the resistance of one piezoresistor and the definitions of Johnson and Hooge noise may be used as given to estimate noise and resolution of the Wheatstone bridge.

2.4.2.3 Noise reduction

Both Hooge noise and Johnson noise are influenced by the dimensions and the doping of the piezoresistors, and these are determined by the fabrication process, lithography and ion implantation, to be exact. If noise is to be reduced, dimensions and doping need to be optimized. The optimization depends on the use the cantilever is to be put to; whether low- or high-frequency measurements require low Hooge noise or low Johnson noise. At high doping concentration, there are many carriers and, hence, improved Hooge noise at low frequencies (equation 2.249 in section 2.4.2.2). The sensitivity is the highest at low doping concentration, because the piezoresistive coefficients decrease if the doping concentration increases (equation 2.221 in section 2.3.2 and equation 2.225 in section 2.3.3) [98, 99]. The low concentration gives the best resolution at high frequency, where Johnson noise is the limiting noise source [99]. At the same time, very shallow piezoresistors are necessary for high sensitivity (see section 2.3.2). However, the small number of carriers they contain results in high Hooge noise (equation 2.249 in section 2.4.2.2). Thicker piezoresistors would have more carriers, but sensitivity would be lost (see section 2.3.2). High bias voltage applied to the piezoresistors improves the signal to noise ratio [66].

Dimension optimization will also depend on whether the application demands measurement of displacement or of force. For high resolution displacement, beam thickness has to be increased and length reduced, and vice versa for high force resolution, with a small width.

Calculated example of minimum detectable force and displacement resolution at fundamental frequency in vacuum

In this example, minimum detectable force and displacement resolution at the fundamental frequency f_1 in vacuum are estimated from equations 2.252 and 2.253 (section 2.4.2.2) for a beam made of a silicon layer with a rectangular cross-section. The thermomechanical noise force $F_{n,thermomechanical}$ (equation 2.235 in section 2.4.2.1), Johnson noise force $F_{Johnson}$ (equation 2.250 in section 2.4.2.2), and Hooge noise force F_{Hooge} (equation 2.251 in section 2.4.2.2) are separately calculated at the fundamental frequency. Concerning the frequency response of the beam, Johnson and Hooge noise may be determined from equations 2.244 and 2.249 (section 2.4.2.2). Piezoresistor and beam dimensions and parameters are listed in Table 2.18. The temperature profile within the beam presented as an example in section 2.2.4 is considered for beam and piezoresistor temperature.

Results are given in Table 2.19. z_{min} is atomic resolution as gained with optical beam deflection detection [4, 5, 117]. At the fundamental frequency f_1, $F_{n,thermomechanical}$ is the largest, whereas F_{Hooge} is the smallest. Johnson noise predominates over Hooge noise, as understood from theory. Their values are in good agreement with different piezoresistive self-sensing cantilevers studied elsewhere [102].

Parameter	Unit	Value
Beam width b_{beam}	µm	150
Beam thickness d_{beam}	µm	6
Beam length L_{beam}	µm	460
Modulus of elasticity E_{beam}	GPa	168.9 [87]
Spring constant k_{beam}	$\frac{\mathrm{N}}{\mathrm{m}}$	14
Absolute beam temperature T_{beam}	K	330
Quality factor Q		1000
Piezoresistor width b_{piezo}	µm	5
Piezoresistor thickness d_{piezo}	nm	100
Piezoresistor length L_{piezo}	µm	20
Absolute temperature of piezoresistor T_{piezo}	K	300
Doping concentration c_{doping}	$\frac{1}{\mathrm{cm}^{-3}}$	10^{25}
Hole mobility μ_p	$\frac{\mathrm{cm}^2}{\mathrm{V \cdot s}}$	120 [118]
Electron charge q	C	$1.603 \cdot 10^{-19}$
Longitudinal piezoresistive coefficient $\pi_{L,<110>,pSi}$	$\frac{10^{-11}}{\mathrm{Pa}}$	71.8 [101]
Transverse piezoresistive coefficient $\pi_{T,<110>,pSi}$	$\frac{10^{-11}}{\mathrm{Pa}}$	-66.3 [101]
Boltzmann's constant k_B	$\frac{\mathrm{J}}{\mathrm{K}}$	$1.38075 \cdot 10^{-23}$
Hooge noise parameter α_{Hooge}		$1.0 \cdot 10^{-7}$ [103]
Wave number $\beta_1 L$ of f_1		1.8751
Effective mass factor M_{eff}		0.24 [93]
DC Wheatstone bridge input voltage $U_{in,bridge,DC}$ = Piezoresistor bias voltage U_{piezo}	V	1
Fundamental frequency f_1 (see example in section 2.2.7)	kHz	48.1
Angular measurement frequency bandwidth $\Delta\omega_{meas}$ at f_1	Hz	$2\pi \cdot 10$
f_{max}	kHz	48.105
f_{min}	kHz	48.095

Table 2.18: Parameters for calculation of minimum detectable force and displacement resolution

Parameter	Unit	Value
F_{min}	pN	0.2
z_{min}	fm	12
$F_{n,thermomechanical}$	$\frac{\text{N}}{\sqrt{\text{Hz}}}$	$5{\cdot}10^{-14}$
$F_{Johnson}$	$\frac{\text{N}}{\sqrt{\text{Hz}}}$	$3{\cdot}10^{-15}$
F_{Hooge}	$\frac{\text{N}}{\sqrt{\text{Hz}}}$	$1{\cdot}10^{-16}$
$\sqrt{\overline{U^2_{Johnson}}}$	$\frac{\text{V}}{\sqrt{\text{Hz}}}$	$2{\cdot}10^{-9}$
$\sqrt{\overline{U^2_{Hooge}}}$	$\frac{\text{V}}{\sqrt{\text{Hz}}}$	$7{\cdot}10^{-11}$

Table 2.19: Minimum detectable force and displacement resolution; noise forces; Johnson and Hooge noise

2.4.3 Air damping

Air damping is one of the mechanisms of energy dissipation which are described by the quality factor (see section 2.4.2.1). Despite other dissipative effects, it is found to be the most significant factor that influences the quality factor of the beam [119]. Air damping limits the beam oscillation, i.e. the maximum amplitude and the fundamental frequency, in dependence on the pressure - which may range from high vacuum to air condition - and on the gaseous composition of air, which may differ as well. The drag force F_{drag} opposes the motion of an oscillating one-layered beam with a rectangular cross-section, which is then a damped DHO [109]

$$F_{drag}(p_{air}) = \beta_{dissipative}(p_{air})v_{beam} - \frac{\beta_{inertial}(p_{air})}{\omega_{m,damped}}\frac{\partial v_{beam}}{\partial t} \tag{2.254}$$

where $\beta_{dissipative}$ the dissipative drag parameter, p_{air} is the air pressure, v_{beam} the beam velocity, $\beta_{inertial}$ the inertial drag parameter, and $\omega_{m,damped}$ the angular frequency of the m^{th} resonance of the damped DHO. The first term shows F_{drag} to be directly proportional to v_{beam}. If the beam oscillates in air, friction occurs due to the viscosity of air. Friction results in energy dissipation, described by $\beta_{dissipative}$. The second term expresses Newton's law of motion. Beam oscillation serves to accelerate air molecules, described by $\beta_{inertial}$ [109, 120].

The quality factor of a damped DHO such as is given by equation 2.238 (section 2.4.2.1) may be calculated. Firstly, the energy stored by the beam is defined [109]

$$W = \frac{1}{2}L_{beam}\left(\rho_{beam}A_{beam} + f_{inertial}(p_{air})\right)\omega^2_{m,damped}\int_0^1 \psi(x)\partial x \tag{2.255}$$

where L_{beam} is the beam length, ρ_{beam} the density, A_{beam} the cross-sectional area, $\psi(x)$ the mode shape function, and the inertial damping parameter [109]

$$f_{inertial}(p_{air}) = \frac{\beta_{inertial}(p_{air})}{\omega_{m,damped}L_{beam}} \tag{2.256}$$

Secondly, the energy lost per cycle or complete oscillation is [109]

$$\Delta W = L_{beam}f_{dissipative}(p_{air})\omega^2_{m,damped}\int_0^1 \omega^2_{m,damped}(x)\partial x\int_0^{t_{cycle}} \cos^2\omega_{m,damped}t\partial t \tag{2.257}$$

where the dissipative damping parameter is [109]

$$f_{dissipative}(p_{air}) = \frac{\beta_{dissipative}(p_{air})}{L_{beam}} \tag{2.258}$$

and t_{cycle} is the time of one cycle or complete oscillation and the time integral is [109]

$$\int_0^{t_{cycle}} \cos^2\omega_{m,damped}t\partial t = \frac{\pi}{\omega_{m,damped}} \tag{2.259}$$

Thus, equation 2.238 (section 2.4.2.1) becomes

$$Q(p_{air}) = \frac{(\rho_{beam} A_{beam} + f_{inertial}(p_{air}))\,\omega_{m,damped}}{f_{dissipative}(p_{air})} \tag{2.260}$$

Since $\rho_{beam} A_{beam} >> f_{inertial}(p_{air})$, this is [109]

$$Q(p_{air}) = \frac{\rho_{beam} A_{beam} \omega_{m,damped}(p_{air})}{f_{dissipative}(p_{air})} \tag{2.261}$$

This definition has, effectively, already been given in equation 2.148 (section 2.2.7), just expressed differently. Through $\omega_{m,damped}(p_{air})$ and $f_{dissipative}(p_{air})$, Q depends on the air pressure p_{air}. The variation of the quality factor with the pressure across the range from vacuum to air is divided into three regions [119]:

1. The first one is the intrinsic region, where the air pressure is so low that air damping is negligible and intrinsic energy dissipation and clamping loss dominate (see section 2.4.2.1).

2. The second one is the molecular or Knudsen region, where air damping becomes dominant. However, as the air molecules are far apart, they do not interact with each other. Individual air molecules exchange momentum with the oscillating beam [119]. Energy is transferred by collisions between air molecules and beam [121]. In this case, the dissipative damping parameter $f_{dissipative}(p_{air})$ can be determined from the kinetic gas theory [109, 122]

$$f_{dissipative}(p_{air}) = \sqrt{\frac{32 M_{air}}{9\pi R_{ideal} T_{air}}}\, b_{beam} p_{air} \tag{2.262}$$

   where M_{air} is molar mass of the air, R_{ideal} the ideal gas constant, T_{air} the absolute temperature of the air, and b_{beam} the beam width. Since $f_{inertial}(p_{air}) = 0$, with equations 2.116 (section 2.2.7) and 2.261, the molecular quality factor is [109]

$$Q(p_{air}) = \frac{(\beta_m L_{beam})^2}{L_{beam}^2} \frac{d_{beam}^2}{p_{air}} \sqrt{\frac{9\pi R_{ideal} T_{air}}{32 M_{air}}} \sqrt{\frac{\rho_{beam} E_{beam}}{12}} \tag{2.263}$$

   where $(\beta_m L_{beam})$ is the wave number of the m^{th} resonance, d_{beam} the beam thickness, and E_{beam} the modulus of elasticity. Q depends on the resonance mode of operation, beam dimensions and properties, and varies inversely with air pressure

$$Q \sim \frac{1}{p_{air}} \tag{2.264}$$

   The molecular region is said to range from 10 Pa to 1,000 Pa [121].

3. The third one is the viscous region, where the air acts as a viscous fluid. It can be considered incompressible, because the velocity of beam oscillation is much smaller than the speed of sound [109]. This region can be divided into two subsections, the laminar-viscous and the turbulent-viscous. In the laminar-viscous subsection, the air viscosity μ_{air} is independent of the air pressure because of the air incompressibility and thus, the quality factor does not depend on air pressure. Using Stokes' law the laminar-viscous quality factor is obtained [119, 122]

$$Q(\mu_{air}) = \frac{b_{beam} d_{beam}^2}{24 L_{beam}^2 \mu_{air}} \sqrt{\rho_{beam} E_{beam}} \tag{2.265}$$

   Q depends on beam dimensions and properties, and varies inversely with the viscosity of the air

$$Q \sim \frac{1}{\mu_{air}} \tag{2.266}$$

   In the turbulent-viscous subsection, turbulent current occurs at the surface of the oscillating beam. It is characterized by the Reynolds number. Using Navier-Stokes equations and the continuity equation the dissipative and the inertial drag parameter are determined: the beam is approximated by an oscillating sphere with the radius R_{sphere} [109, 122]

$$\beta_{dissipative}(p_{air}) = 6\pi \mu_{air} R_{sphere} \left(1 + \frac{R_{sphere}}{d_{boundary}}\right) \tag{2.267}$$

$$\frac{\beta_{inertial}(p_{air})}{\omega_{m,damped}} = \frac{2}{3}\pi R_{sphere}^3 \rho_{air} \left(1 + \frac{9}{2}\frac{d_{boundary}}{R_{sphere}}\right) \tag{2.268}$$

where the thickness of the turbulent boundary layer depends on the air pressure through the air density

$$d_{boundary} = \sqrt{\frac{2\mu_{air}}{\rho_{air}\omega_{m,damped}}} \tag{2.269}$$

This relation is described by the molar form of the ideal gas law

$$\rho_{air} = \frac{M_{air}}{R_{ideal}T_{air}} p_{air} \tag{2.270}$$

Since $f_{inertial}(p_{air}) = 0$, with equations 2.116 (section 2.2.7) and 2.261, the turbulent-viscous quality factor is [109]

$$Q(p_{air}) = \frac{b_{beam}d_{beam}^2}{\beta_{dissipative}(p_{air})} \frac{(\beta_m L_{beam})^2}{L_{beam}} \sqrt{\frac{\rho_{beam}E_{beam}}{12}} \tag{2.271}$$

With equations 2.267, 2.269 and 2.270 it can be concluded that Q varies inversely with the square root of the air pressure

$$Q \sim \frac{1}{\sqrt{p_{air}}} \tag{2.272}$$

On the contrary, a simple inverse dependency on the air pressure is proposed by [122]. The air viscosity is cancelled out in equation 2.271. The viscous region is said to range from 1 kPa to 100 kPa [121].

An estimate of the pressure where the damping changes from that typical of the molecular region to that typical of the viscous region is obtained, if equations 2.263 and 2.265 are equated [119]

$$p_{transition} = (\beta_m L_{beam})^2 \frac{24\mu_{air}}{b_{beam}} \sqrt{\frac{3\pi}{128} \frac{R_{ideal}T_{air}}{M_{air}}} \tag{2.273}$$

The reduction of the maximum amplitude of beam oscillation $z_{AC,max}$ due to air damping is derived from the second definition of the quality factor as the factor by which the deflection on pure beam bending z_{DC} is amplified at resonance (equation 2.154 in section 2.2.7). Furthermore, it can also be derived from the damped non-driven harmonic oscillator, whose amplitude decays exponentially with time (equation 2.147 in section 2.2.7).
The reduction of the fundamental frequency f_1 is drawn from the one-dimensional Euler-Bernoulli beam equation of a non-damped harmonic oscillator (equation 2.101 in section 2.2.7) [109]

$$E_{beam}I_{area}\frac{\partial^4 z}{\partial x^4} + f_{dissipative}(p_{air})\frac{\partial z}{\partial t} + (\rho_{beam}A_{beam} + f_{inertial}(p_{air}))\frac{\partial^2 z}{\partial t^2} = 0 \tag{2.274}$$

where I_{area} the area moment of inertia. The apparent effect of $f_{inertial}$ is to increase the beam mass, as it describes the mass of the air molecules accelerated through beam oscillation [109, 110]. The one-dimensional Euler-Bernoulli beam equation of a damped harmonic oscillator is solved in the same way as that of a non-damped harmonic oscillator (see section 2.2.7). Angular frequency $\omega_{m,damped}$ and frequency $f_{m,damped}$ of the m^{th} resonance of an one-layered damped beam oscillator are [109]

$$\omega_{m,damped}(p_{air}) = 2\pi f_{m,damped}(p_{air}) \tag{2.275}$$

$$= \sqrt{\frac{(\beta_m L_{beam})^4}{L^4} \frac{E_{beam}I_{area}}{\rho_{beam}A_{beam} + f_{inertial}(p_{air})} - \frac{1}{4}\left(\frac{f_{dissipative}(p_{air})}{\rho_{beam}A_{beam} + f_{inertial}(p_{air})}\right)^2} \tag{2.276}$$

The second term may be neglected, because $f_{dissipative}(p_{air})$ is small for beam oscillation in gas and $\rho_{beam}A_{beam} >> f_{inertial}(p_{air})$ [109, 110]. Consequently, equation 2.276 is reduced to [109]

$$\omega_{m,damped}(p_{air}) \approx \sqrt{\frac{(\beta_m L_{beam})^4}{L_{beam}^4} \frac{E_{beam}I_{area}}{\rho_{beam}A_{beam} + f_{inertial}(p_{air})}} \tag{2.277}$$

Through iteration this is approximated by [109]

$$\omega_{m,damped}(p_{air}) \approx \omega_m \left(1 - \frac{1}{2}\frac{f_{inertial}(p_{air})}{\rho_{beam}A_{beam}}\right) = \omega_m \left(1 - \frac{1}{2}\frac{\beta_{inertial}(p_{air})}{\rho_{beam}A_{beam}L_{beam}\omega_{m,damped}}\right) \tag{2.278}$$

where ω_m is the angular frequency of the m^{th} resonance of a one-layered non-damped beam oscillator (equation 2.116 in section 2.2.7). Taking into account that $f_{inertial}$ describes the mass of the accelerated air molecules [109], equation 2.278

may be written as follows

$$\omega_{m,damped}(p_{air}) \approx \omega_m \left(1 - \frac{1}{2}\frac{m_{air}}{m_{beam}}\right) \tag{2.279}$$

with the mass of the accelerated air molecules

$$m_{air} = \frac{\beta_{inertial}(p_{air})}{\omega_{m,damped}} \tag{2.280}$$

and the beam mass

$$m_{beam} = \rho_{beam} A_{beam} L_{beam} \tag{2.281}$$

From this aspect may be derived the air pressure dependency of the frequency. The air mass m_{air} is directly proportional to the number of air molecules $N_{molecule}$

$$m_{air} = N_{molecule} m_{molecule} \tag{2.282}$$

where $m_{molecule}$ is the mass of one air molecule. $N_{molecule}$ is directly proportional to the air pressure p_{air} if the air volume V_{air} is constant as stated by the ideal gas law

$$p_{air} = \frac{N_{molecule}}{V_{air}} k_B T_{air} \tag{2.283}$$

where k_B is the Boltzmann's constant. Accordingly, the angular frequency $\omega_{m,damped}$ or frequency $f_{m,damped}$ of the m^{th} resonance of a one-layered damped beam oscillator is linearly reduced with increasing air pressure

$$\omega_{m,damped} = 2\pi f_{m,damped} \sim m_{air} \sim N_{molecule} \sim p_{air} \tag{2.284}$$

This is in agreement with the following definition of the air mass [120, 123]

$$\frac{m_{air}}{L_{beam}} = \frac{\pi b_{beam}^2 \rho_{air,1atm}}{4 p_{air,1atm}} p_{air} \tag{2.285}$$

where $\rho_{air,1atm}$ is the air density and $p_{air,1atm}$ the air pressure at 1 atm. Thus, the angular frequency $\omega_{m,damped}$ of the m^{th} resonance of an one-layered damped beam oscillator depending on air pressure is

$$\omega_{m,damped}(p_{air}) \approx \omega_m \left(1 - \frac{1}{8}\frac{\pi b_{beam}}{\rho_{beam} d_{beam}}\frac{\rho_{air,1atm}}{p_{air,1atm}} p_{air}\right) \tag{2.286}$$

The fractional change of the angular frequency ω_m or frequency f_m of the m^{th} resonance depending on air pressure change Δp_{air} is

$$\frac{\Delta\omega_m(\Delta p_{air})}{\omega_m} = \frac{\Delta f_m(\Delta p_{air})}{f_m} \approx -\frac{1}{8}\frac{\pi b_{beam}}{\rho_{beam} d_{beam}}\frac{\rho_{air,1atm}}{p_{air,1atm}} \Delta p_{air} \tag{2.287}$$

If the pressure changes from vacuum to air, the fractional change of the angular fundamental frequency ω_1 and the fundamental frequency f_1 may be estimated from [115]

$$\frac{\Delta\omega_1}{\omega_1} = \frac{\Delta f_1}{f_1} = \frac{3\pi\mu_{air,1atm} + \frac{3}{4}\pi b_{beam}\sqrt{2\rho_{air,1atm}\mu_{air,1atm}\omega_1}}{2\rho_{beam} b_{beam} d_{beam} \omega_1} \tag{2.288}$$

where $\mu_{air,1atm}$ is the air viscosity at 1 atm. Another approach to determine the fundamental frequency $f_{1,damped}$ of a one-layered damped beam oscillator in air is given by Sader [124, 125]

$$f_{1,damped,Sader} = f_1 \left[1 + \frac{\pi \rho_{air,1atm} b_{beam}}{4\rho_{beam} d_{beam}} \Gamma(\eta)\right]^{-\frac{1}{2}} \tag{2.289}$$

where $\Gamma(\eta)$ is the hydrodynamic function which is defined by the Padé approximant [125]

$$\Gamma(\eta) = \frac{1 + 0.74273\eta + 0.14862\eta^2}{1 + 0.74273\eta + 0.35004\eta^2 + 0.058364\eta^3} \tag{2.290}$$

and the normalized mode number η

$$\eta = C_n \frac{b_{beam}}{L_{beam}} \tag{2.291}$$

where $C_1 = 1.875104...$ is the smallest positive root of $0 = 1 + \cos C_n \cosh C_n$.

The self-actuating and self-sensing piezoresistive microscale silicon cantilever may be less damped than a simple one-layered beam of the same width and length because of the holes next to the Wheatstone bridge and the triangular free end of the beam, that allow air molecules to pass instead of damping the beam oscillation. In particular, it is possible that Sader's estimation of the fundamental frequency of a damped beam oscillator might differ from measurements.

Calculated example of fractional frequency change at air pressure change of 10^5 Pa

The fractional change of the fundamental frequency f_1 at an air pressure change of 10^5 Pa is estimated for a beam made of a silicon layer with a rectangular cross-section from equations 2.287 and 2.288. The fundamental frequency $f_{1,damped}$ of a one-layered damped beam oscillator in air is calculated from equation 2.289. The transition pressure from the molecular to the viscous region is estimated for the fundamental frequency (equation 2.273). Parameters are listed in Table 2.20 and results in Table 2.21.

Both values of fractional frequency change are in good agreement with literature [109], where the frequency shift is reported to be smaller than 1 %. For cantilevers of similar size and fundamental frequency the transition pressure is found to be between 500 Pa and 700 Pa [120].

Parameter	Unit	Value
Beam width b_{beam}	µm	150
Beam thickness d_{beam}	µm	6
Beam length L_{beam}	µm	460
Beam density ρ_{beam}	$\frac{\text{kg}}{\text{m}^3}$	2329 [75]
Fundamental frequency f_1 (see example in section 2.2.7)	kHz	48.1
Wave number $\beta_1 L$ of f_1		1.8751
Effective mass factor M_{eff}		0.24 [93]
Air viscosity at 1 atm $\mu_{air,1atm}$	Pa·s	$1.81 \cdot 10^{-5}$
Air density at 1 atm $\rho_{air,1atm}$	$\frac{\text{kg}}{\text{m}^3}$	1.184
Air pressure at 1 atm $p_{air,1atm}$	Pa	101,325
Air pressure change Δp_{air}	Pa	100,000
Molar mass of air M_{air}	$\frac{\text{kg}}{\text{mol}}$	0.028964 [109]
Absolute air temperature T_{air}	K	295 (~ 22°C)
Ideal gas constant R_{ideal}	$\frac{\text{J}}{\text{mol} \cdot \text{K}}$	8.314472

Table 2.20: Parameters for calculation of fractional frequency change

Parameter	Unit	Value
$\frac{\Delta f_1(\Delta p_{air})}{f_1}$ (equation 2.287)		-0.005
$\frac{\Delta f_1}{f_1}$ (equation 2.288)		0.001
$f_{1,damped,Sader}$	kHz	47.9
$p_{transition}$	Pa	800

Table 2.21: Fractional frequency change, fundamental frequency in air, and transition pressure

2.4.4 Capacitive crosstalk

At high frequencies, capacitive crosstalk occurs between conductors. When they are placed sufficiently close to each other, capacitance between them becomes large enough to couple significant energy from one conductor to another one. At high frequencies capacitors short-circuit, i.e. they do not become charged any more but conductive.

In the case of the self-actuating and self-sensing piezoresistive microscale silicon cantilever, capacitive crosstalk may be between the aluminium thin film heater and the Wheatstone bridge. Then, energy is coupled from the aluminium conducting traces of the heater through the n-type substrate to those on the bridge situated on the cantilever chip (Figure 2.17). Capacitive crosstalk may be clear from the frequency response of the beam where the AC Wheatstone bridge output voltage $U_{out,bridge,AC}$ suddenly increases at larger frequencies, although the thermal inertia of the cantilever results in a reduced amplitude of beam oscillation z_{AC} (see section 2.2.5).

To prevent capacitive coupling, the aluminium conducting traces of aluminium thin film heater and Wheatstone bridge are separated by ground lines and kept at large distance from each other on the cantilever chip (Figure 2.17). The conducting trace for applying voltage to the conductive tip may introduce capacitive crosstalk. There is another source for capacitive crosstalk in the printed circuit board (PCB) lines of the cantilever PCB.

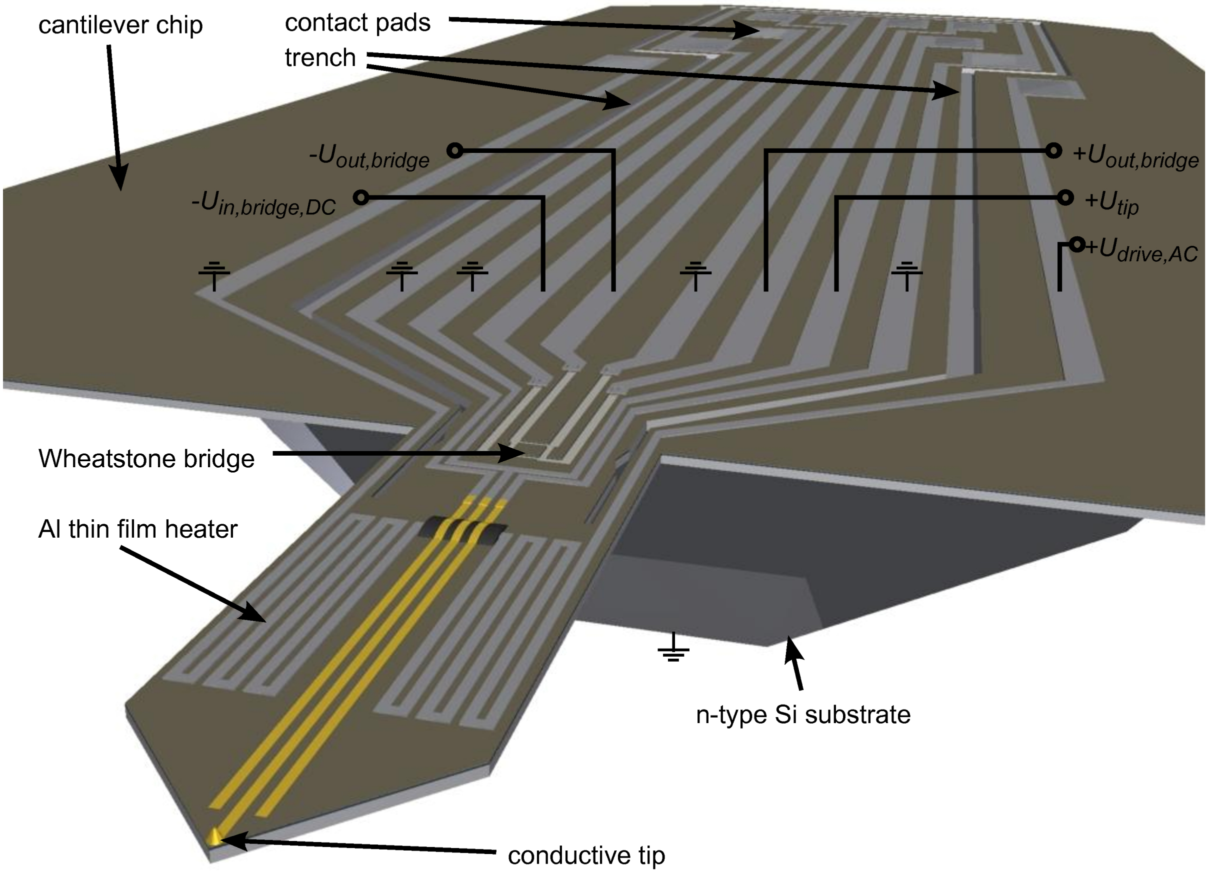

Figure 2.17: Conducting traces of aluminium thin film heater, Wheatstone bridge, and conductive tip

Piezoresistors and piezoresistive conducting traces of the Wheatstone bridge, which are p-type silicon (p-Si and p^+-Si) and embedded in the n-type silicon substrate (n-Si), form a p-n junction with the same (Figure 2.18). It has to be reverse biased, so that no current flows. Otherwise, the Wheatstone bridge output voltage signal $U_{out,bridge}$ would be strongly distorted.

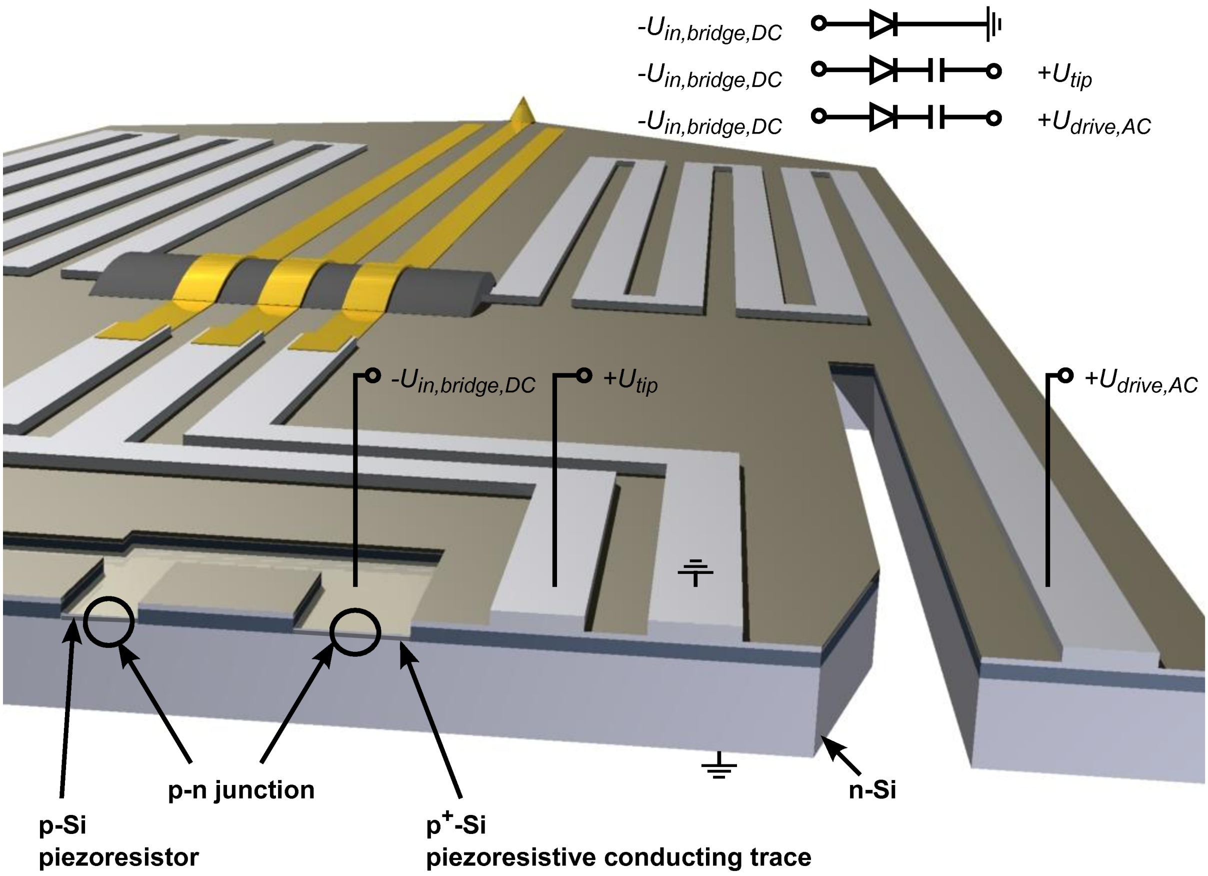

Figure 2.18: Cross-section of Wheatstone bridge and aluminium thin film heater

One possible way of reducing crosstalk is to bias the silicon substrate with a high positive voltage instead of just grounding [71, 99]. Additionally, the length of the aluminium conducting traces should be minimized, i.e. the distance from the cantilever to the bonding pads on the cantilever chip needs to be as short as possible [71].

3 Fabrication process

The fabrication of the self-actuating and self-sensing piezoresistive microscale silicon cantilever was started from scratch. At first, the structure of the cantilever was designed incorporating new features such as holes and the conductive tip. A drawing of the layout was made using the software AutoCAD Mechanical (Autodesk, Inc.). Via electron beam lithography it was transferred to the chromium (Cr) layer on the fused silica mask. Regarding the complexity of the cantilever design several masks had to be done. They were used to lithographically pattern photoresist by ultraviolet (UV) light. To produce the cantilever structure the silicon (Si) wafer and different material layers were wet or dry etched. Ion implantation formed the piezoresistors at the base of the cantilever. For the thin film heater, aluminium (Al) was sputtered. The fabrication process was based on the one introduced by Rangelow's group [27, 35, 50, 51, 126]. Cantilevers were batch-fabricated so that up to 208 devices could be extracted from one 3-inch wafer. Finally, the cantilever was glued onto a PCB and wire bonded. Black epoxy was put on the cantilever chip to protect the gold (Au) wires.

The fabrication of cantilevers was mainly done at the Center for Micro- and Nanotechnologies (Ilmenau University of Technology, Ilmenau, Thüringen, Germany), except for the ion implantation, that was done at the Division of Process Technology (Institute of Ion Beam Physics and Materials Research, Helmholtz-Zentrum Dresden-Rossendorf, Dresden, Sachsen, Germany). Masks were fabricated at the Department of Electron Beam Lithography (Institute of Informatics, Slovak Academy of Sciences, Bratislava, Slovak Republic).

Starting material was a Si wafer with properties as follows (Table 3.1).

Parameter	Values
Material	(100) Si (Czochralski process)
Background doping	n-type (phosphorous doped)
Resistivity	4.5 ± 1.0 Ω·cm
Diameter	3 inches
Thickness	275 ± 10 µm
total thickness variation (TTV)	< 2 µm
Surface	Double-sided polished

Table 3.1: Properties of silicon wafer

Step	Section	Chemicals	Parameters	Mask	Comments
Wafer cleaning	Radio Corporation of America (RCA) clean (Table 3.3)				Right before oxidation
Thermal oxidation	Horizontal furnace (Tempress Systems B.V.)	$1\ \frac{\mathrm{l}}{\mathrm{min}}$ O_2 flow; water vapour	1050°C, 11 h		$d(SiO_2) = 1.7\ \mu m$
Tip forming	UV lithography #1 (Table 3.4)		$t_{exposure}= 5.0$ s $t_{developing}= 60$ s	UW01	Fresh developing solution each time
	SiO_2 dry and wet etching (Table 3.5)				
	Si dry etching #1 (Table 3.6)				
	SiO_2 wet etching #1 (Table 3.7)				
	Thermal oxidation	$1\ \frac{\mathrm{l}}{\mathrm{min}}$ O_2 flow; water vapour	960°C, 8 h		$d(SiO_2) = 1.0\ \mu m$
	Tip sharpening (Table 3.8)				
Piezoresistive conducting traces	UV lithography #2 (Table 3.9)		$t_{exposure}= 20$ s $t_{developing}= 45$ s	UW02	
	SiO_2 wet etching #2 (Table 3.10)				
	Ion implantation #1 (Table 3.11)				Depth $\approx 0.35\ \mu m$
Piezoresistive Wheatstone bridge	UV lithography #3 (Table 3.9)		$t_{exposure}= 23$ s $t_{developing}= 90$ s	UW03	
	SiO_2 wet etching #3 (Table 3.12)				
	Ion implantation #2 (Table 3.13)				Depth ≈ 100 nm
Protective layer of SiO_2 and Si_xN_y (Table 3.14)					$d(SiO_2) = 100$ nm $d(Si_xN_y) = 200$ nm
Contact pads on piezoresistive conducting traces	UV lithography #4 (Table 3.9)		$t_{exposure}= 23$ s $t_{developing}= 60$ s	UW04	
	Si_xN_y and SiO_2 dry etching #1 (Table 3.15)				
Tip sharpening (Table 3.16)					

Table 3.2: Fabrication process for cantilever (to be continued)

continued from previous page

Step	Section	Chemicals	Parameters	Mask	Comments
Al thin film heater and conducting traces	Al sputtering (Table 3.17)				
	UV lithography #5 (Table 3.9)		$t_{exposure}$= 18 s $t_{developing}$= 90 s	UW05	AZ 400K developer (Clariant International Ltd.) : H_2O = 1:1
	Al etching and melting down (Table 3.18)				
Bridge over Al thin film heater and piezoresistive Wheatstone bridge	UV lithography #6 (Table 3.4)		$t_{exposure}$= 20 s $t_{developing}$= 30 s	UW06	Fresh developing solution each time
	Hard bake (Table 3.19)				
Protective layer of Si_xN_y (Table 3.20)					$d(Si_xN_y) \approx 100$ nm
Contact pads on Al conducting traces for connecting tip	UV lithography #7 (Table 3.21)		$t_{exposure}$= 2.7 s $t_{developing}$= 35 s	UW06	Mask is to be moved by 40 µm
	Si_xN_y wet etching (Table 3.22)				
Au conducting traces for conductive tip	UV lithography #8 (Table 3.21)		$t_{exposure}$= 2.7 s $t_{developing}$= 35 s	UW07	Baking only for 5 min Photoresist walls fell over, because too thin. Electron beam lithography instead of UV lithography might be better.
	Au physical vapour deposition (PVD) (Table 3.23)				
Bonding pads on Al	UV lithography #9 (Table 3.9)		$t_{exposure}$= 20 s $t_{developing}$= 60 s	UW08	
	Si_xN_y wet etching (Table 3.22)				Photoresist is not to be removed to protect tips!

Table 3.2: Fabrication process for cantilever (to be continued)

continued from previous page

Step	Section	Chemicals	Parameters	Mask	Comments
SiO_2 backside etching	UV lithography #10 (Table 3.4)		$t_{exposure}$= 5 s $t_{developing}$= 45 s	UW10	Mask is to be moved by 55 µm, because supposed to be for 350 µm thick wafer!
	SiO_2 wet etching #4 (Table 3.24)				
Forming cantilever and etching trenches	UV lithography #11 (Table 3.9)		$t_{exposure}$= 20 s $t_{developing}$= 60 s	UW09	
	Si_xN_y and SiO_2 dry etching #2 (Table 3.25)				
Si backside etching forming the membrane	Si wet and dry etching (Table 3.26)				
Cantilever release	Si dry etching #2(Table 3.27)				
Inspecting each cantilever	Inspecting and measuring structure		Optical microscope Axiotech (Carl Zeiss AG), electron microscope S-4700 (Hitachi, Ltd.) (Figure 3.12)		Tips turned out somewhat blunt, but sharps ones are necessary. Change sequence of fabrication steps and release tip at the end, already successfully done by [74].
	Measuring resistance of piezoresistive Wheatstone bridge and Al thin film heater		Voltmeter with tiny tips		
Push out cantilever with plastic tweezers at the edge					
Mounting cantilever (Table 3.28)					
Bonding cantilever (Table 3.29)					
Putting on black epoxy		Vitralit 1690 (Panacol-Elosol GmbH)	105°C, 30 min		Protect bond wires (Figure 3.13)

Table 3.2: Fabrication process for cantilever (to be continued)

continued from previous page

Step	Section	Chemicals	Parameters	Mask	Comments

Table 3.2: Fabrication process for cantilever

Step	Chemicals	Parameters		Comments
		Temperature	Time	
HF dipping	1 % HF	room temperature	30 s	Oxide clean removes any oxide layer
DI water rinsing	deionized (DI) water	Room temperature	4 min	
RCA-1	$NH_4OH : H_2O_2 : H_2O = 1:1:6$	80°C	10 min	Organic clean removes surface contaminants such as dust and grease
DI water rinsing	DI water	Room temperature	4 min	
RCA-2	$HCl : H_2O_2 : H_2O = 1:1:6$	80°C	10 min	Ionic clean removes any heavy metal ions
DI water rinsing	DI water	Room temperature	4 min	

Table 3.3: RCA clean procedure

Step	Chemicals	Equipment	Parameters			Comments
			Temperature	Time	Rpm	
Preheating		Hot plate CEE 100CB (Brewer Science, Inc.)	115°C	1 min		Preheating removes adsorbed gas and water molecules
Cool down in air or with N_2 gun						
Putting on adhesive layer	TI Prime IA 030 91-35, n.o.s. methylpropyl-acetat (MicroChemicals GmbH)	Spin coater CEE 100CB (Brewer Science, Inc.)		30 s	3000	3 drops in the centre of the wafer
Drying		Hot plate	115°C	1 min		
Cool down in air or with N_2 gun						
Putting on photoresist	AZ 1518 photoresist positive (Clariant International Ltd.)	Spin coater		30 s	3000	Pour in the centre of the wafer covering half of it
Drying		Hot plate	85°C	5 min		
Exposure to UV light		Mask alignment system EV420 (Electronic Visions Co.)	$\sim 6.4 \frac{\mathrm{mW}}{\mathrm{cm}^2}$ irradiance			Wafer in contact with mask
Developing	AZ 400K developer (Clariant International Ltd.) $: H_2O = 1:4$	Plastic beaker				Moving wafer a little bit

Table 3.4: UV lithography procedure #1 (to be continued)

continued from previous page

Step	Chemicals	Equipment	Parameters			Comments
			Temperature	Time	Rpm	
DI water rinsing	DI water					
Drying		Spin coater		30 s	3000	
Checking structure		Optical microscope Axiotech (Carl Zeiss AG)				Developing step may have to be repeated, if structure is not fully developed.
Baking		Hot plate	115°C	20 min		
Measuring structure		Optical microscope Axiotech (Carl Zeiss AG)				

Table 3.4: UV lithography procedure #1

Step	Chemicals	Equipment	Parameters	Comments
SiO_2 dry etching, 80 %: inductive coupled plasma (ICP)-reactive ion etching (RIE)	25.0 Sccm CHF_3 6.0 Sccm CF_4	Vision 320 RIE (STS plc)	120 W radio frequency (RF) power; 50 mTorr pressure; 30 min + 30 min (wafer turned by 180° along [100] crystallographic axis of Si)	RF power results in 470 V DC bias. Turn wafer for even etching.
SiO_2 wet etching, 20 %	NH_4F	Chuck	5 min	Pour solution on wafer in chuck. $v_{etching} \approx 80\ \frac{\text{nm}}{\text{min}}$
Removing photoresist	Caro's acid 25 % H_2O_2 : 97 % H_2SO_4 = 1:1	Gratuated cylinder, quartz beaker, hot plate, thermometer, timer	100°C, 10 min	$(CH_3)_2CO$ is not enough
	1 % HF		5 s	
Checking and measuring structure		Optical microscope Axiotech (Carl Zeiss AG); stylus-type profilometer (Ambios Technology, Inc.)		

Table 3.5: SiO_2 dry and wet etching

Steps	Chemicals	Equipment	Parameters	Comments
Si dry etching	40.0 Sccm SF_6	Plasmalab System 100 (Oxford Instruments Plc)	70 W power; 5 mTorr chamber pressure; 20 mTorr ignition pressure; 10 ramp rate; 30 Torr He pressure; 10°C, 36 min	Power results in 249 V DC bias; He for thermal contact between wafer and electrode
Checking structure		Optical microscope Axiotech (Carl Zeiss AG)		Possibly, more etching is needed.
Cleaning wafer	O_2 plasma	Stripper200 (PVA TePla America, Inc.)	300 W power; 5 min	This removes leftovers of the photoresist.
Checking and measuring structure		Optical microscope Axiotech (Carl Zeiss AG); stylus-type profilometer (Ambios Technology, Inc.)		SiO_2 as dark ring and Si as white point (Figure 3.1). Profile has to be taken at the edge, because the tips are fragile.

Table 3.6: Si dry etching #1

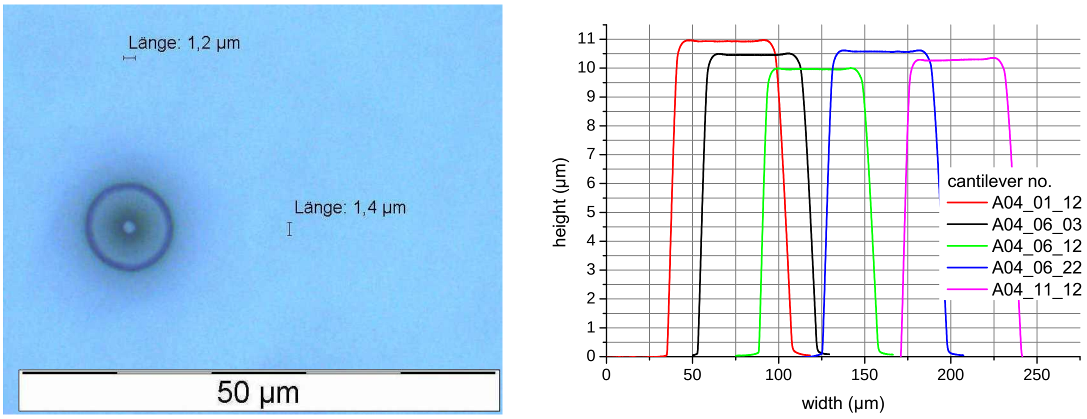

(a) (b)

Figure 3.1: Si dry etching #1: (a) SiO_2 as dark ring and Si as white point; (b) height of orientation marks consisting of leftovers of photoresist, 1.7 µm SiO_2, and ~ 8 µm Si

Steps	Chemicals	Equipment	Parameters	Comments
SiO_2 wet etching	NH_4F	Chuck	22 min (time depends on remaining oxide thickness)	Pour solution on wafer in chuck. $v_{etching} \approx 80\ \frac{\mathrm{nm}}{\mathrm{min}}$
Checking structure		Electron microscope S-4700 (Hitachi, Ltd.) (Figure 3.2)		

Table 3.7: SiO_2 wet etching #1

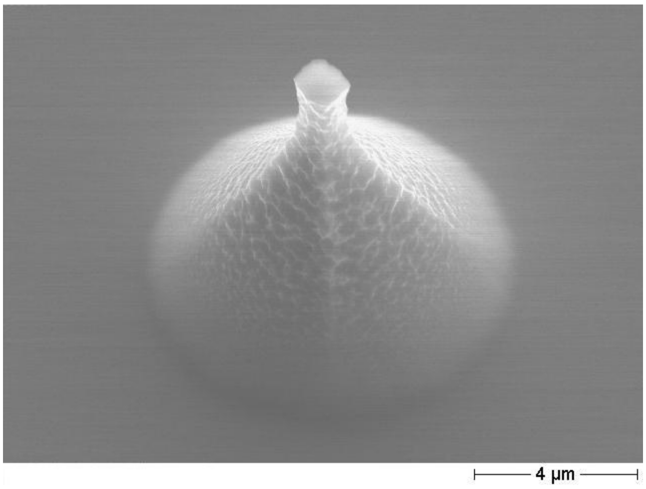

Figure 3.2: Si tip after SiO_2 wet etching #1

Step	Chemicals	Equipment	Parameters			comments
			Temperature	Time	Rpm	
Preheating		Hot plate CEE 100CB (Brewer Science, Inc.)	115°C	1 min		Preheating removes adsorbed gas and water molecules
Cool down in air or with N_2 gun						
Putting on adhesive layer	TI Prime IA 030 91-35, n.o.s. methylpropyl-acetat (MicroChemicals GmbH)	Spin coater CEE 100CB (Brewer Science, Inc.)		30 s	6000	3 drops in the centre of the wafer
Drying		Hot plate	115°C	1 min		
Cool down in air or with N_2 gun						
Putting on photoresist	AZ 1518 photoresist positive (Clariant International Ltd.)	Spin coater		30 s	6000	Pour in the centre of the wafer covering half of it
Drying		Hot plate	115°C	20 min		
Removing photoresist partly	O_2 plasma	Stripper200 (PVA TePla America, Inc.)	300 W power	1 min		Tips are not to be covered in photoresist!
Checking structure		Optical microscope Axiotech (Carl Zeiss AG)				
SiO_2 wet etching	NH_4F	Chuck		15 min		Pour on wafer in chuck
Removing photoresist	O_2 plasma	Stripper200	300 W power	3 min		$(CH_3)_2CO$ is not enough
Checking tip		Optical microscope Axiotech (Carl Zeiss AG), electron microscope S-4700 (Hitachi, Ltd.) (Figure 3.3)				Possibly, tip sharpening has to be done a second time.

Table 3.8: Tip sharpening #1

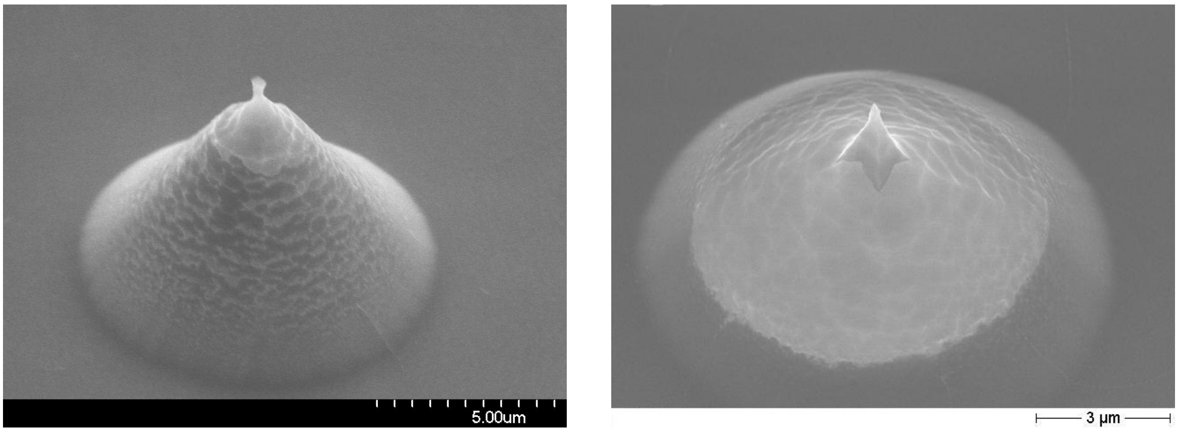

(a) (b)

Figure 3.3: Tip sharpening: (a) the first time; (b) the second time

Step	Chemicals	Equipment	Parameters			Comments
			Temperature	Time	Rpm	
Preheating		Hot plate CEE 100CB (Brewer Science, Inc.)	115°C	1 min		Preheating removes adsorbed gas and water molecules
Cool down in air or with N_2 gun						
Putting on adhesive layer	TI Prime IA 030 91-35, n.o.s. methylpropylacetat (MicroChemicals GmbH)	Spin coater CEE 100CB (Brewer Science, Inc.)		30 s	3000	3 drops in the centre of the wafer
Drying		Hot plate	115°C	1 min		
Cool down in air or with N_2 gun						
Putting on photoresist	AZ 4562 photoresist positive (Clariant International Ltd.)	Spin coater		30 s	3000	Pour in the centre of the wafer covering half of it
Tips have to be covered in photoresist!						
Drying			In air	10 min		
		Hot plate	85°C	2 min		
Cool down in air						
Exposure to UV light		Mask alignment system EV420 (Electronic Visions Co.)	$\sim 6.4 \frac{\text{mW}}{\text{cm}^2}$ irradiance			Wafer in contact with mask
Developing	AZ 400K developer (Clariant International Ltd.) : H_2O = 1:4	Plastic beaker				Moving wafer a little bit

Table 3.9: UV lithography procedure #2 (to be continued)

continued from previous page

Step	Chemicals	Equipment	Parameters			Comments
			Temperature	Time	Rpm	
DI water rinsing	DI water					
Drying		Spin coater		30 s	3000	
Checking structure		Optical microscope Axiotech (Carl Zeiss AG)				Developing step may have to be repeated, if the structure is not fully developed.
Baking		Oven	100°C	20 min		
Removing photoresist from bottom of structure	O_2 plasma	Stripper200 (PVA TePla America, Inc.)	300 W power	2 min		
Measuring structure		Optical microscope Axiotech (Carl Zeiss AG)				

Table 3.9: UV lithography procedure #2

Steps	Chemicals	Equipment	Parameters	Comments
SiO_2 wet etching	NH_4F	Chuck	16 min	Pour solution on wafer in chuck. $v_{etching} \approx 80 \frac{nm}{min}$
Checking structure		Optical microscope Axiotech (Carl Zeiss AG)(Figure 3.4)		
Photoresist is not to be removed!				

Table 3.10: SiO_2 wet etching #2

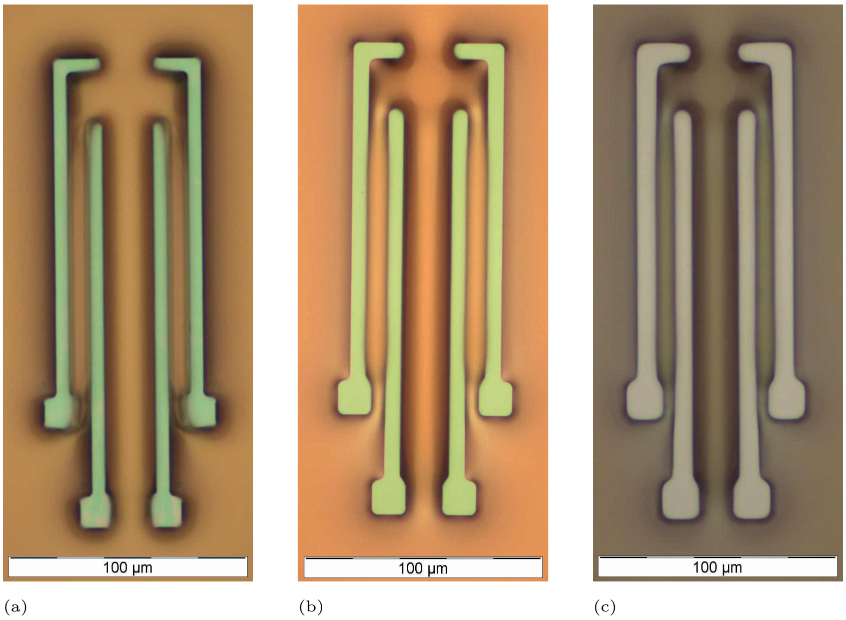

Figure 3.4: Piezoresistive conducting traces: (a) photoresist developed and baked; (b) photoresist removed from bottom of structure; (c) SiO_2 etched, with photoresist ready for ion implantation

Steps	Chemicals	Equipment	Parameters
Ion implantation	$4 \cdot 10^{15} \frac{\text{Boron ions}}{cm^2}$		40 keV power; $\sim 10^{-6}$ mbar chamber pressure
Removing photoresist	$H_2O_2 : H_2SO_4 = 1{:}1$ DI water	Wafer chuck, beaker, hot plate	1) Coarse cleaning: 130°C, 15 min 2) 6 min DI water rinsing 3) Fine cleaning: 130°C, 3 h 4) 6 min DI water rinsing
Checking structure		Optical microscope Axiotech (Carl Zeiss AG)	
Annealing	$3 \frac{l}{min}$ N_2 flow		1) Anneal wafer from 600°C to 1050°C within 35 min 2) Keep for 10 min 3) Cool to 600°C within 1 h

Table 3.11: Ion implantation #1

Step	Chemicals	Equipment	Parameters	Comments
SiO_2 wet etching	NH_4F	Chuck	16 min	Pour solution on wafer in chuck. $v_{etching} \approx 80 \frac{\mathrm{nm}}{\mathrm{min}}$
Checking structure		Optical microscope Axiotech (Carl Zeiss AG)		
Removing photoresist	Caro's acid 25 % H_2O_2 : 97 % H_2SO_4 = 1:1	Gratuated cylinder, quartz beaker, hot plate, thermometer, timer	100°C, 10 min	$(CH_3)_2CO$ and O_2 plasma are not enough
	1 % HF		5 s	
Cleaning wafer	O_2 plasma	Stripper200 (PVA TePla America, Inc.)	300 W power; 2 min	
Checking structure		Optical microscope Axiotech (Carl Zeiss AG)		

Table 3.12: SiO_2 wet etching #3

Steps	Chemicals	Equipment	Parameters
Ion implantation	$1 \cdot 10^{15} \frac{\text{Boron ions}}{\text{cm}^2}$		10 keV power; $\sim 10^{-6}$ mbar chamber pressure
Annealing	$3 \frac{\mathrm{l}}{\mathrm{min}}$ N_2 flow		1000°C, 60 s
Checking structure		Optical microscope Axiotech (Carl Zeiss AG)	

Table 3.13: Ion implantation #2

Steps	Chemicals	Equipment	Parameters
Dry oxidation	1000 Sccm SiH_4 N_2O	Plasmalab 80 Plus (Oxford Instruments Plc)	330°C; 100 W power; $d(SiO_2) = 100$ nm
Si_xN_y ICP chemical vapour deposition (CVD)	1000 Sccm SiH_4 NH_3	Plasmalab 80 Plus (Oxford Instruments Plc)	330°C, 1 min; 30 W power; $d(Si_xN_y) = 200$ nm

Table 3.14: Protective layer of SiO_2 and Si_xN_y

Steps	Chemicals	Equipment	Parameters	Comments
Cleaning chamber	O_2 plasma; 75.0 Sccm N_2 flushing	Plasmalab System 100 (Oxford Instruments Plc)		
Etching	12.0 Sccm CHF_3 38.0 Sccm Ar		200 W power; 30 mTorr chamber pressure; 20 mTorr ignition pressure; 10 ramp rate; 30 Torr He pressure; 20°C, 10 min	Power results in about 500 V DC bias; He for thermal contact between wafer and electrode
Checking structure		Optical microscope Axiotech (Carl Zeiss AG) (Figure 3.5)		
Removing photoresist	Caro's acid 25 % H_2O_2 : 97 % H_2SO_4 = 1:1	Gratuated cylinder, quartz beaker, hot plate, thermometer, timer	100°C, 10 min	$(CH_3)_2CO$ and O_2 plasma are not enough
Checking and measuring structure		Optical microscope Axiotech (Carl Zeiss AG) (Figure 3.5); stylus-type profilometer (Ambios Technology, Inc.)		

Table 3.15: Si_xN_y and SiO_2 dry etching #1

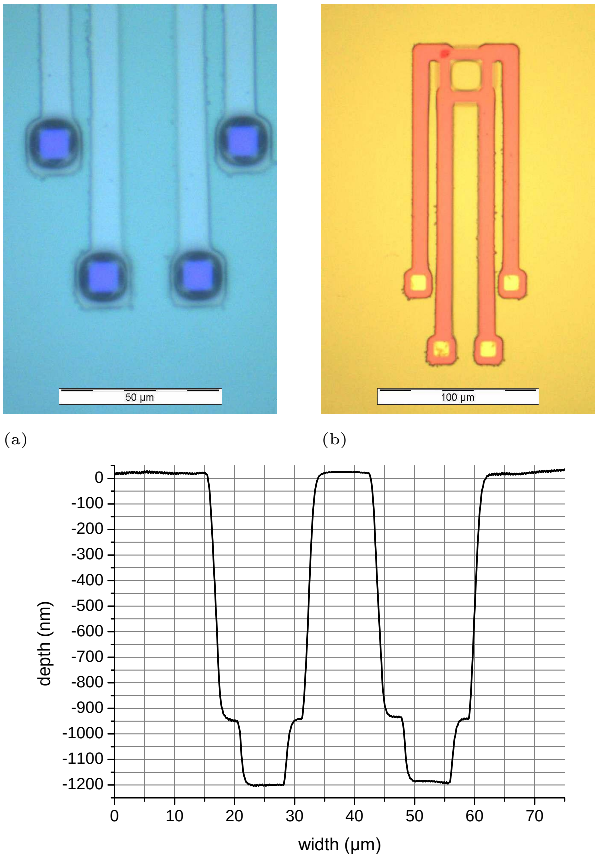

(a) (b)

(c)

Figure 3.5: Contact pads on piezoresistive conducting traces: (a) before and (b) after etching Si_xN_y and SiO_2; (c) etch profile (1 µm SiO_2 + 200 nm Si_xN_y + 100 nm SiO_2)

Step	Chemicals	Equipment	Parameters			comments
			Temperature	Time	Rpm	
Preheating		Hot plate CEE 100CB (Brewer Science, Inc.)	115°C	1 min		Preheating removes adsorbed gas and water molecules
Cool down in air or with N_2 gun						
Putting on adhesive layer	TI Prime IA 030 91-35, n.o.s. methylpropyl-acetat (MicroChemicals GmbH)	Spin coater CEE 100CB (Brewer Science, Inc.)		30 s	6000	3 drops in the centre of the wafer
Drying		Hot plate	115°C	1 min		
Cool down in air or with N_2 gun						
Putting on photoresist	AZ 1518 photoresist positive (Clariant International Ltd.)	Spin coater		30 s	6000	Pour in the centre of the wafer covering half of it
Drying		Hot plate	115°C	20 min		
Removing photoresist partly	O_2 plasma	Stripper200 (PVA TePla America, Inc.)	300 W power	1 min		Tips are not to be covered in photoresist!
Checking structure		Optical microscope Axiotech (Carl Zeiss AG)				
Si_xN_y and SiO_2 wet etching	NH_4F	Chuck		10 min		Pour on wafer in chuck
Removing photoresist	O_2 plasma	Stripper200	300 W power	3 min		$(CH_3)_2CO$ is not enough
Removing oxide	1% HF			5 s		
Checking tips		Optical microscope Axiotech (Carl Zeiss AG); electron microscope S-4700 (Hitachi, Ltd.) (Figure 3.6)				Possibly, tip sharpening has to be repeated.

Table 3.16: Tip sharpening #2

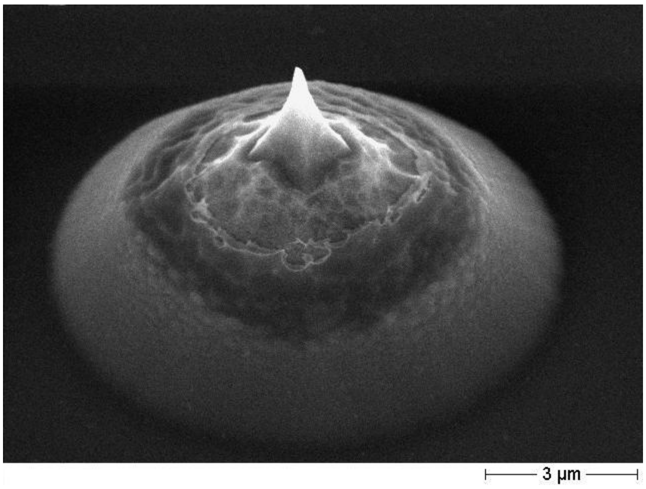

Figure 3.6: Tip sharpening: the third time

Steps	Chemicals	Equipment	Parameters	Comments
Al sputtering		Sputter system LS 250 ClusterSystem; ES (Von Ardenne Anlagentechnik GmbH)		$v_{etching} \approx 0.18\,\frac{\mathrm{nm}}{\mathrm{s}}$; d(Al) ≈ 1 µm

Table 3.17: Al sputtering

Steps	Chemicals	Equipment	Parameters	Comments
Al etching	$H_3PO_4 : HNO_3 : H_2O$ = 20:1:4	Petri dish	1 h 20 min	The etching process has to be watched all the time, since the etching time differs.
Removing photoresist	$(CH_3)_2CO$ and C_3H_7OH	Petri dish		
Measuring structure		Optical microscope Axiotech (Carl Zeiss AG)		
Al melting down	N_2 atmosphere	Furnace	450°C, 25 min	
Checking structure		Optical microscope Axiotech (Carl Zeiss AG); stylus-type profilometer (Ambios Technology, Inc.		

Table 3.18: Al etching and melting down

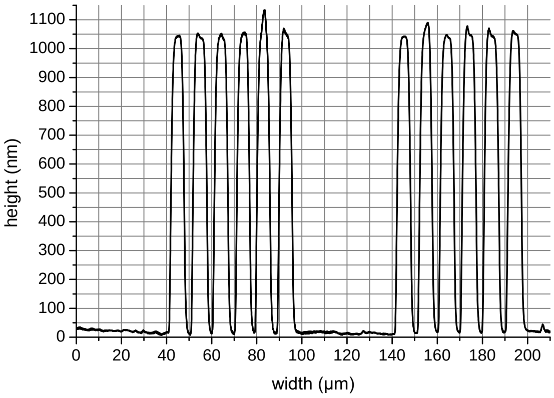

Figure 3.7: Profile of Al thin film heater

Steps	Chemicals	Equipment	Parameters
Removing photoresist from bottom of structure	O_2 plasma	Stripper200 (PVA TePla America, Inc.)	100 W power; 1 min
Hard bake		Hot plate	1) 85°C → 120°C: ~ 2 min 2) 120°C: 2 min 30 s 3) 120°C → 150°C: ~ 2 min 4) 150°C: 2 min 30 s 5) 150°C → 200°C: ~ 4 min 6) 200°C: 2 min 30 s
Checking structure		Optical microscope Axiotech (Carl Zeiss AG) (Figure 3.8); stylus-type profilometer (Ambios Technology, Inc.)	

Table 3.19: Bridge over Al thin film heater and piezoresistive Wheatstone bridge

Steps	Chemicals	Equipment	Parameters	Comments
Si_xN_y ICP CVD	1000 Sccm SiH_4 NH_3	Plasmalab 80 Plus (Oxford Instruments Plc)	120°C	$d(Si_xN_y) \approx 100$ nm

Table 3.20: Protective layer of Si_xN_y

Step	Chemicals	Equipment	Parameters			Comments
			Temperature	Time	Rpm	
Preheating		Hot plate CEE 100CB (Brewer Science, Inc.)	115°C	1 min		Preheating removes adsorbed gas and water molecules

Table 3.21: UV lithography procedure #3 (to be continued)

continued from previous page

Step	Chemicals	Equipment	Parameters			Comments
			Temperature	Time	Rpm	
Cool down in air or with N_2 gun						
Putting on adhesive layer	TI Prime IA 030 91-35, n.o.s. methylpropyl-acetat (MicroChemicals GmbH)	Spin coater CEE 100CB (Brewer Science, Inc.)		30 s	3000	3 drops in the centre of the wafer
Drying		Hot plate	115°C	1 min		
Cool down in air or with N_2 gun						
Putting on photoresist	AZ 5214E photoresist negative (Clariant International Ltd.)	Spin coater		30 s	3000	Pour in the centre of the wafer covering half of it
Drying		Hot plate	85°C	2 min		
Cool down in air						
Exposure to UV light		Mask alignment system EV420 (Electronic Visions Co.)	$\sim 6.4\frac{\mathrm{mW}}{\mathrm{cm}^2}$ irradiance			Wafer in contact with mask
Baking		Hot plate	115°C	2 min		
Exposure to UV light		Mask alignment system EV420 (Electronic Visions Co.)	Flood exposure	60 s		
Developing	AZ 400K developer (Clariant International Ltd.) : H_2O = 1:4	Plastic beaker				Moving wafer a little bit
DI water rinsing	DI water					
Drying		Spin coater		30 s	3000	
Checking structure		Optical microscope Axiotech (Carl Zeiss AG)				Developing step may have to be repeated, if the structure is not fully developed.
Baking		Oven	105°C	30 min		

Table 3.21: UV lithography procedure #3

Steps	Chemicals	Equipment	Parameters	Comments
Si_xN_y wet etching	NH_4F	Chuck	2 min	Pour solution on wafer in chuck
Removing photoresist	$(CH_3)_2CO$ C_3H_7OH	Petri dish		
	O_2 plasma	Stripper200 (PVA TePla America, Inc.)	300 W power; 2 min	This removes leftovers of the photoresist.
Checking structure		Optical microscope Axiotech (Carl Zeiss AG) (Figure 3.8); stylus-type profilometer (Ambios Technology, Inc.)		

Table 3.22: Si_xN_y wet etching

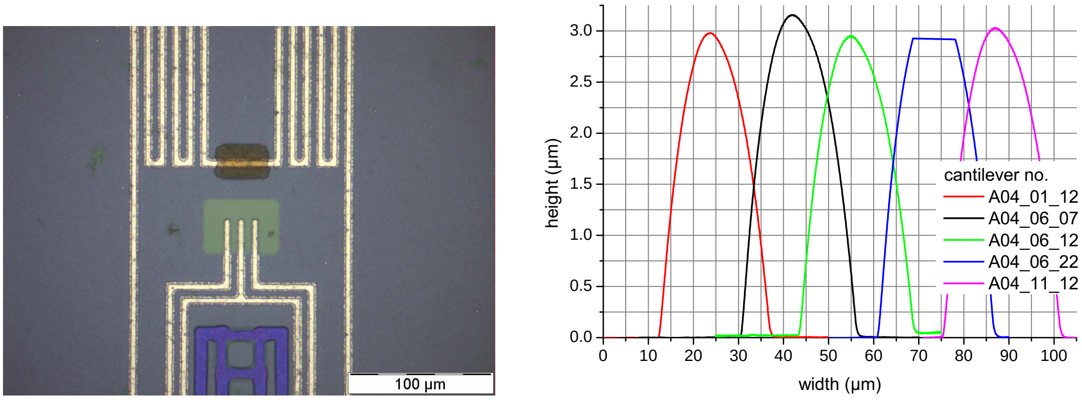

(a)

(b)

Figure 3.8: (a) Bridge over Al thin film heater and contact pads on Al conducting traces (Si_xN_y etched); (b) profile of bridge

Steps	Chemicals	Equipment	Parameters	Comments
Cr and Au PVD		Edwards Auto306 (Edwards Limited)		d(Cr) = 30 nm d(Au) = 120 nm
Lift-off process	$(CH_3)_2CO$	Petri dish		right after PVD
Checking structure		Optical microscope Axiotech (Carl Zeiss AG) (Figure 3.9)		

Table 3.23: Au PVD

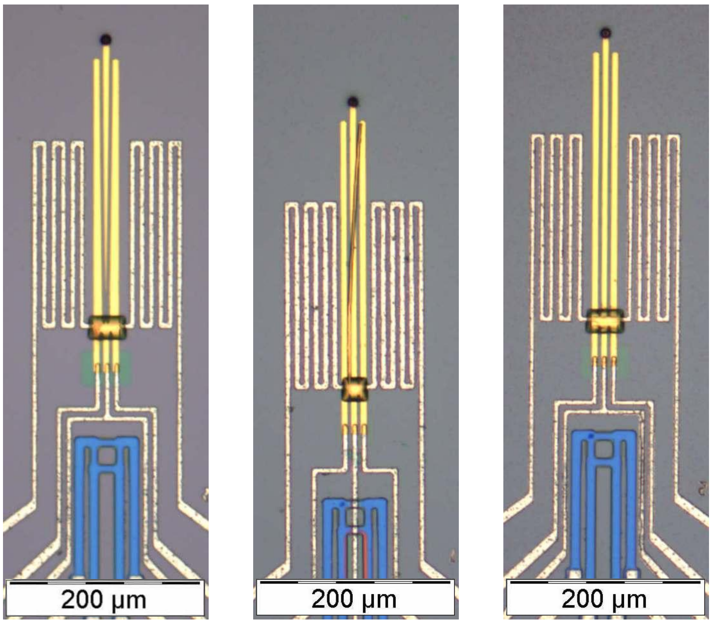

(a) (b) (c)

Figure 3.9: Broken Au conducting traces for conductive tip

Steps	Chemicals	Equipment	Parameters	Comments
SiO_2 wet etching	NH_4F	Chuck	30 min	Pour solution on wafer in chuck $v_{etching} \approx 80 \frac{\mathrm{nm}}{\mathrm{min}}$
Checking structure		Optical microscope Axiotech (Carl Zeiss AG)		
Removing photoresist	$(CH_3)_2CO$	Petri dish		Both sides
Cleaning wafer	O_2 plasma	Stripper200 (PVA TePla America, Inc.)	300 W power; 2 min	
Checking structure		Optical microscope Axiotech (Carl Zeiss AG)		

Table 3.24: SiO_2 wet etching #4

Steps	Chemicals	Equipment	Parameters	Comments
ICP-RIE	25.0 Sccm CHF_3 6.0 Sccm CF_4	Vision 320 RIE (STS plc)	120 W RF power; 50 mTorr pressure; 45 min + 30 min + 15 min + 15 min (wafer turned by 180° along [100] crystallographic axis of Si)	RF power results in 470 V DC bias. Turn wafer for even etching.
Checking structure		Optical microscope Axiotech (Carl Zeiss AG) (Figure 3.10)		
Photoresist is not to be removed!				

Table 3.25: Si_xN_y and SiO_2 dry etching #2

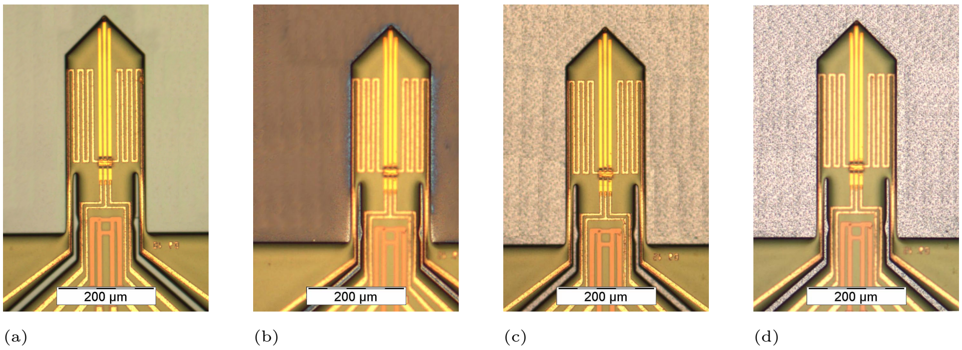

(a) (b) (c) (d)

Figure 3.10: Steps of Si_xN_y and SiO_2 dry etching #2:
(a) before etching; (b) 75 min etching; (c) 90 min; and (d) 105 min etching

Steps	Chemicals	Equipment	Parameters	Comments
KOH etching	40 % KOH	Double wall beaker for constant temperature bath; chuck for wafer	60°C, 14 - 15 h	$v_{etching} \approx 21 \frac{\mu m}{h}$; orange membrane ≈ 10 µm
DI water rinsing	DI water		Room temperature	
Checking structure		Optical microscope Axiotech (Carl Zeiss AG)		
ICP-RIE	130 Sccm SF_6	ICP Multiplex^{ASE} (STS plc)	620 W RF power; 300 V voltage; 9.8 Torr He pressure for wafer cooling; 1 min	Put wafer on top of 4 inch wafer
Checking structure		Optical microscope Axiotech (Carl Zeiss AG) (Figure 3.11)		
Photoresist is not to be removed!				

Table 3.26: Si wet and dry etching

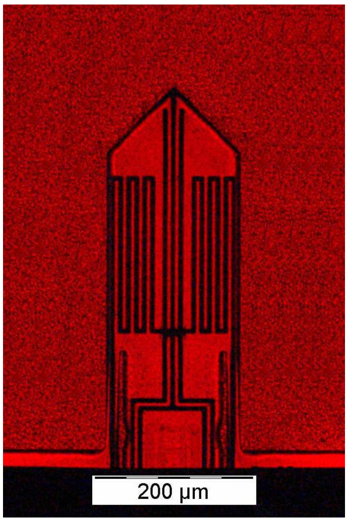

Figure 3.11: Si membrane with light from bottom

Steps	Chemicals	Equipment	Parameters	Comments
ICP-RIE	1) 85 Sccm C_4F_8 2) 130 Sccm SF_6 + 13 Sccm O_2	ICP Multiplex^{ASE} (STS plc)	630 W RF power; 320 V voltage; 9.8 Torr He pressure for wafer cooling; 2 min	Put wafer on top of 4 inch wafer. Carry out both steps in rotation!
Checking structure		Optical microscope Axiotech (Carl Zeiss AG)		
Cleaning wafer	O_2 plasma	Stripper200 (PVA TePla America, Inc.)	300 W; 5 min	
Checking structure		Optical microscope Axiotech (Carl Zeiss AG); electron microscope S-4700 (Hitachi, Ltd.) (Figure 3.12)		

Table 3.27: Si dry etching #2

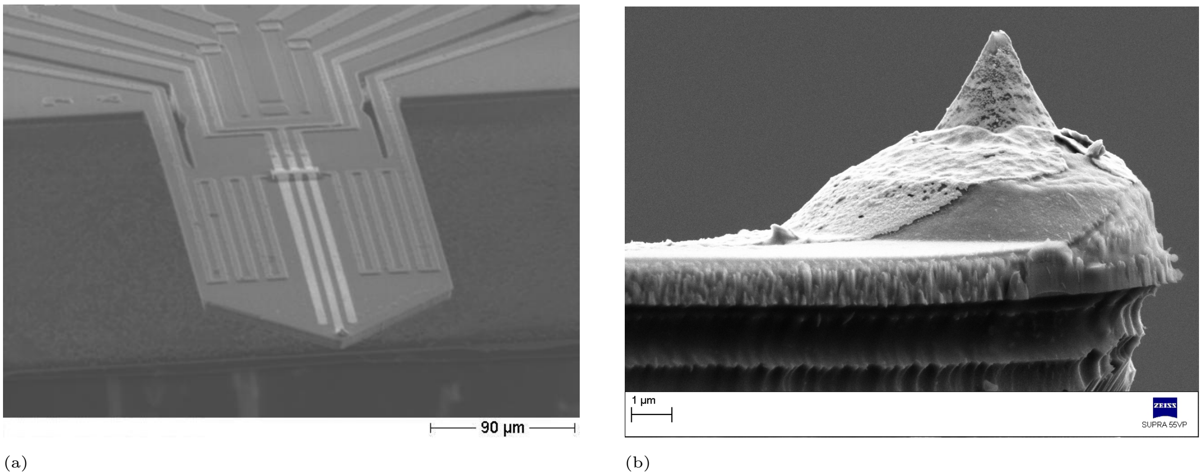

(a)

(b)

Figure 3.12: Cantilever: (a) overview and (b) tip with height of ∼ 5 µm and radius of ∼ 200 nm

Steps	Chemicals	Equipment	Parameters	Comments
Cleaning PCB	$(CH_3)_2CO$ C_3H_7OH	Ultrasonic cleaner		Clean with $(CH_3)_2CO$; C_3H_7OH cleaning in ultrasonic cleaner for 1 h
Gluing cantilever chip on PCB	Electrically conductive Ag epoxy EPO-TEK H31D (Epoxy Technology, Inc.)	Needle, plastic tweezers		Put on glue with needle. Handle cantilever chip with plastic tweezers.
Glue hardening		Hot plate	130°C, 30 min	

Table 3.28: Cantilever mounting

Steps	Equipment	Parameters	Values	
Au wire (25 µm diameter)	Ultrasonic Generator ZFG-010, single head 5610 (F&K Physiktechnik GmbH)	130°C		
			Cantilever chip	PCB
		US time/ ms	30	80
		US power/ digit	40	130
		B-Force start/ cN	35	35
		TD steps/ µ	15	15
		Arch	Low	High
		Z-presign	65	75
		Loop H-Fct	110	110
		Reverse Fct	300	300
		Reverse Height	400	400
Measuring resistance of piezoresistive Wheatstone bridge and Al thin film heater	Voltmeter with tiny tips			

Table 3.29: Cantilever bonding

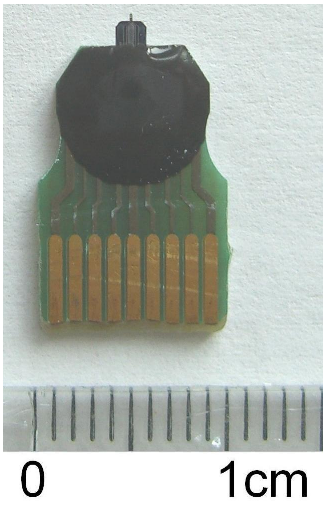

Figure 3.13: Mounted and bonded cantilever: Au wires covered with glob top

4 Characterization and imaging

4.1 Introduction

The foregoing section on theory has described the influence of parasitic heating caused by the mechanisms of thermal beam actuation and deflection detection, and the influence of air damping, noise, and crosstalk on the performance of the self-actuating and self-sensing piezoresistive microscale silicon cantilever. In practice, diverse measurements had been made with the purpose of an extensive characterization of the beam. The experimental set-up was installed inside a SEM chamber (section 4.2). The measured results show the behaviour of fundamental frequency, quality factor, maximum amplitude of beam oscillation, and deflection on pure beam bending (section 4.3). The self-actuation is characterized by the actuation efficiency and the self-sensing by the deflection sensitivity. Noise and capacitive crosstalk limit the cantilever performance. The self-actuating and self-sensing piezoresistive microscale silicon cantilever is demonstrated to be capable of frequency modulation (FM)-AFM imaging (section 4.4).

4.2 Measurement

4.2.1 Set-up

The set-up for the experiments carried out was basically a scanning electron microscope (SEM), electronics for supply and data acquisition, and two personal computers (PC) for control (Figure 4.1 and Table 4.1). The electronics, especially those for data acquisition, were chosen to have low noise, high resolution, and time constants much smaller than the one of the cantilever.

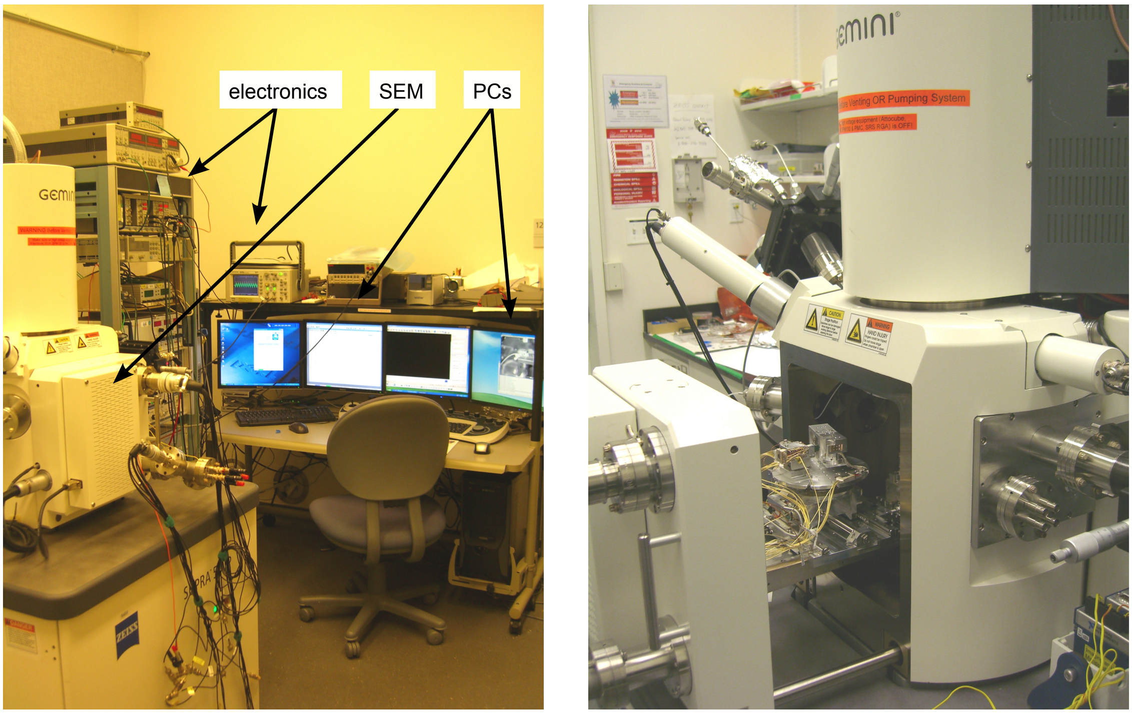

(a) (b)

Figure 4.1: Laboratory: (a) SEM, electronics, and control; (b) SEM with door open and set-up inside

Instrument	Model
Scanning electron microscope	SEM SUPRA 55VP (Carl Zeiss AG)
Stages	x piezo stage ANPx101, 5 mm travel (attocube systems AG) y piezo stage ANPx101, 5 mm travel (attocube systems AG) z piezo stage ANPz101, 5 mm travel (attocube systems AG) xyz piezo shear stack P-143.05, 5 μm travel (Physik Instrumente GmbH & Co. KG)
Platform for small instrumentation modules	SIM900 Mainframe (Stanford Research Systems, Inc.)
Voltage source and ground	SIM928 Isolated Voltage Source (Stanford Research Systems, Inc.)
Scaling amplifier	SIM983 Scaling Amplifier (Stanford Research Systems, Inc.)
Lock-in amplifier	SR830 DSP Lock-In Amplifier (Stanford Research Systems, Inc.)
Function generator	Model DS340 - 15 MHz Function and Arbitrary Waveform Generator (Stanford Research Systems, Inc.)
Current source	Model 2410 High Voltage Source Meter (Keithley Instruments Inc.)
Piezo stage controller	ANC150 (attocube systems AG)
RHK control system	Model SPM100 Revision 8 Control Electronics (RHK Technology, Inc.) PLLpro Universal AFM Control (RHK Technology, Inc.)
RHK software	XPMpro version 2.0.0.3 (RHK Technology, Inc.) PLLpro front-end version 2.2.0 (RHK Technology, Inc.)
Oscilloscope	InfiniiVision 6000 Series Model DSO6012A (Agilent Technologies, Inc.)
Mulitmeter	Multimeter Fluke 77 Digital Multimeter (Fluke Corporation)

Table 4.1: Equipment, sources, measurement instruments, and software

Inside the SEM chamber, the experimental set-up was arranged on a separate platform positioned on the 5-axis specimen stage, an arrangement enabling the user to take the set-up out of the microscope without too much effort, so that the SEM could be used successively by different users doing different experiments. On the platform there were placed three piezo tube stages (x and y stage on top of each other) and one piezo shear stack which held cantilever and sample and moved them (Figures 4.2 and 4.3). They were perpendicularly aligned with the SEM lens, so that a SEM image of the cantilever's side view could be taken, and the pre-bending of the beam measured and the maximum amplitude of beam oscillation z_{AC} recorded (Figure 4.4).

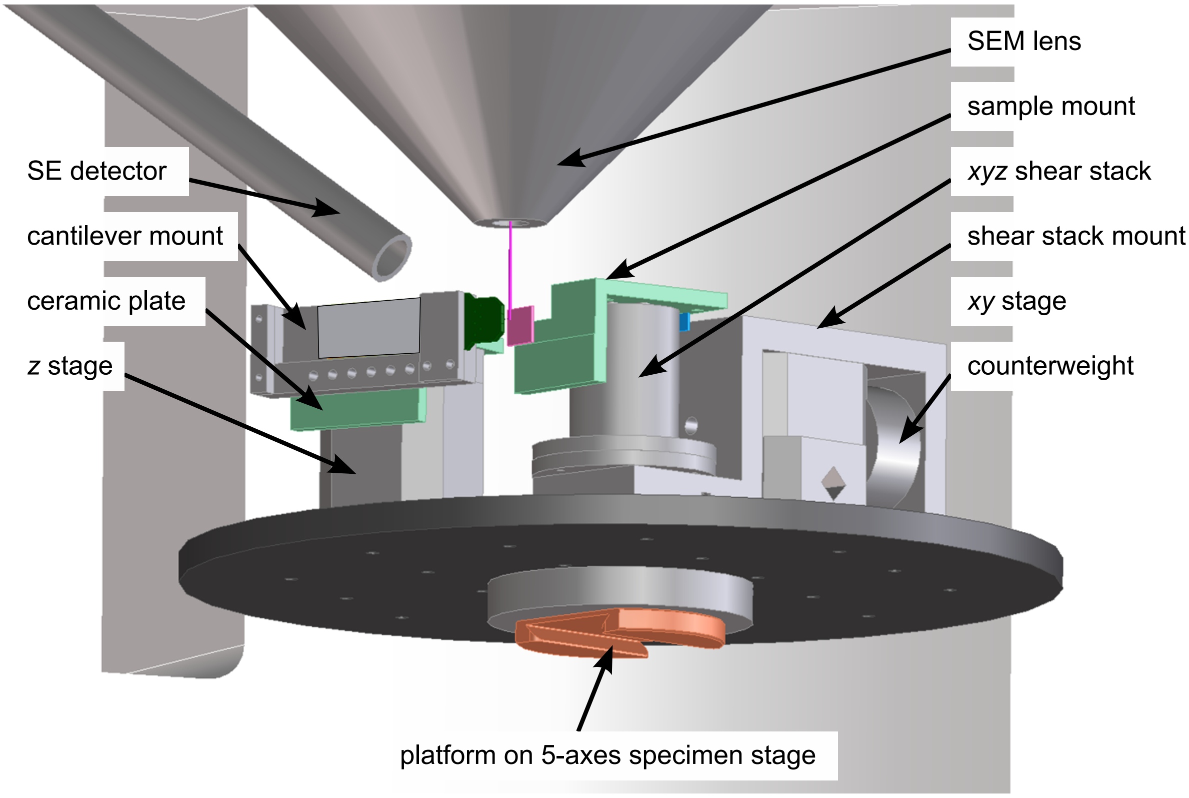

Figure 4.2: Schematic of the set-up in the SEM chamber

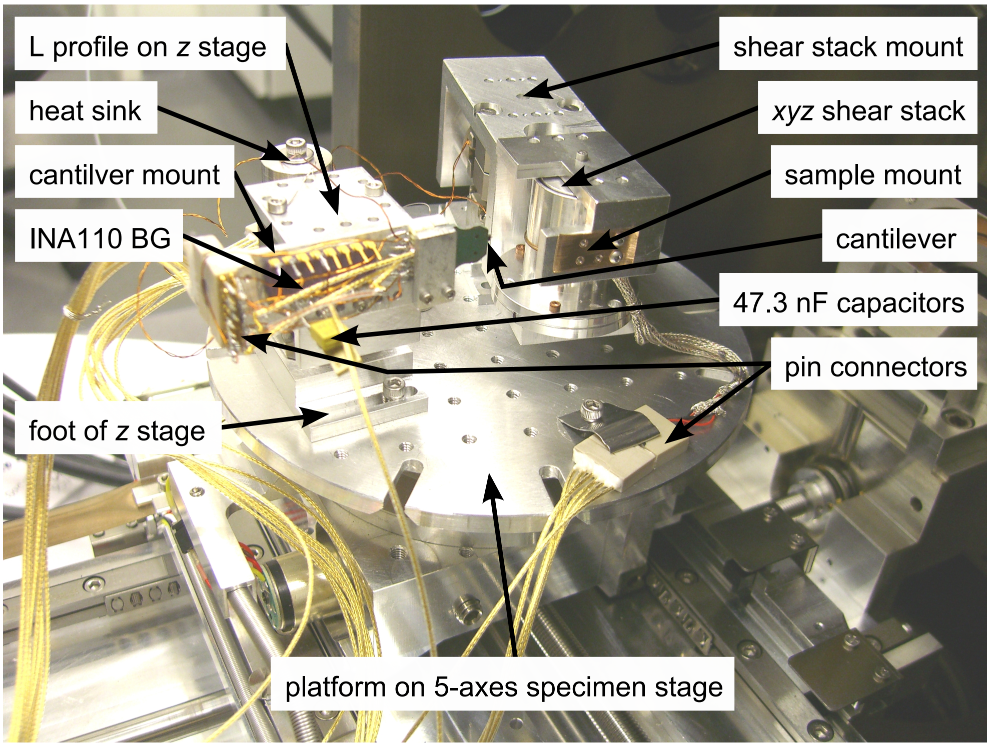

Figure 4.3: Photograph of the set-up in the SEM chamber

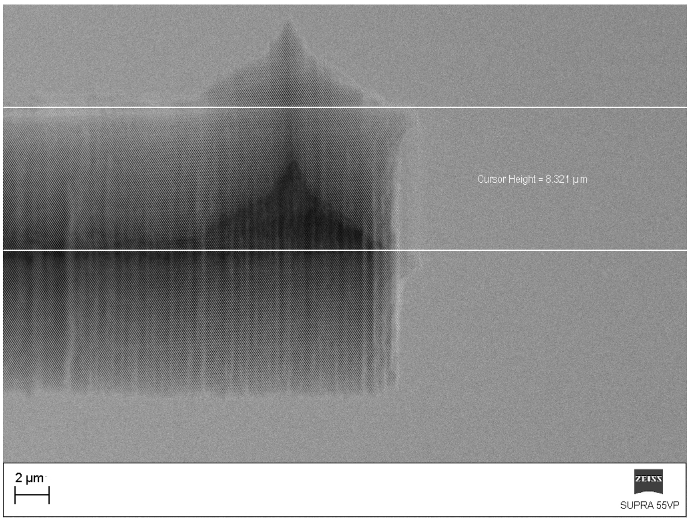

Figure 4.4: Oscillating cantilever (SEM image)

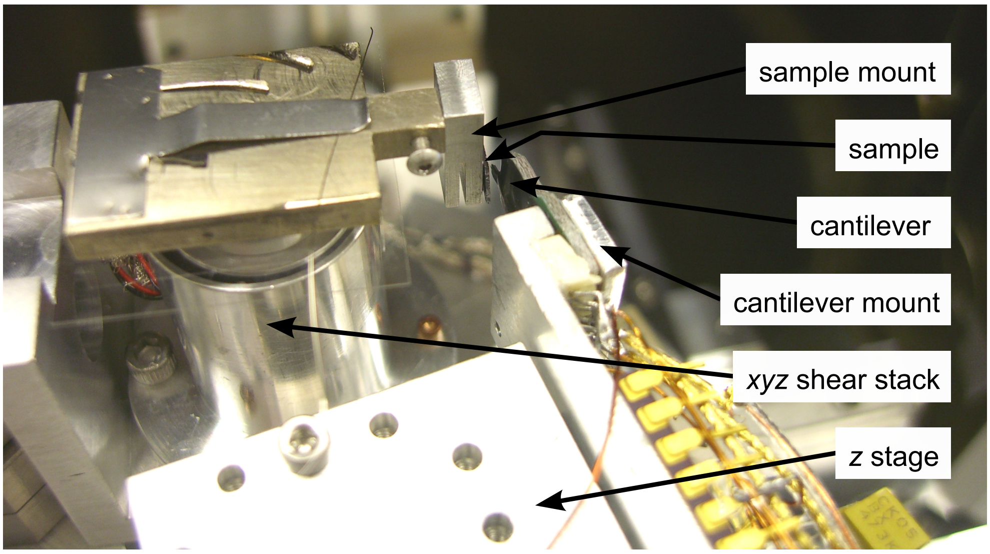

Figure 4.5: Cantilever and stainless steel sample mount - configuration for AFM imaging

Furthermore, it was possible to observe the tip-sample interaction when a cantilever was scanning a sample in AFM mode (Figure 4.5). The piezo stages stood on special feet. On top of the z piezo stage an L profile had been fixed to hold the cantilever mount. The instrumentation amplifier INA110 BG (Texas Instruments Incorporated) amplifying the Wheatstone bridge output voltage signal and a connector for the cantilever PCB were glued onto the front of the cantilever mount, a female pin plug at its edge. Simple non-shielded wires were soldered to connect the amplifier and the two connectors. The instrumentation amplifier was close to the cantilever, i.e. on the cantilever mount, to prevent signal losses and interference between different signals which were being transmitted to cantilever, amplifier and stages. Two 47.3 nF-capacitors CK05 BX 47.3K (AVX Corporation) on the voltage supply pins prevented the amplifier being damaged by high voltage peaks from the voltage source. The amplifier was separately grounded to the SEM chamber. The cantilever PCB was held in place by a screwed clip. Ceramic strips were glued onto the reverse side of the cantilever mount and ceramic washers were used to separate the screws electrically from the L profile and the z piezo stage. An aluminium cylinder acted as a heat sink for the cantilever, being electrically and thermally separated from the platform by the ceramic plate and plastic screw. The shear stack mount was fixed onto the top of the xy piezo stage. To make possible proper movement of the piezo stage and to prevent damage to the piezo tubes a counterweight was suspended opposite the xyz piezo shear stack. The sample mount on a glass slide glided along the top of the stack as the shear stack moved back and forth at a signal pulse. The sample mount and the sample were grounded to the platform and through that to the specimen stage which was floating electrically. Pin connectors for the cantilever and the stages were handmade from plastic, the pins had twisted wire heads and were glued into drilled holes. Ultra miniature coaxial cable type SC (stranded copper conductor) (Lake Shore Cryotronics, Inc.) was soldered to the female pin plugs to connect with the handmade pin plugs which fitted the flange. Through two flanges in the SEM door, the experimental set-up was connected to the supply and data acquisition electronics via standard 50 Ω-cables and Bayonet-Neill-Concelman (BNC) connectors. All metal pieces were handmade from aluminium except for the sample mount, which was made of stainless steel. Epoxy was used for gluing. Solder, epoxy, wires, and cables were vacuum compatible.

4.2.2 Measurement configuration

For the different kinds of measurements, the experimental set-up had to be adjusted each time. Basically, five configurations could be distinguished:

1. Dynamic performance of the self-sensing and self-actuating piezoresistive microscale silicon cantilever - Measurement of the maximum amplitude of beam oscillation z_{AC}, the AC Wheatstone bridge output voltage signal $U_{out,bridge,AC}$, and the fundamental frequency f_1:

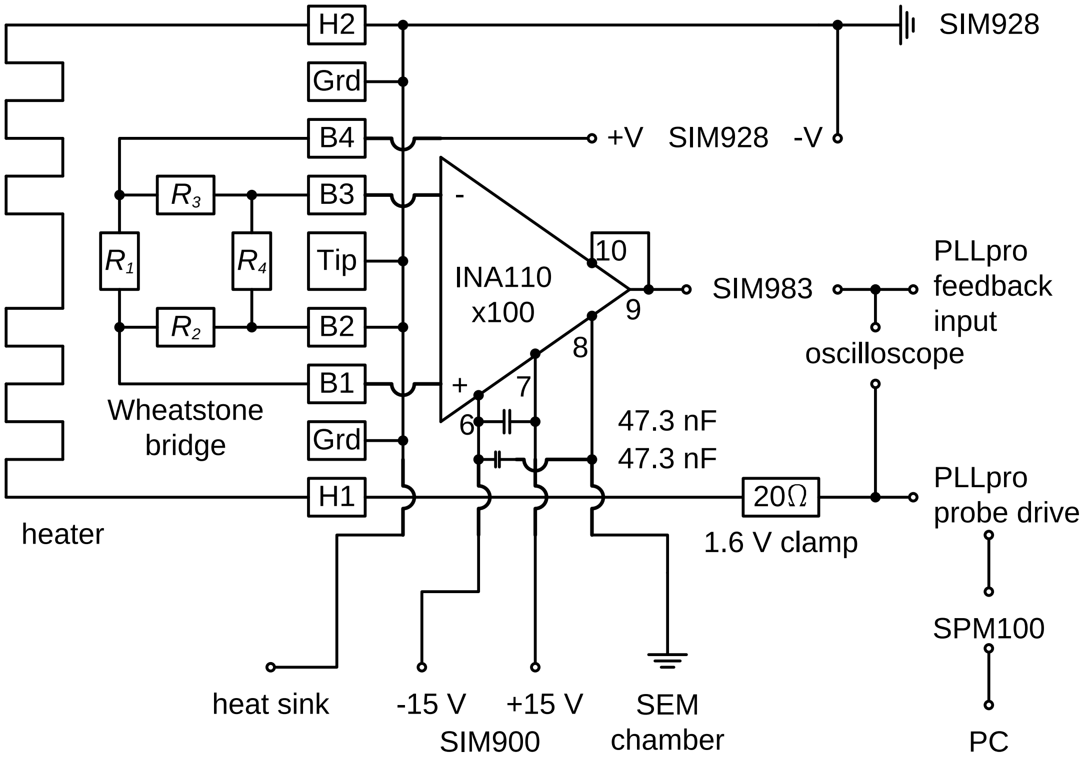

Figure 4.6: Configuration of supply and data acquisition electronics for dynamic measurement

For this, the configuration of the supply and data acquisition electronics is shown in Figure 4.6. The PLLpro front-end software working in PLL mode with constant AC excitation was used to oscillate the cantilever. Drive frequency f_d, the amplitude $\hat{U}_{AC}$ and the offset U_{DC} of the AC drive voltage signal $U_{drive,AC}$ were set. The analogue attenuator for output to the probe drive and the amplifier input gains were set to 1. The amplitude and frequency control gains of the proportional-integral-derivative (PID) controllers were kept as recommended by RHK Technology, Inc.. The digital loop filter was the smallest possible (18.75 Hz) to reduce noise. Resonance peak search and measurement were performed automatically resulting in a pair of graphs providing fundamental frequency f_1, the AC Wheatstone bridge output voltage signal $U_{out,bridge,AC}$, and phase φ. Data could be saved as ASCII file and processed with the software OriginPro (OriginLab Corporation). The theory of the DHO (chapter 2.2.7) was applied to calculate frequencies of the first resonance f_1, i.e. the fundamental frequency, and the second resonance f_2, and the quality factor Q. Results are presented in sections 4.3.2, 4.3.3, 4.3.5, 4.3.6, 4.3.7, and 4.3.9.

2. Static performance of the self-sensing and self-actuating piezoresistive microscale silicon cantilever - Measurement of the DC Wheatstone bridge output voltage signal $U_{out,bridge,DC}$ caused by pure beam bending and the thermal time constant of the beam $\tau_{th,beam}$:

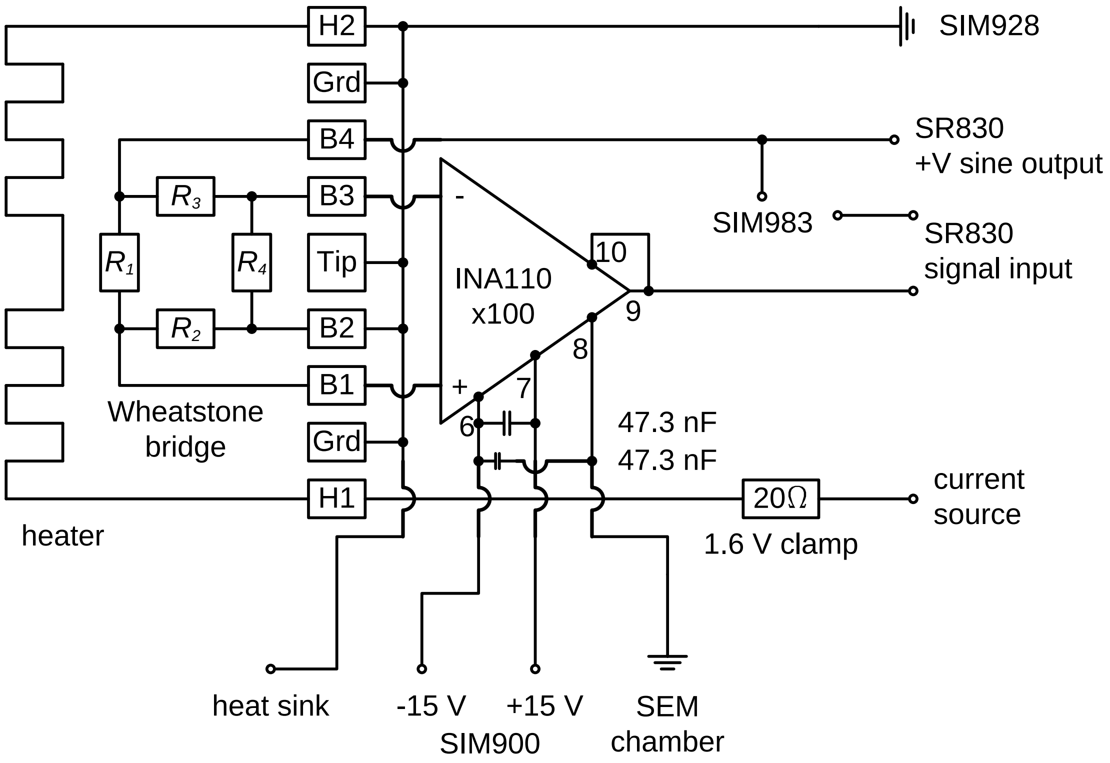

Figure 4.7: Configuration of supply and data acquisition electronics for static measurement

For this, the configuration of the supply and data acquisition electronics is shown in Figure 4.7. The Wheatstone bridge was supplied with an AC input voltage drive signal $U_{in,bridge,AC}$ with a frequency of 10 kHz such as would fulfil the purpose of a less noisy DC Wheatstone bridge output voltage signal $U_{out,bridge,DC}$. Before any measurement, the Wheatstone bridge output voltage signal was cancelled out with the input voltage signal, so that the output voltage signal was set to 0 V and it was possible to detect any small signal change caused by pure beam bending. Results are presented in sections 4.3.4 and 4.3.8.

3. Noise spectra:
   For this, the configuration of the supply and data acquisition electronics was the same as for dynamic measurement (Figure 4.6) except that aluminium thin film heater and Wheatstone bridge were grounded and not supplied by any voltage signal. The voltage noise density was measured from 0 kHz up to 125 kHz. Results are presented in section 4.3.10.

4. Capacitive crosstalk:

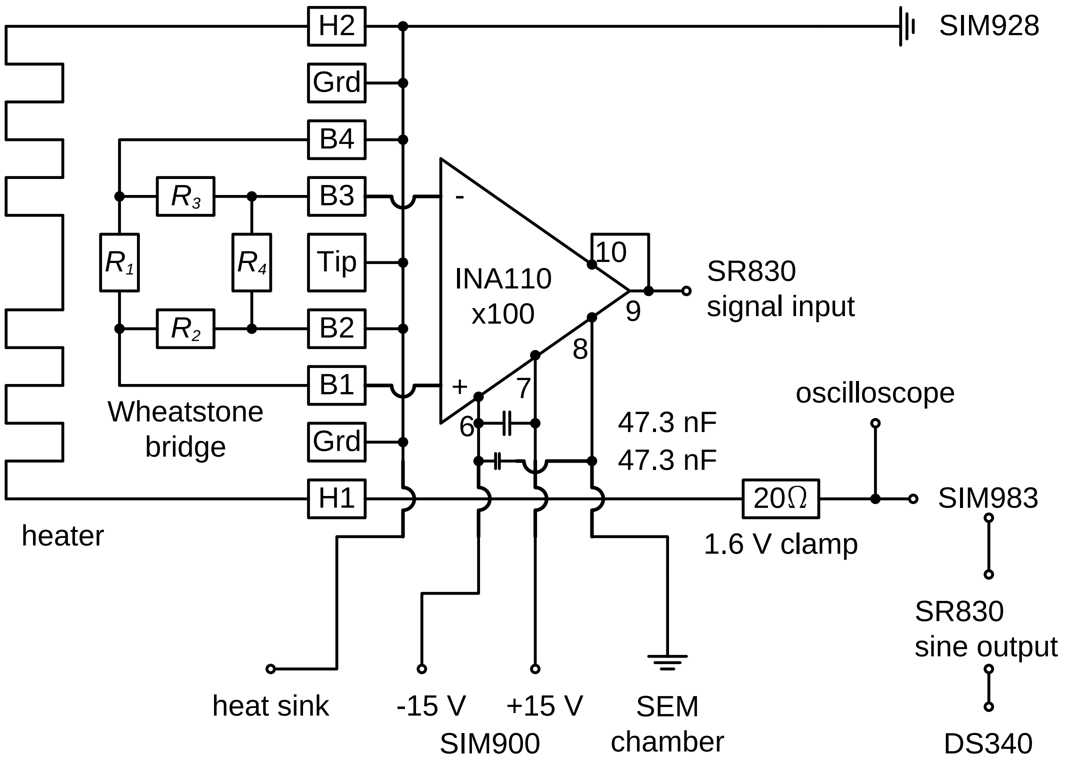

Figure 4.8: Configuration of supply and data acquisition electronics for crosstalk measurement

For this, the configuration of the supply and data acquisition electronics is shown in Figure 4.8. The Wheatstone bridge was not supplied by any voltage signal. The time constant of the lock-in amplifier was adapted to the frequency the cantilever oscillated at. The low pass filter slope was set to 24 dB/ octave. Results are presented in section 4.3.11.

5. FM-AFM imaging: First, cantilever and sample were brought closer to each other in relatively large steps using the three piezo tube stages that were manually driven from the ANC150 controller and the approach was monitored by the user with the SEM. Then, the shear stack run by SPM100 controller moved the sample. Here the approach was controlled by phase-locked loop (PLL) with the cantilever oscillating at constant excitation. The set-up required the x- and z-directions of the shear stack to be switched, i.e. the controller considered the x-axis as the z-axis and vice versa. The cantilever had to be aligned with the sample at a certain angle because the beam was pre-bent. AFM imaging was done in non-contact mode, because the tip was not absolutely sharp and contact mode would make it even blunter. The PLLpro front-end software was used to set the PLL mode with constant AC excitation, drive frequency f_d close to the fundamental frequency f_1, amplitude $\hat{U}_{AC}$ and offset U_{DC} of the AC drive voltage signal $U_{drive,AC}$. The set point of the feedback circuit, and the settings for proportional and integral gain settings were selected at the front panel of the SPM100 controller. Proportional and integral time constants determined the total response time of the feedback loop. In PLL mode with constant AC excitation the frequency changes if the tip-sample distance varies, i.e. the Wheatstone bridge output signal is frequency-modulated (FM). That is why it is called FM-AFM imaging.AFM images were processed with WSxM software [127]. They are presented in section 4.4.

The silicon substrate was always grounded. Before any measurement could be done the cantilever had to be installed into the cantilever mount. Connections had to be checked by using a multimeter and measuring the ohmic resistance of the aluminium thin film heater and the Wheatstone bridge piezoresistors. It was necessary to offset the Wheatstone bridge output voltage signal because the PLLpro feedback input was limited to 1 V. Even if the self-sensing and self-actuating piezoresistive microscale silicon cantilever were neither oscillating nor being deflected, the output voltage signal of the Wheatstone bridge was still not 0 V, because the piezoresistors do not all have the same resistance, due to the fabrication process (see section 2.3.2). Since the PLLpro probe drive was a 50 Ω-signal output and the heater resistance R_{heater} about 20 Ω, up to almost 40 Ω, a 20 Ω-resistor was put between them for balancing purposes. The 1.6 V clamp prevented distortion of the aluminium thin film heater by any voltage peak coming from the switching on and off of the supply and data acquisition electronics that could cause melting of the aluminium. An oscilloscope was used to control drive and output signal. Environmental parameters of measurements are given in Table 4.2.

Parameter	Vacuum	Air
Pressure in Pa	(0.01 - 0.3)$\cdot 10^{-3}$	~ 97,700
Temperature in °C	23±0.2 - 25±0.2	21±1 - 23±1

Table 4.2: Environmental parameters of measurements

4.2.3 Measurement errors

All measurements and calculations are flawed with errors as listed in Table 4.3. Measurement errors are on different scales, in consequence of the various methods of measurement, the supply and data acquisition electronics, the experimental set-up with its wiring and bonding, and the user. In air the Wheatstone bridge output voltage signal $U_{out,bridge,AC}$ is smaller, because the AC amplitude z_{AC} is reduced due to damping, so that the noise plays a bigger role and the measurement error is increased. Measurement errors are not always shown in graphs, because they are on a tiny scale.

Parameter		Measurement error			Measurement device
Thickness	d	± 5		%	SEM image
Pre-bending angle		± 10		%	´´
Maximum amplitude	$z_{AC,max}$	± 5		%	´´
Resistance of Al thin film heater	R_{heater}	± 5		%	Multimeter
Resistance of Wheatstone bridge	R_{bridge}	± 1		%	´´
Frequencies in vacuum	f_1, f_2	± 1	$\cdot 10^{-1}$	Hz	PLLpro Universal AFM Control
Frequencies in air	f_1, f_2	± 3	$\cdot 10^{-1}$	Hz	´´
Amplitude	$\hat{U}_{AC}$	±	10^{-4}	V	´´
Offset	U_{DC}	±	10^{-4}	V	´´
DC drive	$I_{drive,DC}$	±	10^{-4}	A	Current source
DC Wheatstone bridge input voltage	$U_{in,bridge,DC}$	±	10^{-2}	V	Voltage source
AC Wheatstone bridge output voltage	$U_{out,bridge,AC}$	±	10^{-6}	Vrms	PLLpro Universal AFM Control
DC Wheatstone bridge output voltage	$U_{out,bridge,DC}$	± 10		%	SR830 DSP Lock-In Amplifier
Frequencies in vacuum	f_1, f_2	± 1	$\cdot 10^{-1}$	Hz	DHO calculation
Frequencies in air	f_1, f_2	± 3	$\cdot 10^{-1}$	Hz	´´
Quality factor	Q	± 1			´´

Table 4.3: Measurement errors

4.3 Performance of the self-actuating and self-sensing piezoresistive microscale silicon cantilever

4.3.1 Pre-bending

All the self-actuating and self-sensing piezoresistive microscale silicon cantilevers which were studied were found to be pre-bent (Figure 4.9), which was also a finding for similar self-actuating and self-sensing piezoresistive microscale silicon beams by Rangelow's group before [66].

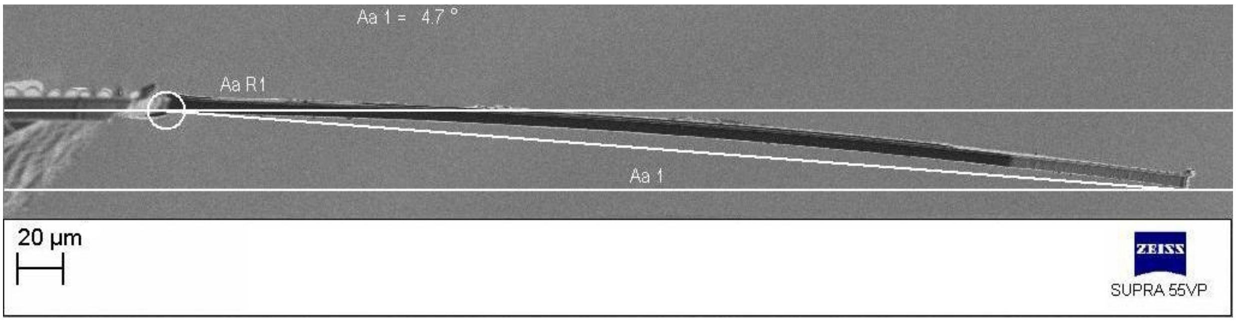

Figure 4.9: Pre-bending of a self-actuating and self-sensing piezoresistive microscale silicon cantilever with a pre-bending angle of 4.7° (SEM image)

The pre-bending is due to stress caused by the composite structure with its multiple material layers having different thermal expansion coefficients. Mainly, it is an interaction between the silicon dioxide (SiO_2) layer and the silicon (Si) layer. The silicon was oxidized at 960°C. At this temperature silicon was expanded and when it cooled down it shrank. Since the thermal expansion coefficient of silicon dioxide is about five times smaller than that of silicon (Table 2.9 in section 2.2.6), compressive stress is introduced to the Si layer. Silicon nitride (Si_xN_y) was deposited at 330°C. Because its thermal expansion coefficient is higher, tensile stress arises within the Si layer on cooling. However, the SiO_2 layer is about four times thicker than the Si_xN_y layer, so that the influence of the silicon dioxide dominates. Since the SiO_2 layer is on the front of the cantilever, where the aluminium thin film heater and the tip are placed, the cantilever is bent back (Figure 4.9). The thinner is the beam, i.e. the thinner the Si layer, the bigger is the pre-bending angle, since the influence of the silicon dioxide increases. This is shown by measurements that may even be approximated by a linear function (Figure 4.10). The difference in beam thickness comes from the difference in thickness of the Si layer - the result of unequal wet etching of the silicon on the rear of the wafer which most likely starts at the edge of the wafer. Additionally, local defects in silicon accelerate etching. The backward pre-bending is supported by the aluminium thin film heater with the highest thermal expansion coefficient. The pre-bending is crucial to the application of the cantilever to imaging. It has to be aligned with the sample at a certain angle: otherwise, the body of the cantilever but not the tip, might be in contact with the sample.

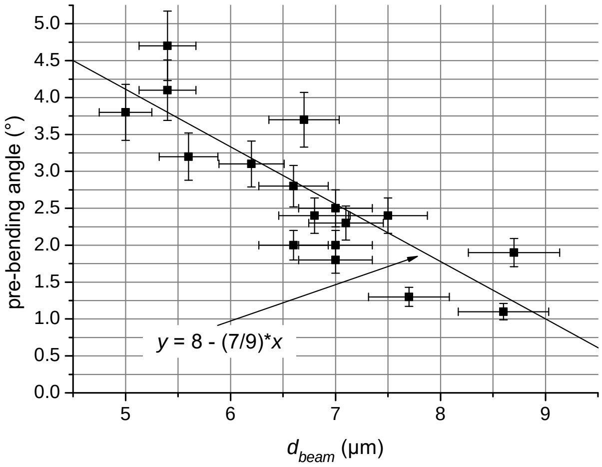

Figure 4.10: Pre-bending angle of a self-sensing and self-actuating piezoresistive microscale silicon cantilevers versus beam thickness in vacuum

4.3.2 Fundamental frequency

The fundamental or natural frequency f_1 is determined by beam dimensions. It is lower if the beam temperature increases, because beam dimensions depend on temperature (see section 2.2.1). The temperature change is caused by the AC drive power which serves the thermal actuation of the beam. In addition, the DC Wheatstone bridge power introduces heat. Air damping also reduces the fundamental frequency (see section 2.4.3). The frequency of the m^{th} resonance is directly proportional to the beam thickness d_{beam} and varies inversely with the square of the beam length L_{beam} (equation 2.122 in section 2.2.7)

$$f_m \sim \frac{d_{beam}}{L_{beam}^2}$$

This is shown by measurements. The fundamental or natural frequency f_1 and the frequency of the second resonance f_2 both increase directly proportionally to beam thickness d_{beam} (Figures 4.11(a) and 4.11(b)), i.e. to the thickness of the silicon layer (see section 4.3.1). At the same thickness a longer beam shows lower frequencies f_1 and f_2. The cantilever is softer and has a smaller spring constant k_{beam} (equation 2.158 in section 2.2.7). Correspondingly, the slope of the linear fit is steeper for longer beams than for shorter ones. The frequency of the second resonance f_2 is a multiple of the fundamental frequency f_1 with the proportionality constant of about 6.3, which is close to the value given by [80] (equation 2.123 in section 2.2.7).

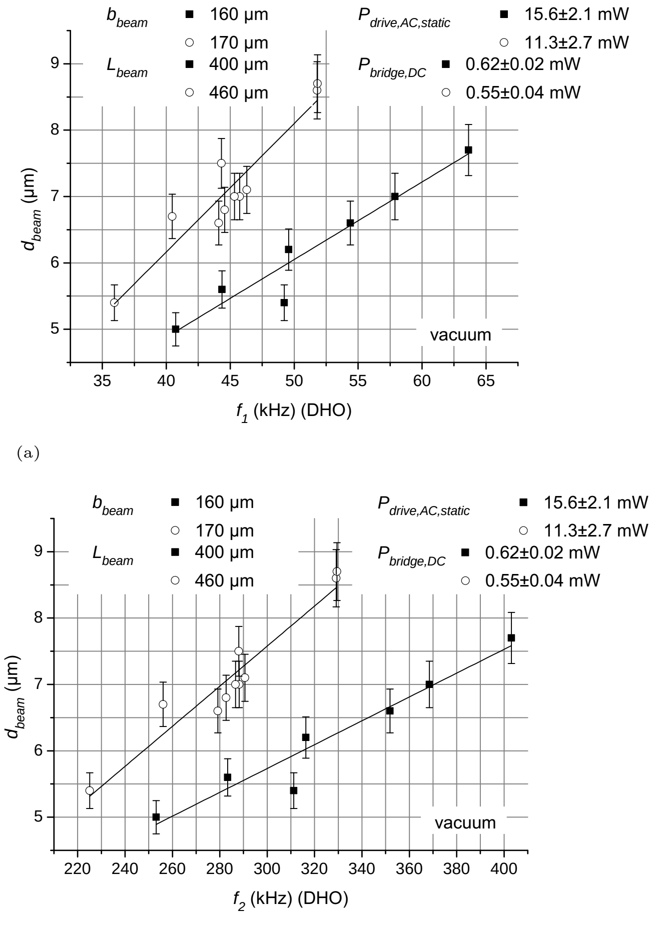

(a)

(b)

Figure 4.11: Frequencies of (a) first resonance and (b) second resonance versus beam thickness in vacuum

The estimated fundamental frequency of a multi-layered beam $f_{1,multi} = 48.1$ kHz, where $d_{beam} \approx 7.5$ µm and $L_{beam} =$ 460 µm (see example in section 2.2.7) is in good agreement with measurements made in the present study. Furthermore, the fundamental frequency f_1 decreases linearly with the static AC drive power $P_{drive,AC,static}$ (Figure 4.12). This is based on the linear temperature dependency of f_1 and the linear relationship between drive power and beam temperature (equation 2.230 in section 2.4.1). At $P_{drive,AC,static} \leq 1$ mW the change in the beam temperature is too small to affect f_1. In air the fundamental frequency is influenced by drive power and air damping. Therefore, f_1 decreases less with $P_{drive,AC,static}$, as can be seen from the slope of the linear fit.

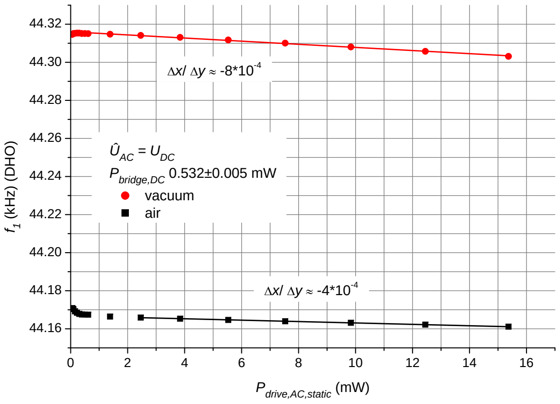

Figure 4.12: Fundamental frequency versus static AC drive power in vacuum and air

If either only the offset U_{DC} or only the amplitude $\hat{U}_{AC}$ of the AC drive voltage $U_{drive,AC}$ increases, the temperature still changes in a linear manner with $P_{drive,AC,static}$ (see example in section 2.2.4). Therefore, f_1 will be in linear dependence on $P_{drive,AC,static}$. The linear change of f_1 also reflects U_{DC}, since the temperature increases linearly with the voltage (see example in section 2.2.4) as found for similar self-actuating and self-sensing piezoresistive microscale silicon beams by Rangelow's group before [35].

Air damping reduces the fundamental frequency f_1 as expected from theory (see section 2.4.3). The fractional frequency change from vacuum to air is of the same order of magnitude as the estimated values (see example in section 2.4.3) and well below 1 % as reported in literature [109].

Sader's calculation of the fundamental frequency of a damped beam oscillator $f_{1,damped}$ (equation 2.289 in section 2.4.3) is compared with the fundamental frequency in air given by the PLLpro front-end software and the DHO theory. The comparison shows a difference of approximately 0.2 % (Figure 4.13). As already suspected, Sader's analysis does not match measurements, because the self-actuating and self-sensing piezoresistive microscale silicon cantilever has holes and a triangular free end. These allow air molecules to pass instead of damping the beam oscillation (see section 2.4.3). In good agreement are the results from the PLLpro front-end software and the DHO theory: the difference is less than 0.01 %.

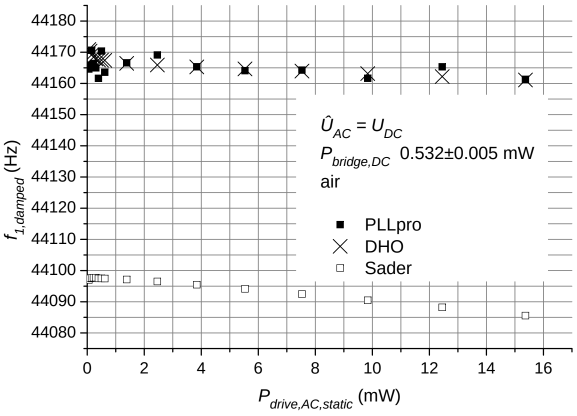

Figure 4.13: Comparison of fundamental frequency versus static AC drive power in air, given by PLLpro, DHO, and Sader

As with drive power, the fundamental frequency f_1 decreases linearly with the DC Wheatstone bridge power $P_{bridge,DC}$ (Figure 4.14). Again, this results from the linear temperature dependency of f_1 and the linear relationship between drive power and beam temperature (equation 2.234 in section 2.4.1). On the small scale of up to 0.53 mW, f_1 already decreases linearly. In contrast, the drive power is, as suspected, too small to have any effect (see section 2.4.1). The slope of the linear fit is steeper than for $P_{drive,AC,static}$. The stronger influence of $P_{bridge,DC}$ might be due to the fact that the Wheatstone bridge is placed at a crucial point, where the beam experiences maximum normal stress. At the free end of the cantilever that is warmed by the aluminium thin film heater the normal stress tends towards zero.

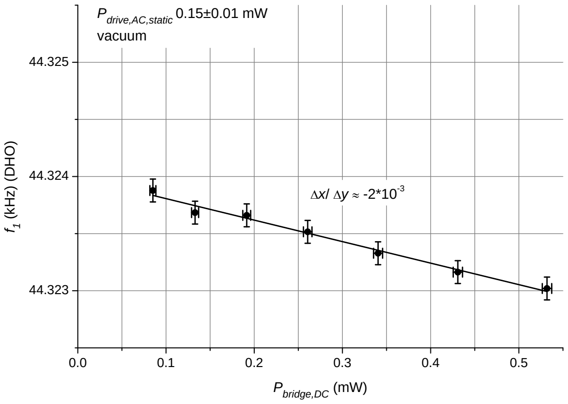

Figure 4.14: Fundamental frequency versus DC Wheatstone bridge power in vacuum

4.3.3 Quality factor

The quality factor Q depends on beam dimensions and beam temperature. The dependence beam dimensions is derived from equation 2.149 (section 2.2.7), if the fundamental or natural frequency (equation 2.122 in section 2.2.7) and the beam mass (equation 2.159 section 2.2.7) are considered. Thus, Q is directly proportional to the beam width b_{beam} and the square of the beam thickness d_{beam} and varies inversely with the beam length L_{beam}

$$Q \sim \frac{b_{beam} d_{beam}^2}{L_{beam}}$$

However, the values of Q are quite scattered within a range of around 2000 depending neither on d_{beam} nor on b_{beam} nor on L_{beam} (Figure 4.15). Q's independence on beam length is reported in literature as well as a linear dependence on beam thickness, which is found at much smaller thickness values, $d_{beam} < 1.5$ µm, indicating that energy loss is surface related [107, 110]. Referring to literature [107], the self-actuating and self-sensing piezoresistive microscale silicon cantilever is not found to be limited by TED.

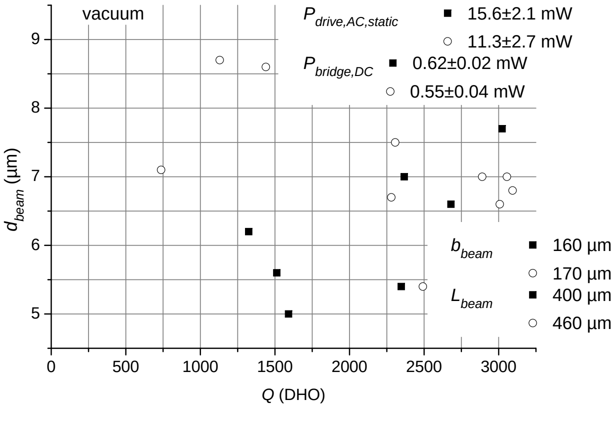

Figure 4.15: Quality factor versus beam thickness in vacuum

The comparison of resonance peaks in vacuum shows that a narrow and sharp peak is synonymous with a high quality factor (Figure 4.16) in accordance with one of the definitions of Q (equation 2.150 in section 2.2.7).

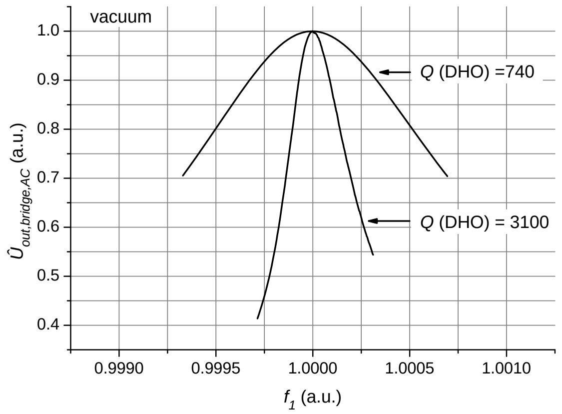

Figure 4.16: Normalized resonance peaks in vacuum

Since the quality factor Q quantifies the energy dissipation through air damping (see section 2.4.3), it is much smaller in air than in vacuum (Figures 4.17 and 4.18). In air the resonance peak is broader, smaller, and less smooth.

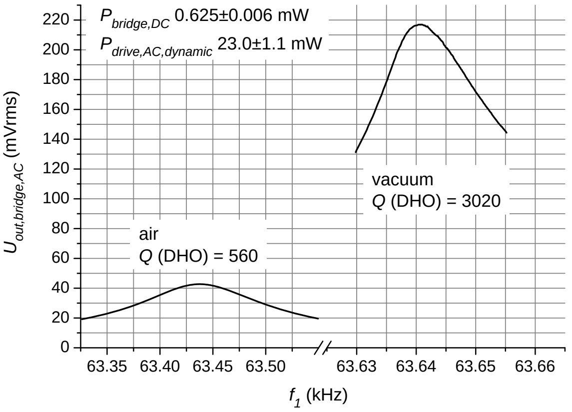

Figure 4.17: Resonance peaks in vacuum and air

The quality factor Q decreases linearly with the static AC drive power $P_{drive,AC,static}$ (Figure 4.18). This results from its linear dependency on the fundamental frequency f_1, the linear temperature dependency of f_1 and the linear relationship between drive power and beam temperature (equation 2.233 in section 2.4.1). For $P_{drive,AC,static} \leq 1$ mW the change of beam temperature is too small to be of any influence on Q. This might be the reason why the DC Wheatstone bridge power $P_{bridge,DC} \leq 0.53$ mW does not have any effect on Q (no figure presented). In air, the quality factor hardly changes with $P_{drive,AC,static}$ (Figure 4.18). Air damping predominates over any other effect.

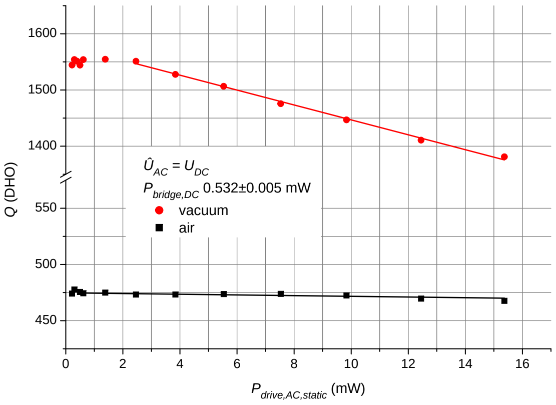

Figure 4.18: Quality factor versus static AC drive power in vacuum and air

If either only the offset U_{DC} or only the amplitude $\hat{U}_{AC}$ of the AC drive voltage $U_{drive,AC}$ increases, there will still be a linear dependence of Q on $P_{drive,AC,static}$ as is the case for the fundamental frequency (see section 4.3.2). Again, this comes from the linear relationship between Q and f_1.

4.3.4 Deflection at pure beam bending

Results (Figure 4.19) show that the DC Wheatstone bridge output voltage signal $U_{out,bridge,DC}$ increases linearly with the DC drive power $P_{drive,DC}$, because $U_{out,bridge,DC}$ is directly proportional to the deflection z_{DC} on pure beam bending (equation 2.222 in section 2.3.2) and z_{DC} is directly proportional to temperature change and drive power (equation 2.87 in section 2.2.6). As z_{DC} is a purely thermal effect and is not influenced by air damping, it is the same in vacuum and air and so is $U_{out,bridge,DC}$.

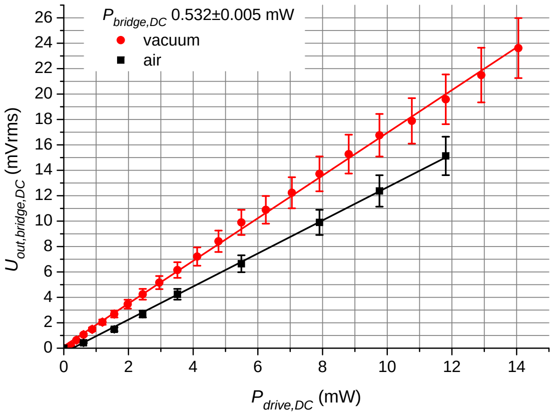

Figure 4.19: DC Wheatstone bridge output voltage versus DC drive power in vacuum and air

4.3.5 Amplitude of beam oscillation at fundamental frequency

The AC Wheatstone bridge output voltage signal $U_{out,bridge,AC}$, which is directly proportional to the maximum amplitude of beam oscillation $z_{AC,max}$ (equation 2.223 in section 2.3.2), increases in linear relation to the dynamic AC drive power $P_{drive,AC,dynamic}$ (Figure 4.20(a)), because z_{AC} is directly proportional to temperature change and drive power (equation 2.161 in section 2.2.7). Measurements show that $z_{AC,max}$ changes linearly with $P_{drive,AC,dynamic}$ (Figure 4.20(b)). Air damping reduces z_{AC} as expected from theory (see section 2.4.3) and, therefore, $U_{out,bridge,AC}$ is smaller. The linear dependency on drive power is still clear.

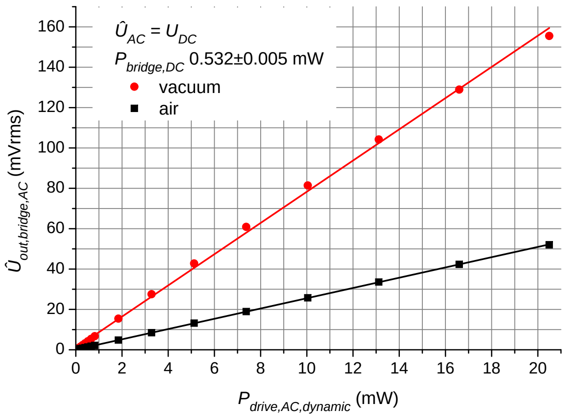

(a)

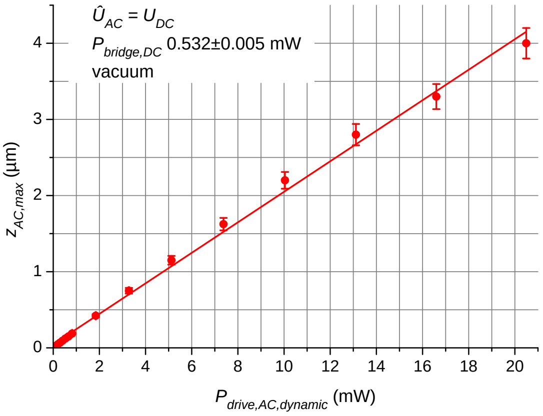

(b)

Figure 4.20: (a) AC Wheatstone bridge output voltage signal versus dynamic AC drive power in vacuum and in air; (b) maximum amplitude versus dynamic AC drive power in vacuum

If either only the offset U_{DC} or only the amplitude $\hat{U}_{AC}$ of the AC drive voltage $U_{drive,AC}$ increases, the sinusoidal temperature change causing beam oscillation is still linear with $P_{drive,AC,dynamic}$ (see example in section 2.2.4). So, $U_{out,bridge,AC}$ will linearly depend on $P_{drive,AC,dynamic}$. The linear change of $U_{out,bridge,AC}$ is replicated with U_{DC} or $\hat{U}_{AC}$, since the temperature increases linearly with the voltage (see example in section 2.2.4) as shown by measurements done elsewhere with similar self-actuating and self-sensing piezoresistive microscale silicon cantilevers from the project PRONANO [35, 128].

The DC Wheatstone bridge power $P_{bridge,DC}$ amplifies $U_{out,bridge,AC}$ (Figure 4.21) parabolically, as stated from theory (equation 2.224 in section 2.3.2). $P_{bridge,DC} \leq 0.53$ mW is too small to have any effect on $z_{AC,max}$ as already found for Q (see section 4.3.3).

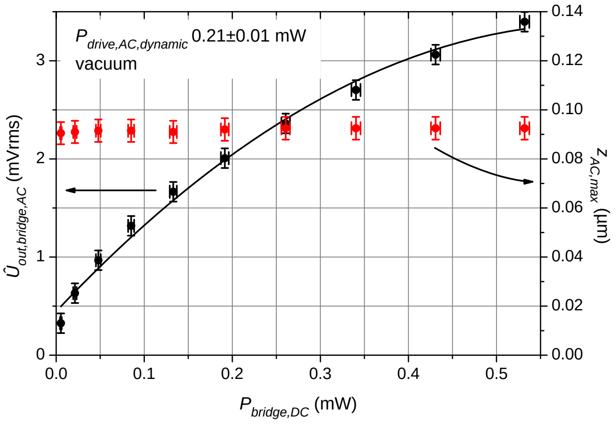

Figure 4.21: AC Wheatstone bridge output voltage signal and maximum amplitude versus DC Wheatstone bridge power in vacuum

4.3.6 Actuation efficiency

The actuation efficiency describing the maximum amplitude of beam oscillation $z_{AC,max}$ caused by the dynamic AC drive power $P_{drive,AC,dynamic}$ of 1 mW depends on beam dimensions. It is directly proportional to the cube of beam length L_{beam} and varies inversely with beam width b_{beam} and the cube of beam thickness d_{beam} (equation 2.183 in section 2.2.8)

$$actuation\ efficiency \sim \frac{L_{beam}^3}{b_{beam} d_{beam}^3}$$

So, big L_{beam} and small d_{beam} increase the actuation efficiency, which is confirmed by measurements (Figure 4.22). The beam thickness changes with the silicon layer thickness as described in section 4.3.1. In this case, the cantilever may be considered as a two-layered beam and it follows that the dependency of $z_{AC,max}$ on the thickness ratio is a bell-shaped distribution (see section 2.2.7 and [86]). Due to the direct proportionality between $z_{AC,max}$ and actuation efficiency, the curve of the actuation efficiency depending on beam thickness is also bell-shaped. The right-hand side of this curve may be seen in the graph (Figure 4.22).

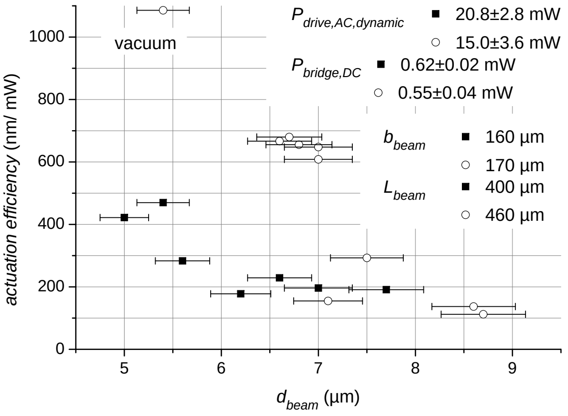

Figure 4.22: Actuation efficiency versus beam thickness in vacuum

4.3.7 Deflection sensitivity

The deflection sensitivity standing for the AC Wheatstone bridge output voltage signal $U_{out,bridge,AC}$ generated by the maximum amplitude of beam oscillation $z_{AC,max}$ of 1 nm depends on beam dimensions. It is directly proportional to the beam thickness d_{beam} and varies inversely with the square of beam length L_{beam} (equation 2.226 in section 2.3.3)

$$\textit{deflection sensitivity} \sim \frac{d_{beam}}{L_{beam}^2}$$

Results show that the deflection sensitivity increases linearly with d_{beam} (Figure 4.23), i.e. with the thickness of the silicon layer (see section 4.3.1). A shorter beam has higher deflection sensitivity, which is attributed to the inverse relation to L_{beam}. The slope of the linear fit is the same for both short and long beams. The values of deflection sensitivity are in good agreement with those for beams of similar size [11]. The deflection sensitivity of a similar self-actuating and self-sensing piezoresistive microscale silicon cantilever is by one magnitude smaller [129], because the beam is longer, which is consistent with the inverse quadratic proportionality.

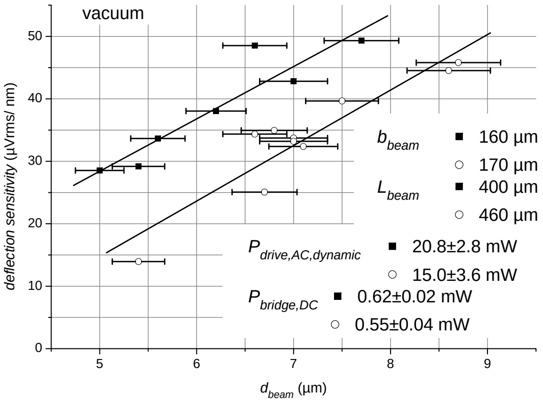

Figure 4.23: Deflection sensitivity versus beam thickness in vacuum

4.3.8 Thermal time constant

The thermal time constant $\tau_{th,beam}$ is derived from the exponential decay of the DC Wheatstone bridge output voltage signal $U_{out,bridge,DC}$ (equation 2.46 in section 2.2.5). The measured value of $\tau_{th,beam} = 2.3$ ms is in good agreement with the one estimated for a multi-layered beam (see example in section 2.2.5). $\tau_{th,beam}$ of a smaller self-actuating and self-sensing piezoresistive microscale silicon cantilever from the project PRONANO is similar [128].

Actually, the decay of $U_{out,bridge,DC}$ does not only give the thermal time constant of the beam, which is derived from the steep exponential decay (Figure 4.24). There is also a flat exponential decay standing for a thermal time constant of $\tau_{th} = 3$ s. At such a high DC drive power $P_{drive,DC} \approx 40$ mW, the cantilever chip and even the cantilever PCB have to be considered in terms of thermal equilibrium. Both of them have bigger thermal time constants due to a larger volume and, therefore, a bigger thermal resistance and heat capacity.

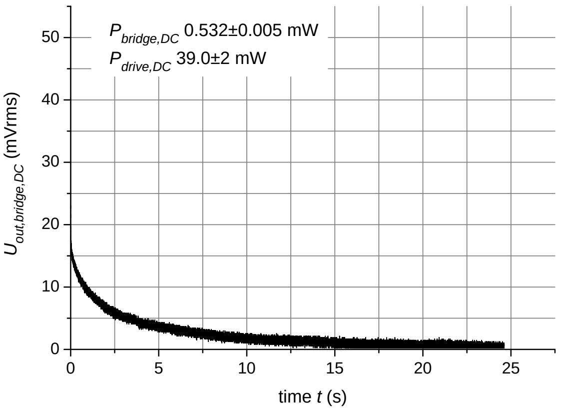

Figure 4.24: DC Wheatstone bridge output voltage signal versus time

Such a dependency on time and on drive power is also clear from the AC Wheatstone bridge output voltage signal

$U_{out,bridge,AC}$ (Figure 4.25). If the dynamic AC drive power is $P_{drive,AC,dynamic} < 0.5$ mW, the signal becomes stable within 15 min or 30 min. It may, however, even take up to 2 h or 3 h at a very high drive power of $P_{drive,AC,dynamic} \approx 20$ mW. By this time, cantilever and cantilever chip will long have been in thermal equilibrium regarding the calculated values of $\tau_{th,beam}$ and $\tau_{th,chip}$ (see example in section 2.2.5). So much heat is provided that the cantilever chip no longer works as a heat sink. It warms up and heat is transferred by conduction to the cantilever PCB, which is a bigger heat sink. Even though the cantilever chip is glued onto the cantilever PCB with conductive epoxy, the fact that the establishment of thermal equilibrium takes so much time shows that heat transfer is not as good as necessary. The direct connection by a simple wire between cantilever chip and external aluminium cylinder, which is an even larger heat sink, is probably not appropriate to good heat conduction.

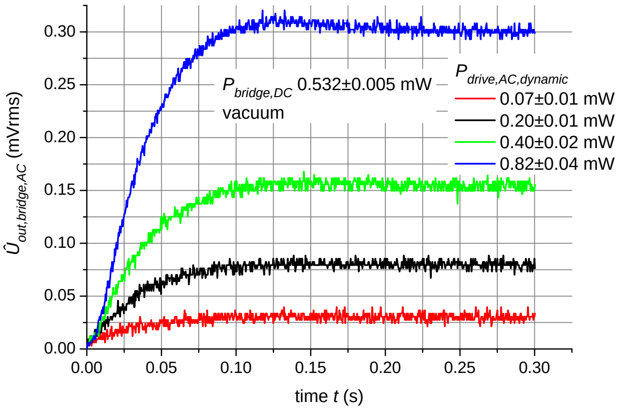

Figure 4.25: AC Wheatstone bridge output voltage signal versus time

At higher dynamic AC drive power $P_{drive,AC,dynamic} > 0.5$ mW, $U_{out,bridge,AC}$ first rises too high and afterwards decreases to come into steady state (Figure 4.25). This is caused by an increase of the heater resistance R_{heater}. The aluminium thin film heater is a linear resistor, whose resistance changes if its temperature changes [64]

$$R_{heater} = R_{heater,0}\left[1 + \alpha_{R_{heater}}\Delta T\right] \tag{4.1}$$

where $R_{heater,0}$ is the heater resistance at room temperature, $\alpha_{R_{heater}}$ the temperature coefficient of the heater resistance, and ΔT the temperature change. The temperature increases if AC drive voltage $U_{drive,AC}$ is supplied and the resistor warms up through Joule heating [64] (see section 2.2.2). Consequently, the AC drive power that generates beam oscillation is reduced (equation 2.10 in section 2.2.2), so that the maximum amplitude of beam oscillation $z_{AC,max}$ and $U_{out,bridge,AC}$ because of direct proportionality (equation 2.223 in section 2.3.2) decrease until thermal equilibrium is reached. The dependency on time and drive power may also be derived from the fundamental frequency f_1 (Figure 4.26). Even if the static AC drive power is only $P_{drive,AC,static} \approx 0.15$ mW, it takes the cantilever at least 1 h to reach thermal equilibrium. If the cantilever has been oscillating at f_1 for 12 h, it is definitely in steady state. In air, damping dominates and any other effect is lost in noise.

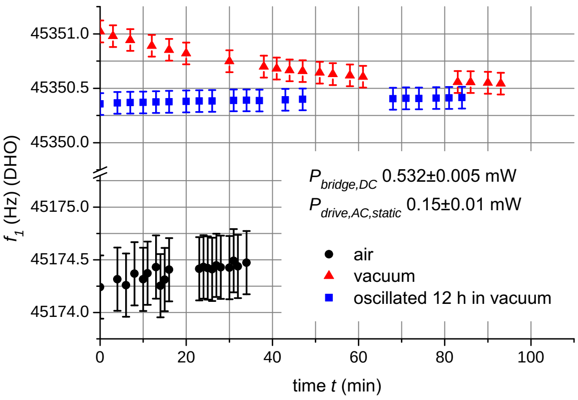

Figure 4.26: Fundamental frequency versus time

This time-dependent behaviour is crucial to any application. The self-actuating and self-sensing piezoresistive microscale silicon cantilever has to oscillate for a certain time - depending on drive power - to come into steady state before any measurement may be done: otherwise, results will be distorted. To reduce the time for establishing thermal equilibrium, the heat should be transferred away from the cantilever fast and continuously, which is being continuously supplied with heat. Large heat sinks have to be thermally well connected to the cantilever.

4.3.9 Pressure dependency of cantilever performance

Air damping causes energy loss that is quantified by the quality factor Q. If the pressure p changes from vacuum to air, air damping increases and, hence, Q decreases. Additionally, the maximum amplitude of beam oscillation $z_{AC,max}$, and the AC Wheatstone bridge output voltage signal $U_{out,bridge,AC}$ because of direct proportionality (equation 2.223 in section 2.3.2), and the fundamental frequency f_1 are reduced (see section 2.4.3). The pressure dependency of Q, $U_{out,bridge,AC}$, and f_1 over a range of 100,000 Pa at different drive power is shown in Figures 4.27, 4.28, and 4.29, respectively.

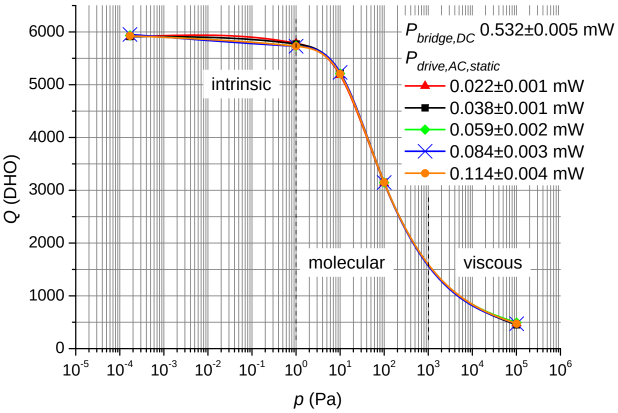

Figure 4.27: Quality factor versus pressure

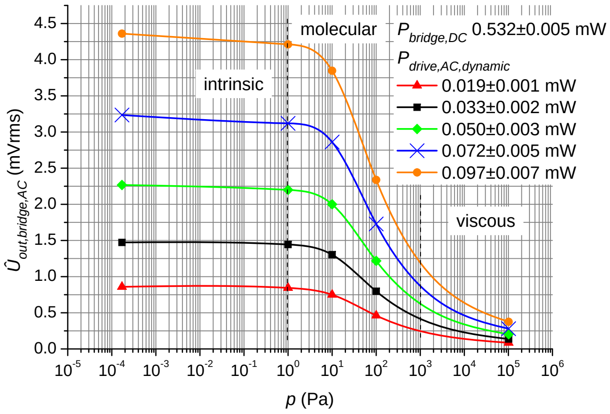

Figure 4.28: AC Wheatstone bridge output voltage signal versus pressure

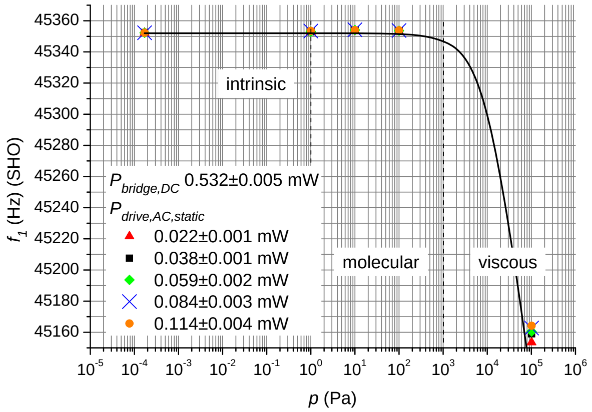

Figure 4.29: Fundamental frequency versus pressure

The variation in the quality factor Q in relation to the pressure ranging from vacuum to air is divided into three regions, given the names intrinsic, molecular, and viscous (see section 2.4.3). These regions are also found with the maximum amplitude z_{AC} ($U_{out,bridge,AC}$) because of the direct proportionality between Q and z_{AC} (equation 2.154 in section 2.2.7). The same variation in Q related to pressure is also reported in literature [120].

1. Intrinsic region: $p < 1$ Pa. Neither Q nor $U_{out,bridge,AC}$ nor f_1 change, i.e. they do not depend on pressure.
2. Molecular region: 1 Pa $< p <$ 1,000 Pa. Here, the air pressure is found to be in the same range as for measurements done elsewhere with the self-actuating and self-sensing piezoresistive microscale silicon cantilevers that were fabricated within the research work for this PhD thesis [105]. Q and $U_{out,bridge,AC}$ drop significantly. In the case of Q, this is in agreement with literature [107]. The molecular region is also reported elsewhere to be in the same pressure range for beams of similar size and fundamental frequency [120]. In addition, it is said to be in a similar range of 10 Pa to 1,000 Pa in general [121].
3. Viscous region: $p >$ 1,000 Pa. Q and $U_{out,bridge,AC}$ are slowly reduced.

The fundamental frequency changes linearly with air pressure as proposed by theory (equation 2.286 in section 2.4.3). The linear fit is calculated from the data of the one-layered beam given in the example in section 2.4.3. The significant drop at $p >$ 10,000 Pa on the logarithmic scale is in good agreement with results from measurements done elsewhere with the self-actuating and self-sensing piezoresistive microscale silicon cantilevers fabricated within this PhD thesis research work [105]. The same variation in f_1 related to pressure is also reported in literature [120]. Over a range of about 100,000 Pa, f_1 changes by 0.5 %. The fractional frequency change is $\sim 4 \cdot 10^{-3}$. This is in good agreement with the values calculated from an one-layered beam (see example in section 2.4.3) and with literature [109], where the frequency shift is reported to be smaller than 1 %. It is hard to tell exactly where the transition from the molecular to the viscous region takes place because of missing measurements in the region from 100 Pa to 10,000 Pa. One may only refer to the example in section 2.4.3, where the transition pressure is estimated to be at $p_{transition} = 800$ Pa.

4.3.10 Noise

The performance of the self-actuating and self-sensing piezoresistive mircoscale cantilever is limited by different sources of noise (see section 2.4.2). At low frequencies Hooge noise is dominant (Figure 4.30). In air, there is a step due to air damping (Figure 4.30(b)). Johnson noise dominates at high frequencies. Hooge noise and Johnson noise are one order of magnitude larger than calculations that assume an ideal piezoresistive Wheatstone bridge and than values given in literature (see example in section 2.4.2 and [102]). It is possible that the real piezoresistors are thicker and then do have a lower doping concentration, both of which would increase noise (see section 2.4.2.2). In addition, the wiring of the experimental set-up and the supply and data acquisition electronics may add noise.

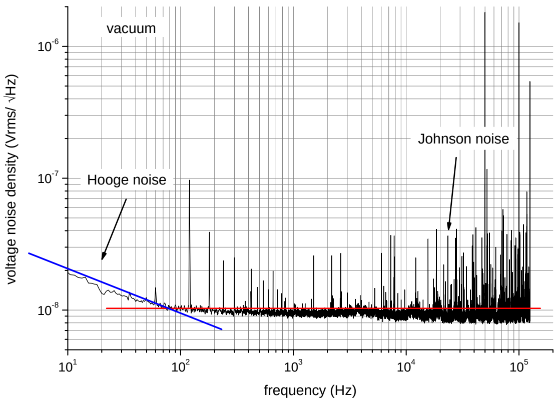

(a)

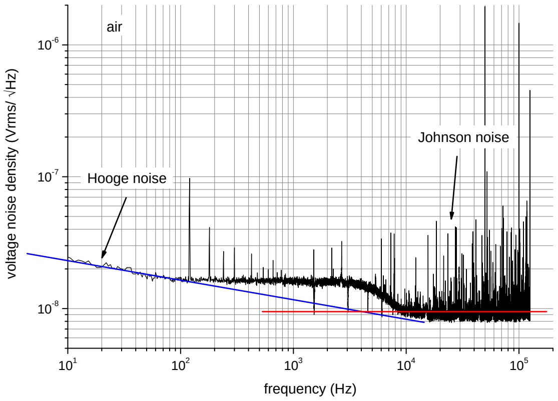

(b)

Figure 4.30: Noise spectra showing Hooge noise and Johnson noise: (a) vacuum and (b) air

4.3.11 Capacitive crosstalk

Another factor which limited the performance of the self-actuating and self-sensing microscale silicon cantilever is capacitive crosstalk, which will do so in all such cases and is derived from the frequency response (Figure 4.31). First, there is the cut-off frequency $f_{cut-off}$. This is the boundary in the frequency response at which the AC Wheatstone bridge output voltage signal $U_{out,bridge,AC}$ falls to $\sqrt{\frac{1}{2}}$ of its original value. $f_{cut-off} \approx 70$ Hz is in good agreement with the value derived from the measured thermal time constant of the beam $\tau_{th,beam}$ (see section 4.3.8). It is also close to the estimated cut-off frequency of a multi-layered beam (see example in section 2.2.5). At some point in the higher frequencies, $f \approx 4$ kHz, $U_{out,bridge,AC}$ increases. The reason for this is capacitive crosstalk. In the present case, with the Wheatstone bridge supplied by a positive voltage and the silicon substrate grounded, piezoresistors and substrate formed p-n junctions which were accidentally forward biased causing capacitive coupling (see section 2.4.4). The frequency response is consistent to the one measured elsewhere with similar self-actuating and self-sensing piezoresistive microscale silicon cantilevers from the project PRONANO [71]. Capacitive crosstalk had been reported for a similar self-actuating and self-sensing piezoresistive microscale silicon cantilever from the project PRONANO [128].

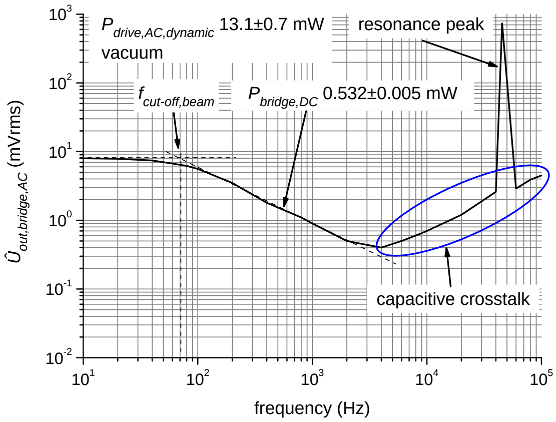

Figure 4.31: Frequency response from 10 Hz to 100 kHz

4.3.12 Summary

This study of the performance of the self-actuating and self-sensing piezoresistive microscale silicon cantilever has provided new results and confirms statements made from theory:

- The beam pre-bending results from stress within the material layers caused by fabrication; it decreases linearly with the thickness of the silicon layer.
- Fundamental frequency f_1 and quality factor Q increases in direct ratio to the static AC drive power, whether there is a change in only the offset, only the amplitude, or in both of them.
- The maximum amplitude of beam oscillation $z_{AC,max}$ increases in a linear manner with the dynamic AC drive power, whether there is a change in only the offset, only the amplitude, or in both of them.
- The deflection on pure beam bending z_{DC} increases linearly with DC drive power.
- The temperature change in the beam produced by Wheatstone bridge DC power has a stronger linear influence on f_1 than does the static AC drive power, because the bridge is placed at a crucial point where there is maximum stress. However, the temperature change is too small to have any effect on Q. The Wheatstone bridge DC power amplifies the Wheatstone bridge output voltage signal parabolically.
- f_1 increases linearly with beam thickness but also depends on beam length.
- Q does not depend on beam dimensions on this diminutive scale.
- The actuation efficiency depending on the beam thickness as a ratio of the silicon layer to the constant thickness of all other layers is a bell-shaped curve.
- The deflection sensitivity increases linearly with the thickness of the silicon layer.
- The time taken to reach thermal equilibrium depends on time and on drive power, i.e. the cantilever has to oscillate for a certain time to reach steady state. The time is reduced if a large heat sink is thermally well connected to the cantilever.
- The variation in Q and in $z_{AC,max}$ in relation to air pressure clearly falls into three regions, intrinsic, molecular and viscous, whereas f_1 decays linearly with air pressure. The estimation of the frequency shift from vacuum to air of less than 1 % is consistent with measurements and literature, whereas Sader's approach to the fundamental frequency of the damped beam oscillator fails to match up.
- Hooge noise is found to be dominant at low frequencies and Johnson noise at high frequencies. Their values are one order of magnitude larger than that for different piezoresistive self-sensing cantilevers reported in literature.
- Capacitive crosstalk occurs at high frequencies.

4.4 AFM imaging

4.4.1 Tip forming

For high resolution AFM imaging, sharp tips are necessary. The cone-shaped tips of the self-actuating and self-sensing piezoresistive microscale silicon cantilever turned out to be somewhat blunt due to the fabrication process and the fact that tips were fabricated at the very beginning of the cantilever-making process with numerous steps to follow. It would be appropriate to change the sequence of fabrication steps, releasing the tip at the very end of the fabrication process. That has meanwhile been successfully done by Rangelow's group [74]. FIB and electron beam deposition was applied to the tip to make it sharp.

In the work for this PhD thesis, the tip forming turned out to be difficult because the cantilever drifted during processing. The drift was caused by the charging associated with a non-conductive silicon nitride layer with which the beam was covered. The gold layer on top of the tip which was supposed to make the tip conductive was of poor quality, i.e. pitted, accidentally in contact with ground lines, or even broken. The last two cases happened when the really thin but relatively high photoresist walls collapsed before gold PVD (see chapter 3). Electron beam lithography instead of UV lithography might be preferable for gold coating fabrication. Repairing the gold layer through deposition would have been too time-consuming because of the length of up to 350 µm. Because of the poor quality of the gold layer, it was impossible to ground the tip to prevent charging. Gold coating across the whole cantilever did not help. Even though, coating was repeated several times there was still drift. Since it was not possible to apply any voltage the tip, there was no possibility of testing whether the equipment was capable of STM.

4.4.1.1 Tip sharpening by FIB

Tip sharpening by FIB is, effectively, the trimming of pieces from the tip until it is sharp. Despite the drift caused by the charging, tip sharpening was done successfully, as pictures of the tip before and after treatment show (Figure 4.32). The diameter of the tip was reduced from about 0.4 µm to 0.1 µm.

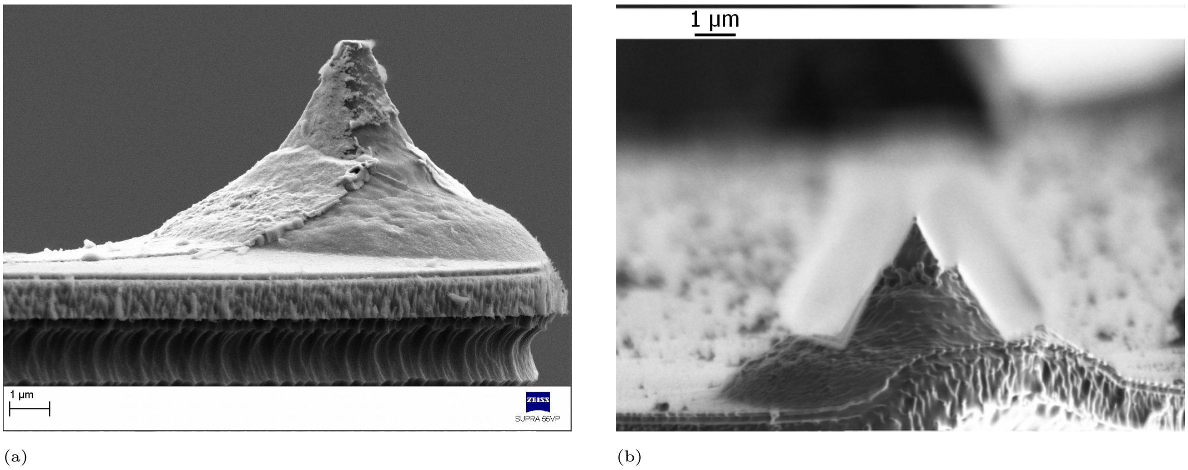

(a) (b)

Figure 4.32: Tip sharpening by FIB: (a) before with diameter of 0.4 µm and (b) after with 0.1 µm (SEM images)

4.4.1.2 Tip growing by electron beam deposition

It had been assumed that electron beam deposition would grow a sharp tip onto the old tip. However, huge drift caused by the charging made this impossible. Growth of the coating occurred randomly on the old tip or the beam surface (Figure 4.33).

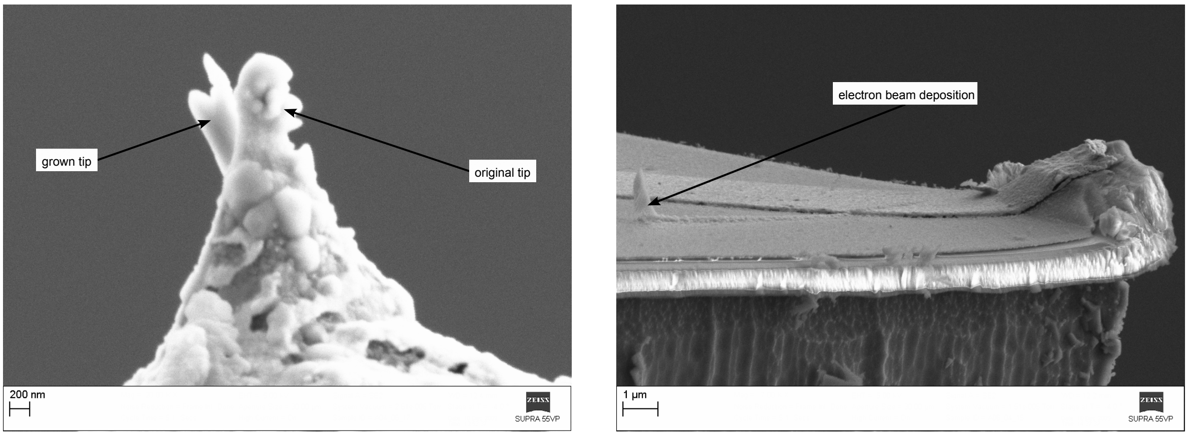

(a) (b)

Figure 4.33: Electron beam deposition: (a) next to the original tip and (b) on the beam surface (SEM images)

4.4.2 FM-AFM imaging in vacuum

The advantage of doing AFM in vacuum is that there is no air damping to affect the performance of the self-actuating and self-sensing piezoresistive microscale silicon cantilever negatively by reducing the quality factor Q, the maximum amplitude $z_{AC,max}$, and the fundamental frequency f_1 (see section 2.4.3). Consequently, the deflection sensitivity is higher, resulting in better quality of AFM images (see section 2.3.3). In addition, a cantilever with high f_1 is more sensitive (see section 2.3.3). The parameters of cantilever and sample are given in Table 4.4.

Parameter	Unit	Value
Fundamental frequency f_1	kHz	63.6
Sample		Calibration grid (Nanosurf AG, Switzerland), posts: 150 nm high, 650 nm x-y periodicity (Figure 4.34(a))
Air pressure p_{air}	mPa	0.1
Scan speed	$\frac{\mu\text{m}}{\text{s}}$	2.00
Scan area	μm^2	2.00 x 2.00
	points	512 x 512

Table 4.4: Cantilever, sample, and imaging parameters

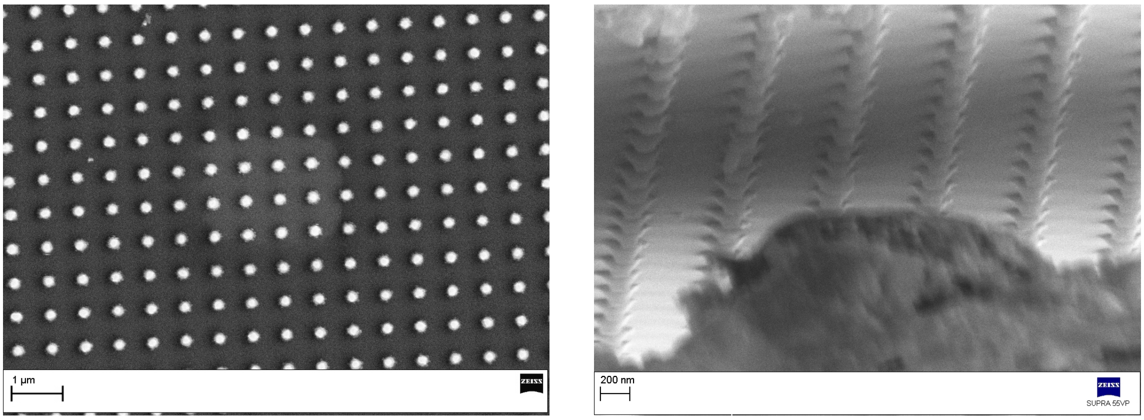

(a) (b)

Figure 4.34: (a) calibration grid and (b) oscillating cantilever above sample (SEM images)

Taking into account the fact that the tip was not absolutely sharp, having a diameter of about 800 nm (Figure 4.34(b)), the quality of the images is reasonable. Since the tip was bigger than the distance between the sample posts, each post had been imaged twice resulting in so-called double-tip features (Figures 4.35 and 4.36). It was not exactly the same area that had been scanned back and forth, a fact due to the hysteresis in the motion of the shear stack which moved the sample forwards and backwards.

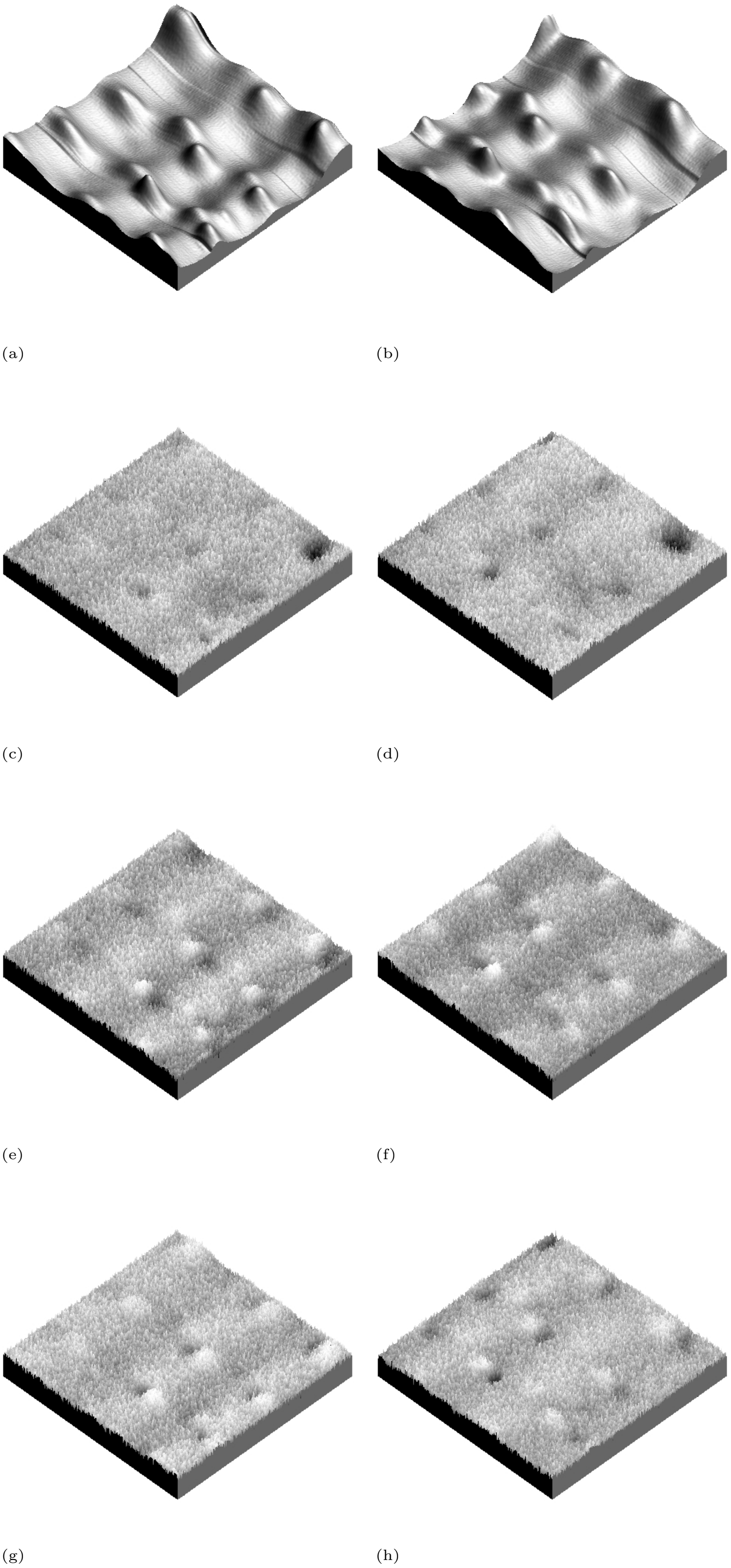

(a) (b)

(c) (d)

(e) (f)

(g) (h)

Figure 4.35: Topography of calibration grid: (a) forward + (b) backward;
$\Delta U_{out,bridge,AC}$ = 89 mVrms: (c) forward + (d) backward;
Δf_1 = 500 mHz: (e) forward + (f) backward;
$\Delta\varphi$ = -5.5 degree: (g) forward + (h) backward

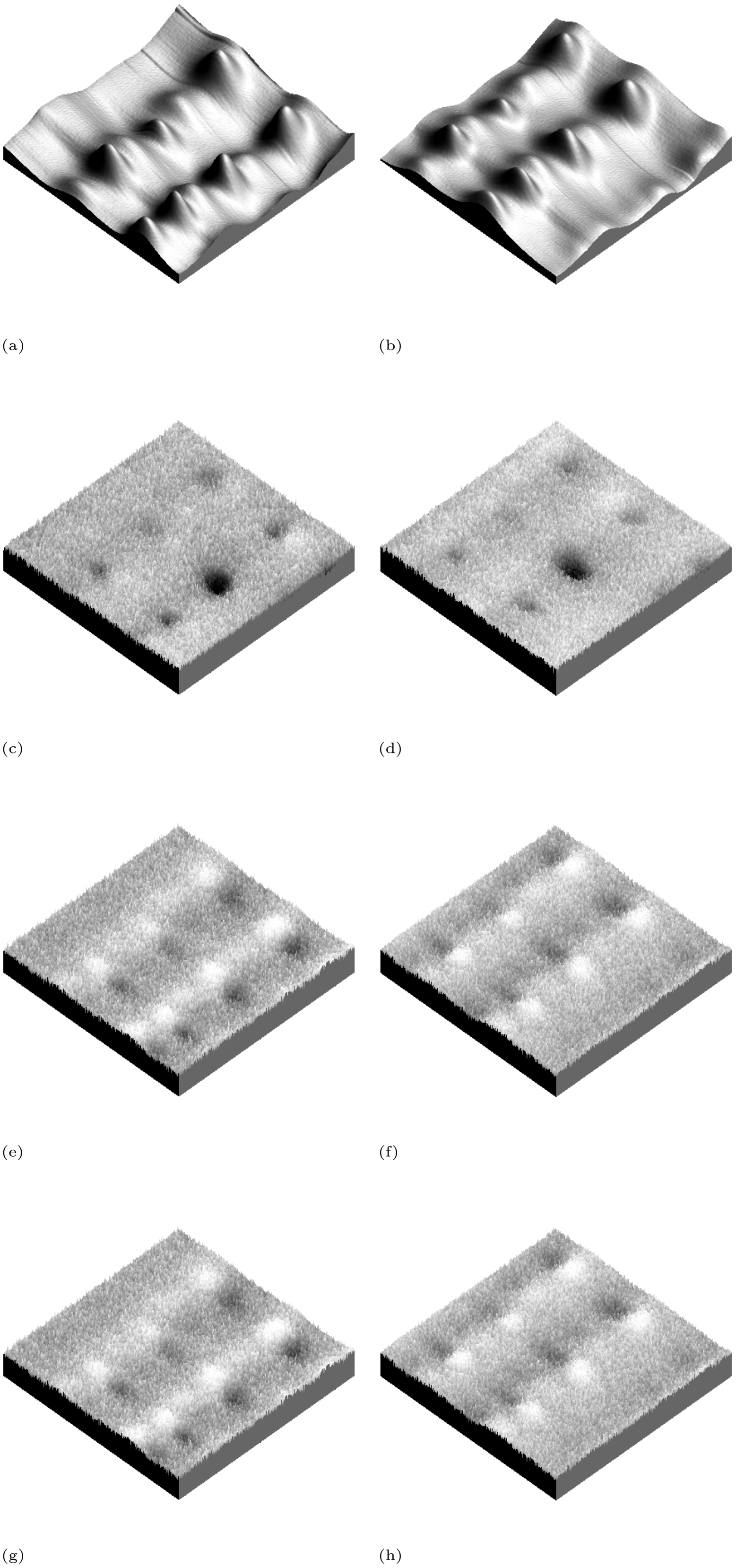
(a) (b) (c) (d) (e) (f) (g) (h)

Figure 4.36: Topography of calibration grid: (a) forward + (b) backward;
$\Delta U_{out,bridge,AC}$ = 90 mVrms: (c) forward + (d) backward;
Δf_1 = 136 mHz: (e) forward + (f) backward;
$\Delta\varphi$ = -2.1 degree: (g) forward + (h) backward

FM-AFM imaging done elsewhere with a similar self-actuating and self-sensting piezoresistive microscale silicon cantilever from the project PRONANO resulted in much higher image quality (Figures 4.37 and 4.38), because the tip was very sharp [130]. Compared to the SEM image, the AFM gives a three-dimensional image, i.e the topography, of the sample surface, making the difference between a “hill” or a “valley” clear. SEM provides only a two-dimensional image, with the contrast shown being due not only to varying height but also to varying material. The parameters of cantilever and sample in this reference are listed in Table 4.5.

Parameter	Unit	Value
Fundamental frequency f_1	Hz	59,047
Spring constant k_{beam}	$\frac{\mathrm{N}}{\mathrm{m}}$	9.2
Sample		Flame-annealed evaporated gold film on mica
Air pressure p_{air}	mPa	Vacuum
Scan speed	$\frac{\mathrm{\mu m}}{\mathrm{s}}$	2.50
Scan area	$\mathrm{\mu m}^2$	2.50 x 2.50
	points	256 x 256

Table 4.5: Cantilever, sample, and imaging parameters [130]

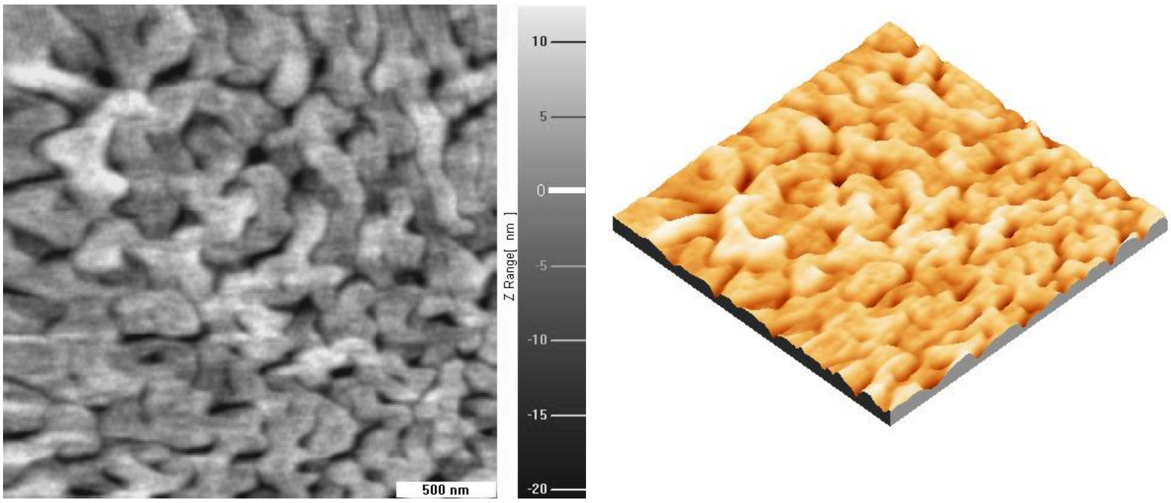

(a) (b)

Figure 4.37: Topography of flame-annealed evaporated gold film on mica [130]

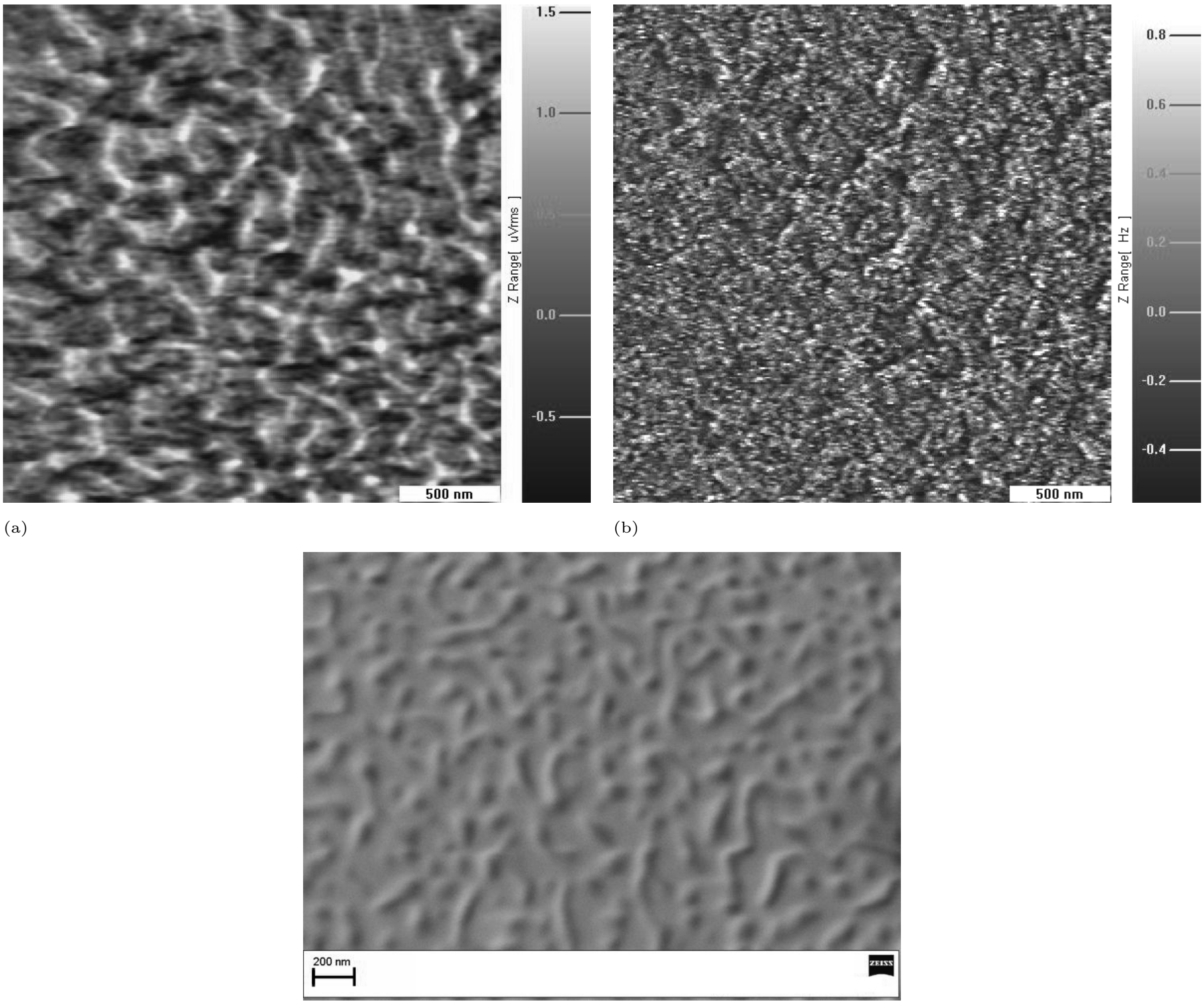

(a)

(b)

(c)

Figure 4.38: (a) $\Delta U_{out,bridge,AC}$; (b) $\Delta f_1 = 1$ Hz (all forward); (c) SEM image [130]

It must be noted that simultaneous AFM and SEM proved impossible. SEM induced charging due to the non-conductive beam surface and also induced heating, both of which caused the cantilever to bend even more, with the result that the tip either lost contact or touched the sample surface. The PLL mode could not compensate for this behaviour.

5 Conclusion

For the first time, the combination of SPM and SEM within one system using a self-actuating and self-sensing piezoresistive microscale silicon cantilever has been successfully demonstrated. The combined system is capable of delivering high resolution AFM and SEM images. The advantage is that AFM gives the topography of the specimen surface, whereas the SEM image is only two-dimensional and it is not necessarily clear where there is a “hill” or a “valley”. Depending on the way the tip is prepared, several AFM methods including measurement of mechanical, electrical, and magnetic properties are possible, so that a vast amount of information may be provided concerning the specimen. If the tip is conductive, STM may carried out. Here, the sample surface is not only characterized but also manipulated. Furthermore, if the vacuum has been turned off, the SPM-SEM system may be run in air for the study of living organisms in liquid. Since everything is done in the same system and a change of instruments is not necessary, the location of the area of interest on the specimen surface is not lost. These aspects are highly relevant for commercial applications and have been, to a certain extent, forced by industry. One drawback is that although there is no need to change instruments, AFM and SEM cannot be carried out at one and the same time because of the charging.

The integration of actuation and sensing into the cantilever not only reduces the size of the AFM and makes a laser system for beam deflection detection redundant, it also offers an easy-to-use system, because there is no need for laser beam alignment. The cantilever is simply put into its holder and connected to the supply and data acquisition electronics before it is brought close to the surface of the specimen for the imaging. SEM can be used to monitor the approximate positioning of the beam. The AFM set-up is, in fact, installed on a separate platform, so that, if necessary, it may be easily taken out of the SEM.

This PhD thesis presents the first extensive characterization of the performance of the self-actuating and self-sensing piezoresistive microscale silicon cantilever. The performance is influenced by parasitic heating resulting from the thermal beam actuation, by air damping, by noise, and by crosstalk. The thermal beam actuation not only causes beam oscillation but also, as an undesired side effect, changes the fundamental frequency and the quality factor. The linear temperature and drive power dependency that is derived from theory has been demonstrated here by measurements. It has been shown for the fundamental frequency, the quality factor, the deflection on pure beam bending, and the maximum amplitude of beam oscillation. The Wheatstone bridge also introduces a temperature change to the beam, exerting a stronger influence on the fundamental frequency than does the drive power, because the bridge is placed at a crucial point where there is maximum stress. Before being put to its ultimate use, the cantilever has to oscillate for a certain time to come into thermal equilibrium. The time is reduced if a large heat sink is thermally well connected to the cantilever. The actuation efficiency depends on the beam thickness as a ratio of the silicon layer to the constant thickness of all other layers. It is a bell-shaped curve. Besides noise and capacitive crosstalk, air pressure limits the beam performance. The variation in quality factor and in maximum amplitude of beam oscillation in relation to air pressure clearly falls into three regions, intrinsic, molecular and viscous, whereas the fundamental frequency decays linearly with air pressure. It would be appropiate for the investigations to be extended by the determination of the spring constant and the force sensitivity. STM could be tested with newly fabricated self-actuating and self-sensing piezoresistive microscale silicon cantilevers possessing sharp and conductive tips.

The results of this PhD thesis research work, done within the project PRONANO (Technology for the production of massively parallel intelligent cantilever probe platforms for nanoscale analysis and synthesis, IP 515739-2 PRONANO), are promising for the analysis of devices in the course of fabrication processes in semiconductor industry. A completely new SPM-SEM system with a self-actuating and self-sensing piezoresistive microscale silicon cantilever is presented here which is capable of high resolution imaging, characterization, and manipulation in different SPM modes.

6 Acknowledgements

supervisor: Univ.-Prof. Dr.-Ing. habil. Ivo W. Rangelow (Department of Microelectronic and Nanoelectronic Systems, Faculty of Electrical Engineering and Information Technology, Ilmenau University of Technology, Ilmenau, Thüringen, Germany)

fabrication process:

- Dr Tzvetan Ivanov, Dr Yanko Sarov, Katerina Ivanova, and prof Rangelow group (Department of Microelectronic and Nanoelectronic Systems, Faculty of Electrical Engineering and Information Technology, Ilmenau University of Technology, Ilmenau, Thüringen, Germany)
- mask fabrication: Dr. Ivan Kostič (Department of Electron Beam Lithography, Institute of Informatics, Slovak Academy of Sciences, Bratislava, Slovak Republic)
- ion implantation: Dr Bernd Schmidt, Dr Michael Zier, Claudia Neisser (Division of Process Technology, Institute of Ion Beam Physics and Materials Research, Helmholtz-Zentrum Dresden-Rossendorf, Dresden, Sachsen, Germany)
- bonding: Gernot Bischoff (Department of Microelectronic and Nanoelectronic Systems, Faculty of Electrical Engineering and Information Technology, Ilmenau University of Technology, Ilmenau, Thüringen, Germany)

characterization and imaging (Ernest Orlando Lawrence Berkeley National Laboratory, Berkeley, California, USA):

- supervisor: Dr D. Frank Ogletree (Imaging and Manipulation of Nanostructures Facility, The Molecular Foundry)
- fast and high quality technical support: Ed Wong (Imaging and Manipulation of Nanostructures Facility, The Molecular Foundry)
- electron beam deposition: Dr Alexander Weber-Bargioni (Imaging and Manipulation of Nanostructures Facility, The Molecular Foundry)
- FIB: Dr Stefano Cabrini (Nanofabrication Facility, The Molecular Foundry)
- scientific staff of Imaging and Manipulation of Nanostructures Facility (The Molecular Foundry)
- scientific staff of Nanofabrication Facility (The Molecular Foundry)
- prof Miquel Salmeron group (Materials Sciences Division)

discussion of results: Dr Jens-Peter Zöllner (Department of Microelectronic and Nanoelectronic Systems, Faculty of Electrical Engineering and Information Technology, Ilmenau University of Technology, Ilmenau, Thüringen, Germany)

This work was funded by the European Commission within the 6^{th} framework programme (IP 515739-2 PRONANO)
The stay in Berkeley (California, USA) to do the research work at the Imaging and Manipulation of Nanostructures Facility (The Molecular Foundry, Ernest Orlando Lawrence Berkeley National Laboratory) was supported by the German Academic Exchange Service through a four and half-monthly scholarship DAAD D/08/45982.
The completion of the PhD thesis was supported by the Gleichstellungsrat (Ilmenau University of Technology, Ilmenau, Thüringen, Germany) through a three-monthly scholarship.

Thanks to my German family and to my American family - whom I stayed with in Berkeley for about nine and a half months - for being who they are and their support.

7 Publications

1. C. Bitterlich, K. Ivanova, T. Ivanov, Ute Wenzel, B. E. Volland, Y. Sarov, E. Guliyev, S. Klett, J.-P. Zöllner, A. Frank, I. W. Rangelow, and B. Ding. Non-contact AFM with self-actuated piezoresistive cantilever. In: *MacroNano Biannual Report 2007/ 2008*, page 106. Ilmenau University of Technology, 2009.
2. Ute Wenzel, T. Ivanov, K. Ivanova, Y. Sarov, D. Filenko, B. E. Volland, C. Bitterlich, I. W. Rangelow, Z. Kazantseva, and K. V. I. Kalchenko. Maskless SPP Nanolithography. In: *MacroNano Biannual Report 2007/ 2008*, page 114. Ilmenau University of Technology, 2009.
3. K. Ivanova, Y. Sarov, Tzv. Ivanov, A. Frank, J. Zöllner, Ch. Bitterlich, Ute Wenzel, B. E. Volland, S. Klett, I. W. Rangelow, P. Zawierucha, M. Zielony, T. Gotszalk, D. Dontzov, W. Schott, N. Nikolov, M. Zier, B. Schmidt, Wolfgang Engl, T. Sulzbach, and I. Kostic. Scanning proximal probes for parallel imaging and lithography. In: *Papers from the 52nd International Conference On Electron, Ion, and Photon Beam Technology and Nanofabrication*, volume 26, pages 2367–2373. AVS, 2008.
4. C. Bitterlich, Ute Wenzel, K. Ivanova, T. Ivanov, B. E. Volland, Y. Sarov, E. Guliyev, S. Klett, J.-P. Zöllner, A. Frank, and I. W. Rangelow. Sub-nanometer resoluton non-contact AFM with self-actuated piezoresistive cantilever in room ambient conditions. In: *Book of Abstracts, The Second Saint-Petersburg International Conference on NanoBioTechnologies "NanoBio' 08" 16 - 18 June 2008*, page 188. Saint-Petersburg Publishing House of Polytechnical University, 2008.
5. C. Bitterlich, T. Ivanov, Y. Sarov, V. Sarova, J.-P. Zöllner, Ute Wenzel, I. W. Rangelow, M. Höche, and W. Hummel. Self-actuated micro-cantilever array with piezoresistive readout for multi-parameter recognition. In: *Sensoren und Messsysteme 2010, Vorträge der 15. ITG/GMA-Fachtagung vom 18. bis 19. Mai in Nürnberg*, paper 53. VDE Verlag-GmbH, 2010. ISBN 978-3-8007-3260-9.
6. Ute Wenzel, T. Ivanov, I. W. Rangelow, and D. F. Ogletree. Integration of self-actuating piezoresistive cantilever based AFM in SEM. In: *MacroNano Biannual Report 2009/ 2010*, page 163. Ilmenau University of Technology, 2011.
7. Y. Sarov, T. Ivanov, A. Frank, V. Sarova, Ute Wenzel, J.-P. Zöllner, I. W. Rangelow, N. Nikolov, P. Zawierucha, M. Woszczyna, and T. Gotszalk. Fabrication of parallel cantilever systems with sharp AFM tips for surface scanning and analysis. In: *Proceedings of the Integrated Project on Massively Parallel Intelligent Cantilever Probe Platforms for Nanoscale Analysis and Synthesis*, pages 163 - 168. Verlagshaus Monsenstein und Vannerdat OHG Muenster, 2010, ISBN 978-3-86991-177-9.
8. Ute Wenzel, T. Ivanov, I. W. Rangelow, and D. F. Ogletree. Integration of self-actuating piezoresistive cantilever based AFM in SEM. In: *Proceedings of the Integrated Project on Massively Parallel Intelligent Cantilever Probe Platforms for Nanoscale Analysis and Synthesis*, pages 295 - 297. Verlagshaus Monsenstein und Vannerdat OHG Muenster, 2010, ISBN 978-3-86991-177-9.

8 Abstract

8.1 English abstract

For the first time, the combination of SPM and SEM within one system using a self-actuating and self-sensing piezoresistive microscale silicon cantilever has been successfully demonstrated. The combined system is capable of delivering high resolution AFM and SEM images. The advantage is that AFM gives the topography of the specimen surface, whereas the SEM image is only two-dimensional and it is not necessarily clear where there is a “hill” or a “valley”. The integration of actuation and sensing into the cantilever does not only reduce the size of the AFM and does make a laser system for beam deflection detection redundant, it also offers an easy-to-use system by obviating the need for laser beam alignment. This PhD thesis presents the first extensive characterization of the performance of the self-actuating and self-sensing piezoresistive microscale silicon cantilever. The performance is influenced by parasitic heating resulting from the thermal beam actuation, by air damping, by noise, and by crosstalk. The linear temperature and drive power dependency of fundamental frequency, quality factor, deflection on pure beam bending, and maximum amplitude of beam oscillation has been demonstrated here by measurements. The Wheatstone bridge also introduces a temperature change to the beam, which affects the fundamental frequency more than does the drive power, because the bridge is placed at a crucial point where there is maximum stress. The variation in quality factor and in maximum amplitude of beam oscillation in relation to air pressure clearly falls into three regions, intrinsic, molecular and viscous, whereas the fundamental frequency decays linearly with air pressure. A completely new SPM-SEM system with a self-actuating and self-sensing piezoresistive microscale silicon cantilever is here presented that is capable of high resolution imaging, characterization, and manipulation in different SPM modes.

8.2 German abstract

Zum ersten Mal ist eine Kombination aus SPM und REM in einem System mit einem selbstaktuierenden und selbstdektierenden piezoresistiven mikrometerkleinen Siliziumcantilever erfolgreich demonstriert worden. Dieses System ermöglicht hochauflösende AFM- und REM-Aufnahmen. Der Vorteil besteht darin, dass das AFM die Topographie der Probenoberfläche liefert, während REM-Aufnahmen nur zweidimensional sind und nicht eindeutig zeigen, wo sich “Berg” oder “Tal” befindet. Die Integration von Aktuation und Detektion im Cantilever reduziert nicht nur die Größe des AFMs und macht das Lasersystem für die Erfassung der Cantileververbiegung überflüssig, sondern bietet ein einfach zu bedienendes System, weil der Laserstrahl nicht mehr justiert werden muss. Die vorliegende Doktorarbeit präsentiert die erste umfassende Charakterisierung der Verhaltens eines selbstaktuierenden und selbstdektierenden piezoresistiven mikrometerkleinen Siliziumcantilevers. Das Verhalten ist von parasitärer Wärme beeinflusst, die von der thermischen Anregung herrührt, von der Luftdämpfung, dem Rauschen und dem Übersprechen. Die lineare Abhängigkeit von der Temperatur und der Anregungsleistung zeigen die Resonanzfrequenz, die Güte, die statische Verbiegung und die Schwingungsamplitude in den Messungen. Auch die Wheatstone-Brücke bringt Temperaturänderung in den Cantilever, die die Resonanzfrequenz stärker beeinflusst als die Anregungsleistung, denn die Brücke ist an einer kritischen Stelle plaziert, wo die mechanische Spannung am größten ist. Die Änderung der Güte und der Schwingungsamplitude mit dem Luftdruck lässt sich in den intrinsischen, den molekularen und den viskosen Bereich einteilen, während die Resonanzfrequenz linear mit dem Luftdruck abfällt. Ein komplett neues SPM-REM-System mit einem selbstaktuierenden und selbstdektierenden piezoresistiven mikrometerkleinen Siliziumcantilever, das hochauflösende Bilder, Charakterisierung und Manipulation der Probenoberfläche in verschiedenen SPM-Moden ermöglicht, ist präsentiert worden.

9 Theses

- For the first time, the combination of SPM and SEM within one system using a a self-actuating and self-sensing piezoresistive microscale silicon cantilever has been successfully demonstrated.
- The capability of high resolution AFM and SEM in combination is shown.
- AFM gives a three-dimensional image of the specimen surface, whereas it is not necessarily clear from the SEM image where there are “hills” or “valleys”.
- AFM and SEM cannot be done simultaneously because of the charging.
- The thermal beam actuation does not only cause beam oscillation but also changes fundamental frequency and quality factor as an undesired side effect.
- The theoretically derived linear temperature and drive power dependency of fundamental frequency, quality factor, deflection on pure beam bending, and maximum amplitude of beam oscillation is demonstrated by measurements.
- The Wheatstone bridge introduces a temperature change to the beam, which affects the fundamental frequency than does the drive power, because the bridge is placed at a crucial point where there is maximum stress.
- The actuation efficiency depending on the beam thickness as a ratio of the silicon layer to the constant thickness of all other layers is a bell-shaped curve.
- The time taken to reach thermal equilibrium is reduced if a large heat sink is thermally well connected to the cantilever.
- The variation in quality factor and in maximum amplitude of beam oscillation in relation to air pressure clearly falls into three regions, intrinsic, molecular and viscous, whereas the fundamental frequency decays linearly with air pressure.

10 Affidavit

Ich versichere, dass ich die vorliegende Arbeit ohne unzulässige Hilfe Dritter und ohne Benutzung anderer als der angegebenen Hilfsmittel angefertigt habe. Die aus anderen Quellen direkt oder indirekt übernommenen Daten und Konzepte sind unter Angabe der Quelle gekennzeichnet. Weitere Personen waren an der inhaltlich-materiellen Erstellung der vorliegenden Arbeit nicht beteiligt gewesen. Insbesondere habe ich hierfür nicht die entgeltliche Hilfe von Vermittlungs- beziehungsweise Beratungsdiensten (Promotionsberater oder anderer Personen) in Anspruch genommen. Niemand hat von mir unmittelbar oder mittelbar geldwerte Leistungen für Arbeiten erhalten, die im Zusammenhang mit dem Inhalte der vorgelegten Dissertation stehen. Die Arbeit wurde bisher weder im In- noch im Ausland in gleicher oder ähnlicher Form einer Prüfungsbehörde vorgelegt. Ich bin darauf hingewiesen worden, dass die Unrichtigkeit der vorstehenden Erklärung als Täuschungsversuch angesehen wird und den erfolglosen Abbruch des Promotionsverfahrens zur Folge hat.

Ilmenau, den 21. Juni 2011

I hereby declare that this submission is my own work and that, to the best of my knowledge and belief, it contains no material previously published or written by another person nor material which to a substantial extent has been accepted for the award of any other degree or diploma of the university or other institute of higher learning, except where due acknowledgement has been made in the text.

Ilmenau, 21st June 2011

11 Curriculum vitae

Personal information
Date of birth: October, 19th 1982
Place of birth: Hildburghausen, German Democratic Republic
Citizenship: German

Education/ working experience

PhD thesis: "Fabrication and characterization of self-sensing and self-actuating piezoresistive microscale silicon cantilevers for an integrated scanning probe microscopy and scanning electron microscopy system" Department of Microelectronic and Nanoelectronic Systems, Faculty of Electrical Engineering and Information Technology, supervisor: Univ. Prof. Dr.-Ing. habil. Ivo W. Rangelow. *(Ilmenau University of Technology, Ilmenau, Thüringen, Germany, May 2008 - present)*

PhD thesis research work: completely new combination of scanning probe microscopy and scanning electron microscope Imaging and Manipulation of Nanostructures Facility, The Molecular Foundry, supervisor: Dr D. Frank Ogletree *(Ernest Orlando Lawrence Berkeley National Laboratory, Berkeley, California, USA, April 2009 - January 2010)*

Research assistant: PRONANO - Technology for the production of massively parallel intelligent cantilever probe platforms for nanoscale analysis and synthesis (funded by the European Commission within the 6th framework programme, IP 515739-2 PRONANO) Department of Microelectronic and Nanoelectronic Systems, Faculty of Electrical Engineering and Information Technology, supervisor: Univ.-Prof. Dr.- Ing. habil. Ivo W. Rangelow. *(Ilmenau University of Technology, Ilmenau, Thüringen, Germany, October 2007 - March 2010)*

Student/ graduate assistant Department of Inorganic Non-metallic Materials, Faculty of Mechanical Engineering, supervisor: Dr.-Ing. Susanne Mrotzek. *(Ilmenau University of Technology, Ilmenau, Thüringen, Germany, May 2005 - September 2007)*

Diplom-Ingenieur für Werkstoffwissenschaft Theoretical, technical, and practical aspects of materials science. Excellent (1.2). *(Ilmenau University of Technology, Ilmenau, Thüringen, Germany, October 2001 - May 2007)*

Diploma thesis: "Field-enhanced ion exchange on glass" Good (1.7). Department of Inorganic Non-metallic Materials, Faculty of Mechanical Engineering, supervisor: Univ.-Prof. Dr.-Ing. habil. Dr. rer. oec. Dagmar Hülsenberg *(Ilmenau University of Technology, Ilmenau, Thüringen, Germany, May 2007)*

Internship project: "Creation of a 50 µm thick pure hydroxylapatite coating on Ti-6Al-4V substrate which is biocompatible using HA suspension and inductively coupled plasma" Centre de Recherche en Technologie des Plasmas, Faculté de génie, Département de génie chimique, supervisor: Ph. D. Ing. Francois Gitzhofer, Professeur titulaire *(Université de Sherbrooke, Sherbrooke, Québec, Canada, October 2005 - March 2006)*

Student research project: "Studies on thermal stability of Zerodur" Excellent (1.0). Department of Inorganic Non-metallic Materials, Faculty of Mechanical Engineering, supervisor: Univ.-Prof. Dr.-Ing. habil. Dr. rer. oec. Dagmar Hülsenberg *(Ilmenau University of Technology, Ilmenau, Thüringen, Germany, May 2005)*

Studies on Russian language and intercultural communication *(South-Russian Public University of Technology, Novocherkassk, Russia, August - September 2005)*

Abitur Very good (1.3). *(Gymnasium Georgianum, Hildburghausen, Thüringen, Germany, 2001)*

Awards

Student research project awarded with **"Innovative Gläser und Glasverbundwerkstoffe"** (*Lauscha Fiber International GmbH, Thüringen, Germany, January 2006)*

First place in regional round of 36. Deutsche Mathematik-Olympiade *(Gymnasium Georgianum, Hildburghausen, Thüringen, Germany, 1996)*

Appendices

Nomenclature

$(CH_3)_2CO$	dimethyl ketone, acetone
Ag	silver
Al	aluminium
Ar	argon
Au	gold
C_3H_7OH	propan-2-ol, isopropanol, isopropyl alcohol
CF_4	tetrafluoromethane
C_4F_8	octafluorocyclobutane
CHF_3	trifluoromethane
Cr	chromium
Cu	copper
H_2SO_5	peroxymonosulfuric acid, Caro's acid
H_2O	DI water
He	helium
HF	hydrofluoric acid
HNO_3	nitric acid
H_3PO_4	phosphoric acid
H_2O_2	hydrogen peroxide
H_2SO_4	sulphuric acid
KOH	potassium hydroxide
N_2	nitrogen
NH_4OH	ammonium hydroxide
NH_4F	ammonium fluoride
NH_3	ammonia
N_2O	nitrous oxide, laughing gas
O_2	oxygen
SF_6	sulfur hexafluoride
Si	silicon
$\mathrm{Si_xN_y}$	silicon nitride
SiH_4	silane
SiO_2	silicone dioxide
$v_{etching}$	etching rate
$\mathrm{A_A}$	arbitrary constant
$\mathrm{A_{heater}}$	heater area
$\mathrm{A_i}$	cross-section of layer i
α	thermal expansion coefficient

α_{Hooge}	Hooge noise paramenter
$\alpha_{\mathrm{R_{heater}}}$	temperature coefficient of heater resistance
$\delta_{\mathrm{Anderson-Gruneisen}}$	Anderson-Gruneisen parameter
$\mathrm{A_{piezo}}$	cross-sectional area of piezoresistor
β	temperature coefficient of Young's modulus
$\beta_{<110>}$	temperature coefficient of Young's modulus for the <110> crystallographic direction
$\beta_{<110>,\mathrm{Si}}$	temperature coefficient of Young's modulus for the <110> crystallographic direction of silicon
$\beta_{\mathrm{dissipative}}$	dissipative drag parameter
β_{eff}	efficiency factor
$\beta_{\mathrm{inertial}}$	inertial drag parameter
β_{m}	auxiliary parameter
$\beta_{\mathrm{m}}\mathrm{L}$	wave number
$\mathrm{b_i}$	width of layer *i*
$\mathrm{b_{piezo}}$	width of piezoresistor
c	constant
$\mathrm{C_{beam}}$	heat capacity of cantilever
$\mathrm{c_{doping}}$	doping density or concentration
$\mathrm{C_{ij}}$	stiffness coefficient
$\mathrm{C_{1,2,3,4}}$	constants of integration
$\mathrm{c_p}$	specific heat capacity at constant pressure
κ	beam curvature
d	thickness
D	damping ratio
$\mathrm{d_{boundary}}$	thickness of turbulent boundary layer
θ_{Debye}	Debye temperature
$\Delta\mathrm{b}$	change of width
$\Delta\mathrm{d}$	change of thickness
$\Delta\rho$	change of density
$\Delta\mathrm{f}$	width of amplitude resonance at half the maximum value
$\Delta\mathrm{f_{noise}}$	noise bandwidth
$\Delta\mathrm{f_{relative}}$	relative frequency shift
$\Delta\mathrm{L}$	change of length
$\mathrm{R_{piezo,T}}$	piezoresistivity change
$\mathrm{R_{piezo,T}}$	resistance change of longitudinal piezoresistor
$\mathrm{R_{piezo,T}}$	resistance change of transverse piezoresistor
$\Delta\mathrm{T}$	change of temperature
$\Delta\mathrm{T}$	temperature change
ρ_{beam}	density of the cantilever
$\rho_{\mathrm{air,1atm}}$	density of the air at 1 atm
ρ	density
ρ_{air}	density of the air

$\Delta \mathrm{f}_1$	width of the resonance amplitude peak at half the maximum value
d_i	thickness of layer i
d_k	thickness of reference layer
$\mathrm{d}_\mathrm{piezo}$	thickness of piezoresistor
$\mathrm{E}_{<110>}$	Young's modulus for the <110> crystallographic direction
ϵ_j	strain component
$\mathrm{E}_\mathrm{reference}$	Young's modulus of the reference material
$\mathrm{E}_{<110>,\mathrm{Si}}$	Young's modulus for the <110> crystallographic direction of silicon
η	thermal diffusivity
f_d	drive frequency
$\mathrm{F}_\mathrm{damping}$	damping force
$\mathrm{F}_\mathrm{n,damping}$	damping noise force
$\mathrm{f}_\mathrm{dissipative}$	dissipative damping parameter
F_drag	drag force
$\mathrm{F}_\mathrm{spring}$	external force
$\mathrm{F}_\mathrm{spring}$	spring force
$\mathrm{f}_\mathrm{inertial}$	inertial damping parameter
f_max	maximum frequency of measurement bandwidth
f_max	measurement bandwidth
f_min	minimum frequency of measurement bandwidth
f_1	fundamental frequency, first harmonic
υ	frequency ratio
$\mathrm{F}_\mathrm{n,thermomechanical}$	thermomechanical noise force
f_2	second harmonic
F_0	amplitude of external force
$\gamma_\mathrm{Gruneisen}$	Gruneisen paramter
h_conv	convection heat transfer coefficient
I_area	area moment of inertia
$\mathrm{I}_\mathrm{area,sum}$	sum of area moments of inertia of beam made of different materials layers
$\mathrm{I}_\mathrm{drive,DC}$	drive direct current
k_B	Boltzmann's constant
$\mathrm{K}_{\mathrm{C}_\mathrm{ij}}$	temperature coefficient of elasticity
k_SB	Stefan-Boltzmann constant
k_th	thermal conductivity
λ_th	thermal de Broglie wavelength
L_i	length of layer i
$\mathrm{l}_2, \mathrm{m}_2, \mathrm{n}_2$	direction cosines between the transverse piezoresistor direction and the cubic crystal axes
$\mathrm{l}_1, \mathrm{m}_1, \mathrm{n}_1$	direction cosines between the longitudinal piezoresistor direction and the cubic crystal axes
$\mathrm{L}_\mathrm{piezo}$	length of piezoresistor
$\mathrm{m}_\mathrm{molecule}$	mass of one air molecule
$\mathrm{m}_\mathrm{molecule}$	mass of the air

$\widehat{\mathrm{P}}_{\mathrm{drive,AC}}$	maximum AC drive power
$\mathrm{M}_{\mathrm{eff}}$	effective mass factor
$\mathrm{M}_{\mathrm{eff}}$	molar mass of the air
μ_{p}	hole mobility
ψ	mode shape function
$\mathrm{m}_{\mathrm{sum}}$	mass of beam made of several layers
$\mathrm{M(x)}$	moment of the beam
N	number of carriers
$\mathrm{N}_{\mathrm{molecules}}$	number of the air molecules
ω_1	angular fundamental frequency, angular first harmonic
ω_{d}	angular drive frequency
$\omega_{\mathrm{m,damped}}$	damped angular frequency of the harmonic of the *m*th order
$\omega_{\mathrm{m,damped}}$	damped angular fundamental frequency
ω_{m}	angular frequency of the harmonic of the *m*th order
$\mathrm{p}_{\mathrm{air}}$	air pressure
$\mathrm{p}_{\mathrm{air,1atm}}$	air pressure at 1 atm
$\mathrm{P}_{\mathrm{bridge,DC}}$	DC Wheatstone bridge power
$\mathrm{P}_{\mathrm{drive,AC}}$	AC drive power
$\mathrm{P}_{\mathrm{drive,DC}}$	DC drive power
π_{ij}	piezoresistive coefficient
π_{L}	longitudinal piezoresistive coefficient
$\pi_{\mathrm{L,<110>}}$	longitudinal piezoresistive coefficient for the <110> crystallographic direction
$\pi_{\mathrm{L,<110>,pSi}}$	longitudinal piezoresistive coefficient for the <110> crystallographic direction of p-type silicon
$\pi_{\mathrm{L,<110>,Si}}$	longitudinal piezoresistive coefficient for the <110> crystallographic direction of silicon
π_{T}	transversal piezoresistive coefficient
$\pi_{\mathrm{T,<110>}}$	transverse piezoresistive coefficient for the <110> crystallographic direction
$\pi_{\mathrm{T,<110>,pSi}}$	transverse piezoresistive coefficient for the <110> crystallographic direction of p-type silicon
$\pi_{\mathrm{T,<110>,Si}}$	transverse piezoresistive coefficient for the <110> crystallographic direction of silicon
$\mathrm{p}_{\mathrm{transition}}$	transition pressure where damping changes from molecular to viscous region
q	electron charge
q	heat flux, heat transfer rate
$\dot{\mathrm{q}}$	energy generation rate per unit volume
$\mathrm{q}_{\mathrm{s}}^{\prime\prime}$	heat flux at the surface
Q	quality factor, Q factor
$\mathrm{R}_{\mathrm{bridge}}$	Wheatstone bridge resistance
R_{c}	radius of curvature
$\mathrm{R}_{\mathrm{heater,0}}$	resistance of aluminium thin film heater at room temperature
$\mathrm{R}_{\mathrm{heater,0}}$	resistance of aluminium thin film heater
ρ_{piezo}	isotropic resistivity of unstressed piezoresistor
$\mathrm{R}_{\mathrm{ideal}}$	ideal gas constant
$\mathrm{R}_{\mathrm{piezo}}$	resistance of piezoresistor

$\mathrm{R}_{\mathrm{sphere}}$	radius of an oscillating sphere the cantilever is approximated with
$\mathrm{R}_{\mathrm{thermal,beam}}$	thermal resistance of the cantilever
$\mathrm{R}_{\mathrm{thermal,i}}$	thermal resistance of layer i
τ_{j}	shear stress component
$\sigma_{<110>}$	normal stress for the <110> crystallographic direction
$\sigma_{\mathrm{i}}, \sigma_{\mathrm{j}}$	normal stress component
$\sigma_{<110>,\mathrm{max}}$	maximum bending stress for the <110> crystallographic direction
S_{ij}	compliance coefficient
$\mathrm{P}_{\mathrm{drive,AC,static}}$	part of AC drive power causing static bending
T_{a}	ambient temperature
$\mathrm{tau}_{\mathrm{response}}$	response time of the cantilever
$\mathrm{tau}_{\mathrm{thermal}}$	thermal time constant of the cantilever
$t_{developing}$	developing time
$t_{exposure}$	exposure time
E	Young's modulus
F	force
k	spring constant, stiffness
l,m,n	direction cosines between an arbitrary crystallographic direction and the cubic crystal axes
T_{∞}	fluid temperature
T_{0}	initial temperature
$\mathrm{t}_{\mathrm{cycle}}$	time of one cycle of oscillation
T_{s}	surface temperature
$\mathrm{T}_{\mathrm{sur}}$	surrounding temperature
U_{AC}	amplitude of AC drive voltage signal
$\mathrm{U}_{\mathrm{AC,RMS}}$	root mean square value of AC drive voltage amplitude
$\mathrm{U}_{\mathrm{bias,piezo}}$	bias voltage across piezoresistor
U_{DC}	offset of AC drive voltage signal
$\mathrm{U}_{\mathrm{in,bridge,DC}}$	DC Wheatstone bridge input voltage signal for bridge driving
$\mathrm{U}_{\mathrm{drive,AC}}$	AC drive voltage
$\mathrm{U}_{\mathrm{Hooge}}$	Hooge noise, $1/f$ noise
$\mathrm{U}_{\mathrm{in,bridge}}$	Wheatstone bridge input voltage signal for bridge driving
$\mathrm{U}_{\mathrm{Johnson}}$	Johnson noise
$\mathrm{U}_{\mathrm{out,bridge}}$	Wheatstone bridge output voltage signal
$\mathrm{U}_{\mathrm{out,bridge,AC}}$	AC Wheatstone bridge output voltage signal
$\mathrm{U}_{\mathrm{out,bridge,DC}}$	DC Wheatstone bridge output voltage signal
U_{0}	voltage amplitude
V	volume
$\mathrm{V}_{\mathrm{air}}$	volume of air
φ	phase
φ_{A}	arbitrary constant
μ_{air}	air viscosity

$\mathrm{V_{piezo}}$	volume of piezoresistor
$\mathrm{V}(\upsilon)$	enhancement of dynamic displacement
$\mathrm{W_{dissipation}}$	energy lost per cycle of oscillation
$\mathrm{W_{kin}}$	kinetic oscillation energy
ξ	efficiency coefficient
ζ	emissivity
$\mathrm{z_c}$	centroid
$\mathrm{z_i}$	axis of symmetry of layer i
$\mathrm{z_{AC,max}}$	amplitude at resonance
$\mathrm{z_N}$	neutral axis of beam
$\mathrm{z_{dynamic}}, \mathrm{z_{AC}}$	amplitude of displacement
$\mathrm{z_{dynamic}}, \mathrm{z_{AC}}$	amplitude of dynamic displacement, AC amplitude
$\mathrm{z_{dynamic}}, \mathrm{z_{AC}}$	static displacement, DC deflection
A	cross-sectional area
atm	atmosphere
b	width
h	Planck's constant
I	current
L	length
m	cantilever mass
R	ohmic resistance
r	damping coefficient
rpm	rounds per minute
Sccm	Standard cubic centimetre
T	absolute temperature
t	time
U	voltage
x	x direction
z	displacement in z direction

Acronyms

AC	alternating current
AFM	atomic force microscopy
BNC	Bayonet-Neill-Concelman
CTE	coefficient of thermal expansion
CVD	chemical vapour deposition
DC	direct current
DHO	driven harmonic oscillator
DI	deionized
FEM	finite element method
FIB	focused ion beam
FM	frequency modulation
ICP	inductive coupled plasma
PCB	printed circuit board
PID	proportional-integral-derivative
PLL	phase-locked loop
PVD	physical vapour deposition
RCA	Radio Corporation of America
RIE	reactive ion etching
RF	radio frequency
SEM	scanning electron microscope
SPM	scanning probe microscopy
STM	scanning tunnelling microscope
TED	thermoelastic dissipation
TTV	total thickness variation
UV	ultraviolet

Bibliography

[1] G. Binnig, C. F. Quate, and Ch. Gerber. Atomic Force Microscope. *Physical Review Letters*, 56(9):930–933, March 1986. doi: 10.1103/PhysRevLett.56.930. URL `http://link.aps.org/doi/10.1103/PhysRevLett.56.930`.

[2] T. R. Albrecht, S. Akamine, T. E. Carver, and C. F. Quate. Microfabrication of cantilever styli for the atomic force microscope. *Journal of Vacuum Science & Technology A: Vacuum, Surfaces, and Films*, 8(4):3386–3396, July 1990. doi: 10.1116/1.576520. URL `http://link.aip.org/link/?JVA/8/3386/1`.

[3] S. Akamine, R. C. Barrett, and C. F. Quate. Improved atomic force microscope images using microcantilevers with sharp tips. *Applied Physics Letters*, 57(3):316–318, July 1990. doi: 10.1063/1.103677. URL `http://link.aip.org/link/?APL/57/316/1`.

[4] T. R. Albrecht and C. F. Quate. Atomic resolution imaging of a nonconductor by atomic force microscopy. *Journal of Applied Physics*, 62(7):2599–2602, October 1987. doi: 10.1063/1.339435. URL `http://link.aip.org/link/?JAP/62/2599/1`.

[5] O. Marti, B. Drake, and P. K. Hansma. Atomic force microscopy of liquid-covered surfaces: Atomic resolution images. *Applied Physics Letters*, 51(7):484–486, August 1987. doi: 10.1063/1.98374. URL `http://link.aip.org/link/?APL/51/484/1`.

[6] Yves Martin, David W. Abraham, and H. Kumar Wickramasinghe. High-resolution capacitance measurement and potentiometry by force microscopy. *Applied Physics Letters*, 52(13):1103–1105, March 1988. doi: 10.1063/1.99224. URL `http://link.aip.org/link/?APL/52/1103/1`.

[7] Kees O. van der Werf, Constant A. J. Putman, Bart G. de Grooth, and Jan Greve. Adhesion force imaging in air and liquid by adhesion mode atomic force microscopy. *Applied Physics Letters*, 65(9):1195–1197, August 1994. doi: 10.1063/1.112106. URL `http://link.aip.org/link/?APL/65/1195/1`.

[8] T. Ando, Ta. Uchihashi, N. Kodera, A. Miyagi, R. Nakakita, H. Yamashita, and M. Sakashita. High-Speed Atomic Force Microscopy for Studying the Dynamic Behavior of Protein Molecules at Work. *Japanese Journal of Applied Physics*, 45(3B):1897–1903, March 2006. doi: 10.1143/JJAP.45.1897. URL `http://jjap.ipap.jp/link?JJAP/45/1897/`.

[9] G. E. Fantner, W. Schumann, R. J. Barbero, A. Deutschinger, V. Todorov, D. S. Gray, A. M. Belcher, I. W. Rangelow, and K. Youcef-Toumi. Use of self-actuating and self-sensing cantilevers for imaging biological samples in fluid. *Nanotechnology*, 20(43):434003, October 2009. URL `http://stacks.iop.org/0957-4484/20/i=43/a=434003`.

[10] S. C. Minne, G. Yaralioglu, S. R. Manalis, J. D. Adams, J. Zesch, A. Atalar, and C. F. Quate. Automated parallel high-speed atomic force microscopy. *Applied Physics Letters*, 72(18):2340–2342, May 1998. doi: 10.1063/1.121353. URL `http://link.aip.org/link/?APL/72/2340/1`.

[11] M. Lutwyche, C. Andreoli, G. Binnig, J. Brugger, U. Drechsler, W. Häberle, H. Rohrer, H. Rothuizen, P. Vettiger, G. Yaralioglu, and C. Quate. 5x5 2D AFM cantilever arrays a first step towards a Terabit storage device. *Sensors and Actuators A: Physical*, 73(1–2):89–94, March 1999. ISSN 0924-4247. doi: 10.1016/S0924-4247(98)00259-3. URL `http://www.sciencedirect.com/science/article/B6THG-3WWKPDW-16/2/2bca5d1a5f9a4590479ed8085a1f2a85`.

[12] P. Vettiger, G. Cross, M. Despont, U. Drechsler, U. Durig, B. Gotsmann, W. Häberle, M. A. Lantz, H. E. Rothuizen, R. Stutz, and G. K. Binnig. The "millipede" - nanotechnology entering data storage. *Nanotechnology, IEEE Transactions on*, 1(1):39–55, March 2002. ISSN 1536-125X. doi: 10.1109/TNANO.2002.1005425. URL `http://ieeexplore.ieee.org/stamp/stamp.jsp?tp=&arnumber=1005425&isnumber=21698`.

[13] S. C. Minne, S. R. Manalis, A. Atalar, and C. F. Quate. Independent parallel lithography using the atomic force microscope. *Journal of Vacuum Science and Technology B: Microelectronics and Nanometer Structures*, 14(4):2456–2461, July 1996. doi: 10.1116/1.588753. URL `http://link.aip.org/link/?JVB/14/2456/1`.

[14] K. Wilder, H. T. Soh, A. Atalar, and C. F. Quate. Nanometer-scale patterning and individual current-controlled lithography using multiple scanning probes. *Review of Scientific Instruments*, 70(6):2822–2827, June 1999. doi: 10.1063/1.1149802. URL `http://link.aip.org/link/?RSI/70/2822/1`.

[15] Khalid Salaita, Yuhuang Wang, Joseph Fragala, Rafael A. Vega, Chang Liu, and Chad A. Mirkin. Massively parallel dip-pen nanolithography with 55 000-Pen two-dimensional arrays. *Angewandte Chemie*, 118(43):7378–7381, November 2006. doi: 10.1002/ange.200603142. URL `http://dx.doi.org/10.1002/ange.200603142`.

[16] S. R. Manalis, S. C. Minne, and C. F. Quate. Atomic force microscopy for high speed imaging using cantilevers with an integrated actuator and sensor. *Applied Physics Letters*, 68(6):871–873, February 1996. doi: 10.1063/1.116528. URL `http://link.aip.org/link/?APL/68/871/1`.

[17] Georg E. Fantner, Georg Schitter, Johannes H. Kindt, Tzvetan Ivanov, Katarina Ivanova, Rohan Patel, Niels Holten-Andersen, Jonathan Adams, Philipp J. Thurner, Ivo W. Rangelow, and Paul K. Hansma. Components for high speed atomic force microscopy. *Ultramicroscopy*, 106(8-9):881 – 887, 2006. ISSN 0304-3991. doi: DOI:10.1016/j.ultramic.2006.01.015. URL `http://www.sciencedirect.com/science/article/B6TW1-4JTR4KH-1/2/ceacab959e83239d3f9fdc3d25516571`. Proceedings of the Seventh International Conference on Scanning Probe Microscopy, Sensors and Nanostructures, Proceedings of the Seventh International Conference on Scanning Probe Microscopy, Sensors and Nanostructures.

[18] A. Ruf, M. Abraham, J. Diebel, W. Ehrfeld, P. Güthner, M. Lacher, K. Mayr, and J. Reinhardt. Integrated Fabry-Pérot distance control for atomic force microscopy. *Journal of Vacuum Science & Technology B: Microelectronics and Nanometer Structures*, 15(3):579–585, May 1997. doi: 10.1116/1.589295. URL `http://link.aip.org/link/?JVB/15/579/1`.

[19] Young-Sik Kim, Caroline Sunyong Lee, Won-Hyeog Jin, SeongSoo Jang, Hyo-Jin Nam, and Jong-Uk Bu. 100x100 Thermo-piezoelectric cantilever array for SPM nano-data-storage application. *Sensors and Materials*, 17(2):57–63, 2005. URL `http://122.249.91.209/myukk/Journal/Download.php?fn=SM0586.pdf`.

[20] J. Brugger, N. Blanc, Ph. Renaud, and N.F. de Rooij. Microlever with combined integrated sensor/actuator functions for scanning force microscopy. *Sensors and Actuators A: Physical*, 43(1-3):339 – 345, May 1994. ISSN 0924-4247. doi: DOI:10.1016/0924-4247(93)00701-5. URL `http://www.sciencedirect.com/science/article/B6THG-448R94P-1Y/2/9f6d66e3a5cc8bfb89ef5c11a54c1920`.

[21] Scott A. Miller, Kimberly L. Turner, and Noel C. MacDonald. Microelectromechanical scanning probe instruments for array architectures. *Review of Scientific Instruments*, 68(11):4155–4162, 1997. doi: 10.1063/1.1148361. URL `http://link.aip.org/link/?RSI/68/4155/1`.

[22] D. Rugar, R. Budakian, H. J. Mamin, and B. W. Chui. Single spin detection by magnetic resonance force microscopy. *Nature*, 430(6997):329–332, July 2004. doi: 10.1038/nature02658. URL `http://dx.doi.org/10.1038/nature02658`.

[23] G. Binnig, M. Despont, U. Drechsler, W. Häberle, M. Lutwyche, P. Vettiger, H. J. Mamin, B. W. Chui, and T. W. Kenny. Ultrahigh-density atomic force microscopy data storage with erase capability. *Applied Physics Letters*, 74(9): 1329–1331, 1999. doi: 10.1063/1.123540. URL `http://link.aip.org/link/?APL/74/1329/1`.

[24] M. Tortonese, R. C. Barrett, and C. F. Quate. Atomic resolution with an atomic force microscope using piezoresistive detection. *Applied Physics Letters*, 62(8):834–836, February 1993. doi: 10.1063/1.108593. URL `http://link.aip.org/link/?APL/62/834/1`.

[25] S. C. Minne, S. R. Manalis, and C. F. Quate. Parallel atomic force microscopy using cantilevers with integrated piezoresistive sensors and integrated piezoelectric actuators. *Applied Physics Letters*, 67(26):3918–3920, December 1995. doi: 10.1063/1.115317. URL `http://link.aip.org/link/?APL/67/3918/1`.

[26] R. Linnemann, T. Gotszalk, L. Hadjiiski, and I. W. Rangelow. Characterization of a cantilever with an integrated deflection sensor. *Thin Solid Films*, 264(2):159–164, August 1995. ISSN 0040-6090. doi: 10.1016/0040-6090(94)05829-6. URL `http://www.sciencedirect.com/science/article/B6TW0-3YF4GJ9-3B/2/fb86c38facd2b8e052bcd80b8245f6c`.

[27] Tzv. Ivanov, T. Gotszalk, P. Grabiec, E. Tomerov, and I. W. Rangelow. Thermally driven micromechanical beam with piezoresistive deflection readout. *Microelectronic Engineering*, 67–68:550–556, June 2003. ISSN 0167-9317. doi: 10.1016/S0167-9317(03)00113-8. URL `http://www.sciencedirect.com/science/article/B6V0W-483BMTS-2/2/1517293eb50fce2e83d590555a10ef4f`. Proceedings of the 28th International Conference on Micro- and Nano-Engineering.

[28] Tzv. Ivanov, T. Gotszalk, T. Sulzbach, I. Chakarov, and I. W. Rangelow. AFM cantilever with ultra-thin transistor-channel piezoresistor: quantum confinement. *Microelectronic Engineering*, 67-68:534–541, June 2003. ISSN 0167-9317. doi: DOI:10.1016/S0167-9317(03)00111-4. URL `http://www.sciencedirect.com/science/article/B6V0W-4846NKV-1/2/6d01a20aa842265a96340a78569034ef`. Proceedings of the 28th International Conference on Micro- and Nano-Engineering.

[29] Zunxian Yang, Ying Yu, Xinxin Li, and Haifei Bao. Nano-mechanical electro-thermal probe array used for high-density storage based on NEMS technology. *Microelectronics and Reliability*, 46(5–6):805–810, May–June 2006. ISSN 0026-2714. doi: 10.1016/j.microrel.2005.07.117. URL `http://www.sciencedirect.com/science/article/B6V47-4H3YFC8-2/2/76bbbe84356723d9bf510dfcf3a0bcf4`.

[30] Javier Malo and José Ignacio Izpura. Simultaneous magnetic and electrostatic driving of microcantilevers. *Sensors and Actuators A: Physical*, 136(1):347–357, May 2007. ISSN 0924-4247. doi: DOI:10.1016/j.sna.2006.11.034. URL

`http://www.sciencedirect.com/science/article/B6THG-4MP5KNP-2/2/856bf1e979217bbef07bf94507ecd035`. 25th Anniversary of Sensors and Actuators A: Physical.

[31] S. Akamine, T.R. Albrecht, M.J. Zdeblick, and C.F. Quate. Microfabricated scanning tunneling microscope. *Electron Device Letters, IEEE*, 10(11):490–492, November 1989. ISSN 0741-3106. doi: 10.1109/55.43113. URL `http://ieeexplore.ieee.org/stamp/stamp.jsp?tp=&arnumber=43113&isnumber=1650`.

[32] T. Itoh and T. Suga. Piezoelectric force sensor for scanning force microscopy. *Sensors and Actuators A: Physical*, 43(1-3):305–310, May 1994. ISSN 0924-4247. doi: DOI:10.1016/0924-4247(93)00665-Q. URL `http://www.sciencedirect.com/science/article/B6THG-448R94P-1R/2/f5717b0243497f3c3e4b224ef69d45bd`.

[33] O. Marti, A. Ruf, M. Hipp, H. Bielefeldt, J. Colchero, and J. Mlynek. Mechanical and thermal effects of laser irradiation on force microscope cantilevers. *Ultramicroscopy*, 42-44(Part 1):345–350, July 1992. ISSN 0304-3991. doi: DOI:10.1016/0304-3991(92)90290-Z. URL `http://www.sciencedirect.com/science/article/B6TW1-46RVYXC-1Y/2/33dc42d001e53e2ac5b1557cbede8527`.

[34] Andrew C. Hillier and Allen J. Bard. AC-mode atomic force microscope imaging in air and solutions with a thermally driven bimetallic cantilever probe. *Review of Scientific Instruments*, 68(5):2082–2090, May 1997. doi: 10.1063/1.1148101. URL `http://link.aip.org/link/?RSI/68/2082/1`.

[35] R. Pedrak, Tzv. Ivanov, K. Ivanova, T. Gotszalk, N. Abedinov, I. W. Rangelow, K. Edinger, E. Tomerov, T. Schenkel, and P. Hudek. Micromachined atomic force microscopy sensor with integrated piezoresistive sensor and thermal bimorph actuator for high-speed tapping-mode atomic force microscopy phase-imaging in higher eigenmodes. *Journal of Vacuum Science and Technology B: Microelectronics and Nanometer Structures*, 21(6):3102–3107, November–December 2003. doi: 10.1116/1.1614252. URL `http://link.aip.org/link/?JVB/21/3102/1`.

[36] Jungchul Lee and William P. King. Microcantilever actuation via periodic internal heating. *Review of Scientific Instruments*, 78(12):126102, December 2007. doi: 10.1063/1.2818805. URL `http://link.aip.org/link/?RSI/78/126102/1`.

[37] N. Abedinov, C. Popov, Zh. Yordanov, Tzv. Ivanov, T. Gotszalk, P. Grabiec, W. Kulisch, I. W. Rangelow, D. Filenko, and Yu. Shirshov. Chemical recognition based on micromachined silicon cantilever array. *Journal of Vacuum Science and Technology B: Microelectronics and Nanometer Structures*, 21(6):2931–2936, December 2003. doi: 10.1116/1.1624261. URL `http://link.aip.org/link/?JVB/21/2931/1`.

[38] Denis Filenko, Tzvetan Ivanov, Burkhard E. Volland, Katerina Ivanova, Ivo W. Rangelow, Nikolay Nikolov, Teodor Gotszalk, and Jerzy Mielczarski. Experimental setup for characterization of self-actuated microcantilevers with piezoresistive readout for chemical recognition of volatile substances. *Review of Scientific Instruments*, 79(9):094101, September 2008. doi: 10.1063/1.2976038. URL `http://link.aip.org/link/?RSI/79/094101/1`.

[39] DME Danish Micro Engineering A/S. The BRR^{TM}. http://www.dme-spm.com/remafm.html, June 2011.

[40] M. Tortonese, H. Yamada, R.C. Barrett, and C.F. Quate. Atomic force microscopy using a piezoresistive cantilever. In *Solid-State Sensors and Actuators, 1991. Digest of Technical Papers, TRANSDUCERS '91., 1991 International Conference on*, pages 448–451, San Francisco, CA, June 1991. doi: 10.1109/SENSOR.1991.148908. URL `http://ieeexplore.ieee.org/stamp/stamp.jsp?tp=&arnumber=148908&isnumber=3940`.

[41] B. W. Chui, T. D. Stowe, T. W. Kenny, H. J. Mamin, B. D. Terris, and D. Rugar. Low-stiffness silicon cantilevers for thermal writing and piezoresistive readback with the atomic force microscope. *Applied Physics Letters*, 69(18):2767–2769, October 1996. doi: 10.1063/1.117669. URL `http://link.aip.org/link/?APL/69/2767/1`.

[42] R. P. Ried, H. J. Mamin, B. D. Terris, Long-Sheng Fan, and D. Rugar. 6-MHz 2-N/m piezoresistive atomic-force microscope cantilevers with INCISIVE tips. *Journal of Microelectromechanical Systems*, 6(4):294–302, December 1997. ISSN 1057-7157. doi: 10.1109/84.650125. URL `http://ieeexplore.ieee.org/stamp/stamp.jsp?tp=&arnumber=650125&isnumber=14164`.

[43] J. A. Harley and T. W. Kenny. High-sensitivity piezoresistive cantilevers under 1000 A thick. *Applied Physics Letters*, 75(2):289–291, July 1999. doi: 10.1063/1.124350. URL `http://link.aip.org/link/?APL/75/289/1`.

[44] I. Bargatin, E. B. Myers, J. Arlett, B. Gudlewski, and M. L. Roukes. Sensitive detection of nanomechanical motion using piezoresistive signal downmixing. *Applied Physics Letters*, 86(13):133109, March 2005. doi: 10.1063/1.1896103. URL `http://link.aip.org/link/?APL/86/133109/1`.

[45] J. L. Arlett, J. R. Maloney, B. Gudlewski, M. Muluneh, and M. L. Roukes. Self-sensing micro- and nanocantilevers with attonewton-scale force resolution. *Nano Letters*, 6(5):1000–1006, 2006. ISSN 1530-6984. doi: 10.1021/nl060275y. URL `http://dx.doi.org/10.1021/nl060275y`.

[46] P. A. Rasmussen, O. Hansen, and A. Boisen. Cantilever surface stress sensors with single-crystalline silicon piezoresistors. *Applied Physics Letters*, 86(20):203502, May 2005. doi: 10.1063/1.1900299. URL `http://link.aip.org/link/?APL/86/203502/1`.

[47] J. Thaysen, A. Boisen, O. Hansen, and S. Bouwstra. Atomic force microscopy probe with piezoresistive read-out and a highly symmetrical Wheatstone bridge arrangement. *Sensors and Actuators A: Physical*, 83(1–3):47–53, May 2000. ISSN 0924-4247. doi: 10.1016/S0924-4247(00)00299-5. URL `http://www.sciencedirect.com/science/article/B6THG-407981K-9/2/09792d9c7667681363c8dfee65d2867b`.

[48] T. C. Duc, J. F. Creemer, and P. M. Sarro. Piezoresistive Cantilever Beam for Force Sensingin Two Dimensions. *Sensors Journal, IEEE*, 7(1):96–104, January 2007. ISSN 1530-437X. doi: 10.1109/JSEN.2006.886992. URL `http://ieeexplore.ieee.org/stamp/stamp.jsp?tp=&arnumber=4039318&isnumber=4039313`.

[49] Jian Lu, Tsuyoshi Ikehara, Yi Zhang, Takashi Mihara, Toshihiro Itoh, and Ryutaro Maeda. Characterization and improvement on quality factor of microcantilevers with self-actuation and self-sensing capability. *Microelectronic Engineering*, 86, April–June 2009. ISSN 0167-9317. doi: 10.1016/j.mee.2008.12.073. URL `http://www.sciencedirect.com/science/article/B6V0W-4V94WW0-4/2/f64c57c902064a94b1f7fe479c529e4e`. MNE 2008 - The 34th International Conference on Micro- and Nano-Engineering.

[50] I. W. Rangelow, S. Skocki, and P. Dumania. Plasma etching for micromechanical sensor applications. *Microelectronic Engineering*, 23(1-4):365–368, 1994. ISSN 0167-9317. doi: DOI:10.1016/0167-9317(94)90174-0. URL `http://www.sciencedirect.com/science/article/B6V0W-46K4PNN-CT/2/9902b74981dd07577327056a4226c7b7`.

[51] Ivo W. Rangelow, Feng Shi, Peter Hudek, Teodor Gotszalk, Piotr B. Grabiec, and Piotr Dumania. Fabrication of piezoresistive-sensed AFM cantilever probe with integrated tip. In Stella W. Pang and Shih-Chia Chang, editors, *Micromachining and Microfabrication Process Technology II*, volume 2879/1, pages 56–64. SPIE, 1996. doi: 10.1117/12.251232. URL `http://link.aip.org/link/?PSI/2879/56/1`.

[52] Teodor Gotszalk, R. Linnemann, Ivo W. Rangelow, Piotr Dumania, and Piotr B. Grabiec. AFM with piezoresistive Wheatstone bridge cantilever: noise performance and applications in contact and noncontact mode. In Benedykt W. Licznerski and Andrzej Dziedzic, editors, *Metal/Nonmetal Microsystems: Physics, Technology, and Applications*, volume 2780/1, pages 376–379, Polanica Zdroj, Poland, 1996. SPIE. doi: 10.1117/12.238192. URL `http://link.aip.org/link/?PSI/2780/376/1`.

[53] Teodor Gotszalk, Ivo W. Rangelow, Piotr Dumania, and Piotr B. Grabiec. Lateral force microscopy using cantilevers with integrated wheatstone bridge piezoresistive deflection sensor. In Michael T. Postek, Jr., and Craig R. Friedrich, editors, *Microlithography and Metrology in Micromachining II*, volume 2880/1, pages 256–263. SPIE, 1996. doi: 10.1117/12.250958. URL `http://link.aip.org/link/?PSI/2880/256/1`.

[54] Teodor Gotszalk, Ivo W. Rangelow, Piotr Dumania, and Piotr B. Grabiec. Cantilever with integrated wheatstone bridge piezoresistive deflection sensor: analysis of force interaction measurement sensitivity. In Michael T. Postek, Jr., and Craig R. Friedrich, editors, *Microlithography and Metrology in Micromachining II*, volume 2880/1, pages 264–271. SPIE, 1996. doi: 10.1117/12.250959. URL `http://link.aip.org/link/?PSI/2880/264/1`.

[55] R. Linnemann, T. Gotszalk, I. W. Rangelow, P. Dumania, and E. Oesterschulze. Atomic force microscopy and lateral force microscopy using piezoresistive cantilevers. *Journal of Vacuum Science and Technology B: Microelectronics and Nanometer Structures*, 14(2):856–860, March 1996. doi: 10.1116/1.589161. URL `http://link.aip.org/link/?JVB/14/856/1`.

[56] T. Gotszalk, J. Radojewski, P. B. Grabiec, P. Dumania, F. Shi, P. Hudek, and I. W. Rangelow. Fabrication of multipurpose piezoresistive wheatstone bridge cantilevers with conductive microtips for electrostatic and scanning capacitance microscopy. *Papers from the 42nd international conference on electron, ion, and photon beam technology and nanofabrication*, 16(6):3948–3953, November 1998. doi: 10.1116/1.590443. URL `http://link.aip.org/link/?JVB/16/3948/1`.

[57] T. Gotszalk, P. Grabiec, and I. W. Rangelow. Piezoresistive sensors for scanning probe microscopy. *Ultramicroscopy*, 82(1–4):39–48, February 2000. ISSN 0304-3991. doi: 10.1016/S0304-3991(99)00171-0. URL `http://www.sciencedirect.com/science/article/B6TW1-3YF9X0K-6/2/8eb415418c8acac12cd7ad14cc39252d`.

[58] N. Abedinov, P. Grabiec, T. Gotszalk, Tz. Ivanov, J. Voigt, and I. W. Rangelow. Micromachined piezoresistive cantilever array with integrated resistive microheater for calorimetry and mass detection. *Journal of Vacuum Science and Technology A: Vacuum, Surfaces, and Films*, 19(6):2884–2888, November 2001. doi: 10.1116/1.1412654. URL `http://link.aip.org/link/?JVA/19/2884/1`.

[59] M. Woszczyna, T. Gotszalk, P. Zawierucha, M. Zielony, Tzv. Ivanow, K. Ivanowa, Y. Sarov, N. Nikolov, J. Mielczarski, E. Mielczarska, and I.W. Rangelow. Thermally driven piezoresistive cantilevers for shear-force microscopy. *Microelectronic Engineering*, 86(4–6):1212–1215, April–June 2009. ISSN 0167-9317. doi: 10.1016/j.mee.2009.01.043. URL

`http://www.sciencedirect.com/science/article/B6V0W-4VFK7PV-5/2/8a69e4c3df7640ca52eae1746b092779`. MNE 2008 - The 34th International Conference on Micro- and Nano-Engineering.

[60] I.W. Rangelow, T. Ivanov, K. Ivanova, B.E. Volland, P. Grabiec, Y. Sarov, A. Persaud, T. Gotszalk, P. Zawierucha, M. Zielony, D. Dontzov, B. Schmidt, M. Zier, N. Nikolov, I. Kostic, W. Engl, T. Sulzbach, J. Mielczarski, S. Kolb, Du P. Latimier, R. Pedreau, V. Djakov, S.E. Huq, K. Edinger, O. Fortagne, A. Almansa, and H.O. Blom. Piezoresistive and self-actuated 128-cantilever arrays for nanotechnology applications. *Microelectronic Engineering*, 84(5-8):1260–1264, 2007. ISSN 0167-9317. doi: DOI:10.1016/j.mee.2007.01.219. URL `http://www.sciencedirect.com/science/article/B6V0W-4N14643-6/2/3bddabb060885d7c2f5dedaeadfa4897`. Proceedings of the 32nd International Conference on Micro- and Nano-Engineering.

[61] J. B. Wachtman, W. E. Tefft, D. G. Lam, and C. S. Apstein. Exponential temperature dependence of Young's modulus for several oxides. *Physical Review*, 122(6):1754–1759, June 1961. doi: 10.1103/PhysRev.122.1754. URL `http://link.aps.org/doi/10.1103/PhysRev.122.1754`.

[62] M. L. Nandanpawar and S. Rajagopalan. Wachtman's equation and temperature dependence of bulk moduli in solids. *Journal of Applied Physics*, 49(7):3976–3979, July 1978. doi: 10.1063/1.325408. URL `http://link.aip.org/link/?JAP/49/3976/1`.

[63] U. Gysin, S. Rast, P. Ruff, E. Meyer, D. W. Lee, P. Vettiger, and C. Gerber. Temperature dependence of the force sensitivity of silicon cantilevers. *Physical Review B*, 69(4):045403, January 2004. doi: 10.1103/PhysRevB.69.045403. URL `http://link.aps.org/doi/10.1103/PhysRevB.69.045403`.

[64] Stephen D. Senturia. *Microsystem Design.* Springer Science+Business Media, LLC, 1st ed. 2000. corr. 2nd printing edition, 2001. ISBN 978-0-7923-7246-2.

[65] Frank P. Incropera, David P. DeWitt, Theodore L. Bergman, and Adrienne S. Lavine. *Introduction to Heat Transfer.* John Wiley & Sons, Inc., 2007. ISBN 978-0-470-05553-3.

[66] Tzvetan Ivanov. *Piezoresistive cantilevers with an integrated bimorph actuator.* PhD thesis, University of Kassel, Germany, 2004.

[67] Edited by Robert Hull. *Properties of crystalline silicon.* INSPEC, Institution of Engineering and Technology, 1999. ISBN 0-85296-933-3.

[68] Accuratus Corporation. Materials. http://www.accuratus.com/materials.html, May 2010.

[69] C. R. Nave. Hyper Physics. http://hyperphysics.phy-astr.gsu.edu/HBASE/hph.html#hph, 2005.

[70] David D. Hsu. Chromium element facts. http://www.chemicool.com/elements/chromium.html, June 2010.

[71] Andreas Frank, J.-P. Zöllner, Y. Sarov, T. Ivanov, S. Klett, T. Gotszalk, M. Zielony, P. Zawierucha, B. Schmidt, M. Zier, M. Nikolov, W. Engl, T. Sulzbach, D. Dontsov, E. Langlotz, W. Schott, and I.W. Rangelow. Investigation of Crosstalk in Cantilever Arrays. *Proceedings Eurosensors, Dresden, Germany*, XXII:744–747, 2008.

[72] J.-P. Zöllner. Beam calculations. Department of Microelectronic and Nanoelectronic Systems, Ilmenau University of Technology, Germany, February 2011.

[73] Andreas Frank, J.-P. Zoellner, Y. Sarov, Tz. Ivanov, I. Kuhnholz, St. Klett, I. W. Rangelow, M. Swiatkowski, T. Gotszalk, and N. Nikolov. Compact Modelling of Electrical, Mechanical and Thermal Behaviour for MEMS with SPICE. *MRS Proceedings*, page 1083, 2008. doi: 10.1557/PROC-1083-R02-08. URL `http://dx.doi.org/10.1557/PROC-1083-R02-08`.

[74] Thomas Michels. *Evaluation of functionalized cantilevers regarding their sensitivity to water and alcohol.* Diploma thesis, 2011.

[75] Ioffe Physico-Technical Institute. Electronic archive: New Semiconductor Materials. Characteristics and Properties. http://www.ioffe.ru/SVA/NSM/, May 2010.

[76] Ferro-Ceramic Grinding Incorporated. Ceramic properties tables. http://www.ferroceramic.com/silicon_nitride.htm, June 2010.

[77] J.K. Gimzewski, Ch. Gerber, E. Meyer, and R.R. Schlittler. Observation of a chemical reaction using a micromechanical sensor. *Chemical Physics Letters*, 217(5-6):589–594, January 1994. ISSN 0009-2614. doi: DOI:10.1016/0009-2614(93)E1419-H. URL `http://www.sciencedirect.com/science/article/B6TFN-44J6DF8-CP/2/ed69a01cb761e82e3435431c04bd963d`.

[78] J. R. Barnes, R. J. Stephenson, C. N. Woodburn, S. J. O'Shea, M. E. Welland, T. Rayment, J. K. Gimzewski, and Ch. Gerber. A femtojoule calorimeter using micromechanical sensors. *Review of Scientific Instruments*, 65(12):3793–3798, December 1994. doi: 10.1063/1.1144509. URL `http://link.aip.org/link/?RSI/65/3793/1`.

[79] František Kašpar. *Thermobimetalle in der Elektrotechnik.* VEB Verlag Technik Berlin, 1960. ISBN B0000BK0D6.

[80] Steen Krenk. *Mechanics and Analysis of Beams, Columns and Cables: A Modern Introduction to the Classic Theories.* Springer, 2001. ISBN 3-540-41713-3.

[81] Raymond Parnes. *Solid Mechanics in Engineering.* John Wiley & Sons, Ltd., 2001. ISBN 978-0-471-49300-6.

[82] Gerald Gerlach and Wolfram Dötzel. *Einführung in die Mikrosystemtechnik: Ein Kursbuch für Studierende.* Fachbuchverlag Leipzig im Carl Hanser Verlag GmbH & Co. KG, February, 2006. ISBN 978-3-446-22558-9.

[83] S. Timoshenko. Analysis of bi-metal thermostats. *Journal of the Optical Society of America*, 11(3):233–233, September 1925. doi: 10.1364/JOSA.11.000233. URL `http://www.opticsinfobase.org/abstract.cfm?URI=josa-11-3-233`.

[84] Wen-Hwa Chu, M. Mehregany, and R. L. Mullen. Analysis of tip deflection and force of a bimetallic cantilever microactuator. *Journal of Micromechanics and Microengineering*, 3(1):4–7, March 1993. doi: 10.1088/0960-1317/3/1/002. URL `http://stacks.iop.org/0960-1317/3/i=1/a=002`.

[85] Chang Liu. *Foundations of MEMS.* Pearson Education, Inc., 2006. ISBN 9780131472860.

[86] Stephan Bechtold. *Kompakte Modellierung von thermischen Effekten in Mikrosystemen.* PhD thesis, Universität Bremen, Germany, 2003.

[87] Warren P. Mason. *Physical acoustics and the properties of solids.* D. Van Nostrand Company, Inc., 1958. ISBN B0006AVL5M.

[88] Mark Winter (The University of Sheffield and UK) WebElements Ltd. WebElements: the periodic table on the WWW. http://webelements.com/, December 2010.

[89] Peter Hagedorn. *Technische Mechanik, Band 3 Dynamik.* Verlag Harri Deutsch, 4., überarbeitetee auflage edition, 2008. ISBN 978-3-8171-1835-9.

[90] Dror Sarid. *Scanning Force Microscopy With Applications to Electric, Magnetic and Atomic Forces.* Oxford University Press, revised edition edition, 20 October 1994. ISBN 978-0-19-509204-2.

[91] H. J. Pain. *The Physics of Vibrations and Waves.* John Wiley & Sons Ltd., 5 edition, March 5, 1999. ISBN 978-0-471-98543-3.

[92] Martin W. McCall. *Classical Mechanics: A Modern Introduction.* John Wiley & Sons, Ltd., 2001. ISBN 0-471-49711-8.

[93] John E. Sader, Ian Larson, Paul Mulvaney, and Lee R. White. Method for the calibration of atomic force microscope cantilevers. *Review of Scientific Instruments*, 66(7):3789, July 1995. doi: 10.1063/1.1145439. URL `http://link.aip.org/link/RSINAK/v66/i7/p3789/s1`.

[94] Warren C. Young and Richard G. Budynas. *Roark's formulas for stress and strain.* MacGraw-Hill, September 13, 2001. ISBN 9780071501811.

[95] W. A. Brantley. Calculated elastic constants for stress problems associated with semiconductor devices. *Journal of Applied Physics*, 44(1):534–535, January 1973. doi: 10.1063/1.1661935. URL `http://link.aip.org/link/?JAP/44/534/1`.

[96] H. J. McSkimin, W. L. Bond, E. Buehler, and G. K. Teal. Measurement of the elastic constants of silicon single crystals and their thermal coefficients. *Physical Review*, 83(5):1080, September 1951. doi: 10.1103/PhysRev.83.1080. URL `http://link.aps.org/doi/10.1103/PhysRev.83.1080`.

[97] Yozo Kanda. A graphical representation of the piezoresistance coefficients in silicon. *Electron Devices, IEEE Transactions on*, 29(1):64–70, January 1982. ISSN 0018-9383. doi: 10.1109/T-ED.1982.20659. URL `http://ieeexplore.ieee.org/stamp/stamp.jsp?tp=&arnumber=1482156&isnumber=31848`.

[98] Yozo Kanda. Piezoresistance effect of silicon. *Sensors and Actuators A: Physical*, 28(2):83–91, July 1991. ISSN 0924-4247. doi: DOI:10.1016/0924-4247(91)85017-I. URL `http://www.sciencedirect.com/science/article/B6THG-449TTHY-34/2/985768037ece87e839dc770cb97f4cf9`.

[99] J. A. Harley and T. W. Kenny. 1/f noise considerations for the design and process optimization of piezoresistive cantilevers. *Journal of Microelectromechanical Systems*, 9(2):226–235, June 2000. doi: 10.1109/84.846703. URL `http://ieeexplore.ieee.org/stamp/stamp.jsp?tp=&arnumber=846703&isnumber=18375`.

[100] O. N. Tufte and E. L. Stelzer. Piezoresistive properties of silicon diffused layers. *Journal of Applied Physics*, 34(2):313–318, February 1963. doi: 10.1063/1.1702605. URL `http://link.aip.org/link/?JAP/34/313/1`.

[101] Charles S. Smith. Piezoresistance Effect in Germanium and Silicon. *Physical Review*, 94(1):42–49, April 1954. doi: 10.1103/PhysRev.94.42. URL `http://link.aps.org/doi/10.1103/PhysRev.94.42`.

[102] J. R. Mallon Jr., A. J. Rastegar, A. A. Barlian, M. T. Meyer, T. H. Fung, and B. L. Pruitt. Low 1/f noise, full bridge, microcantilever with longitudinal and transverse piezoresistors. *Applied Physics Letters*, 92(3):033508, January 2008. doi: 10.1063/1.2825466. URL `http://link.aip.org/link/?APL/92/033508/1`.

[103] Joseph C. Doll, Sung-Jin Park, and Beth L. Pruitt. Design optimization of piezoresistive cantilevers for force sensing in air and water. *Journal of Applied Physics*, 106(6):064310, September 2009. doi: 10.1063/1.3224965. URL `http://link.aip.org/link/?JAP/106/064310/1`.

[104] Michael Ilg. *Entwicklung von selbstaktuierten piezoresistiven Siliziumresonatoren für die Echtzeit-Rasterkraftmikroskopie.* Master thesis. Ilmenau University of Technology, Germany, 2010.

[105] J. Schwartz, C. Bitterlich, V. Sarova, P. Michealides, J. Frank, Y. Sarov, I. Ivanov, J.-P. Zöllner, and I. W. Rangelow. Pressure, relative humidity and temperature measurement using microcantilevers with integrated bimorph actuator and piezo-resistive read-out. *Proceedings of the Integrated Project on Massively Parallel Intelligent Cantilever Probe Platforms for Nanoscale Analysis and Synthesis*, pages 307–316, 2010. ISSN 978-3-86991-177-9. URL `http://www.mv-buchshop.de/catalog/product_info.php/products_id/1650?osCsid=1a0j1sg47sb63k96f9gh20rtsh7pbkot`.

[106] T.B. Gabrielson. Mechanical-thermal noise in micromachined acoustic and vibration sensors. *Electron Devices, IEEE Transactions on*, 40(5):903–909, May 1993. ISSN 0018-9383. doi: 10.1109/16.210197. URL `http://ieeexplore.ieee.org/stamp/stamp.jsp?tp=&arnumber=210197&isnumber=5453`.

[107] K.Y. Yasumura, T.D. Stowe, E.M. Chow, T. Pfafman, T.W. Kenny, B.C. Stipe, and D. Rugar. Quality factors in micron- and submicron-thick cantilevers. *Journal of Microelectromechanical Systems*, 9(1):117–125, March 2000. ISSN 1057-7157. doi: 10.1109/84.825786. URL `http://ieeexplore.ieee.org/stamp/stamp.jsp?tp=&arnumber=825786&isnumber=17875`.

[108] H.-J. Butt and M. Jaschke. Calculation of thermal noise in atomic force microscopy. *Nanotechnology*, 6(1):1, January 1995. URL `http://stacks.iop.org/0957-4484/6/i=1/a=001`.

[109] F. R. Blom, S. Bouwstra, M. Elwenspoek, and J. H. J. Fluitman. Dependence of the quality factor of micromachined silicon beam resonators on pressure and geometry. *Journal of Vacuum Science & Technology B: Microelectronics and Nanometer Structures*, 10(1):19–26, January 1992. doi: 10.1116/1.586300. URL `http://link.aip.org/link/?JVB/10/19/1`.

[110] D. Lange, O. Brand, and H. Baltes. *CMOS Cantilever Sensor Systems: Atomic-Force Microscopy and Gas Sensing Applications.* Microtechnology and MEMS. Springer, 2002. ISBN 978-3-540-43143-5.

[111] Clarence Zener. Internal Friction in Solids. I. Theory of Internal Friction in Reeds. *Physical Review*, 52(3):230–235, August 1937. doi: 10.1103/PhysRev.52.230. URL `http://link.aps.org/doi/10.1103/PhysRev.52.230`.

[112] Clarence Zener. Internal Friction in Solids II. General Theory of Thermoelastic Internal Friction. *Physical Review*, 53(1):90–99, January 1938. doi: 10.1103/PhysRev.53.90. URL `http://link.aps.org/doi/10.1103/PhysRev.53.90`.

[113] C. Zener, W. Otis, and R. Nuckolls. Internal Friction in Solids III. Experimental Demonstration of Thermoelastic Internal Friction. *Physical Review*, 53(1):100–101, January 1938. doi: 10.1103/PhysRev.53.100. URL `http://link.aps.org/doi/10.1103/PhysRev.53.100`.

[114] M. R. Paul, M. T. Clark, and M. C. Cross. The stochastic dynamics of micron and nanoscale elastic cantilevers in fluid: fluctuations from dissipation. *Nanotechnology*, 17(17):4502, September 2006. URL `http://stacks.iop.org/0957-4484/17/i=17/a=037`.

[115] Hiroshi Hosaka, Kiyoshi Itao, and Susumu Kuroda. Damping characteristics of beam-shaped micro-oscillators. *Sensors and Actuators A: Physical*, 49(1-2):87–95, June 1995. ISSN 0924-4247. doi: DOI:10.1016/0924-4247(95)01003-J. URL `http://www.sciencedirect.com/science/article/B6THG-3YVCYNB-H/2/b15a7e4c279388cc90695e2f0ea1b283`.

[116] F. N. Hooge. 1/f noise sources. *Electron Devices, IEEE Transactions on*, 41(11):1926–1935, November 1994. ISSN 0018-9383. doi: 10.1109/16.333808. URL `http://ieeexplore.ieee.org/stamp/stamp.jsp?tp=&arnumber=333808&isnumber=7859`.

[117] G. Binnig, Ch. Gerber, E. Stoll, T.R. Albrecht, and C.F. Quate. Atomic resolution with atomic force microscope. *Surface Science*, 189-190:1–6, October 1987. ISSN 0039-6028. doi: DOI:10.1016/S0039-6028(87)80407-7. URL `http://www.sciencedirect.com/science/article/pii/S0039602887804077`. Proceedings of the Ninth European Conference on Surface Science.

[118] G. Masetti, M. Severi, and S. Solmi. Modeling of carrier mobility against carrier concentration in arsenic-, phosphorus-, and boron-doped silicon. *IEEE Transactions on Electron Devices*, 30(7):764–769, July 1983. ISSN 0018-9383. doi: 10.1109/T-ED.1983.21207. URL `http://ieeexplore.ieee.org/stamp/stamp.jsp?tp=&arnumber=1483108&isnumber=31879`.

[119] William E. Newell. Miniaturization of Tuning Forks. *Science*, 161(3848):1320–1326, September 1968. doi: 10.1126/science.161.3848.1320. URL `http://www.sciencemag.org`.

[120] O. Paul, O. Brand, R. Lenggenhager, and H. Baltes. Vacuum gauging with complementary metal–oxide–semiconductor microsensors. *Journal of Vacuum Science & Technology A: Vacuum, Surfaces, and Films*, 13(3):503–508, May 1995. doi: 10.1116/1.579774. URL `http://link.aip.org/link/?JVA/13/503/1`.

[121] Fredy Zypman. Internal damping for noncontact atomic force microscopy cantilevers. *Journal of Vacuum Science and Technology B: Papers from the 12th International Conference on noncontact Atomic Force Microscopy: Instrumentation and Method Development*, 28(3):C4E24–C4E27, May 2010. doi: 10.1116/1.3374736. URL `http://link.aip.org/link/?JVB/28/C4E24/1`.

[122] H.-W. Drawin. Theoretische Ableitung der Eichkurven für kontinuierlich anzeigende Reibungs- und Wirbelvakuummeter. *Vakuum-Technik*, 11(2):45–49, February 1962.

[123] W.K. Blake. The radiation from free-free beams in air and in water. *Journal of Sound and Vibration*, 33(4):427–450, April 1974. ISSN 0022-460X. doi: DOI:10.1016/S0022-460X(74)80227-0. URL `http://www.sciencedirect.com/science/article/B6WM3-4MJ527C-4/2/2bebfdd1e4e7ae89c87336ac3bf3dba0`.

[124] John Elie Sader. Frequency response of cantilever beams immersed in viscous fluids with applications to the atomic force microscope. *Journal of Applied Physics*, 84(1):64–76, July 1998. doi: 10.1063/1.368002. URL `http://link.aip.org/link/?JAP/84/64/1`.

[125] Cornelis A. Van Eysden and John E. Sader. Resonant frequencies of a rectangular cantilever beam immersed in a fluid. *Journal of Applied Physics*, 100(11):114916, 2006. doi: 10.1063/1.2401053. URL `http://link.aip.org/link/?JAP/100/114916/1`.

[126] I. W. Rangelow. Sharp silicon tips for AFM and field emission. *Microelectronic Engineering*, 23(1-4):369–372, January 1994. ISSN 0167-9317. doi: DOI:10.1016/0167-9317(94)90175-9. URL `http://www.sciencedirect.com/science/article/B6V0W-46K4PNN-CV/2/cb25188d75e396a0a7faaa20f4cf2c49`.

[127] I. Horcas, R. Fernández, J. M. Gómez-Rodríguez, J. Colchero, J. Gómez-Herrero, and A. M. Baro. WSXM: A software for scanning probe microscopy and a tool for nanotechnology. *Review of Scientific Instruments*, 78(1):013705, January 2007. doi: 10.1063/1.2432410. URL `http://link.aip.org/link/?RSI/78/013705/1`.

[128] Georg E. Fantner, Daniel J. Burns, Angela M. Belcher, Ivo W. Rangelow, and Kamal Youcef-Toumi. DMCMN: In depth characterization and control of AFM cantilevers with integrated sensing and actuation. *Journal of Dynamic Systems, Measurement, and Control*, 131(6):061104, November 2009. doi: 10.1115/1.4000378. URL `http://link.aip.org/link/?JDS/131/061104/1`.

[129] I. W. Rangelow, P. Grabiec, T. Gotszalk, and K. Edinger. Piezoresistive SXM sensors. *Surface and Interface Analysis*, 33:59–64, February 2002. doi: 10.1002/sia.1162. URL `http://onlinelibrary.wiley.com/doi/10.1002/sia.1162/pdf`.

[130] D. F. Ogletree, T. Ivanov, Y. Sarov, and I. W. Rangelow. SPM-SEM for In-Situ Nanoscale Characterization Using a Thermally-Actuated, Piezoresistive Cantilever Sensor under Dynamic Frequency Control. In *AVS 55th International Symposium: From Nano to Astronomical: The Science & Technology of Materials, Interfaces, & Processing*, October, 19 - 24 2008.

List of Figures

1.1 Self-actuating and self-sensing piezoresistive microscale silicon cantilever . . . 2

2.1 Self-actuating and self-sensing piezoresistive microscale silicon cantilever . . . 5
2.2 Two-layered beam: (a) unbent and (b) bent . . . 6
2.3 Temperature profile within beam depending on time: (a) DC drive power and (b) AC drive power at $f_d =$ 50 kHz . . . 13
2.4 Temperature change of temperature profile: (a) DC drive power and (b) static AC drive power at $f_d = 50$ kHz 13
2.5 Sinusoidal temperature change: (a) versus time depending on drive frequency; (b) versus dynamic AC drive power at $f_d = 1$ kHz . . . 14
2.6 Sinusoidal temperature change versus voltage . . . 14
2.7 (a) and (c) decaying drive DC and DC Wheatstone bridge output voltage; (b) and (d) increasing drive DC and DC Wheatstone bridge output voltage . . . 15
2.8 Multi-layered beam: (a) unbent and (b) bent . . . 17
2.9 Estimation of deflection of bent multi-layered beam . . . 21
2.10 (a) Beam curvature on pure beam bending and (b) deflection depending on DC drive power . . . 23
2.11 Oscillation of the beam: (a) non-oscillating beam; oscillating beam: (b) beam up and (c) beam down . . . 24
2.12 Forces acting on oscillating beam . . . 26
2.13 Resonance peak . . . 29
2.14 Non-uniform stress distribution within beam along length . . . 31
2.15 Piezoresistive coefficient: longitudinal (top) and transverse (bottom) . . . 36
2.16 Wheatstone bridge of four p-type silicon piezoresistors at base of beam in <110> crystallographic direction 38
2.17 Conducting traces of aluminium thin film heater, Wheatstone bridge, and conductive tip . . . 52
2.18 Cross-section of Wheatstone bridge and aluminium thin film heater . . . 53

3.1 Si dry etching #1: (a) SiO_2 as dark ring and Si as white point; (b) height of orientation marks consisting of leftovers of photoresist, 1.7 µm SiO_2, and ∼ 8 µm Si . . . 62
3.2 Si tip after SiO_2 wet etching #1 . . . 63
3.3 Tip sharpening: (a) the first time; (b) the second time . . . 65
3.4 Piezoresistive conducting traces: (a) photoresist developed and baked; (b) photoresist removed from bottom of structure; (c) SiO_2 etched, with photoresist ready for ion implantation . . . 67
3.5 Contact pads on piezoresistive conducting traces: (a) before and (b) after etching Si_xN_y and SiO_2; (c) etch profile (1 µm SiO_2 + 200 nm Si_xN_y + 100 nm SiO_2) . . . 70
3.6 Tip sharpening: the third time . . . 72
3.7 Profile of Al thin film heater . . . 73
3.8 (a) Bridge over Al thin film heater and contact pads on Al conducting traces (Si_xN_y etched); (b) profile of bridge . . . 75
3.9 Broken Au conducting traces for conductive tip . . . 76
3.10 Steps of Si_xN_y and SiO_2 dry etching #2: (a) before etching; (b) 75 min etching; (c) 90 min; and (d) 105 min etching . . . 77
3.11 Si membrane with light from bottom . . . 77
3.12 Cantilever: (a) overview and (b) tip with height of ∼ 5 µm and radius of ∼ 200 nm . . . 78
3.13 Mounted and bonded cantilever: Au wires covered with glob top . . . 79

4.1 Laboratory: (a) SEM, electronics, and control; (b) SEM with door open and set-up inside . . . 81
4.2 Schematic of the set-up in the SEM chamber . . . 83
4.3 Photograph of the set-up in the SEM chamber . . . 83
4.4 Oscillating cantilever (SEM image) . . . 84
4.5 Cantilever and stainless steel sample mount - configuration for AFM imaging . . . 84
4.6 Configuration of supply and data acquisition electronics for dynamic measurement . . . 85
4.7 Configuration of supply and data acquisition electronics for static measurement . . . 86
4.8 Configuration of supply and data acquisition electronics for crosstalk measurement . . . 87
4.9 Pre-bending of a self-actuating and self-sensing piezoresistive microscale silicon cantilever with a pre-bending angle of 4.7° (SEM image) . . . 89

4.10 Pre-bending angle of a self-sensing and self-actuating piezoresistive microscale silicon cantilevers versus beam thickness in vacuum 89
4.11 Frequencies of (a) first resonance and (b) second resonance versus beam thickness in vacuum 90
4.12 Fundamental frequency versus static AC drive power in vacuum and air 91
4.13 Comparison of fundamental frequency versus static AC drive power in air, given by PLLpro, DHO, and Sader 91
4.14 Fundamental frequency versus DC Wheatstone bridge power in vacuum 92
4.15 Quality factor versus beam thickness in vacuum 92
4.16 Normalized resonance peaks in vacuum 93
4.17 Resonance peaks in vacuum and air 93
4.18 Quality factor versus static AC drive power in vacuum and air 94
4.19 DC Wheatstone bridge output voltage versus DC drive power in vacuum and air 94
4.20 (a) AC Wheatstone bridge output voltage signal versus dynamic AC drive power in vacuum and in air; (b) maximum amplitude versus dynamic AC drive power in vacuum 95
4.21 AC Wheatstone bridge output voltage signal and maximum amplitude versus DC Wheatstone bridge power in vacuum 96
4.22 Actuation efficiency versus beam thickness in vacuum 96
4.23 Deflection sensitivity versus beam thickness in vacuum 97
4.24 DC Wheatstone bridge output voltage signal versus time 97
4.25 AC Wheatstone bridge output voltage signal versus time 98
4.26 Fundamental frequency versus time 98
4.27 Quality factor versus pressure 99
4.28 AC Wheatstone bridge output voltage signal versus pressure 99
4.29 Fundamental frequency versus pressure 100
4.30 Noise spectra showing Hooge noise and Johnson noise: (a) vacuum and (b) air 101
4.31 Frequency response from 10 Hz to 100 kHz 102
4.32 Tip sharpening by FIB: (a) before with diameter of 0.4 µm and (b) after with 0.1 µm (SEM images) 103
4.33 Electron beam deposition: (a) next to the original tip and (b) on the beam surface (SEM images) 104
4.34 (a) calibration grid and (b) oscillating cantilever above sample (SEM images) 104
4.35 Topography of calibration grid: (a) forward + (b) backward; $\Delta U_{out,bridge,AC}$ = 89 mVrms: (c) forward + (d) backward; Δf_1 = 500 mHz: (e) forward + (f) backward; $\Delta\varphi$ = -5.5 degree: (g) forward + (h) backward 106
4.36 Topography of calibration grid: (a) forward + (b) backward; $\Delta U_{out,bridge,AC}$ = 90 mVrms: (c) forward + (d) backward; Δf_1 = 136 mHz: (e) forward + (f) backward; $\Delta\varphi$ = -2.1 degree: (g) forward + (h) backward 107
4.37 Topography of flame-annealed evaporated gold film on mica [130] 108
4.38 (a) $\Delta U_{out,bridge,AC}$; (b) Δf_1 = 1 Hz (all forward); (c) SEM image [130] 109

List of Tables

2.1 Dimensions of layers of composite beam . . . 9
2.2 Parameters for heat transfer processes . . . 9
2.3 Thermal conductivity of materials . . . 9
2.4 Normalized heat transfer rates of layers . . . 10
2.5 Density and specific heat capacity of materials . . . 12
2.6 Parameters for temperature profile estimation . . . 12
2.7 Dimensions of layers of cantilever chip . . . 16
2.8 Thermal time constant and cut-off frequency of beam, and thermal time constant of cantilever chip . . . 16
2.9 Linear thermal temperature coefficient and modulus of elasticity of materials . . . 22
2.10 Parameters for deflection estimation . . . 22
2.11 Dimensions of layers of composite beam according to equivalent width method . . . 33
2.12 Fundamental frequency and spring constant . . . 33
2.13 Compliance coefficients and Young's modulus of single-crystal silicon [87] . . . 34
2.14 Temperature coefficients of elasticity and temperature coefficient of Young's modulus of single-crystal silicon [96] . . . 35
2.15 Resistivity and piezoresistive coefficients of n-type and p-type single-crystal silicon [101] . . . 37
2.16 Parameters for estimation of force sensitivity and value of force sensitivity . . . 41
2.17 Change of fundamental frequency and spring constant due to beam temperature change . . . 42
2.18 Parameters for calculation of minimum detectable force and displacement resolution . . . 46
2.19 Minimum detectable force and displacement resolution; noise forces; Johnson and Hooge noise . . . 47
2.20 Parameters for calculation of fractional frequency change . . . 51
2.21 Fractional frequency change, fundamental frequency in air, and transition pressure . . . 51

3.1 Properties of silicon wafer . . . 55
3.2 Fabrication process for cantilever (to be continued) . . . 56
3.2 Fabrication process for cantilever (to be continued) . . . 57
3.2 Fabrication process for cantilever (to be continued) . . . 58
3.2 Fabrication process for cantilever . . . 59
3.3 RCA clean procedure . . . 60
3.4 UV lithography procedure #1 (to be continued) . . . 60
3.4 UV lithography procedure #1 . . . 61
3.5 SiO_2 dry and wet etching . . . 61
3.6 Si dry etching #1 . . . 62
3.7 SiO_2 wet etching #1 . . . 62
3.8 Tip sharpening #1 . . . 64
3.9 UV lithography procedure #2 (to be continued) . . . 65
3.9 UV lithography procedure #2 . . . 66
3.10 SiO_2 wet etching #2 . . . 67
3.11 Ion implantation #1 . . . 67
3.12 SiO_2 wet etching #3 . . . 68
3.13 Ion implantation #2 . . . 68
3.14 Protective layer of SiO_2 and Si_xN_y . . . 68
3.15 Si_xN_y and SiO_2 dry etching #1 . . . 69
3.16 Tip sharpening #2 . . . 71
3.17 Al sputtering . . . 72
3.18 Al etching and melting down . . . 72
3.19 Bridge over Al thin film heater and piezoresistive Wheatstone bridge . . . 73
3.20 Protective layer of Si_xN_y . . . 73
3.21 UV lithography procedure #3 (to be continued) . . . 73
3.21 UV lithography procedure #3 . . . 74
3.22 Si_xN_y wet etching . . . 75
3.23 Au PVD . . . 75
3.24 SiO_2 wet etching #4 . . . 76

3.25 Si_xN_y and SiO_2 dry etching #2 . . . 76
3.26 Si wet and dry etching . . . 77
3.27 Si dry etching #2 . . . 78
3.28 Cantilever mounting . . . 78
3.29 Cantilever bonding . . . 79

4.1 Equipment, sources, measurement instruments, and software . . . 82
4.2 Environmental parameters of measurements . . . 88
4.3 Measurement errors . . . 88
4.4 Cantilever, sample, and imaging parameters . . . 104
4.5 Cantilever, sample, and imaging parameters [130] . . . 108